Multiwavelength observations of Active Galactic Nuclei from the radio to the hard X-rays

Multiwellenlängenbeobachtungen Aktiver Galaxienkerne von den Radiowellen bis hin zum harten Röntgenlicht

Der Naturwissenschaftlichen Fakultät
der Friedrich-Alexander-Universität
Erlangen-Nürnberg

zur

Erlangung des Doktorgrades Dr. rer. nat.

vorgelegt von

Tobias Beuchert
aus Erlangen

FRIEDRICH-ALEXANDER
UNIVERSITÄT
ERLANGEN-NÜRNBERG

NATURWISSENSCHAFTLICHE
FAKULTÄT

ERLANGEN CENTRE
FOR ASTROPARTICLE
PHYSICS

Als Dissertation genehmigt
von der Naturwissenschaftlichen Fakultät
der Friedrich-Alexander-Universität Erlangen-Nürnberg

Tag der mündlichen Prüfung:

Vorsitzender des Promotionsorgans: Prof. Dr. Georg Kreimer
Gutachter: Prof. Dr. Jörn Wilms
Prof. Dr. Matthias Kadler, Universität Würzburg

To my

mother, Hermia Szabo-Beuchert†,
and father, Roger Beuchert,

who have given me the strength and love
to be able to pursue my dreams,
to study one of them,
and to pass one milestone with the present work.

ZUSAMMENFASSUNG

Aktive Galaxien bilden eine besondere Klasse von Galaxien. Ihre Kerne sind die leuchtstärksten Objekte im Universum. Der Großteil der beobachtbaren Energie wird von einer kompakten Region im Zentrum dieser aktiven Galaxienkerne (AGN) abgestrahlt. Der Durchmesser der Galaxie selbst beträgt dabei mehrere Kiloparsec (1 parsec $\sim$ 3.3 Lichtjahre) und übersteigt den der kompakten Region um einen Faktor von mehr als 10^8. Im Zentrum dieser AGN befindet sich mit hoher Sicherheit ein supermassives schwarzes Loch, welches Millionen bis Milliarden Sonnenmassen in sich vereint. Schwarze Löcher sind in der Lage das Raum-Zeit Gefüge derart zu verzerren, dass auch Licht nicht aus ihrem Einflussbereich, dem Ereignishorizont, entweichen kann. Für schwarze Löcher der oben beschriebenen Masse, ist die Ausdehnung des Ereignishorizonts vergleichbar mit dem Orbit Plutos in unserem Sonnensystem. Ihr tiefes Gravitationspotential hat einen signifikanten Einfluss auf die Dynamik der Materie sowohl in direkter als auch in weiter entfernter Umgebung. Nach aktuellem Kenntnisstand beziehen AGN ihre enorme Energie aus Materie, die durch den Prozess der Akkretion ihren Drehimpuls verliert und damit in Richtung des gravitativen Zentrums kanalisiert wird. Damit bildet sich eine Scheibe um das schwarze Loch aus, welche in Folge der Akkretion thermische Photonen emittiert. Hochenergetische Elektronen in der sogenannten Corona in direkter Umgebung zur Scheibe sind in der Lage diesem thermischen Photonfeld mittels des inversen Comptoneffekts Energie zu übertragen. Das Resultat ist die beobachtete hochenergetische Röntgenemission, deren spektraler Verlauf einem Potenzgesetz entspricht. Die Geometrie der Corona ist Gegenstand aktueller Forschung. Man geht dabei von einer extrem kompakten Röntgenquelle aus, die sich hinter Gas und Staub innerhalb des AGN verbirgt und deren Strahlung durch eben diese absorbiert wird. Durch die Einstrahlung der Röntgenquelle bildet sich ein radialer Ionisationsgradient in dieser Materie aus, welche sich dabei höchstwahrscheinlich verstärkt in der Nähe der Akkretionsebene konzentriert. Die genaue Verteilung ist jedoch noch weitestgehend unbekannt. Das "unified paradigm" postuliert, dass sich die Kerne aktiver Galaxien intrinsisch gleichen und insbesondere ihre Röntgenspektren abhängig von der Orientierung der Kerne zum Beobachter verändert in Erscheinung treten. In ca. 20% benachbarter Galaxien finden sich darüberhinaus von magnetischen Feldern kollimierte Materieausflüsse, sogenannte Jets, entlang der Symmetrieachse der AGN. Diese Jets beschleunigen Materie bis hin zu relativistischen Geschwindigkeiten und emittieren dabei starke Synchrotronstrahlung im Radiolicht. Akkretierende schwarze Löcher können im weitesten Sinne mit Antrieben verglichen werden, deren Treibstoff (die akkretierte Materie) das Freiwerden immenser Energien (sowohl hochenergetisches Licht als auch beschleunigte Materie) bedingt und deren Wirkungsgrad den der Nuklearfusion um circa eine Größenordnung übersteigt.

Es ist Gegenstand dieser Arbeit die Prozesse in dieser kompakten Region näher zu verstehen, welche den Energiehaushalt von AGN und deren Umwelt maßgeblich bestimmen. Die folgenden Themen werden im Weiteren näher beleuchtet:

1. Die Verteilung absorbierender Materie in AGN, ihre Geometrie und Dynamik;
2. Die Lage, Geometrie und Dynamik der Corona;
3. Die Physik kollimierter Jets entlang ebendieser Pole;

Ich konzentriere mich dabei auf tiefgreifende Analysen der aktiven Galaxien NGC 3227, NGC 4151 und 3C 111. Die sogenannten Seyfert Galaxien NGC 3227 und NGC 4151 weisen keine Spuren prominenter Radiojets auf, sind aber bekannt für einen Röntgen-hellen Kern. Kollimierte Radiojets sind dagegen das Markenzeichen der sogenannten Radiogalaxie 3C 111, welche, im Gegensatz zu anderen jet-dominierten Galaxien, ebenfalls eine Studie des Kernes im Röntgenlicht gestattet. Diese drei Fälle decken weite Teile des bekannten Parameterraums aktiver Galaxien ab.

Die Massen derer schwarzen Löcher erreichen Werte zwischen 6×10^6 und 1.8×10^8 Sonnenmassen. Ihre Rotverschiebungen finden sich innerhalb $z \sim 0.003 - 0.05$, ihre Radioleuchtkräfte innerhalb $\sim 10^{36} - 10^{42}\,\mathrm{erg\,s^{-1}}$ (bei 5 GHz).

Der Schauplatz der Akkretion und Röntgenemission sowie der Haupteinflussbereich der absorbierenden Materie messen jedoch nur Bruchteile eines Parsecs im Zentrum der AGN. Diese Skalen können mit modernen Teleskopen nicht räumlich aufgelöst werden. Ich bediene mich in meiner Arbeit daher indirekter Methoden und analysiere die zeitliche Veränderung charakteristischer Röntgenspektren. Durch die Analyse großer Mengen archivierter Daten moderner allgebundener Röntgentenobservatorien, ist es mir möglich weitreichende Informationen über die Corona als Röntgenquelle, sowie die absorbierende Materie zu gewinnen.

Im Bezug auf die AGN NGC 3227 und NGC 4151 studiere ich insbesondere die zeitliche Entwicklung des absorbierenden, höchst variablen Mediums und dessen Ionisationsstruktur. Obwohl es auf Grund der allgemeinen Datenlage nicht gestattet ist die gesamte Bandbreite an Zeitskalen und damit ein lückenloses Bild der umgebenden Materie zu erfassen, erlauben die untersuchten Variabilitätszeitskalen von Tagen bis Jahren sowie eine Reihe verschiedenster Ionisationszustände das Bild bestmöglich zu rekonstruieren. Die Entdeckung einzelner Wolken, Filamente und Winde tragen dabei zu einem revolutionierten Bild der Strukturen in AGN bei, welche eine deutliche Verbesserung zur ursprünglichen Vorstellung eines homogenen torusähnlichen Bandes von Materie stehen.

Hervorzuheben ist die Galaxie NGC 4151. Eine Zerlegung ihres komplexen Röntgenspektrums trägt zwei herausragende Modellkomponenten zu Tage. Beide Komponenten beschreiben einen ähnlichen spektralen Verlauf des Kontinuums und sind nur bei guter Datenlage voneinander zu trennen. Die erste Spektralkomponente birgt weitreichende Informationen über die Variabilität des absorbierenden Mediums innerhalb des AGN. Die zweite Komponente zeugt von coronalem Röntgenlicht, welches den inneren Teil der Akkretionsscheibe beleuchtet und anschließend in unsere Sichtlinie reflektiert wird. Da sich hier das einfallende und reflektierte Licht durch den deutlichen Einfluss des Gravitationspotentials auf gekrümmten Bahnen bewegt, sowie energetisch unter dessen Einfluss steht, erlaubt das reflektierten Spektrums Rückschlüsse auf eine vertikal, entlang der Symmetrieachse des Systems ausgedehnte Corona. Diese stellt dabei womöglich auch die Basis des schwachen Jets dar, welcher im Radiolicht erkennbar ist.

Des Weiteren konzentriert sich meine Arbeit auf eben diese Jets, ihre Physik und Dynamik. Eine offene und relevante Frage ist hierbei die Interaktion des inneren Teils des Jets mit dem AGN als antreibende Kraft. Die Radiogalaxie 3C 111 erweist sich als prädestiniert, um diese Frage zu beantworten. Um den höchst kompakten inneren Teil des Jets abbilden zu können, stütze ich mich auf eine Anzahl großer Radioteleskope, welche, über den Globus verteilt, ein umfassendes Interferometernetzwerk bilden. Die Auflösung dieses Interferometers erreicht die Größenordnung von Millibogensekunden (Bruchteile eines Parsecs für den Fall von 3C 111), welche ein 50-faches besser ist als die des Hubble Weltraumteleskops. Die hohen Geschwindigkeiten der geführten Materie und der geringe Winkel (10–25°) des Jets zur Sichtlinie führt zu einer relativistischen Verstärkung der Synchrotronemission des uns zugewandten Jets. In meiner Arbeit analysiere ich einen umfassenden Datensatz monatlicher Beobachtungen über einen Zeitraum von fünf Jahren. Deutlich erkennbar sind einzelne kompakte Emissionsregionen, die am Fuß des Jets erscheinen und sich gleichförmig bis beschleunigt nach außen bewegen. Die physikalischen und dynamischen Prozesse innerhalb des magnetisierten Plasmas lassen sich hierbei ideal im polarisierten Radiolicht ergründen. Die Veränderung der elektrischen Vektoren einzelner Emissionskomponenten über die Zeit und die zunehmende Distanz vom Fuß des Jets, lässt mich auf das Vorliegen komplexer zugrundeliegender Prozesse schließen. In Frage kommen hierfür entweder eine strukturelle Veränderung der magnetischen Felder oder eine Interaktion propagierender Schockfronten mit einem Rekollimationsschock innerhalb des Jets.

In den meisten Fällen ist das gesamte abgestrahlte Spektrum vom Radiolicht bis hin zu den höchsten Energien in γ-Bereich dominiert durch die Emission dieser Jets. 3C 111 hingegen gestattet eine direkte Sichtlinie zum akkretierenden Kern und damit die Untersuchung dessen “Fußabdrucks” im Röntgenlicht. In meiner Arbeit ergänze ich vorhandene Studien und bestätige eine deutliche gegenseitige Abhängigkeit von Jets und akkretierter Materie am Beispiel von 3C 111. Dies geht zurück auf die Entdeckung einer Reihe von Einbrüchen der Röntgenemission, welche den beobachteten Auswurf neuer Emissionskomponenten bedingen. Gleichzeitig zu einer solchen Ejektion dokumentiere ich darüberhinaus einen erstmalig signifikanten γ-Strahlenausbruch, welcher eine solide Diskussion über den Ursprung der γ-Strahlung in 3C 111 erlaubt.

Diese Arbeit gewährt umfassende Einblicke in die mannigfaltigen Erscheinungsformen aktiver Galaxien und ihrer Kerne. Obwohl die hier studierten AGN durch die hohen Massen ihrer zentralen schwarzen Löcher nur Momentaufnahmen akkretierender Systeme darstellen, welche sich auf kosmologischen Zeitskalen entwickeln, erlaubt diese Schrift tiefe Einblicke in die zugrundeliegenden physikalischen Vorgänge. Sie ergründet fundamentale Aspekte im Zusammenhang mit dem Umsatz enormer Energien in AGN. Dazu gehören eine Studie der Akkretion und Rückkopplung von Materie sowie der Geometrie der Röntgenquelle innerhalb der aktiven Galaxienkerne, welche mit bildgebenden Verfahren nicht räumlich aufzulösen sind.

ABSTRACT

Active Galaxies form a peculiar type of galaxies. Their cores, the so-called “Active Galactic Nuclei” (AGN), are the most persistent luminous objects in the universe. The bulk of the radiated energy emerges from a compact region in the center of the AGN. This region is smaller by a factor of about 10^8 than its host galaxy, which measures multiple kiloparsecs (1 parsec $\sim$ 3.3 light years). Supermassive black holes (SMBHs) reside in the center of these nuclei, which concentrate millions to billions of solar masses roughly within the size of our solar system. These SMBHs deform space-time in a way that even light can not escape their event horizon. The deep gravitational potential of SMBHs also has significant influence on the environmental dynamics. From what we know, AGN draw their enormous energy from the disk-accretion of circumnuclear matter and the associated loss of angular momentum. This disk emits a thermal seed photon field that is Comptonized by coronal, highly energetic electrons to form an X-ray power-law spectrum. The geometry of the corona is still largely unknown. This compact X-ray source is thought to be embedded inside an envelope of gas and dust, which obscures our direct line of sight towards the nuclear X-rays. Due to the nuclear irradiation, the absorbing matter will form a radial ionization gradient. The overall distribution of matter likely concentrates to the plane of accretion but is largely unknown. The “unified paradigm” assumes that AGN are intrinsically identical. They may, however, appear differently depending on their orientation to the absorber. This would in particular imply different appearences of their absorbed X-ray spectra. In about 20% of nearby AGN, massive outflows and jets are also found along their polar axis. These jets are most likely magnetically collimated funnels and transport relativistic matter at nearly the speed of light. These jets are also a strong source of synchrotron radiation in the radio bands. Black-hole accreting systems can therefore be seen as extremely efficient engines located in the center of circumnuclear gas and dust that interface between the consumption and release of energy, both via radiation and mechanical outflows.

These processes, however, occur in a compact region that only measures fractions of a parsec. It can not be spatially resolved with modern X-ray instruments and telescopes, which is why most of its physics remains hidden from our direct perspective. It is the subject of this thesis to unveil the processes inherent to this region, which determines the global energy budget of AGN and their environment. I assess a number of open questions related to

1. the compact distribution of obscuring gas and dust in AGN, its geometry and dynamics
2. the location, shape and dynamics of the corona
3. the physics of the jetted outflows.

To do so, I concentrate on dedicated studies of the galaxies NGC 3227, NGC 4151 and 3C 111. The so-called Seyfert galaxies NGC 3227 and NGC 4151 show no signs of strong radio jets but a dominant, nuclear X-ray continuum. The so-called radio galaxy 3C 111, on the other hand, reveals both prominent jets but also a line of sight to the X-ray emitting nucleus. These three sources cover a medium range in redshift ($z \sim 0.003-0.05$) and black-hole mass ($M_\mathrm{BH} = 6\times10^6-1.8\times10^8\,M_\odot$), and a wide range in radio luminosity $L_{5\,\mathrm{GHz}} \sim 10^{36} - 10^{42}\,\mathrm{erg\,s^{-1}}$ and obscured fraction and therefore allow one to probe a significant part of the parameter space of AGN.

Because the compact X-ray emitting and absorbing region of AGN can not be spatially resolved, I use the indirect method of time-resolved X-ray spectroscopy. By analyzing and modeling a wealth of archival, high-resolution X-ray spectra from all modern space-born X-ray observatories, I can infer information on the X-ray emitting corona and the absorbing matter, i.e., address the first two questions in the list above.

In particular, I study the evolution of the column densities as well as ionization states of the

absorbing environments of NGC 3227 and NGC 4151. These turn out to be highly dynamical in both cases. Although it is challenging to probe all variability time scales, i.e., the entire distribution of matter at all distances from the black hole, the data reveal a wide range of time scales from days to years as well as a range in ionization states and therefore distances to the ionizing source. I find clouds, filaments and wind outflows as opposed to a homogeneous distribution of gas and dust. In both sources, the individual absorbing structures are most likely located at the inner side of the dusty absorbing medium or even closer to the illuminating center. By studying these different structures, this thesis contributes to a picture of AGN beyond the outdated and simplified idea of a near-homogeneous toroidally shaped gas distribution.

The peculiar Seyfert galaxy NGC 4151 reveals a rather complex spectrum. In this thesis, I find two main spectral components that are related to the circumnuclear absorber and the X-ray emitting corona. Both describe similar spectral features that are difficult to disentangle without a sufficiently high data quality. The first points towards a strongly variable absorber. The latter to reflection of coronal X-rays off the inner accretion disk in close vicinity to the black hole. Consequently, the effects of strong gravity lead to a reflection spectrum, where intrinsically narrow line features become relativistically broadened. This reflection component is best fitted with the most recent ray-tracing code `relxill`, which considers a realistic and self-consistent lamp-post geometry. The results presented here, strongly suggest an X-ray corona that extends along the system polar axis and potentially forms the base of a weak jet that has been observed in NGC 4151.

Eventually, I concentrate on collimated jets, their physics, and dynamics. As a target, I choose 3C 111, which is known for its powerful radio jets that carry enourmous amounts of energy far into the intergalactic medium. In order to address their physics and connection with the central engine one needs to study the inner jet in close vicinity to the launching site. I use the technique of “Very Long Baseline Interferometry (VLBI)” to image the radio emission of this region of 3C 111 with a network of large radio telescopes spread all over the globe. VLBI reaches a unique resolution of milliarcseconds (sub-parsec scales for 3C 111) that is 50-times better than that of the Hubble Space Telescope. The system orientation of 3C 111 results in a foreshortened jet that appears one-sided due to relativistic beaming. Monthly spaced observations over five years allow one to identify distinct emission features that follow a common downstream trajectory after being ejected from the jet-base. The additional information contained in the polarized light enables one to assess the underlying magnetic field structure of the inner jet of 3C 111. The downstream evolution of the electric vectors indicates complex processes that involve either structural changes in the magnetic field configuration of the jet or the interaction of propagating shocks with a standing shock of the underlying magnetohydrodynamical flow.

The electromagnetic emission of many jetted AGN is dominated by the synchrotron and Comptonized emission of their jets. 3C 111 is peculiar in a sense that it shows both strong and beamed jet emission and a prominent X-ray spectrum originating from the nuclear environment. This provides a great chance to improve our understanding on how jets are fed by matter from the compact accreting environment. I can confirm previous investigations of the disk-jet connection in 3C 111 and detect numerous dips of the X-ray flux followed by radio-jet ejecta. Also, I observe a significant γ-ray flare in coincidence with a radio ejection event, which allows one to discuss the much-debated γ-ray emitting site.

In summary, this thesis provides comprehensive insights into the various appearances of AGN. Due to the large masses of their black holes, AGN evolve on cosmological time scales, too long to be probed during the life time of a human being. Instead, this work illuminates a number of snap-shots of AGN and offers deep insights into all aspects of energy consumption and release, i.e., inflow and feedback processes and also touches upon the intrinsic geometry of these engines.

CONTENTS

CHAPTER 1

THE MULTIFACETED FACES OF AGN

AN INTRODUCTION

Active Galactic Nuclei (AGNs) are the most luminous ($L = 10^{44-48}\,\mathrm{erg\,s^{-1}}$; Lusso et al., 2012) objects in the present universe. Their host galaxies usually reach diameters of kiloparsecs [1 pc $\approx$ 3.2 light years] and emit a thermal spectrum dominated by starlight. AGN outshine the host-galaxy emission by many orders of magnitude from within a compact region on sub-parsec scales, where matter gets accreted onto the central Supermassive Black Hole (SMBH) with $M_{\mathrm{SMBH}} = 10^{6-9}\,M_{\odot}$ (Kaspi et al., 2000; Woo & Urry, 2002). As these compact objects can hardly be spatially resolved in the hearts of their host galaxies, their geometry, and composition has endured as long-lasting question. I outline the early steps towards an unification of the different appearances of AGN in Sect. 1.1. In Sect. 1.2, I provide the background on black holes and their role as engines in the process of accretion and feedback. Processes that lead to the observed spectral appearance of AGN from the radio to the γ-rays are also part of this section. I will eventually touch upon the global context of compact accreting object and their dynamic channels of energy release in Sect. 1.3.

1.1 THE UNIFYING PARADIGM OF AGN – A CRITICAL SUMMARY

Fath (1909) was the first to find emission lines in the active galaxy NGC 1068 that were reminiscent of planetary nebulae. Later, Carl Seyfert (Seyfert, 1943) studied the line emission of [O II] and H α for a number of these extragalactic "nebulae" and found in particular broad H α lines in their spectra. As we know today, these lines appear Doppler broadened due to the orbital motion of line-emitting material within the deep gravitational potential of the central black hole (e.g., Osterbrock, 1989). Until today, AGN are classified in the optical via their narrow forbidden and broad Balmer lines (e.g., Cid Fernandes et al., 2011, for a study using the SDSS). Most Seyfert galaxies are found nearby at intermediate flux levels. Quasars likely represent a class of extremely luminous AGN that are therefore also found at larger redshifts (Schmidt, 1963, for the first estimate of a redshifted line in 3C 273 at $z = 0.158$; see also Vanden Berk et al. 2001 for a study of AGN in the redshift range of 0.04–4.8 using 2200 optical SDSS spectra).

AGN split into a number of sub-classes that show characteristic properties in different wavebands such as luminous infrared galaxies (LIRGs), radio-loud or radio-quiet AGN, Low Ionization Nuclear Emission Line Regions (LINERs) and many more. AGN harbor a central SMBH that is fed by an accretion flow. The SMBH acts as an interface between the consumption and release of energy via different channels: the gravitational energy of the accreted matter is converted into strong X-ray radiation. Parts of this matter, however, are also ejected through powerful collimated jets and outflows. The common picture expects optically thin gas to prevail along the symmetry

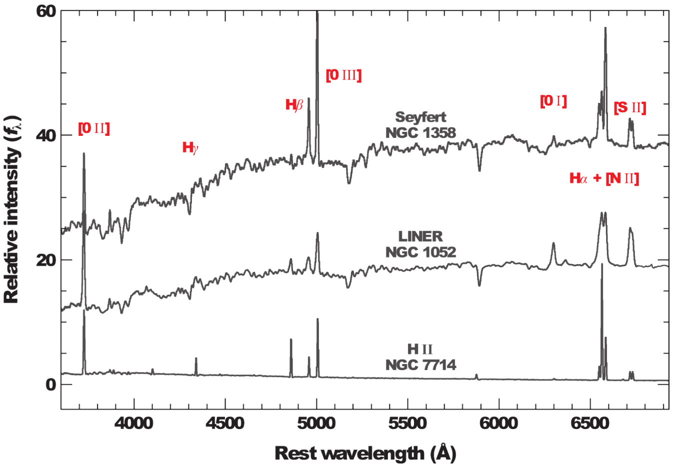

Figure 1.1. Example optical emission-line spectra for two Seyfert nuclei and a H II region for comparison. The figure is adapted from Ho (2008).

axis of this system, which emits the observed narrow forbidden lines. The corresponding region is therefore called the Narrow Line Region (NLR). The "unified paradigm" (Antonucci, 1993) proposed to embed the compact accreting object into an envelope of material that is orbiting the black hole at a range of distances. In a picture used by Urry & Padovani (1995), this material may form a "torus"-like structure. The phrase "the torus" has been frequently used by the community although no direct evidence yet exists for this specific geometry. Gas closer to the SMBH forms the Broad Line Region (BLR), which emits Balmer emission lines. Lines from this region appear Doppler-broadened to a distant observer. At larger distance, the paradigm expects neutral gas and dust to orbit the center of mass. The baseline of the unified paradigm is to identify sub-classes of AGN as different appearances of the same underlying object that one observes under varying inclination angles with respect to the line of sight. The most basic type 1/type 2 classification is based on whether the broadened lines from the nuclear region can be observed or not (Osterbrock, 1977, 1981; Osterbrock & Shaw, 1988).

In type 2 Seyferts, the distant "torus" may block the line of sight to the nucleus and absorb X-rays that are emitted from that region. This characterizes "Seyfert 2" galaxies. If there are no signs of X-ray absorption, the term "bare Seyfert 1" is chosen. The original classification as type 1/type 2 AGN, however, originates in the optical and is particularly solid as it only relies on a few assumptions on the AGN itself.

A typical Seyfert spectrum is characterized by strong forbidden ([O II], [O III] or [N II]) and Balmer (H α, H β) lines. It was early found that AGN can be separated from Galactic H II regions by their strong Balmer lines (Fig. 1.1). A strong and broad H β line relative to narrow, forbidden lines establishes the classification as type 1. Reverberation studies (Bentz et al., 2009a,b) could trace back this emission to the BLR close to the black hole. In contrast, a narrow H β line is indicative for a type 2 AGN, while this does not imply that the H α line is equally narrow. One defines intermediate classes as type 1.2, 1.5, and 1.8 (Osterbrock, 1977). This optical classification can be extended with three more observational parameters: the source luminosity, the grade of variability, and the radio loudness, which allows one to position all known classes of AGN in the diagram of Fig. 1.2.

AGN furthermore cover a wide range in radio loudness. For a long time quasars were believed to dominate the class of the most radio loud objects. Dedicated spectroscopic investigations, however, revealed that the majority of quasars is actually lacking strong radio emission (Kellermann et al., 2016). Optical photometric surveys have misleadingly identified those as blue Quasi-Stellar Objects (QSOs) – a term that is still used for radio-quiet quasars that show broad optical and UV emission lines and are similar to Seyferts at lower luminosities. Osmer & Smith (1976) could use these lines to improve the classification of AGN in large surveys. Independent of their radio

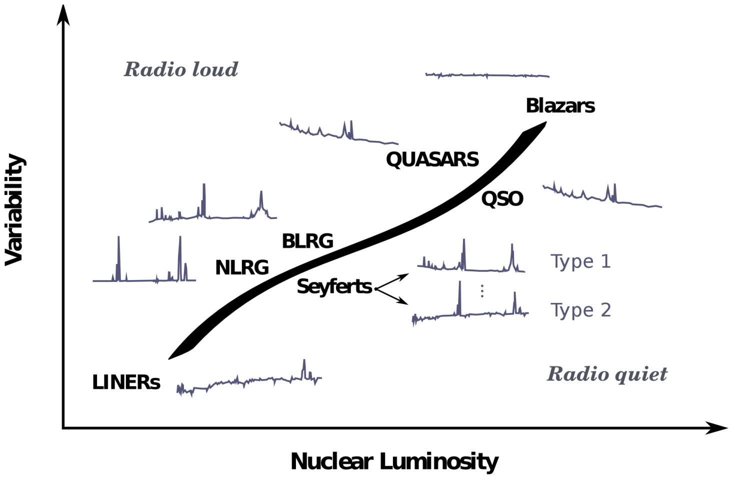

Figure 1.2. AGN classifications in the plane defined by the nuclear luminosity and variability. The figure shows optical spectra for the individual classes. The figure is adapted from Fotopoulou, S; PhD thesis

flux, quasars appear as exceptionally luminous objects in (optical) catalogs, for example, the SDSS (e.g., Schneider et al., 2003, 2010, while Schneider et al. 2010 make use of color cuts by Richards et al. 2009).

Luminous quasars that are lacking strong optical emission lines but instead show strong and highly variable radio emission are classified as blazars. This term was chosen in 1987 at the Pittsburgh conference on BL Lac objects (see also Stein et al., 1976). BL Lacs are a sub-class of blazars with properties similar to the prototypical blazar BL Lacertae. Blazars also emit polarized radiation (Angel & Stockman, 1980) from the radio to the optical. Due to the rapid radio-flux variability, their powerful radio jets (Readhead et al., 1979) are argued to point close to the line of sight, which enhances their relativistically beamed synchrotron radiation. This is confirmed for blazars by observations of one-sided and strongly foreshortened jets on (sub-)parsec scales at highest spatial resolution. Radio galaxies are believed to be yet another appearance of the same underlying object. Their jets are pointed away from our line of sight with inclination angles of up to 90°, which results in a radio morphology that extends on kiloparsec scales.

AGN that unify the properties of quasars and blazars, i.e., largest luminosities, strong optical emission lines as well as high radio luminosities are called “Flat Spectrum Radio Quasars” (FSRQs). It is a general feature of radio-loud AGN at lower luminosities that their optical emission lines become increasingly apparent. These objects are called Broad/Narrow line Radio Galaxies (B/NLRG) and are the radio-loud representatives of Seyfert galaxies. Eventually, LINERs contrast with blazars in all aspects. They are the least luminous (also called low luminosity AGN, LLAGN) and least variable AGN known, which show weak emission lines from low ionized gas and no radio emission.

For establishing a solid source classification across all detected AGN, it is indispensable to study large samples of galaxies as provided, e.g., by the SDSS (York et al., 2000; Richards et al., 2006b)[1]. Here, observations of the NLR are particularly useful: because of its large extent, it should be omnipresent and observable in both type 1 and type 2 AGN. Narrow emission lines are therefore an invaluable isotropic tracer in surveys. In particular, ratios of narrow forbidden line fluxes over Balmer line fluxes are useful to infer the excitation state of extragalactic sources in general. They define the Baldwin–Phillips–Terlevich (BPT) diagram, which has been used, e.g., by Kauffmann et al. (2003) and Kewley et al. (2006) to separate star forming galaxies and

---

[1] Note that surveys will never be absolutely homogeneous or complete and are always biased with respect to intrinsic properties. Flux-limited samples for example are biased towards a larger number of intrinsically bright objects. Also, the SDSS is particularly biased towards a clustering of galaxies at larger distances (Cresswell & Percival, 2009)

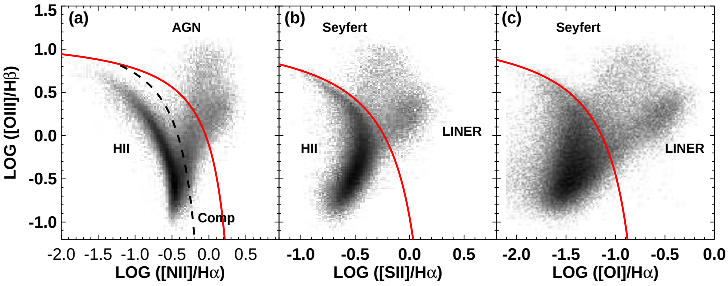

Figure 1.3. BPT diagnostic diagrams as adopted from Kewley et al. (2006) containing the optical information for a total of 85 224 galaxies from the SDSS above a S/N of 3. The dashed black line and the solid red line denote upper limits below which a galaxy can ionize its environment with starlight or, in the extreme case, with starburst activity. Above this line the AGN serves as additional source of ionization.

starbursts from AGN, which are further divided into Seyferts and LINERs as shown in Fig. 1.3.

Going one step further, one can add also the information on the radio emission (e.g., Best & Heckman, 2012; Tadhunter, 2016) to the results of BPT diagrams (Buttiglione et al., 2010; Smolčić, 2009) and thus separate two further states of AGN: Low/High Excitation Radio Galaxies (L/HERGs). Smolčić (2009) finds a bimodal distribution for Seyferts that show highly excited optical spectra and low excitation LINER galaxies (redder) in a plane of g-r color and stellar mass. Active galaxies are also known to be bright in the infrared (IR) with a luminosity that is comparable between Seyfert galaxies and quasars (Sanders & Mirabel, 1996) and is indicative for a high excitation state. The BPT diagram was therefore further complemented with IR data by Morić et al. (2010), which utilized the separation of quasar states. Richards et al. (2006a) solely concentrate on the IR bands by using *Spitzer* data and can show an even more pronounced bimodiality between inactive galaxies, stars, and quasars in color-color and color-magnitude diagrams. As part of the EXTraS project (De Luca et al., 2016), Kreikenbohm et al. (2015) use information from multiple wavebands to push forward the classification of the 3XMM X-ray catalog using a machine learning approach (see also Farrell et al., 2015, for an application of a machine learning algorithm to the 3XMM catalog).

The classification of samples based on radio-loudness, IR/optical line emission and color is solid and makes no a priori assumptions on the geometry of an AGN although using emission lines from the NLR as isotropic tracers[2]. Aside from their extended NLR, AGN are extremely compact and have not yet been spatially resolved (see, however, Tristram et al., 2014, for first attempts). Their internal dynamics could so far only be traced using indirect methods such as time-resolved spectroscopy and numerical simulations. A related mistake that has often been done is to mix the original optical type 1/type 2 classification with X-ray unabsorbed/absorbed Seyfert 1/Seyfert 2 galaxies. Essentially, this means that one has misused a generic classification that relies only on isotropic tracers to make statements on the geometry and inclination of the system and therefore also on the line-of-sight dependent absorption of nuclear X-rays. It is also a weak point of the traditional unifying paradigm to use the simplified toroidal geometry to classify AGN by their strength of absorption. The participants at the AGN conference "What's in a name"[3] positioned themselves strongly against the classical orientation-based unification as well as "the torus". In contrast, many observations (e.g., Risaliti et al., 2011; Kaastra et al., 2014; Markowitz et al., 2014; Beuchert et al., 2015) imply a more a dynamical than static torus with orbiting clouds and clumps as well as outflowing filamentary structures. Models that support these observations involve a clumpy nature of the dusty torus (Elitzur & Shlosman, 2006; Nenkova et al., 2008a; Asensio Ramos & Ramos Almeida, 2009), which may form a continuous structure with the inner, dust-free BLR (e.g., Elitzur, 2007; Gaskell et al., 2008) as well as outflows that, e.g., Hopkins et al. (2016) observe in simulations. These outflows may even form

---

[2] The NLR of prominent AGN are spatially coincident with ionization cones that spread along the polar axes of AGN (e.g., Wang et al., 2011a).

[3] `http://www.eso.org/sci/meetings/2016/AGN2016.html`

and support the obscuring structures themselves (e.g., Czerny & Hryniewicz, 2011). Nicastro (2000) postulates a strong relation between the accretion rate and BLR cloud properties such as the FWHM of the emitted Balmer lines (Nicastro et al., 2003; Laor, 2003). These galaxies are also called "true Type 2" galaxies, where broad optical lines are not hidden by a molecular outer torus but are intrinsically absent due to the break-down of the BLR at lowest luminosities and accretion rates (see, however, Antonucci, 2012). On the other hand, Balmaverde & Capetti (2014) find evidence for broad lines even in low luminosity AGN. The torus as the dusty phase of a continuous obscuring distribution of matter may equally be sustained by mass outflows that are limited by the accretion rate. In this picture, the torus should therefore also break down at lowest luminosities (Elitzur & Shlosman, 2006; Elitzur, 2007; Hönig & Beckert, 2007; Elitzur & Ho, 2009). At highest luminosities, strong mass outflows may eventually lead to a "receding torus". Observational evidence comes from Lawrence (1991), who finds a type 2 fraction of $\propto L^{-1/2}$ and similarly by Simpson (2005), who independently demonstrates a lack of type 1 relative to type 2 Seyfert galaxies at low luminosities. Yet another indication for the torus to be sustained by radiation pressure comes from cosmological population studies of the obscured fraction of AGN by Ueda et al. (2014) and Buchner et al. (2015). These results complement the previously mentioned observational implications of a clumpy, filamentary and dynamical absorbing environment. This can also explain why many galaxies seem to switch between a Seyfert 1 and Seyfert 2 classification, i.e., unabsorbed and absorbed states, on short time scales (Elitzur, 2007). On the other hand, recent results also point towards an evolutionary relation between Seyfert 1 and Seyfert 2 galaxies by studying their environment with the SDSS (Villarroel & Korn, 2014).

As a result of these complexities, it is important to be cautious about using the term "unification" and "the torus". Instead, one needs to study the various aspects and appearances of AGN across the electromagnetic spectrum. In a personal interpretation, the unifying paradigm is not obsolete in general but has to be seen from a different, more conservative point of view. This approach would favor simple relations such as the type 1/type 2 dichotomy and results from sample studies.

While deep surveys are indispensable for understanding the bigger picture, I concentrate on dedicated studies of four AGN: the two Seyfert galaxies NGC 3227 and NGC 4151, and the two radio galaxies 3C 111 and PKS 1718−649. These sources cover a wide range in luminosity and radio loudness (see also Fig. 1.2). They are the ideal objects to consolidate and extend on knowledge that has been gained from larger samples. Before presenting the results, I will introduce the concept of AGN engines and their components.

1.2 AGN ENGINES AND THEIR ENVIRONMENT

In the following, I will outline in detail what is known about AGN as cosmic engines, address questions on how the energy throughput works and in particular how one can observe AGN in action.

1.2.1 BLACK HOLES

Meier (2012) introduces black holes as massive and highly effective engines that interface between the consumption and release of energy. Black holes cover a wide range of masses from stellar-sized to SMBHs with 10^6 to 10^9 solar masses. The highly efficient process of accretion exploits the large reservoir of energy given by the accreted mass falling into the deep gravitational well of the black hole and the released angular momentum of that mass (Shakura & Sunyaev, 1973). Black holes essentially concentrate their mass inside a singularity and influence spacetime in their close vicinity.

For flat spacetime, one can describe the proper distance ds between two events in the four-

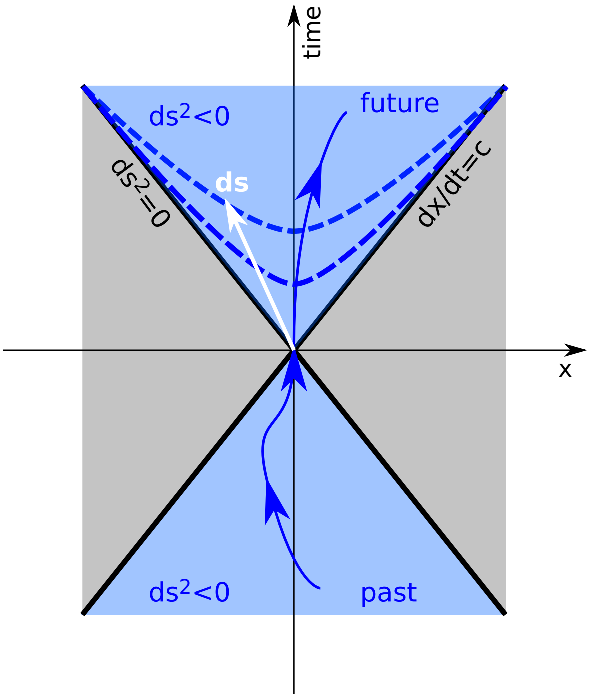

Figure 1.4. Visualization of the Minkowski metric in a *dt*-*dx* diagram (see for example Meier, 2012). The blue light cone encloses "time-like" geodesics like the one shown as blue solid line and encloses events that will affect a present observer in the center or that will be affected by an event happening right now; the gray region contains events and "space-like" geodesics that are causally disconnected. Inside the cone, $ds < 0$. The border of the light cone marks the limit for propagating information and is given by a straight line of events at different dx that emit light traveling with $v = \mathrm{c}$ ("light-like" geodesics). Events with the same proper distance ds lie on hyperbolas, while the light cone is an extreme hyperbola with $ds = 0$. Although the edge of the cone includes a range of events at different coordinates x, all appear to happen at the same present time for the observer.

dimensional Minkowski metric. Such events are defined in space and time. The metric therefore carries one time dimension and three dimensions of Euclidean space (x, y, z). It is given by $g_{\mu\nu} = \mathrm{diag}(-1, 1, 1, 1)$ with $g_{tt} = -1$ and $g_{rr} = \mathrm{diag}(1, 1, 1)$. The corresponding line element ds (see Fig. 1.4) is

$$\left(\frac{ds}{d\tau}\right)^2 = g_{\mu\nu}\frac{dx^\mu}{d\tau}\frac{dx^\nu}{d\tau}, \tag{1.1}$$

where $d\tau$ is the proper time that passes between two events.

The Schwarzschild metric (Schwarzschild, 1916) deviates from the Minkowski metric in presence of strong gravity, i.e., in close vicinity of black holes. This metric is a solution of the Einstein equation for a point mass. It is expressed in spherical coordinates (t, r, θ, ϕ) with the line element of the first two dimensions

$$ds^2 = -c^2\left(1 - \frac{r_\mathrm{S}}{r}\right)dt^2 + \left(1 - \frac{r_\mathrm{S}}{r}\right)^{-1}dr^2. \tag{1.2}$$

At the so-called event horizon (EH), "Schwarzschild radius" or gravitational radius r_g

$$r_\mathrm{EH} = r_\mathrm{S} = \frac{2GM}{c^2} \quad \text{or} \quad r_\mathrm{g} = 2r_\mathrm{S}, \tag{1.3}$$

the matrix shows a singularity for $g_{tt} \to 0$ and $g_{rr} \to \infty$. This defines the "size" of the black hole. The event horizon of a SMBH with $10^9\,M_\odot$ would just fit into the orbit of Pluto. The physics around $r = r_\mathrm{S}$ can be best described with help of the light cones in Fig. 1.5 together with some light-like geodesics. We as observers are located at some large distance $r \gg r_\mathrm{S}$ from the black hole. A spacecraft approaches the black hole and continuously emits radio signals. As it comes closer, these signals can still reach us but the time delays dt reach towards infinity, i.e., time decelerates and eventually appears to freeze out for us as observer. When solving Eq. 1.2 for a light-like line element with $ds^2 = 0$, one finds $v = dr/dt \to 0$, i.e., the spacecraft seems to stop. Corresponding geodesics close to the black hole can be calculated as described, for example, by Falkner (2013) and Dauser et al. (2010). It turns out that spacetime close to the black hole is strongly deformed and photons move on curved trajectories. The closer the spacecraft approaches

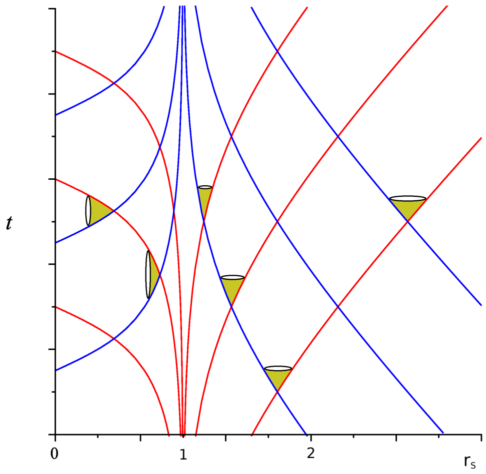

Figure 1.5. Evolution of light cones around the EH of a black hole together with the photon paths. The figure is adapted from Quinzacara & Salgado (2012).

the black hole, the narrower the light cones become and flip at the EH, i.e., the cone now points in spatial direction and there exists no geodetic of photons that can reach the observer any more.

The Kerr metric describes black holes that carry angular momentum (Kerr, 1963). The coordinates of the metric tensor form derived quantities. Again, the EH is defined via a singularity in the metric with $g_{tt} = 0$ and $g_{rr} \to \infty$. The first condition satisfies

$$r_0 = \left(1 + \sqrt{1 - a^2 \cos^2\theta}\right) r_\mathrm{g}, \tag{1.4}$$

the second

$$r_\mathrm{EH} = \left(1 + \sqrt{1 - a^2}\right) r_\mathrm{g}, \tag{1.5}$$

where a is the dimensionless angular momentum J/M ranging between 0 and 1, r_0 stands for the outer "ergosphere" and r_EH the radius of the EH. Both values describe singularities. In Kerr metric, the EH forms an ellipsoid, which equals the outer ergosphere on the z-axis. In the x/y-plane, the outer ergosphere extends to $\sim 2r_\mathrm{EH}$. The ergosphere corresponds to the space contained in between r_EH and r_0.

Orbits can be derived by considering the centrifugal force that is balanced by gravity. Under consideration of the Kerr metric, one finds the orbital motion $v_\phi = f(\Sigma, \Delta, r, r_\mathrm{g}, a)$ in the equatorial plane to be a function of quantities defining the Kerr metric (e.g., Bardeen et al., 1972; Meier, 2012). Note that for $r \to r_\mathrm{s}$, the orbital speed reaches infinity. Photon orbits (light-like geodesics) are found at $r_\mathrm{ph} = 1\,r_\mathrm{g}$ for prograde co-rotation of the photon with the black hole spin[4] and at $r_\mathrm{ph} = 4\,r_\mathrm{g}$ for retrograde rotation (e.g., Meier, 2012). The photon orbit also defines the inner orbit below which neither mass-rich nor mass-less particles can escape. The innermost stable circular orbit (ISCO or the orbit of "marginal stability" r_ms) of particles can be calculated by considering angular momentum conversion and the solution for v_ϕ (e.g., Bardeen et al., 1972). The ISCO is a function also of spin (Fig. 1.6). The radius r_ms equals the ISCO in the Schwarzschild metric for $a = 0$, approaches the EH for a maximal black hole spin with prograde orbits and goes up to $9\,\mathrm{r_g}$ for retrograde orbits.

The peculiarity of the Kerr metric is that it defines two singularities, the ergosphere and EH, which differ in the equatorial plane (e.g., Misner et al., 1973). The particles inside the ergosphere can still escape the gravitational potential but are forced to co-rotate with the spacetime of the spinning black-hole, also known as "frame dragging" (e.g., Meier, 2012), which provides the basis for the formation of jets (see Sect. 1.2.5.2). This goes back to the off-diagonal metric element $g_{\phi t}$ being non-zero while time points in direction of rotation. Also, g_{tt} switches sign from < 0 to > 0 at the ergosphere, which enables negative energies and negative redshifting for particles crossing

---

[4] Note that a distance of $1\,r_\mathrm{g}$ can never be reached (Thorne, 1974).

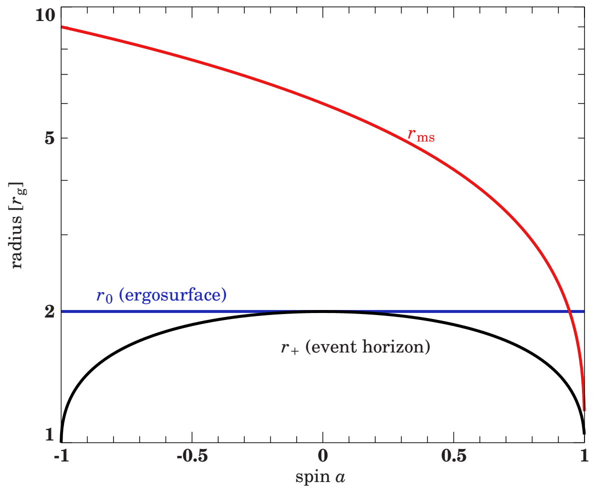

Figure 1.6. Dependence of the EH (here: r_+), radius of the ergosphere (r_0) and the ISCO (r_{ms}) in the equatorial plane (adopted from Dauser, 2010). Here, also negative spins are considered for black holes spinning in retrograde direction with respect to the accretion disk.

the ergosphere. This is called the "Penrose process" (Penrose, 1969), which is also described in Sect. 1.2.5.2.

1.2.2 POWERING AGN VIA ACCRETION

Accretion of matter produces most of the energy released by AGN (Shakura & Sunyaev, 1973). This process can be about 10 to 50 times more efficient than nuclear fusion. For material to be accreted, angular momentum needs to be transported outwards. Viscosity is the main mechanism to do so and to form an accretion disk. In contrast to microphysical friction, magneto-rotational instability (MRI, Balbus & Hawley, 1991) is the most effective contributor to viscosity (Simon et al., 2011). The effect of viscosity on matter inside the disk is usually described by the non-linear diffusion of the surface density Σ (Pringle, 1981) which carries the units of cm^{-2}, i.e.,

$$\frac{\partial \Sigma}{\partial t} = \frac{3}{r}\frac{\partial}{\partial r}\left[r^{1/2}\frac{\partial}{\partial r}\left(\nu r^{1/2}\Sigma\right)\right]. \tag{1.6}$$

It describes how the drag caused by the viscosity ν acting on the gas at a certain radius r causes the gas to loose gravitational energy and sink inwards. For a constant viscosity ν, Pringle (1981) can further show that a ring of optically thick gas around a black hole with a certain angular momentum will spread out radially and form a thin disk on the viscous time scale $t_{\mathrm{visc}} \sim r/v_{\mathrm{r}}$ where v_{r} is the radial drift velocity. The scale height can be derived as $c_{\mathrm{s}}/v_{\mathrm{K}}\, R \ll R$, where c_{s} is the sound speed (proportional to $\rho^{-1/2}$) and R the radius of a mass element moving at the Keplerian speed v_{K}.

For deriving the diffusion equation (Eq. 1.6) one makes use of the relations for conservation of mass and angular momentum. Mass conservation can be described by the continuity equation

$$r\frac{\partial \Sigma}{\partial t} + \frac{\partial}{\partial r}\left(r\Sigma v_{\mathrm{r}}\right) = 0, \tag{1.7}$$

where the change in surface density with time is just given by the radial change of the mass enclosed in an annulus within $[r, r + \Delta r]$. The equation for conservation of angular momentum is given by

$$r\frac{\partial}{\partial t}\left(\Sigma r^2 \omega\right) + \frac{\partial}{\partial r}\left(r\Sigma v_{\mathrm{r}} r^2 \omega\right) = \frac{1}{2\pi}\frac{\partial}{\partial r}G, \tag{1.8}$$

where $\omega(r)$ is the angular velocity at the radius r and G corresponds to the torque resulting in matter to drift with v_{r} due to the outward loss of angular momentum and the viscous drag. In steady state, i.e., $\partial/\partial t = 0$, Eq. 1.7 results in a constant accretion rate over radius with

$$\dot{M} \sim -v_\mathrm{r} r \Sigma. \tag{1.9}$$

With Eq. 1.8 it follows that

$$\nu\Sigma = \frac{\dot{M}}{3\pi}\left[1 - \left(\frac{r_\mathrm{ISCO}}{r}\right)^{1/2}\right]. \tag{1.10}$$

Here, one assumes a thin disk that extends all the way down to r_ISCO, which corresponds to $6\,r_\mathrm{g}$ for a non-rotating Schwarzschild black hole and $1\,r_\mathrm{g}$ for a maximally rotating black hole (Kerr, 1963; Shapiro & Teukolsky, 1983; Bardeen et al., 1972; Jefremov et al., 2015). The authors in particular discuss that the orbit of a mass element inside the ISCO cannot be Keplerian, i.e., energy dissipation via viscous heating does not work below that radius. For slim disks or advection dominated accretion flows (ADAFs), where the energy is advected into the disk instead of radiated away, the inner side of the disk can, however, also be located below the ISCO (Abramowicz & Fragile, 2013). For a rotating Kerr black hole, the ISCO will change with spin (Bardeen et al., 1972; Jefremov et al., 2015), although deviations of the actual inner side of the disk from the ISCO may exist due to magnetic coupling (Gan et al., 2007).

The energy lost via viscous heating is dissipated via thermal radiation. The dissipated energy at both sides of the disk is given by

$$D(r) = \frac{1}{2}\nu\Sigma\left(r\frac{d\omega}{dr}\right) = \frac{3GM\dot{M}}{8\pi r^3}\left[1 - \left(\frac{r_\mathrm{ISCO}}{r}\right)^{1/2}\right], \tag{1.11}$$

if one inserts the Keplerian angular velocity $\omega_\mathrm{K} = \sqrt{GM/r^3}$. For an optically thick α-disk[5] (Shakura & Sunyaev, 1973), the Stefan-Boltzmann law holds with $D(r) = \sigma T(r)^4$ and

$$T(r) = \left(\frac{3GM\dot{M}}{8\pi r^3 \sigma}\left[1 - \left(\frac{r_\mathrm{ISCO}}{r}\right)^{1/2}\right]\right)^{1/4} \tag{1.12}$$

holds for the temperature distribution of the disk.

The emitted spectrum — Assuming that the entire energy is dissipated via viscous heat, one can insert the temperature distribution (Eq. 1.12) into the Planck law. It turns out that observed UV spectra are well described by the superposition of multiple blackbody spectra at different temperatures, just as expected for a multi-temperature disk. A corresponding model has been successfully applied to data of Galactic X-ray binaries (Mitsuda et al., 1984) that form accretion disks similar to AGN but are much closer to Earth and therefore easier to observe. Later, Gierliński et al. (1999) corrected for the inconsistency that the temperature in Eq. 1.12 becomes unrealistically high at smallest radii. Instead of requiring the orbital angular speed to be Keplerian down to r_ISCO, they apply a pseudo-Newtonian potential (Paczyńsky & Wiita, 1980). In Fig. 1.7 a typical multi-temperature disk spectrum is illustrated with a contribution from the hot inner parts shaping the spectrum in the far-ultraviolet (FUV) as well as the outer parts contributing in the near-ultraviolet (NUV). For a typical AGN with a maximally spinning black hole of $M_\mathrm{BH} \sim 10^7\,M_\odot$, the temperature at the ISCO is about 10^{5-6} K. On top, the blue spectrum shows a disk-blackbody spectrum that is Comptonized in a corona around the disk and reaches up to the X-rays. Observational bias comes from Galactic absorption and dust extinction, which obscured our view onto the hard UV and soft X-rays below ~ 0.1 keV. This makes it particularly difficult to constrain the inner disk temperature, which is a common parameter, for example of the `diskpn` model. This temperature decisively determines the disk luminosity, which

---

[5] In the accretion disk theory of Shakura & Sunyaev (1973), the parameter α corresponds to the efficiency of angular momentum transport in the disk and can be set as $\alpha \sim 1$.

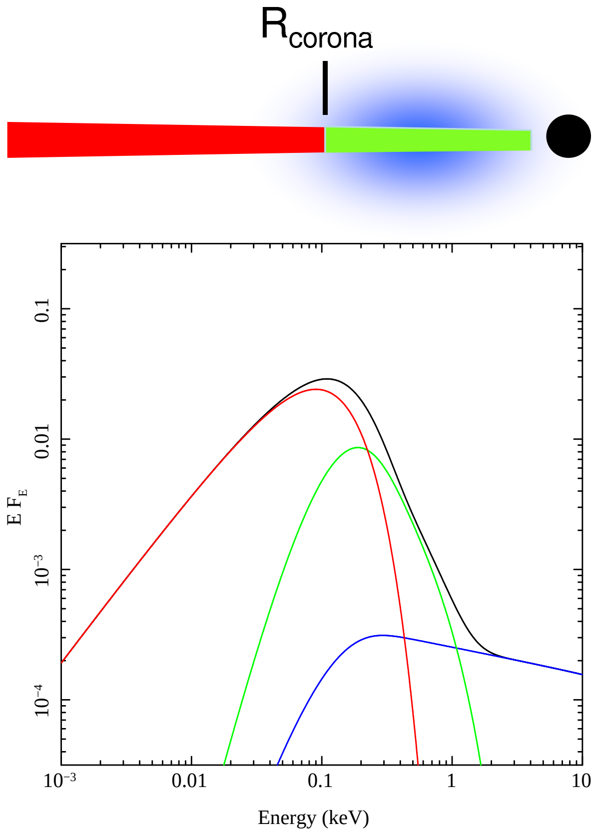

Figure 1.7. Schematic composition of a multi-temperature blackbody spectrum (*bottom*) as adopted from Done et al. (2012). The red and green spectra correspond to the thermal contributions from the outer and inner accretion disk, while the higher energetic, green spectrum also suffers Compton losses. The blue spectrum corresponds to the Comptonized disk spectrum. Note that the geometry of the corona most likely deviates from the one shown in this figure as I will outline in Sect. 3.2.

is a main contributor also to the bolometric luminosity, L_{bol} (Vasudevan et al., 2010).

The Eddington luminosity — Observations tell that the energy production via accretion cannot be infinite. The limiting factors are (1) the matter to be accreted and (2) the produced radiation pressure itself, which counteracts the gravitational infall of matter. The Eddington luminosity L_{Edd} is a limit with respect to isotropic nuclear radiation. It can be derived by equating the outward force of radiation $F_{\mathrm{r}} = \sigma_{\mathrm{T}} F/c$ (F is the photon flux) with the inward force of gravity. One finds

$$L_{\mathrm{Edd}} = \frac{4\pi G M m_{\mathrm{p}} c}{\sigma_{\mathrm{T}}} \approx 1.3 \times 10^{47} \left(\frac{M}{10^9\, M_{\odot}} \right) \mathrm{erg\, s^{-1}}. \tag{1.13}$$

There is a direct proportionality of the accretion rate $\dot{M}$ (Eq. 1.9) and the radiated disk luminosity L. One can therefore also write that $L_{\mathrm{Edd}} = \epsilon \dot{M}_{\mathrm{Edd}} c^2$ with the radiative efficiency ϵ, i.e., it holds that

$$\frac{L}{L_{\mathrm{Edd}}} \propto \frac{\dot{M}}{\dot{M}_{\mathrm{Edd}}} \propto \frac{\dot{M}}{M}. \tag{1.14}$$

The efficiency $\epsilon = r_{\mathrm{g}}/R$ (e.g., Meier, 2012) for the conversion of gravitational into radiated energy changes with black-hole mass ranging between ~0.03 for $M = 10^7\, M_{\odot}$ to ~0.4 for $M = 10^9\, M_{\odot}$ (Davis & Laor, 2011) and also depends strongly on the ISCO.

1.2.3 THE X-RAY CORONA

All studies of the compact emission of AGN cores essentially assume a corona of hot electrons that is located in the vicinity of the disk. Its geometry and distance from the disk are still widely discussed (e.g., Dauser et al., 2012; Svoboda et al., 2012, and references therein).

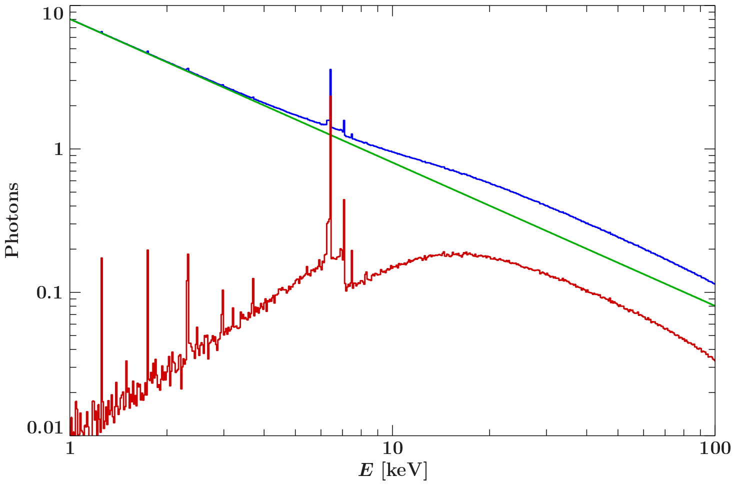

Figure 1.8. Reflected spectrum (red) due to the irradiation of a semi-infinite slab with an incident power-law of slope $\Gamma = 2$ (green). The reflected spectrum is averaged over all inclination angles and calculated using a Monte Carlo code (Eikmann et al., 2012). The sum of both the incident and reflected spectra is shown in blue.

1.2.3.1 COMPTONIZATION AND REFLECTION PROCESSES

One can show that a Maxwellian distribution of hot coronal electrons can Comptonize the thermal disk seed photons (e.g., Haardt, 1993; Titarchuk, 1994; Dove et al., 1997b; Belmont et al., 2008). Multiple inverse Compton upscattering processes lead to a power-law distributed X-ray spectrum with the flux

$$F(E) = N\,E^{-\Gamma}, \tag{1.15}$$

where Γ is the photon index (Rybicki & Lightman, 2004). For AGN, Lusso & Risaliti (2016) independently confirm that disk and corona must be physically connected: they manifest a strong and solid correlation between the luminosities at 2 keV (3XMM catalog) and 2500 Å (SDSS catalog) probing the UV accretion disk. The details on the derivation can be found in Beuchert (2013). Thermal Comptonization processes naturally predict a cutoff (Rybicki & Lightman, 2004), which is found at the energy $E_{\mathrm{cut}} \sim 2$–$3\,kT_{\mathrm{e}}$ (García et al., 2015; Petrucci et al., 2001) with the electron temperature T_{e}. This is because per single scattering, no more than the available electron energy can be transferred to the photon field.

The Comptonized power law can both be observed directly or as reflected spectrum off the disk. The reflected spectrum offers plenty of information on the disk and its ionization structure. For example, the cutoff energy has been measured in data of the *Compton Gamma Ray Observatory* (Zdziarski et al., 2000), *INTEGRAL* (Malizia et al., 2014), *Swift*/BAT (Vasudevan et al., 2013) as well as more recently, with *NuSTAR* (e.g., Marinucci et al., 2014; Baloković et al., 2015). Figure 1.8 shows the spectra incident to and reflected off a semi-infinite slab. The characteristic continuum shape of the disk-reflected spectrum above ~ 7 keV is the result of two competing mechanisms, i.e., photoelectric absorption of soft X-rays (e.g., George & Fabian, 1991; García et al., 2013) and scattering processes of hard X-rays. The cross section for photoabsorption goes with E^{-3} and is therefore most dominant at low energetic X-rays ($\lesssim 10\,keV$) due to larger abundances of high-Z elements in this energy regime. The characteristic Compton hump around 20 keV is the product of near-elastic (Thomson) scattering of photons out of the line of sight, while at energies above $\sim$10 keV, Klein-Nishina quantum corrections are essential to describe anisotropic and inelastic scattering (e.g., Eikmann et al., 2012). This hump has been early discussed for cold reflecting matter in AGN disks (Matt et al., 1991; Haardt & Maraschi, 1991) and later also for ionized disks with the disk reflection models by Ross & Fabian (1993) and Matt et al. (1993). Zycki et al. (1994) further extended on their work by using Monte Carlo runs. As a great improvement, `xillver` (García & Kallman, 2010; García et al., 2011, 2013) makes use of the advanced atomic database `xstar` (Kallman & Bautista, 2001) to model reflection off a geometrically thin and optically thick accretion disk. It therefore guarantees the most precise modeling of the soft X-rays, where photoabsorption, emission of fluorescent photons as well as

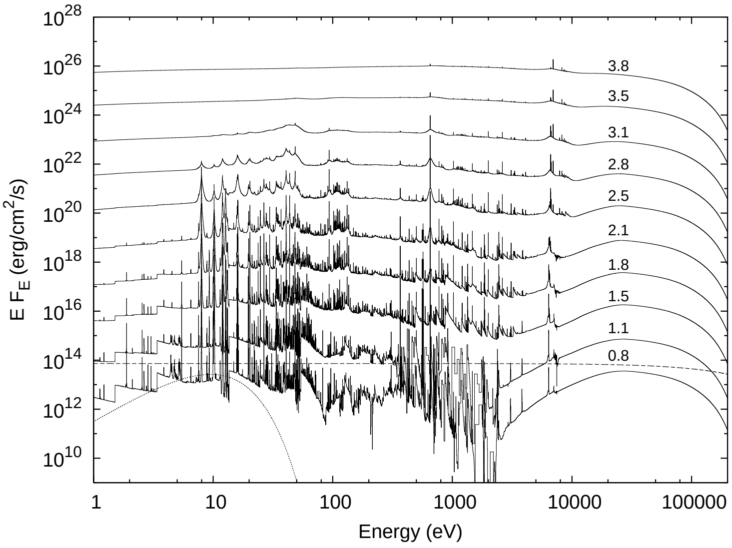

Figure 1.9. Reflection spectra for different ionization states from $\log\xi = 0.8$ to $\log\xi = 3.8$ as calculated with `xillver`. The incident spectrum is a power-law indicated as dashed line. The spectra are translated on the y-axis for visibility reasons. The plot is adopted from García & Kallman (2010).

recombination processes produce a large number of emission lines.

Figure 1.9 shows disk reflection spectra for different ionization states. For highly ionized disks, the irradiating flux penetrates to large optical depths. Most atoms are entirely stripped. Therefore, the strongest emission lines of N, O, Ne, Mg, Si, S, Ar, and Ca are most dominant at lower ionization states. The energy range between 6 keV and ~7 keV is dominated by line emission due to neutral iron (Fe I K α) as well as the ionized species Fe I–Fe VII. This is because of the strong fluorescent yield ($\propto Z^4$). The neutral Fe I K α line is found at the characteristic energy of 6.4 keV. The line flux for neutral K β is about 11–13% of the K α line flux. This ratio as well as the centroid energies increase with increasing ionization state García et al. (2013). The model `xillver` accounts for all of these ions.

1.2.3.2 The coronal geometry and inner disk reflection

Many "bare" and unabsorbed Seyfert 1 galaxies are supposed to be observed under shallow inclination angles that provide a direct line-of-sight to the inner disk. Radiation from the corona that gets reflected from this region experiences the effects of strong gravity on its way to the observer. Figure 1.10 illustrates how the peculiar shape of observed iron-line profiles can be used to infer fundamental information on the geometry of the X-ray source and the orientation of the reflecting disk. The figure illustrates its dependence on the inclination (top) and the lamp-post (LP) height (bottom) for the inner-disk reflection code `relxill` in a LP geometry (Dauser et al., 2013). In both cases, the intrinsically narrow Fe K α line is distorted due to relativistic Doppler shifts, light bending, and gravitational redshifts. The latter occurs when photons escape the deep gravitational potential on their way to the observer. These effects act differently in different cases. In the top panel the Doppler shift is most apparent at larger inclinations, where light bending preferentially projects the high orbital velocities from the inner disk into our line of sight. This results in double-peaked profiles. At the same time, the line profiles are increasingly smeared out at larger inclinations, while the blue wing shifts towards higher energies. This can also be explained by light bending, which leads to a significant fraction of photons to reach the observer from the inner disk. In projection, the gravitational redshift as well as Doppler energy shift are therefore stronger. Consequently, the red part of measured line profiles directly probes the black-hole spin, which determines the inner extent of the accretion disk, i.e., the ISCO. As shown in the bottom panel of Fig. 1.10. the model assumes a point-like source of photons above the disk. The lower the source is located above the black hole, the more photons are focused onto the inner parts of the disk due to the strong gravitational potential before they become

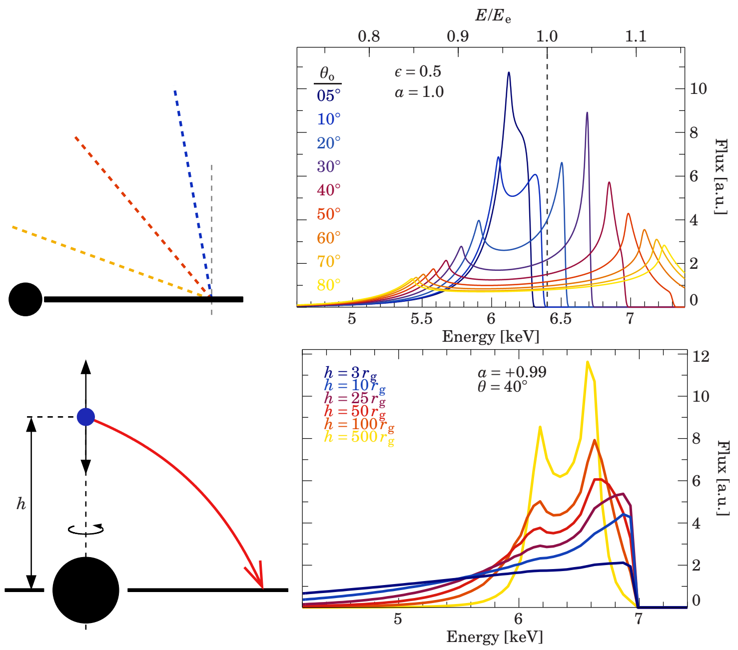

Figure 1.10. *Top:* Inclination dependence of the broadened iron line profile for a flat emissivity of $\epsilon = 0.5$ and a maximally spinning black hole. *Bottom:* Height dependence for an inclination of 40°. Image courtesy: T. Dauser, see also Dauser et al. (2010), and Dauser et al. (2013). See the text for further explanations.

reflected into our line of sight. Consequently, these reflected photons feature all the relativistic effects that occur in close vicinity to the black hole. In the figure, lower source heights therefore lead to line profiles that are increasingly smeared out towards soft energies, primarily because of gravitational redshifting.

1.2.3.2.1 An overview over past developments

As I have demonstrated, broad iron lines have strong diagnostic power for studying the physics in presence of strong gravity. While Miller et al. (2008) and Turner et al. (2009) explain these broad spectral features exclusively with partially covering absorption of dense material, Walton et al. (2010) conclude on it as being unphysical. In particular, bare AGN are known to show no signs of strong line-of-sight absorption (e.g., Walton et al., 2013). Walton et al. (2010) demonstrate that inner-disk reflection is a more physically motivated scenario, where corresponding models serve well to fit the spectra.

As shown in Fig. 1.10, the shape of relativistically smeared iron lines are a strong function of the coronal geometry. Such lines can therefore be used to test relativistic reflection models that assume different geometries for the corona[6]. The first models designed consider a slab corona above an optically thick and geometrically thin α-disk (Shakura & Sunyaev, 1973) and directly allow one to fit X-ray spectra. They are based on relativistic transfer functions with the formalism established by Cunningham (1975). While the `diskline` kernel by Fabian et al. (1989) does not yet consider the spin, the relativistic `laor` kernel (Laor, 1991) is calculated in the Kerr metric for a maximally spinning black hole and has found frequent applications (e.g., Miller et al., 2002; Miniutti et al., 2004; Nandra et al., 2007; Fabian et al., 2009). Later models by Dovčiak et al. (2004), Guainazzi et al. (2006), Longinotti et al. (2008) as well as the `kerrdisk` model (Brenneman & Reynolds, 2006; Patrick et al., 2011) for the first time allowed one to fit for the spin as free parameter. Further improvements on the derived parameters have been made by considering not only the iron line but the entire reflected spectrum, which has been convolved with the above relativistic transfer functions (e.g., Vaughan & Fabian, 2004; Larsson

---

[6] The accretion disk emits in the optical/UV and is supposed to operate at sub-parsec scales (e.g., ~0.01 pc), which translates to ~ 0.2 milliarcseconds for a nearby AGN at 10 Mpc. This is much more compact than the resolution limit of optical interferometers and even hits the limit of Very Long Baseline Radio Interferometers that provide the best resolution of all instruments at all wavebands.

et al., 2007; Zoghbi et al., 2010; Fabian et al., 2012a,b). Dauser et al. (2010) extended on the `kerrdisk` model by providing the tabulated model `relconv`, which has successfully been used to describe the broad-band spectra of the Galactic X-ray binary Cyg X-1 (Duro et al., 2011), the popular Seyfert 1 galaxy 1H 0707−495 (Dauser et al., 2012) as well as a large sample of bare AGN (Walton et al., 2013).

1.2.3.2.2 Modeling reflection in a self-consistent lamp-post geometry

The above studies consistently find larger disk emissivities closer to the black hole, while the outer disk can be well described with a power-law emissivity law of an α-disk (e.g., Brenneman & Reynolds, 2006; Larsson et al., 2007; Wilms et al., 2001, for MCG−6-30-15 as well as a number of other AGN studied by Ponti et al. 2010, Brenneman et al. 2011, Wilkins & Fabian 2011, Dauser et al. 2012, and Risaliti et al. 2013). The steep inner emissivities provide a strong motivation for a corona that is concentrated at the symmetry axis, i.e., a corona in a LP geometry (Svoboda et al., 2012) as opposed to a slab geometry. The LP model was first proposed by Matt et al. (1991) and Martocchia & Matt (1996) and further developed by Martocchia et al. (2000), Miniutti & Fabian (2004), Miniutti et al. (2004), Suebsuwong et al. (2006), Niedźwiecki & Miyakawa (2010), and Cackett et al. (2014).

The first model that makes it possible to directly fit the broad Fe K α line in a self-consistent LP geometry is named `relxill_lp` and provided by Dauser et al. 2013 (see Fig. 1.10 for a number of model evaluations). As a further improvement, García et al. (2014) link the reflected spectrum `xillver` (García et al., 2013) from each point of an ionized disk with the correct relativistic transfer function. Their tabulated model `relxill_lp` therefore provides the to date only model that allows one to self-consistently fit for a primary source at a certain height above the disk in an angle-dependent way.

1.2.3.2.3 Independent constraints on the coronal geometry

As Walton et al. (2016) demonstrate, when trying to obtain black hole parameters from reflection modeling, there is a strong need for data coverage above 10 keV. In this regime, the model parameters are sensitive to changes in the spectral shape (Dauser et al., 2016). *NuSTAR* is the first X-ray focusing satellite with significant effective area above 10 keV. The validity of the model `relxill_lp` has been demonstrated in a number of studies of strongly smeared lines, which consistently require a compact corona located at a low height (Dauser et al., 2012; Parker et al., 2014; Keck et al., 2015).

Independent approaches are invaluable to cross-check these results. For several sources the reflected flux (0.3–1 keV) lags the incident hard flux (1–4 keV) on time scales of seconds (e.g., Vaughan et al., 2003, for MCG−6-30-15). Fabian et al. (2009) and Zoghbi et al. (2010) interpret these time lags as reverberation lags probing spatial scales of less than a few gravitational radii, which strongly argues for a compact corona. In yet another timing study, Wilkins & Fabian (2012) consider the corona to have some radial extent. Their results show that the corona still has to be located just a few gravitational radii above the disk to explain the data. In contrast, other reverberation studies for example of Ark 564 (Zoghbi et al., 2010), Mrk 335 (Kara et al., 2013) or IRAS 13224−3809 (Wilkins & Gallo, 2015) describe well their data with vertically extended coronae. Cackett et al. (2014), on the other hand, suggest a compact corona to be located at a somewhat larger height of ~ 5–$10\,r_\mathrm{g}$ for NGC 4151. These results show that different sources open space for a wide range of coronal sizes and distances from the black hole. All reverberation studies, however, agree in the LP geometry. Comptonization may also be a common process in the base of collimated jets (Markoff et al., 2005; Wilkins & Gallo, 2015; King et al., 2017), where the effects of the prevalent magnetic fields need to be better understood in the future. Me and my collaborators have been able to make detailed statements on the coronal geometry of

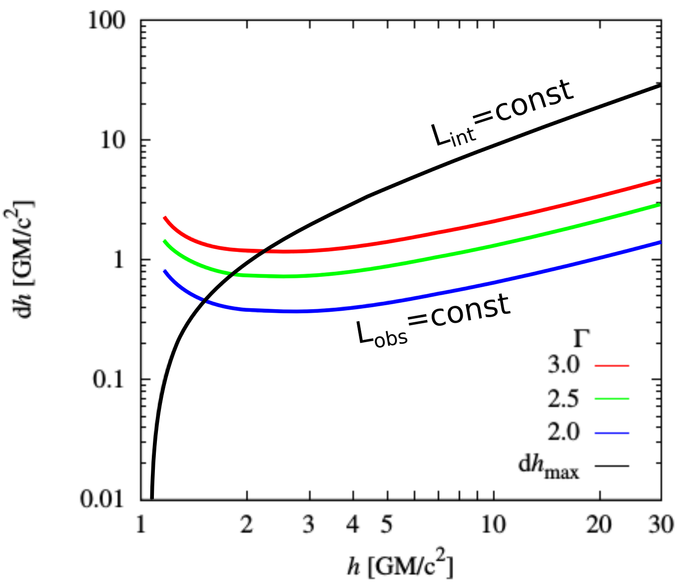

Figure 1.11. Corona size dh over its height h above the black hole. The colored lines describe the height dependence of dh for a constant luminosity in the observer frame and different power-law photon-indices, the black curve for constant intrinsic luminosity. The figure is adapted from Dovčiak & Done (2016).

NGC 4151 by applying the model `relxill_lp` to long-look X-ray observations with *Suzaku* and *NuSTAR* (Sect. 3.2).

The following paragraph is partly based on and occasionally taken in verbatim from Beuchert et al. (2017). On the theoretical side, Dovčiak & Done (2016) provide strong arguments for an extremely compact (spherical) corona. They estimate its spatial extent depending on its height above the accretion disk by considering the effects of strong gravity acting on the seed photons between the disk and the corona. Figure 1.11 shows the height dependence of a spherical corona above the disk. For an observed X-ray luminosity of $L_{\mathrm{X,obs}} = 0.001\,L_{\mathrm{Edd}}$ and a photon index of $\Gamma = 2$, the extent of a corona at a height of 10–20 r_{g} grows to values larger than $1\,r_{\mathrm{g}}$. The size is decreasing to $\sim 0.4\,r_{\mathrm{g}}$ at lower heights and again increasing to $\sim 1\,r_{\mathrm{g}}$ for a height close to $1\,r_{\mathrm{g}}$. One has to distinguish two cases, one where the intrinsic luminosity is held constant and one, where the observed luminosity is constant. The black curve shows the first case, where the coronal size is mainly determined by the gravitational redshift of disk seed photons between the disk and the corona. The latter case of $L_{\mathrm{obs}} = \mathrm{const}$ is more relevant for us as observers. There is a general trend for the corona size to increase with increasing height. The higher the corona lies above the disk, the more energy is lost by the seed photons due to gravitational redshifting between the disk as source and the corona as target, where the seed photons become Comptonized. This can be compensated with the target-size of the corona. At very low heights, however, the corona size must increase again as only a reduced amount of photons can reach the corona due to light bending.

1.2.3.2.4 The compactness parameter

The extreme case of a compact corona at low heights above the BH brings physical complications. If the density of photons with sufficient energy is large enough, runaway cooling via pair production becomes an issue. In particular, the photon-photon cross section for pair production as a ratio of the Thomson cross section starts to rise at the single-photon energy of $m_{\mathrm{e}}c^2 = 511\,\mathrm{keV}$ with a maximum of $\tau_{\gamma\gamma}/\tau_{\mathrm{T}} \sim 0.2$ between 500 keV and 1 MeV, and decreases after that (e.g., Eungwanichayapant & Aharonian, 2009). The optical depths with respect to photon-photon interactions can be written as

$$\tau_{\gamma\gamma} \approx n_\gamma \sigma_{\mathrm{T}} R \tag{1.16}$$

with the photon density $n_\gamma = L_\gamma / 4\pi R^2 m_{\mathrm{e}} c^3$ and the depth R. Here, I set $\sigma_{\gamma\gamma} \approx \sigma_{\mathrm{T}}$, which tentatively holds for the maximum of $\sigma_{\gamma\gamma}$. The compactness parameter is defined as (Guilbert

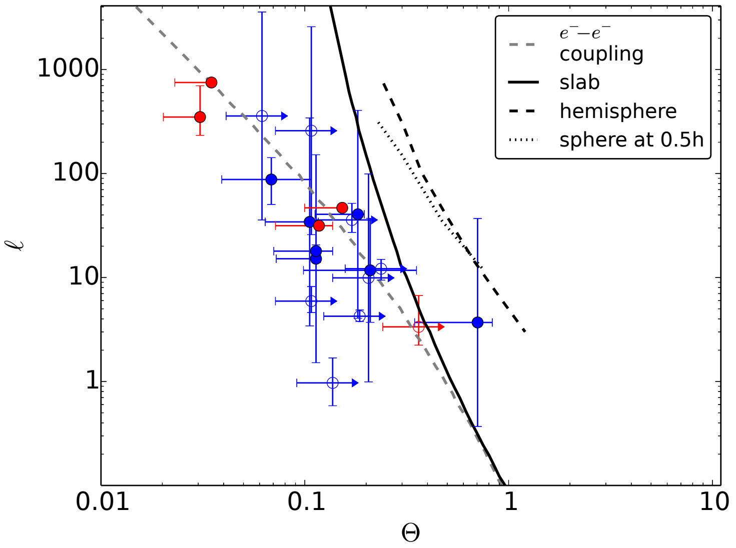

Figure 1.12. Compactness over the parameter $\Theta = kT_\mathrm{e}/m_\mathrm{e}c^2$ for a number of AGN (blue points) and X-ray binaries (red points); the lines correspond to thresholds for runaway pair production in different geometries (Stern et al., 1995). This plot has been adopted from Fabian et al. (2015).

et al., 1983)

$$\ell = \frac{L_\gamma \sigma_\mathrm{T}}{m_\mathrm{e} c^3 R} \tag{1.17}$$

and is a measure for the effectiveness of pair production. In units of the Eddington luminosity, one can also write

$$\ell = \frac{8\pi c G M m_\mathrm{p}}{\sigma_\mathrm{T}} \left(\frac{L}{L_\mathrm{Edd}}\right) \frac{c^2}{2GM} \left(\frac{r_\mathrm{g}}{r}\right) \frac{\sigma_\mathrm{T}}{m_\mathrm{e} c^3} = 4\pi \frac{m_\mathrm{p}}{m_\mathrm{e}} \left(\frac{L}{L_\mathrm{Edd}}\right) \left(\frac{r_\mathrm{g}}{R}\right) \tag{1.18}$$

with the gravitational radius $r_\mathrm{g} = GM/c^2$. Models for the corona have been tested against X-ray data with respect to the cutoff energy in their Comptonized spectra (e.g., Dove et al., 1997b, for Cyg X-1). A relevant parameter related to the cutoff energy and therefore the electron temperature (see Sect. 1.2.3.1) is $\Theta = kT_\mathrm{e}/m_\mathrm{e}c^2$. Fabian et al. (2015) use a recent set of *NuSTAR* observations of compact accreting objects (AGN and X-ray binaries) to find constraints on the electron temperature. *NuSTAR* covers the hard X-rays, which are most sensitive to this parameter and therefore allow the authors to probe previous models for the corona (e.g., Stern et al., 1995). They calculate the compactness values for these sources and plot them in dependence of the parameter Θ. The inferred cutoff energies range between ∼100 and ∼1000 keV and can be measured with codes describing (inner) disk reflection with `relxill_lp` or `xillver`, respectively. The hard X-ray coverage of *NuSTAR* is invaluable for determining the electron temperature and to make statements on the relevance of pair production. Figure 1.12 shows a sample of AGN and X-ray binaries, where *NuSTAR* data have been used. The figure also shows geometry-dependent thresholds above which pair production is strongly relevant. Within the uncertainties, none of the sources crosses this border. This also holds for a recent study of MCG−5-23-16 using a number of long-exposure *NuSTAR* pointings (Zoghbi et al., 2017). In both studies, the authors did take into account gravitational energy shifts of the parameter Θ depending on the height of the primary source of Comptonized photons.

1.2.4 ABSORPTION IN SEYFERT GALAXIES

Soft X-rays ($\lesssim 4-5$ keV) are preferentially photo-absorbed by metals, i.e., elements with Z larger than one that are contained in both gas and dust. Although the contribution of neutral hydrogen is only minor, the amount of X-ray absorption is measured with the equivalent column density N_H relative to neutral hydrogen. The column density carries the units (cm^{-2}).

Usually, the measured N_H contains contributions from many different layers of absorbing matter on a given line of sight to the AGN nucleus. In-orbit X-ray observatories with focusing optics usually provide angular resolutions of $5''$–$20''$ with *Chandra* even going down to $0.4''$ (Karovska et al., 2001). For typical distances of AGN, however, the angular resolution needs to be as low as milliarcseconds to resolve distinct absorbing structures as part of the torus, the BLR or structures in between.

One well-known contributor is the Galactic column density N_Gal. It has been measured along all lines of sight through our Milky Way using radio telescopes as part of the Leiden/Argentine/Bonn survey (LAB Kalberla et al., 2005), which are sensitive to neutral H I. This survey has just recently been extended by the Effelsberg-Bonn H I Survey (EBHIS) and the Galactic All-Sky Survey (GASS). See the HI4PI Collaboration et al. (2016) for further information. By the knowledge of N_Gal, one can isolate the intrinsic column density N_int, which includes contributions from any absorbing structure of the AGN and its host galaxy on our line of sight. The source flux can be written as

$$F(E) \sim E^{-\Gamma} \times e^{-\sigma_\mathrm{X} N_\mathrm{Gal}} \times e^{-\sigma_\mathrm{X} N_\mathrm{int}}, \tag{1.19}$$

with σ_X corresponding to the photoabsorption cross section in the X-rays with contributions from gas, molecules, and dust grains (e.g., for the interstellar medium (ISM), Balucinska-Church & McCammon, 1992; Verner & Yakovlev, 1995; Wilms et al., 2000, and references therein).

While soft X-rays are absorbed by both gas and dust, the optical/UV flux, however, is only attenuated by dust. Simultaneous X-ray and optical/UV data therefore have a great potential to disentangle contributions from dust and gas.

In Sect. 1.2.4.1, I will first concentrate on dust and its implications to the broad-band spectrum of radio-quiet Seyfert galaxies. In Sect. 1.2.4.2, I will motivate the study of X-ray absorbers and the conclusions that can be drawn on their nature.

1.2.4.1 OPTICAL/UV EXTINCTION AND X-RAY ABSORPTION

Figure 1.13 shows a typical Seyfert broad-band spectral energy distribution (SED) from the far-infrared (FIR) to the X-rays with unabsorbed model components (white) that have been found for the Seyfert galaxy NGC 3227 (see Sect. 3.1). This SED compares well with averaged type 1 quasar SEDs shown by Elvis et al. (1994) and Richards et al. (2006a); see also the review by Mushotzky et al. (1993). As compared to quasar SEDs, those of Seyfert galaxies show a stronger host galaxy contribution due to starlight peaking around 1 µm (solid line in Fig. 1.13) and strong absorption in the extreme-ultraviolet (EUV)–soft X-ray gap (Vasudevan et al., 2010). In Sect. 1.2.2, I have introduced the multi-temperature disk blackbody spectrum forming the “Big Blue Bump” (BBB) that is seen to dominate in the NUV–EUV (dotted-dashed line, modeled with `diskpn`). In Sect. 1.2.3.1, I also introduced the thermal Comptonization component (dashed line), which dominates the X-ray spectrum. In the example SED, this component is modeled with a combination of an incident power law and a `xillver` reflection component with the characteristic hump at around 30 keV.

Excess emission in the FIR–NIR can be attributed to reprocessed X-ray emission from a distribution of heated dust around the nucleus. This emission is usually modeled with a superposition of blackbodies at different temperatures. Dust scattering and absorption both combine to the effect of dust extinction. These processes are complex as reviewed for example by Mathis (1990). Dust extinction increases roughly with λ^{-1}, i.e., it is more efficient at bluer wavelengths. Objects, where interstellar dust intercepts the direct line of sight therefore appear redder. A “color” is defined as the magnitude difference at different wavelengths, i.e., $m(\lambda_1) - m(\lambda_2) = -2.5 \log F(\lambda_1)/F(\lambda_2)$. If dust obscures the line of sight, this will result in a

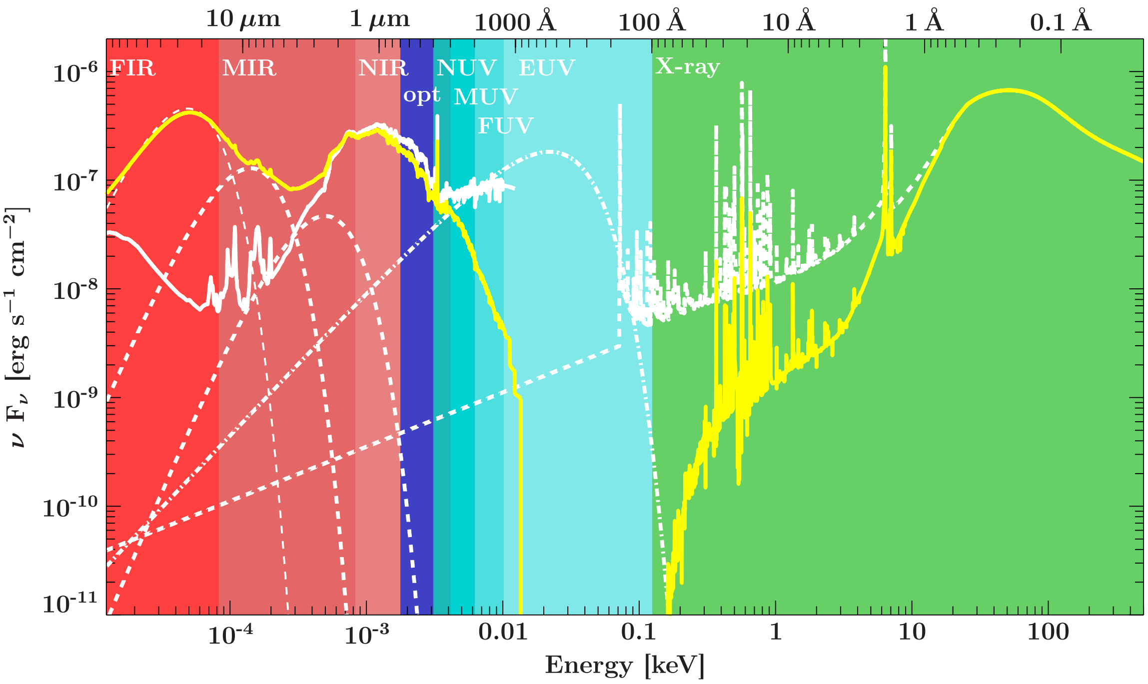

Figure 1.13. Example Seyfert IR–X-ray SED with model components from a fit to the galaxy NGC 3227. The yellow SED corresponds to the sum of the absorbed model components; unabsorbed model components are plotted in white: three blackbodies at different temperatures due to cold/warm dust (dashed curves in the IR); a template for the host-galaxy stellar population peaking in the near-infrared (NIR)/optical (solid curve); a multi-temperature accretion-disk model forming the "big blue bump" in the UV (dotted-dashed line); reflected Comptonized emission off the disk in the X-rays (dashed line).

color difference, which directly relates to a difference in optical depths via

$$[m_1(\lambda_1) - m_1(\lambda_2)] - [m_2(\lambda_1) - m_2(\lambda_2)] \propto \tau_{\lambda,1} - \tau_{\lambda,2} \propto E(\lambda_1 - \lambda_2) = A(\lambda_1) - A(\lambda_2). \quad (1.20)$$

Here, $E(\lambda_1 - \lambda_2)$ corresponds to the amount of reddening with respect to the wavelengths λ_1 and λ_2 and can also be expressed via the difference in extinction with the coefficients A_λ. The flux at the wavelength λ will be attenuated according to

$$F_{\text{obs}} \propto F_{\text{source}} \times 10^{-A_\lambda}. \quad (1.21)$$

If one normalizes the color difference of any wavelength λ and the visual to that of the blue and the visual (defined in the Johnson photometric system; Johnson & Morgan, 1953), one finds

$$\frac{E(\lambda - V)}{E(B - V)} = \frac{A_\lambda - A_{\text{V}}}{E(B - V)} = k(\lambda) - R_{\text{V}}. \quad (1.22)$$

The latter relation is particularly helpful as it describes the wavelength dependent extinction via the extinction curve $k(\lambda) = A_\lambda / E(B - V)$ minus the parameter R_{V}.

The first broad-band Galactic extinction curves were measured in the UV using satellites (see the review by Witt, 1973, as well as the studies by Seaton 1979 and Savage & Mathis 1979). They in particular found a broad excess peak around 2200Å. Later, Cardelli et al. (1988) and Cardelli et al. (1989) consider photometric data between the IR and the UV. They established an expression for $k(\lambda)$ that is consistent with previous data in the UV for the parameter $R_{\text{V}} \approx 3.1$. As mentioned before, the extinction curve roughly behaves as $\propto \lambda^{-1}$, which meets the prediction of Mie-scattering off spherical particles. Witt (1973) shows for the first time that the broad-band extinction curve harbors information on the physics of interstellar dust. He was able to

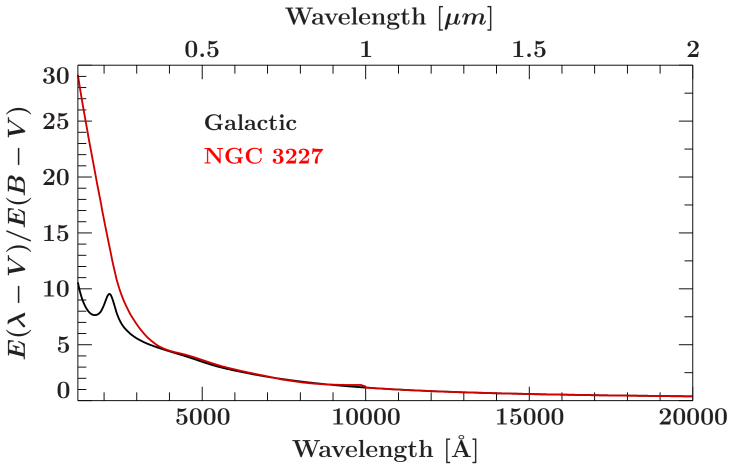

Figure 1.14. Extinction curves for the Galactic ISM as parameterized by Fitzpatrick 1999 (black) and for extragalactic dust inside the Seyfert galaxy NGC 3227 from Crenshaw et al. 2001 (red).

reconstruct the observed extinction curves with a component due to dust scattering (see also Witt & Lillie, 1973) and dust absorption, which peaks around 2200Å. Mathis et al. (1977) described the interstellar extinction in the optical/UV using a power-law distribution of gain sizes a (including graphite and other molecules) that follows $\propto a^{-3.5}$. They find small graphite grains to be the major contributor to the broad 2200Å feature with additional silicate molecules (see also Laor & Draine, 1993, for spectroscopic constraints on the composition in AGN). Contrary to expectations, common dust models such as that by Mathis et al. (1977) require an overabundance of carbon of up to a factor of 60 with respect to the sun. Successor models are therefore considering fluffy dust grains made of silicate and amorphous carbon with 40% enclosed vacuum, which reduces the required abundance by half. A yet different possibility is Polycyclic Aromatic Hydrocarbons (PAHs), which also contain carbon and are claimed to account for ~50% of the 2200Å feature (Léger et al., 1989, see, however, Verstraete & Léger 1992). A model by Desert et al. (1990) therefore includes both PAHs with sizes less than 1.2 nm and a range of dust grain sizes to explain the whole 2200Å feature. More complicated distributions of dust grain sizes have been modeled for the Milky Way, the Large Magelanic Cloud (LMC), and Small Magelanic Cloud (SMC) by Weingartner & Draine (2001).

I use the parameterization of the extinction curve by Fitzpatrick (1999) as shown in Fig. 1.14 (black curve) in comparison with an updated extinction law for NGC 3227. As Crenshaw et al. (2001) conclude, the difference implies that dust inherent to AGN may be composed of a different size distribution of grains compared to our Galaxy.

On the other hand, X-rays can be absorbed by both dust and dust-free gas (e.g., Guainazzi et al., 2005). Dust absorption has already been implemented in the `xspec` model `tbnew` (Wilms et al., 2000) and the model `ISMabs` (Gatuzz et al., 2015) for ionized species of elements that are abundant in the ISM. `tbnew` is an improved version of the absorption model of Wilms et al. (2000), using cross sections from Verner et al. (1996) and abundances from Wilms et al. (2000). Smith et al. (2016) extend on this work by also considering dust scattering. The differences are particularly obvious for absorption edges in data with highest spectral resolution. For data with resolution of Charged Coupled Devices (CCDs), it is sufficient to neglect dust scattering. The cross section σ_X (see Wilms et al., 2000) is largest in the soft X-rays due to larger abundances of high-Z elements. A major prospect is to understand the relation between extinction in the optical/UV and absorption in the X-rays. Predehl & Schmitt (1995) observed dust scattering halos around Galactic X-ray binaries and studied both the extinction A_V at visual and the column density N_H to infer the Galactic gas-to-dust ratio $N_\mathrm{H} = A_\mathrm{V} \cdot 1.79 \times 10^{21}\,\mathrm{cm}^{-2}\,\mathrm{mag}^{-1}$. Nowak et al. (2012) use the improved cross sections and abundances of `tbnew` and the optical depth of $\tau = 0.486\,N_\mathrm{H}$ measured by Predehl & Schmitt (1995) to find the corrected Galactic ratio of $N_\mathrm{H} = A_\mathrm{V} \cdot 2.69 \times 10^{21}\,\mathrm{cm}^{-2}\,\mathrm{mag}^{-1}$, which I apply in the remainder of this work. Burtscher et al. (2016) find that the gas-to-dust ratios of AGN exceed the Galactic value significantly. They explain this with an increased amount of sublimated dust, which raises the AGN-intrinsic absorption column density but leaves A_{V} unaffected.

Source intrinsic absorption with large contributions from gaseous states is apparently a common feature for AGN. The question therefore arises, how the absorbing material distributes. As outlined in Sect. 1.1, dust can be observed mainly in the IR via reprocessed nuclear emission. Hönig et al. (2010a) and Hönig & Kishimoto (2010) therefore used mid-infrared (MIR) spectroscopy and interferometry to test for a cloudy nature of that dust. Tristram et al. (2014) were the first to use MIR interferometry to image the dusty environment down to parsec scales in the Circinus galaxy. They confirm the $L^{1/2}$-dependence (Kishimoto et al., 2009, 2011; Koshida et al., 2014) of the distance of dust from reverberation studies[7] but also show that the vaguely resolved MIR-emitting structure aligns with the symmetry axis of the system. This result leads Hönig et al. (2012) to claim a deviation of the traditional idea of a "torus" as a well-confined structure in the equatorial plane. This deviation is further strengthened by observations of a tight correlation between the MIR flux and the nuclear X-ray radiation for large samples of Seyferts (e.g., González-Martín et al., 2013; Asmus et al., 2015). In the picture of Hönig et al. (2012) and Asmus et al. (2015) the, MIR emission originates from optically thin dust that is outflowing along the polar region (see Fig. 9 of Hönig et al. 2012), while the NIR seems to still probe the "classical torus". It is challenging to further increase the spatial resolution and perform direct imaging of the dusty structures in AGN that are evidently driven by large dynamics. This difficulty strongly motivates the use of second means, such as time-resolved spectroscopy.

1.2.4.2 STUDYING SOURCE INTRINSIC ABSORPTION IN THE X-RAYS

The indirect method of time-dependent X-ray spectroscopy is extremely valuable to access and interpret the structure and dynamics of source-intrinsic absorbers that remain unresolved with modern instruments. The study of absorption signatures in the soft X-rays allows us to probe different states of the circumnuclear matter at a range distances to the black hole and across a range of ionization states: this involves the torus, the BLR, disk outflows, and a mixture of these or more complex structures.

Figure 1.15 provides a simplified picture of the AGN components, its absorbing environment and scattering paths of nuclear radiation. It is subject of this section to build up a more realistic picture from the observational perspective. Emission from the BLR in form of optical lines and X-rays from the corona can follow similar paths to the observer. Different paths, however, are seen under different viewing angles onto the AGN. This is shown exceedingly simplified in Fig. 1.15, which I composed based on information contained in Smith et al. (2004). Seyfert 1 galaxies turn out to be either optically unpolarized or exhibit polarized lines, where the light got scattered off the equatorial plane or accretion disk. For Seyfert 2 galaxies, in contrast, one mainly measures polarized lines that are scattered off a polar region, where the NLR is a realistic candidate. At the same time, the BLR and the NLR contain photoionized gas that is itself an emitter of soft X-ray photons (e.g., Guainazzi & Bianchi, 2007a). With these results in mind, Smith et al. (2004) identify 12 additional Seyfert 1 galaxies where the optical line emission is characteristic for Seyfert 2 galaxies. They conclude based on a simple torus-like geometry that these "polar-scattered Seyfert 1 galaxies" appear under an intermediate inclination close to $i \sim 45°$ where large portions of the equatorial scattered light are absorbed. This may hold even for a strongly dynamic absorber. As it is shown in the figure, the line of sight can likely pass through the outer rim of a dense conglomeration of absorption structures of gas and dust that

---

[7] The ionization parameter is defined as $\xi \sim L/n_{\mathrm{e}}r^2$ with the electron density n_{e} and the incident luminosity L Tarter et al. (1969); Netzer (2008). For constant ξ and n_{e}, dust is therefore expected to be found outside of $r \sim L^{1/2}$.

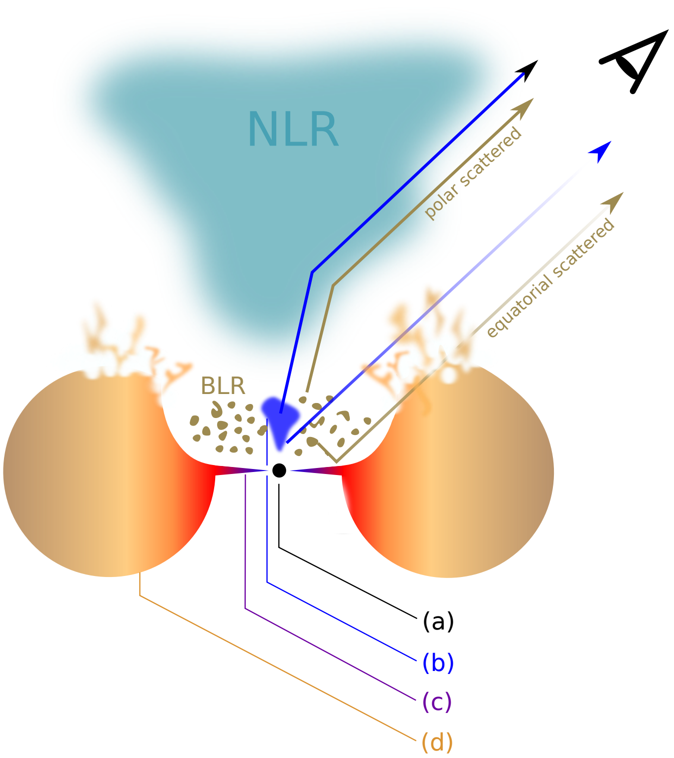

Figure 1.15. Simplified and highly exaggerated picture of an AGN with (a) the SMBH, (b) the X-ray emitting corona, (c) the multi-temperature disk, and (d) the obscuring torus. The NLR is shown as blue region above the system, the B(E)LR is denoted with a number of clouds immediately above the disk. The relative sizes of these components are not to scale. Different scattering paths for broad emission lines (dark green) and the coronal X-rays (blue) are shown with arrows pointing towards the observer. Although the conventional wisdom implies $r_{\mathrm{torus}} \gg r_{\mathrm{disk}}$, the size of the accretion disk is enlarged in this figure. Note that although recent studies have given deeper insights, the geometries of these components are still subject of debate.

are stripped off by radiation pressure. The major expectation is that the coronal X-rays follow a similar path as the broad emission lines. X-ray spectra should therefore be strongly affected by variable line-of-sight absorption.

In fact, I find X-ray absorption variability for all sources of this sample (8 out of 12), where sufficient archival data are available (Beuchert et al., 2013). This set of polar scattered Seyfert 1s may therefore indicate that (1) the picture in Fig. 1.15 holds and that AGN orientation does play a role for distinguishing absorbed and unabsorbed Seyfert galaxies and (2) that the symmetry braking character of polarized lines helps to put constraints on the orientation. The question arises, whether the Seyfert 1/Seyfert 2 dichotomy based on the X-ray absorption strength may on average be related to the original type 1/type 2 optical classification, i.e., are intermediate type 1.5 galaxies also prone to X-ray absorption?

The following paragraph is partly taken in verbatim from Beuchert et al. (2015). For a few prominent sources of the sample of Smith et al. (2004), i.e., ESO 323-G77 (Miniutti et al., 2014), Fairall 51 (Svoboda et al., 2015) and NGC 3227 (Beuchert et al., 2015), we were able to perform dedicated studies of the absorbers. Variable absorption also has been found for a number of other Seyfert galaxies with intermediate optical classifications, where no optical polarimetry information is available. These are, for example, NGC 4051 (Guainazzi et al., 1998), MCG−6-30-15 (McKernan & Yaqoob, 1998), and NGC 3516 (Turner et al., 2008). Risaliti et al. (2002) also studied an X-ray selected set of 25 Seyfert 2 galaxies and found soft X-ray variability on both long and short timescales. Short-term ($\sim$1 d) absorption events have been detected, e.g., for NGC 4388 (Elvis et al., 2004), NGC 1365 (Risaliti et al., 2007, 2009a,b), Mrk 766 (Risaliti et al., 2011), Swift J2127.4+5654 (Sanfrutos et al., 2013), NGC 5506 (Markowitz et al., 2014), or NGC 4151 (Beuchert et al., 2017). Long-term events ($\geq$ 7 d, Markowitz et al., 2014) have been found for, e.g., Cen A (Rivers et al., 2011a), or NGC 3227 in 2000/2001 (Lamer et al., 2003), thanks to Rossi X-ray Timing Explorer (*RXTE*) monitoring.

Large parts of the following four paragraphs are taken in verbatim after Beuchert et al. (2015). These absorption events can be explained by transits of discrete clouds or clumps of gas across the line of sight to the central X-ray source (e.g., Risaliti et al., 2002; Lohfink et al., 2012; Markowitz et al., 2014). They support a new generation of “clumpy-torus” models, where the molecular torus consists of a distribution of clumps rather than a homogeneous barrier (Elitzur, 2007; Nenkova et al., 2002, 2008a,b), which is indicated in Fig. 1.15. In these models, clouds are typically concentrated towards the equatorial plane with a soft-edge angular distribution and may be embedded in a tenuous intercloud medium (Stalevski et al., 2012). The clouds are furthermore assumed to be moving on near-Keplerian orbits. Outside the dust sublimation radius[8], the presence of a clumpy component is supported by corresponding model fits to infrared SEDs (Asensio Ramos & Ramos Almeida, 2009; Alonso-Herrero et al., 2011). Closer to the SMBH, the population of dusty clouds may transition to the dust-free clouds that comprise the BLR (Elitzur, 2007). A clumpy X-ray absorbing medium located at distances commensurate with the BLR also has been suggested by Risaliti et al. (2009a) and Risaliti et al. (2011) even for nearly face-on lines of sight towards Seyfert 1 galaxies (Elvis, 2000).

Arav et al. (1998) used high-resolution spectroscopy with the Keck I optical telescope but were unable to find signatures of individual BEL clouds for the example of NGC 4151. They conclude that there must be more than 10^8 small emitting clouds in the BLR, which may be an extreme case. From an observational point of view, MIR studies are only sensitive to matter outside the dust sublimation zone, while X-ray absorption probes the full radial range. Many of the short-term X-ray absorption events have therefore been interpreted as BLR clouds (Risaliti et al., 2007). Whenever long-term events have been found, e.g., by Markowitz et al. (2014, with durations of more than a few days to more than a year,), these were inferred to be due to clouds residing in the outer BLR or the inner dusty torus.

When adequate data are available, i.e., when sustained sampling on timescales longer than the eclipse duration that resolves the eclipses is available, one is able to pinpoint their ingress and egress and to obtain time-resolved information on the column density profile $N_{\mathrm{H}}(t)$ along the transverse direction (Markowitz et al., 2014). Only a few density profiles have been resolved so far. The events in NGC 3227 and Cen A mentioned above feature symmetric, nonuniform, and centrally-peaked column density profiles. Maiolino et al. (2010) report more exotic profiles that argue in favor of comet-shaped clouds, with dense “heads” and less-dense “tails”, in NGC 1365. So far, the only source to show a double-peaked profile is NGC 3783 (Markowitz et al., 2014). These results indicate a broad variety of profile shapes, hinting at a range in the cloud origins and/or the physical mechanisms that shape clouds. Investigating these issues is one of the central points of my thesis.

To add further complexity to the interpretation of X-ray spectra, a significant number of Seyferts also show evidence of multiple layers of differently ionized absorbers. The ionization states cover the full range from mildly to fully stripped elements. One often finds highly ionized absorbers at intermediate outflowing speeds up to about 10% of the speed of light. The following sections will further illuminate these so-called “warm absorbers”.

1.2.5 The exhaust of Black Hole engines and their environment

In the above sections, I have introduced AGN as powerful engines that effectively exploit the reservoir of gravitational energy in their surrounding. In the process of accretion, their central black holes convert portions of this fuel into thermal and reprocessed radiation that is emerging from the nucleus. In addition, AGN also release large amounts of mechanical and radiated energy via collimated jet outflows and extensive winds along their symmetry axis.

The exhaust of AGN engines not only reflects a necessary channel of energy release but also act as the feedback mechanism that couples to the large-scale environment of AGN (see Sect. 1.3).

---

[8] The radial distance from the illuminating source, where dust sublimates, radius depends on the black-hole mass and accretion rate. This area is typically several light weeks away from the SMBH

They establish the M_{BH}-σ relation (King, 2003, 2010) or quench star formation (SF; Moster et al., 2010; Cano-Díaz et al., 2012). Outflows can also regulate the overcooling and condensation of galaxy clusters (Burns et al., 1981; Binney & Tabor, 1995), which is commonly referred to as the "cooling flow problem" (Tabor & Binney, 1993; Croton et al., 2006).

1.2.5.1 OUTFLOWS AND WINDS

The soft X-ray spectra of more than 50% of the known Seyfert galaxies reveal signs for absorption, mainly by ionized species of O VII and O VIII (Reynolds, 1997; George et al., 1998). Often, multiple layers of differently ionized gas are found along the line of sight (e.g., Blustin et al., 2005; Turner et al., 2008; Wang et al., 2011a), which are also called "warm absorbers". Blue-shifted absorption features indicate that some warm absorbers are outflowing at mild speeds of $\leq 1000\,\mathrm{km/s}$ (e.g., Kaastra et al., 2000; Kaspi et al., 2000; Collinge et al., 2001; Blustin et al., 2005; McKernan et al., 2007, and many others). Typical ionization states and column densities are $\log\xi \sim 0$–2 and $N_{\mathrm{H}} \sim 10^{20}$–$10^{22}\,\mathrm{cm}^{-2}$ (Tombesi et al., 2013b). These gas phases may either be launched from the accretion disk (Proga et al., 2000; Elvis, 2000; Krongold et al., 2007; Dorodnitsyn & Kallman, 2012) or the torus (Reynolds, 1997; Krolik & Kriss, 2001; Blustin et al., 2005) via radiative line driving (e.g., Matthews et al., 2017) or magnetohydrodynamics (MHD) forces (Blandford & Payne, 1982; Contopoulos & Lovelace, 1994; Königl & Kartje, 1994b; Fukumura et al., 2010). The gas may even form clouds that are in pressure equilibrium and driven by radiation pressure (Chelouche & Netzer, 2001). Reynolds & Fabian (1995) also consider radiative driving as underlying mechanism but further discuss turbulent, mechanical mixing that can heat the gas environment and produce the observed features.

The ionization state of a gas is given by the (photo-)ionization rate over the recombination rate. There are two common definitions, which are both proportional to the ratio of ionizing photons per volume over the number of electrons per volume (Tarter et al., 1969; Netzer, 2008), i.e.,

$$U = \frac{Q}{4\pi r^2 c n_{\mathrm{e}}} \tag{1.23}$$

$$\xi = \frac{L_{\mathrm{ion}}}{n_{\mathrm{e}} r^2}, \tag{1.24}$$

where the ionizing photon rate Q and the ionizing luminosity L_{ion} are defined as

$$Q = \int_{13.6\,\mathrm{eV}}^{13.6\,\mathrm{keV}} L_{\mathrm{ion},\nu}/h\nu \, d\nu \tag{1.25}$$

$$L_{\mathrm{ion}} = \int_{13.6\,\mathrm{eV}}^{13.6\,\mathrm{keV}} L_{\mathrm{ion},\nu} \, d\nu. \tag{1.26}$$

As typical power-law spectra drop off rapidly above 10 keV, one can also integrate to infinity. The general idea is to compare the surface density of ionizing photons, e.g., $Q/4\pi r^2$, with the gas density n_{e}. With the additional factor of c in the denominator, this equals to the number of ionizing photons per atom (here, ones assumes that $n_{\mathrm{H}} \sim n_{\mathrm{e}}$). The conversion factor f translates between ξ and U and depends on the spectral shape of the ionizing continuum:

$$\xi = f\,U \tag{1.27}$$

$$f = \frac{L_{\mathrm{ion}}}{Q} 4\pi c \tag{1.28}$$

McKernan et al. (2007) raised the question, how these winds are related to the black-hole mass and the accretion rate. The angular momentum transport in accretion disks, however, is

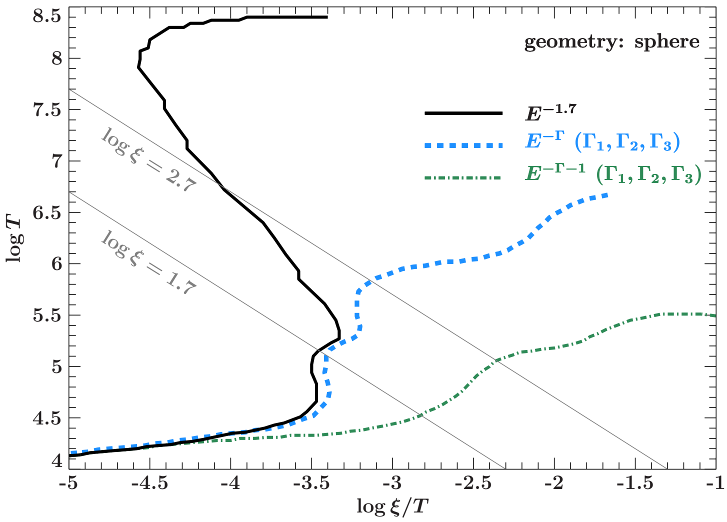

Figure 1.16. Gas stability curves calculated with `xstar` (Kallman & Bautista, 2001) for an optically thin spherical shell of gas with constant density $n_\mathrm{e} = 10^4\,\mathrm{cm}^{-2}$ and the thickness ΔR. The sphere is illuminated from its interior with a luminosity of $L = 10^{-28}\,\mathrm{erg\,s}^{-1}$. The inner radius is defined by the incident luminosity and the ionization parameter $\log \xi = 5$. The photoionization equilibrium is calculated at each radius of the shell, where the ξ and the temperature T are continuously decreasing outwards. The pressure is proportional to ξ/T. Here, three stability curves are plotted for two different input spectra. The black solid line corresponds to a simple power law with $\Gamma = 1.7$, the blue dashed line to the double-broken power law defined for NGC 4151 (Eq. 3.16) and the green dotted-dashed line to the same SED but $\Gamma \to \Gamma + 1$. Two lines of constant ionization are drawn in gray.

most likely not catalyzed by outflows or winds but viscous forces alone suffice. Also, Pelletier & Pudritz (1992) and Königl & Pudritz (2000) find from hydrodynamical simulations that the wind outflow rate is only 10% of the accretion rate. In either case, the black-hole mass and accretion rate are directly related to the radiated luminosity (Eq. 1.14), which can launch the observed outflows. Morales & Fabian (2002) therefore attempt to estimate upper limits on the black-hole mass using the luminosity but disregard the possibility of MHD driving.

The internal structure of warm absorbers can be characterized by gas stability curves (e.g., Chakravorty et al., 2009, and references therein). For a gas with constant density, the stability curve is defined as the relation between the ionization parameter ξ and the quantity $\xi/T \sim L_\mathrm{ion}/R^2 p$, which is proportional to the radiation pressure over the gas pressure. Figure 1.16 demonstrates the significant dependence of the gas stability curve on the spectral shape of the incident spectrum. The curve marks the equilibrium between photoionization and Compton heating as well as recombination and Compton cooling. An isobaric change away from equilibrium therefore leads to cooling/heating back to equilibrium only where the slope of the curve is positive. For negative slopes, a multi-phase medium with different temperatures and ionization states can be formed. The figure shows that multi-phase media are found for example around $\log \xi/T \sim -3.4$ or $\log \xi/T \sim -3.2$. Multiple stable gas phases are a realistic scenario and have been confirmed for warm absorbers, e.g., by Krongold et al. (2003), Netzer et al. (2003) and Krongold et al. (2007).

On the other hand, many Seyferts also show signs of much faster outflows, the so-called Ultrafast Outflows (UFOs), with velocities from ~10 000–100 000 km/s. Typical examples are the so-called PG quasars from the Palomar-Green survey (Schmidt & Green, 1983) where powerful outflows have been found for example by Chartas et al. (2003), Pounds et al. (2003b), or Pounds et al. (2003a). Another prominent example is the quasar PDS 456 (Reeves et al., 2003). In contrast to WAs, the signatures are found in strongly blueshifted absorption features of highly ionized iron above ~7 keV (see Tombesi et al., 2011, 2013a, and references therein). Tombesi et al. (2013b) are convinced of a common nature of WAs and UFOs and propose a stratified wind with increasing outflow speeds closer to the SMBH. Popular models explain this behavior with spherical “Eddington winds” (King & Pounds, 2003; Pounds et al., 2016), where the AGN accrets close to the Eddington rate. When the luminosity approaches L_{Edd}, matter becomes optically thick and is effectively accelerated within shocks reaching speeds of $\gtrsim$0.1 c (King, 2010). In quasars, measured outflow speeds are consistent with this value (e.g., Chartas et al., 2003; Dadina et al., 2005; Markowitz et al., 2006). For Eddington winds, there may in fact be a connection between accretion flow and black-hole mass (Pounds et al., 2016). Interestingly, we found an UFO around the speed of 0.1 c in the sub-Eddington galaxy NGC 4151 (Beuchert et al., 2017).

Absorbers have also been found to be outflowing in the UV via blueshifted, narrow absorption lines of Seyfert 1 galaxies (Crenshaw et al., 1999). Yet, it is subject to discussion, if these UV absorbers are possibly connected to X-ray warm absorbers (e.g., Krolik & Kriss, 1995; Morales & Fabian, 2002, and references therein). Prominent sources, where this was confirmed are NGC 3516 (Kriss et al., 1996b,a) and NGC 4151 (Kraemer et al. 2005; Couto et al. 2016; Beuchert et al. 2017). In other examples no connection was found (Collinge et al., 2001, for NGC 4041).

1.2.5.2 THEORETICAL BACKGROUND ON COLLIMATED JET OUTFLOWS

Besides outflows and winds, powerful, collimated, and relativistic jets are an effective feedback mechanism of AGN. The first astrophysical jets were observed in M87 (Curtis, 1918; Baade & Minkowski, 1954) and 3C 273 (Hazard et al., 1963). The interpretation of jets as collimated beams that carry charged particles was later discussed for example by Morrison (1969), who searched for parallels to pulsars. Blandford & Rees (1974) and Scheuer (1974) later discuss the extended lobes of radio galaxies with respect to collimated outflows.

A series of (recent) studies agree that jets carry plasma within a funnel that is threaded and collimated by magnetic fields with strengths around $\sim 10^{2-4}$ G close to the launching region of the jet (e.g., Baczko et al., 2016) down to ~0.01–0.1 G at around 1 pc distance (e.g., O’Sullivan & Gabuzda, 2009)[9]. These magnetic fields and the relativistic bulk speed of the flow make jets strong emitters of polarized and beamed non-thermal synchrotron radiation in the radio bands. It is subject of this section to collect what is known from dedicated studies of extragalactic AGN jets.

1.2.5.2.1 Magnetohydrodynamics of jets

First, I outline the principles of MHD to pave the way for explaining jet-launching process as well as how they propagate within the first parsecs. I refer to standard textbooks of electrodynamics (Jackson, 1975), (magneto)hydrodynamics, and in particular the textbooks of Meier (2012) and Boettcher et al. (2012) as well as the lecture notes of Röpke (2011) and Steigies (2012) for the necessary details[10].

When discussing magnetized plasma and the propagation of perturbations in the same, one has to combine the formalisms of electrodynamics with those of fluid dynamics. Note that jets are relativistic, which is why some of the following equations need to be corrected for that.

Electrodynamics — In the most general co-variant form, the electrodynamics can be expressed with the four-dimensional and fully relativistic electromagnetic rank-2 tensor $F_{ik} = \partial A_k/\partial x^i - \partial A_i/\partial x^k$ and the four-vector potential $A_k = (\phi, \mathbf{A})$; see Jackson (1975). The Maxwell

---

[9] 1 Gauss equals 10^{-4} Tesla.

[10] see also `https://de.wikibooks.org/wiki/Maxwell-Gleichungen_in_der_klassischen_Elektrodynamik`

equations follow directly with

$$\frac{\partial \tilde{F}^{ik}}{\partial x^k} = 0 \left.\begin{matrix} \boldsymbol{\nabla B} = 0 \\ \boldsymbol{\nabla} \times \boldsymbol{E} = -\partial \boldsymbol{B}/c\,\partial t \end{matrix}\right\} \qquad \frac{\partial F^{ik}}{\partial x^k} = -\frac{4\pi}{c} j^i \left.\begin{matrix} \boldsymbol{\nabla} \times \boldsymbol{B} = -4\pi j/c + \partial \boldsymbol{E}/c\,\partial t \\ \boldsymbol{\nabla E} = 4\pi\rho. \end{matrix}\right\}$$

The stress-energy tensor describes the forces acting in an electromagnetic field and can be written as

$$T^{ik} = F^{ij} F^k_j - \frac{1}{4} g^{ik} F_{lm} F^{lm} \quad = 1/4\pi \begin{pmatrix} (E^2+B^2)/2 & (\boldsymbol{E}\times\boldsymbol{B})^T \\ \boldsymbol{E}\times\boldsymbol{B} & (E^2+B^2) g_{\alpha\beta}/2 - E_\alpha E_\beta - B_\alpha B_\beta \end{pmatrix} \tag{1.29}$$

(Jackson, 1975) where T^{00} is the energy density, $T^{0\beta}$ and $T^{\alpha 0}$ the energy flux or "Poynting vector", $g_{\alpha\beta}$ the metric tensor of space and $T^{\alpha\beta}$ the stress tensor with $\alpha, \beta = 1, 2, 3$. The stress tensor emerges from the variation of the action of an electromagnetic field with respect to $g_{\alpha\beta}$. The corresponding force per unit volume onto plasma that is moving in the outer field is given by the derivative of the stress tensor in all directions, $\boldsymbol{f} = -\nabla_k T^{ik}$, yielding

$$\boldsymbol{F}/V = q\boldsymbol{E} + \boldsymbol{j}/c \times \boldsymbol{B} \tag{1.30}$$

(Jackson, 1975) with the Lorentz-force $\boldsymbol{F}_\mathrm{L} = \boldsymbol{j} \times \boldsymbol{B}$.

MHD — Having calculated the electromagnetic force onto moving charges, I can complement the electromagnetic stress tensor $T^{\alpha\beta}$ and the energy flux $T^{0\beta}$ with the fluxes in the equations of momentum and energy conservation from hydrodynamics. With respect to the equation of momentum conservation in hydrodynamics, the Navier-Stokes equation describes the dynamics of a compressible fluid with the Newtonian stress tensor $\Pi^{\alpha\beta} = p\,\delta^{\alpha\beta} - \pi^{\alpha\beta}$, where p is the isotropic pressure and π the tensor expressing the fluid viscosity (e.g., Goedbloed & Poedts, 2004; Röpke, 2011). When adding the electromagnetic stress tensor, the Navier-Stokes equation becomes complemented with the Lorentz force and one finds the second equation of MHD with the first being the equation of continuity (e.g., Choudhuri, 1998). Also, the total isotropic pressure extends to $p = p_\mathrm{fluid} + p_\mathrm{magn}$, where $p_\mathrm{magn} = B^2/8\pi$ (e.g., Goedbloed & Poedts, 2004).

Based on Eq. 1.30, the current density of plasma moving in an outer field is given by Ohm's law $\boldsymbol{J} = \sigma(\boldsymbol{E} + \boldsymbol{v}/\boldsymbol{c} \times \boldsymbol{B})$ with the conductivity σ. When assuming ideal MHD, changes in magnetic flux through an outer line element is given by

$$d\Psi/dt = -\int_C \frac{\boldsymbol{J}}{\sigma} dS = 0 \tag{1.31}$$

(e.g., Goedbloed & Poedts, 2004) with $\sigma \to \infty$, i.e., the magnetic flux through an arbitrary contour remains unchanged and the electric field vanishes. In this case, the magnetosphere is called "force-free" and the magnetic field lines are frozen inside the plasma.

When assuming a magnetic flux tube threaded by a helical field that is frozen in some plasma, the acting forces are determined by the Lorentz force. The latter can be re-written as the sum of the magnetic pressure gradient and the magnetic tension ("hoop stress"), i.e.,

$$F_\mathrm{L} = \boldsymbol{\nabla}(B^2/8\pi) + (\boldsymbol{B\nabla})\boldsymbol{B}/4\pi \tag{1.32}$$

(e.g., Choudhuri, 1998; Goedbloed & Poedts, 2004). The magnetic pressure will be largest where the magnetic field lines convene with each other and results in an accelerating force that relaxes the field along the symmetry axis and increases the pitch angle of the helix. The hoop stress is directed radially towards the center of the flux tube and attempts to straighten the field lines, thus acting as a collimating force.

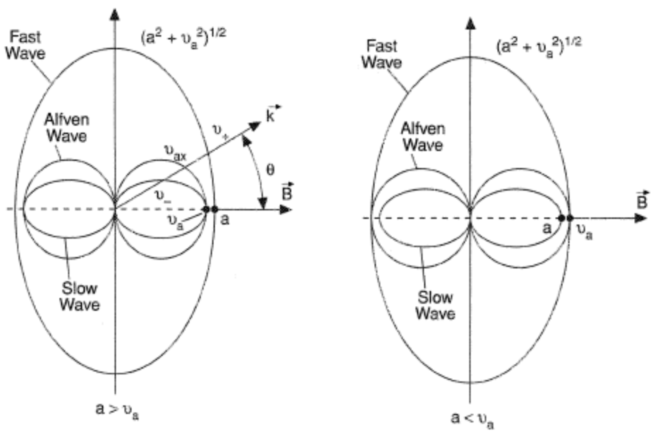

Figure 1.17. Phase-velocity diagram demonstrating the direction of propagation and the velocity of the three MHD waves. The speed of the slow magnetosonic wave is denoted as a, the Alfvén speed as c_A. The magnetic field is assumed to be homogeneous and given as $\boldsymbol{B} = B\boldsymbol{e}_z$. Source: `http://www.thermopedia.com/content/935/`

MHD waves — When neglecting magnetic forces, one can derive sound waves as the solution of the linearized Euler equation, which is a border case of the Navier-Stokes equation for the limit of zero viscosity. The sound speed $c_\mathrm{S} \sim \sqrt{\rho}^{-1}$ (e.g., Choudhuri, 1998) is given by changes of the gas pressure with changes of the density. Accordingly, MHD waves can be derived from linearized MHD equations with respect to infinitesimal changes in the gas density δn, velocity $\delta \boldsymbol{v}$ and magnetic field $\delta \boldsymbol{B}$ (e.g., Choudhuri, 1998).

The result are three different dispersion relations for different kinds of MHD waves, which are summarized nicely by, e.g., Goedbloed & Poedts (2004) and Meier (2012). Their phase-velocity diagrams are illustrated in Fig. 1.17. The *Alfvén wave* and the *slow magnetosonic wave* can only propagate in direction the magnetic field line. While the Alfvén wave can only carry magnetic perturbations, the slow-mode magnetosonic wave also compresses the gas. The *fast magnetosonic wave*, in contrast, propagates in all directions and can compress the magnetic field and the gas against the (magnetic) pressure. The resulting dispersion relations are

$$\begin{aligned} \omega_\mathrm{A} &= \pm k_\parallel c_\mathrm{A} && \text{Alfvén wave } (c_\mathrm{A}) \\ \omega^2 &= 1/2\, k_\perp^2 \left(c_\mathrm{fms}^2 + c_\mathrm{fms}^2\right) && \text{fast magnetosonic wave } (c_\mathrm{fms}, \boldsymbol{k} = k\boldsymbol{e}_\perp) \\ \omega^2 &= 1/2\, k_\parallel^2 \left(c_\mathrm{S}^2 + c_\mathrm{A}^2 \pm \left(c_\mathrm{S}^2 - c_\mathrm{A}^2\right)\right) && \text{slow/fast magnetosonic waves } (c_\mathrm{sms}/c_\mathrm{fms}, \boldsymbol{k} = k\boldsymbol{e}_\parallel) \end{aligned} \tag{1.33}$$

(e.g., Goedbloed & Poedts, 2004; Meier, 2012). The velocity of the Alfvén wave is given by

$$c_\mathrm{A} = c^2 B^2 / \left(B^2 + 4\pi h\right) \tag{1.34}$$

(Boettcher et al., 2012), where

$$h = \rho + P/c^2 \tag{1.35}$$

is the specific enthalpy with the relativistic density ρ (Perucho et al., 2004a). It holds that if $P_\mathrm{fluid} \gg P_\mathrm{magn}$, $c_\mathrm{S} \gg c_\mathrm{A}$ and vice versa.

1.2.5.2.2 Jet launching

In the simplest models, jets are launched with a magneto-centrifugal sling shot, where Blandford & Payne (1982), hereafter BP, proposed a first non-relativistic formulation. As shown in Fig. 1.18 the initial setup is a force-free magnetic tower with a poloidal field that is frozen in the perfectly conducting plasma of the accretion disk in the approximation of ideal MHD. As the disk starts rotating, charges separate in the plane of the disk due to the Lorentz force (Eq. 1.30). Charge balance can be re-established if the charges are expelled, being driven by the centrifugal force. The

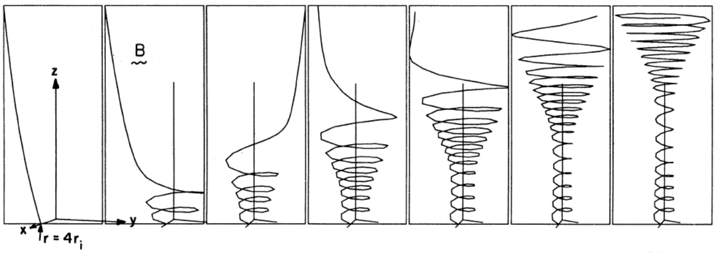

Figure 1.18. Magneto-centrifugal launch of a jet with an initial poloidal field. A description is given in the text. Adopted from Ustyugova et al. (1995).

charges have to follow the initial poloidal magnetic field, as Eq. 1.31 holds. In the approximation of ideal MHD and infinite conductivity, electric fields vanish and the induced current $\boldsymbol{j}$ of the outward moving charges causes a toroidal magnetic field component via the third Maxwellian equation (Ampère's law), where $\boldsymbol{j} \sim -\boldsymbol{\nabla} \times \boldsymbol{B}$. In the second and third panel of Fig. 1.18, the field thus becomes helical with the rotation of the disk. In principle, the jet is therefore launched by a torsional Alfvén wave. In the simulation of Ustyugova et al. (1995) shown in Fig. 1.18, in contrast, the jet plasma is initially accelerated by gas pressure, i.e., slow-mode magnetosonic waves. After the slingshot mechanism was published, it has been used in many MHD simulations with the first performed with respect to protostar jets and molecular winds by Pudritz & Norman (1983), Uchida & Shibata (1985), and Pudritz & Norman (1986).

The force-free magnetic tube is further accelerated by magnetic pressure (first term in Eq. 1.32) that starts to act in the fourth panel of Fig. 1.18 and causes fast magnetosonic waves to propagate downstream. At the same time, the jet is actively collimated by the hoop stress (second term in Eq. 1.32; last three panels in Fig. 1.18).

In an alternate scenario, jets can also be launched by extracting energy from the rotation of a black hole (Blandford & Znajek, 1977, hereafter BZ). In the original idea by Penrose (1969), the ergosphere of a rotating Kerr black hole (see Sect. 1.2.1) harbors free energy that can be released. The "Penrose process" considers the conservation of momentum as source of energy. Inside the ergosphere, close to the rotating black hole, particles can have negative redshifted energy, while every particle escaping from outside the ergosphere must have a positive gravitational redshift. If two particles interact inside the ergosphere, one is reaching outwards and one towards the black hole, the escaping particle will gain energy. This effect is relatively inefficient with ~20% energy gain (Chandrasekhar, 1983). Wald (1974) showed that if the black hole was placed into a homogeneous poloidal magnetic field like the one lancing the accretion disk, GR will lead to the formation of an electric field that breaks the force-free condition of ideal MHD. This field can cause a vacuum gap similar to those found in pulsar magnetospheres (Ruderman & Sutherland, 1975) and particles to be accelerated into the jet (e.g., Ptitsyna & Neronov, 2016). The accelerated particles can form in electromagnetic cascades and via pair production of highly energetic photons from the accretion disk. Eventually the plasma can fill the vacuum gap and re-establish a force-free magnetosphere (e.g., Contopoulos et al., 2013), where the poloidal magnetic field lines become wound up by the frame-dragging effect of space-time in the ergosphere. The helical field accelerates the flow by its own pressure. With this mechanism, Tchekhovskoy et al. (2011) show that more than ~40% energy can be extracted from a maximally spinning black hole and be transferred to the jet.

1.2.5.2.3 Jet propagation

Above, I introduced how jets can form and how they can be filled with plasma. Modern general relativistic magnetohydrodynamic (GRMHDs) simulations extend on these formalisms (e.g., McKinney & Gammie, 2004; Tchekhovskoy et al., 2011). A general result is that the jet magnetization increases towards the launching spot. When both the BP and BZ mechanisms co-act, a spine/sheath structure can be formed (e.g. Ghisellini et al., 2005; Pushkarev et al., 2005;

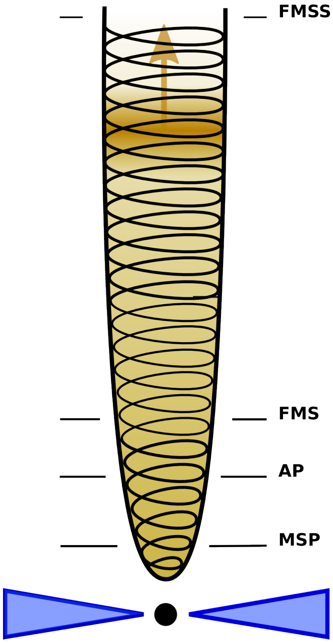

Figure 1.19. Sketch of a parabolic jet funnel threaded by a helical magnetic field. The underlying jet plasma is indicated in orange, the accretion disk as blue triangles. The shocked flow gradually reaches higher speeds at different points in the jet that are marked accordingly. Those are the modified slow point (MSP), Alfvén point (AP), fast magnetosonic point (FMS), and the fast magnetosonic separatrix surface (FMSS). The shock is indicated with an arrow in downstream direction. See the text and Meier (2013) for further details.

Asada et al., 2010; Croke et al., 2010). In theory (e.g., McKinney, 2006; Mizuno et al., 2007; Hawley & Krolik, 2006), a Poynting flux dominated flow can form a slower moving sheath layer within a fast centrifugal funnel that is driven by magnetic fields anchored in the accretion disk.

Such an ordered field configuration acts accelerating and in particular self-collimating if the jet nozzle is parabolic shaped. This triggered the idealized picture of an "Acceleration and Collimation Zone" (AC) as proposed by, e.g., Meier (2013) and Marscher 2006 (see Fig. 1.19). This zone finds support by observations of the sub-parsec scales of close-by AGN jets (e.g., Marscher, 1996; Marscher et al., 2008; Junor et al., 1999; Lister & Smith, 2000; Nakamura & Asada, 2013; Homan et al., 2015). For accelerating the jet in the AC zone, Poynting flux gets converted to kinetic energy. The points at which the jet speed exceeds these characteristic velocities are the MSP, where $j_{\mathrm{j}} > c_{\mathrm{sms}}$, the AP, where $j_{\mathrm{j}} > c_{\mathrm{A}}$, the FMS, where $j_{\mathrm{j}} > c_{\mathrm{fms}}$, and the FMSS. As Meier (2013) points out, the jet is super-fast magnetosonic downstream of the FMS but can still be further accelerated by the hoop stress of the field. After the FMSS the jet is hyper-fast magnetosonic and equipartition between the magnetic and particle energy density may be reached, i.e., the jet would continue as a kinetically dominated flow, become unstable and over-collimated. This behavior has been confirmed by calculations considering stationary, axisymmetric MHD solutions (Beskin et al., 1998; Beskin & Nokhrina, 2006), self-similar, semi-analytic solutions to the MHD equations (Vlahakis et al., 2000; Vlahakis & Königl, 2003a,b, 2004) and numerical simulations (Komissarov et al., 2007). Note, however, that this description is oversimplified and a direct link to observations may only be drawn with caution.

Independent on the magnetization of the continuing flow, the predicted over-collimation downstream of the FMSS may trigger the formation of a recollimation shock (e.g., Polko et al., 2010; Meier, 2013). RHD and RMHD simulations predict a series of such shocks for steady state solutions of overpressured jets (Gómez et al., 1997; Agudo et al., 2001; Mimica et al., 2009; Roca-Sogorb et al., 2009; Perucho, 2013; Mizuno et al., 2015; Fromm et al., 2016). The formation of a recollimation is explained by Daly & Marscher (1988) for a pure hydrodynamical flow: Fig. 1.20 shows an overpressured flow with respect to the ambient pressure P_1. The jet flows into the z-direction. As soon as the overpressured gas flows into the ambient with lower pressure, it starts to expand adiabatically (with the adiabatic index $\gamma = 4/3$). If one neglects the terms of viscosity and compressibility, the Navier-Stokes equation yields the Bernoulli equation

$$\Gamma\, P^{1/4} = \mathrm{const.} \tag{1.36}$$

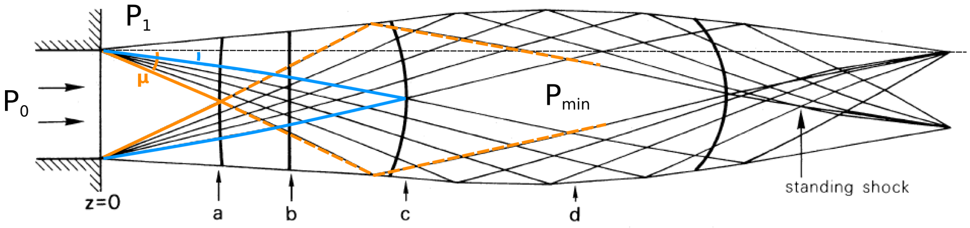

Figure 1.20. Sketch of the recollimation of a flow with pressure P_0 entering a medium with pressure P_1 as adapted from Daly & Marscher (1988). The straight lines indicate Mach cones for different speeds of the flow. The letters point to cuts through the flow where Daly & Marscher (1988) calculate the ratio P_1/P_0. The initial ratio is $P_1/P_0 = 2.5$ and the initial Lorentz factor $\Gamma_0 = 2$. For a detailed description, see the text.

The lower pressure P and therefore the lower specific enthalpy h (Eq. 1.35) of the ambient cause the gas to accelerate into the same. The velocity and pressure field of the expanding and accelerating flow are calculated by Daly & Marscher (1988) using the standard equations of hydrodynamics and is entirely determined by the initial Lorentz factor at $z = 0$ as well as the pressure ratio P_0/P_1. The recollimation observed in Fig. 1.20 can be best explained with the occurrence of Mach shock waves that form inside the accelerated supersonic gas and are highlighted with the dashed-orange line in the figure. As the flow is symmetric, these Mach shocks enclose a so-called "Mach cone" that has the characteristic angle μ with respect to the flow direction z. This angle depends on the Lorentz factor of the flow and the flow speed

$$\mu = \sin^{-1}\frac{1}{M} \quad \text{with} \quad M = \frac{\Gamma v_\mathrm{j}}{c_\mathrm{S}}. \tag{1.37}$$

As the flow accelerates, the Mach cones steepen. As the Mach waves are reflected off the boundary to the ambient, a region close to the center is formed where the pressure reaches a minimal value of $P = P_\mathrm{min}$. The flow will re-collimate into this region. In other words: the information on the sudden expansion of the flow can be propagated only with the local (magneto-)sonic wave speed. As the jet is super (magneto-)sonic, the jet will over-expanded before the interior can realize, causing a delayed re-collimation.

1.2.5.2.4 Jet instabilities

The above sections treated the idealistic physics of jetted plasma. Realistic jets, however, are prone to perturbations and instabilities. One has to distinguish current-driven (CD) or "kink" instabilities and instabilities related to a kinetically dominated flow, such as the Kelvin-Helmholtz (KH) instabilities (e.g., Hardee, 2004; Mizuno et al., 2007). The first can arise for a kinked toroidally dominated magnetic field, where magnetic pressure acts as restoring force that can lead to a disruption of the flow. To prevent that from happening in numerical simulations, Hardee et al. (2007), Hardee (2007), Mizuno et al. (2007), and Mizuno et al. (2015) embed the jet into a protecting axial field envelope. While CD instabilities may be negligible in the AC region (Appl, 1996), they are increasingly relevant further downstream. Even if these instabilities would prevent a large-scale toroidal field to form, collimation can also be achieved by small-scale magnetic fields causing a significant global toroidal component (Li, 2002). Recently, Martí et al. (2016) investigated the physics and stability of jets for a range of magnetizations, Mach numbers and internal energies and discuss the dependence of CD driven pinch modes on these parameters.

KH instabilities arise if two media of different pressure (P_1, P_2) and enthalpy (h_1, h_2; see Eq. 1.35) form a boundary layer with a relative velocity that is close to the sound speed. This can be a relevant process for jets with a spine/sheath configuration. For KH modes to arise, a trigger has to be set by perturbing the pressure at the boundary layer with $P_1 \to P_1' = P_1 + \delta P$.

If the layer points in x-direction and the y-coordinate is perpendicular to the layer, a wave will form that equalizes the pressure difference. One can therefore write the perturbation as $\delta P = A\,\exp\left[-ky + i(kx - \omega t)\right]$. It will therefore be exponentially damped in the y-direction and propagate in the x-direction. If the corresponding wavelength is on the order of the jet radius, KH instabilities can be disruptive. The growth rate of KH modes is particularly large for small Mach numbers. The dispersion relation of such waves was calculated early by Blandford & Pringle (1976) and Turland & Scheuer (1976). The process of mixing withdraws kinetic energy from the flow and converts it to internal energy, which increases the enthalpy. Perucho et al. (2004a,b) propose simulations that use the jet-to-ambient enthalpy ratio as indicator for stable or unstable jets: stable configurations are only found if the enthalpy ratio is small for a large Lorentz factor or vice versa.

In this work we make instead use of properties describing the jet flow itself, i.e., the fast magnetosonic speed c_{fms} and the internal energy ϵ instead of the jet-to-ambient enthalpy ratio (Martí et al., 2016). The magnetosonic Mach number is

$$M_{\mathrm{fms}} = \frac{\Gamma_{\mathrm{j}}}{\Gamma_{\mathrm{fms}}} \frac{v_{\mathrm{j}}}{c_{\mathrm{fms}}}. \tag{1.38}$$

The Lorentz factor

$$\Gamma_{\mathrm{fms}} = \sqrt{1 - c_{\mathrm{fms}}^2}^{\,-1} \tag{1.39}$$

can be eliminated and the fast magnetosonic speed c_{fms} derived as a function of the jet speed and the Mach number.

1.2.5.3 OBSERVATIONAL PROPERTIES OF JETS

In this section, I outline how realistic jets appear to the observer and how these properties can be interpreted in the theoretical framework of steady-state jets that I provided above.

1.2.5.3.1 Shocks in jets

Magnetosonic shocks can form and propagate through the magnetized jet plasma. Independent of the geometry and order of the magnetic field, such magnetosonic waves will cause locally peaking gas and magnetic pressure that enhances the magnetic field order (e.g., Laing, 1980, 1981; Hughes et al., 1985; Cawthorne et al., 1993a; Laing, 1996; Wardle, 1998). In the presense of these fields, bunches of charged particles that are carried by the flow are the ideal candidates to give rise to the observed strong and polarized non-thermal synchrotron radiation of shocks in jets[11]. The broad synchrotron spectrum of an electron distribution $N(\Gamma) = N_0 \Gamma^{-p}$ with the Lorentz boost Γ is given by

$$P_\nu = \frac{2}{3} c \sigma_{\mathrm{T}} N_0 \frac{U_B}{\omega_{\mathrm{L}}} \left(\frac{\omega}{\omega_{\mathrm{L}}}\right)^{-\frac{p-1}{2}} \tag{1.40}$$

(Rybicki & Lightman, 2004). This spectrum describes an optically thin and steep tail $\propto \nu^\alpha$ with $\alpha = -(p-1)/2$ at frequencies above the turnover and an inverted spectrum at lower frequencies with $\alpha = 5/2$ due to synchrotron self-absorption (SSA).

Since the early work by Blandford & Königl (1979), such shocks are what observers usually denote as distinct and propagating "superluminal features" or "knots" in Very Long Baseline Interferometry (VLBI) maps of jets at non-vanishing angles (e.g., Lister et al., 2013, and Sect. 2.1). As the emission component expands, it looses energy adiabatically, SSA becomes less effective, and the peak frequency of the observed radio spectrum drops (as observed, e.g., by Fuhrmann et al., 2016). Königl (1981) extends on this model by calculating the synchrotron (radio) and

---

[11] See Beuchert (2013) for details on the radiative processes of synchrotron emission and absorption.

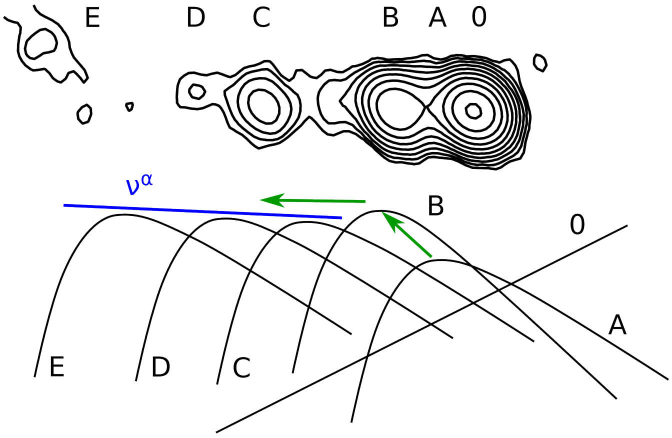

Figure 1.21. Composition of the observed radio spectrum of compact jets. *Top:* total intensity contours of the compact parsec-scale radio jet of 3C 111 at 15 GHz in March 2007. Example shocked emission components are marked with the capital letters A–E. After being ejected from the core (0), the component A first rises in flux to continue as component B–E at an approximately equal flux level. *Bottom:* corresponding synchrotron spectra forming the observed radio spectrum $S \sim \nu^{\alpha}$.

inverse-Compton (X-ray/γ-ray) spectra. He does, however, not consider inverse Compton losses of the synchrotron-emitting electrons, which Marscher & Gear (1985) can use to explain the cm–IR spectral variability of 3C 273 (Robson et al., 1983) with propagating shocks. This "shock-in-jet model" (Marscher & Gear, 1985) has, for example, successfully been applied in total intensity by Fromm et al. (2011, 2013, 2015, 2016) and Fromm (2015), who study variations in light-curves, spectra and VLBI maps for the blazar CTA 102.

The main result of the shock-in-jet model is a flat radio spectrum emitted by compact radio jets as well as the consecutive spectral steepening as the particle distribution looses energy (see Hovatta et al., 2014, for a sample study of the MOJAVE (Monitoring of Jets in AGN with VLBA Experiments) sample[12], who determine spectral indices for the core and the jet components, and a study with the 100-m Effelsberg radio telescope by Fuhrmann et al. 2016). As illustrated in Fig. 1.21, the flat radio spectrum can be explained as the superposed emission from different evolved synchrotron emitting components in the jet (see also Marscher, 1988). The core itself is dominated by SSA and is characterized by a flat or inverted spectrum[13] with $\alpha > 0$.

Observational evidence for the spine/sheath configuration is provided by recent VLBI observations at highest spatial resolution that imply limb-brightened jets, while relativistic shocks propagate in the central spine with high Lorentz factors. Those are, for example, M87 (Kovalev et al., 2007), 3C 84 (Nagai et al., 2014), and Cygnus A (Boccardi et al., 2016b).

1.2.5.3.2 Observational evidence for recollimation shocks

Individual or even a series of shocks have been associated with stationary features in radio galaxies and blazars close to the radio core at millimeter wavelengths (Jorstad et al., 2001; Kellermann et al., 2004; Jorstad et al., 2005; Britzen et al., 2010; Jorstad et al., 2013) with the prominent examples of BL Lac (Cohen et al., 2014; Gómez et al., 2016) or 3C 120 (León-Tavares et al., 2010; Agudo et al., 2012). They provide observational support for recollimation shocks that give rise to particularly enhanced synchrotron radiation. There also exist speculations that the most upstream and bright core feature in VLBI jets at millimeter wavelengths may not only be the $\tau = 1$ surface with respect to synchrotron self-absorption but also coincident with a standing shock at least in some cases (Daly & Marscher, 1988; Impey & Neugebauer, 1988; Marscher et al., 2008). In that regard, these authors claim a "master" recollimation of the flow immediately downstream of the AC zone that has been postulated for example by Beskin & Nokhrina (2006). As Meier (2013) points out, the nature of the jet may be determined by this "master" recollimation, where equipartition may or may not yet be reached. The only possibility

---

[12] See Lister et al. (2009a) and `http://www.physics.purdue.edu/MOJAVE/`

[13] Note the differences in the spectral slope between the sub-classes of BL Lacs and FSRQs (e.g., Fuhrmann et al., 2016).

to assess this question is to observe closeby radio galaxies, where the AC region has been resolved with the technique of VLBI.

The most prominent example is M87 with the standing feature HST-1 (Hada et al., 2011; Doeleman et al., 2012; Nakamura & Asada, 2013). For this source, Hada et al. (2011) push back the $\tau = 1$ surface to a distance of no more than tens of Schwarzschild radii from the black hole. Their results contradict existing speculations that relate the radio core to a recollimation shock at high observing frequencies. Instead, HST 1 is discussed as a popular candidate of a (the first) standing shock. Its distance to the black hole could be estimated to be on the order of $5 \times 10^5\, r_\mathrm{s}$ (Nakamura & Asada, 2013). This scale is consistent with that of observed recollimation shocks in BL Lac, when being foreshortened by an inclination of 6° and assuming a black-hole mass of $1.6 \times 10^8\, M_\odot$ (Woo & Urry, 2002) and also Cygnus A with an even larger mass of $2.5 \times 10^9\, M_\odot$ (Boccardi et al., 2016b,a). Gómez et al. (2016) even detected a series of two recollimation shocks, whose relative distance translates to a deprojected distance of $7 \times 10^4\, r_\mathrm{s}$ and is comparable to the distance of the HST-1 feature to the black hole as established for M87.

1.2.5.3.3 Beaming and jet one-sideness

The relativistic bulk speed of jets leads to a number of intriguing observational consequences. First, the emitted synchrotron radiation is strongly beamed in direction of the flow. This anisotropy challenges the interpretation of the Eddington luminosity, which is defined for isotropic radiation.

The speeds of jetted components often appear superluminal (Rees, 1966; Blandford et al., 1977; Begelman et al., 1984), which can be explained with the projection effect of a foreshortened jet. After Boettcher et al. (2012), the apparent speed is given by

$$\beta_\mathrm{app} = \frac{\beta' \sin\theta}{1 - \beta' \cos\theta} \tag{1.41}$$

with the viewing angle θ and the intrinsic jet speed β', with $\beta' = v'/c$. Figure 1.22 (left panel) shows the apparent speeds for different intrinsic speeds and viewing angles. The apparent speed can be directly derived from the angular speed v_ang with

$$\beta_\mathrm{app} = \frac{v_\mathrm{ang}\, D_\mathrm{L}}{1+z}, \tag{1.42}$$

where D_L is the luminosity distance and z the redshift of the source. The unknowns are therefore the intrinsic jet speed β' and the viewing angle θ. These parameters not only define the apparent speed but also the relativistic Doppler factor

$$\mathcal{D} = \frac{\nu_\mathrm{obs}}{\nu_\mathrm{em}} = \frac{1}{\Gamma\,(1 - v\cos\theta/c)} = \frac{\sqrt{1-(\beta')^2}}{1-\beta'\cos\theta}, \tag{1.43}$$

which I plot in dependence of θ in Fig 1.22 (right panel).

When plasma is intrinsically ejected in the directions of both the jet and the counterjet, this may result in two intrinsically bright and isotropically emitting components that travel in opposed directions. Depending on the inclination θ of the system, the ratio of the flux S_1 of a component pointing towards us and the flux S_2 of a component moving away from us, can change (e.g., Eichler & Smith, 1983, for a first discussion of this issue for M87). The flux of a component over its emitting frequency cubed turns out to be Lorentz invariant (e.g., Rybicki & Lightman, 2004). Given the power-law flux $S \sim \nu^{-\alpha}$, the observed flux can therefore be written as

$$S(\nu_\mathrm{obs}) = \mathcal{D}^{3-\alpha} S(\nu_\mathrm{em}) \tag{1.44}$$

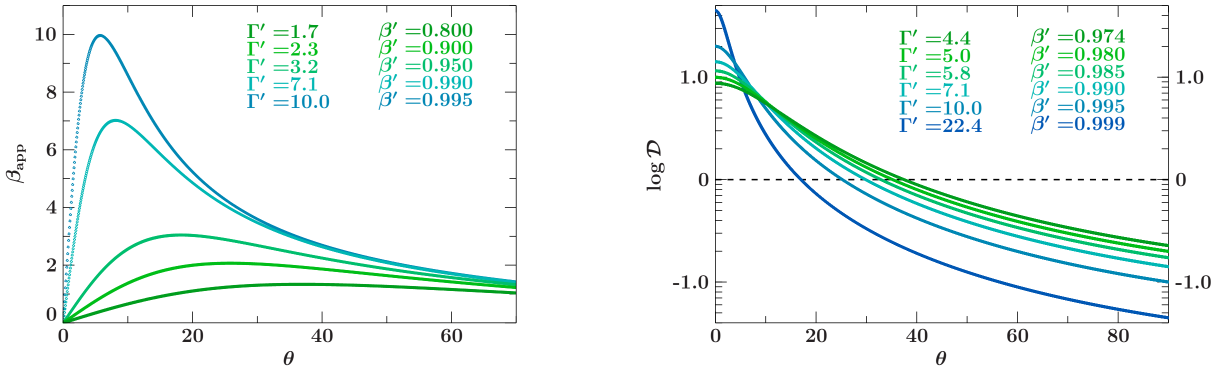

Figure 1.22. Dependence of the apparent speed $\beta_{\rm app}$ (*left panel*) and the Doppler factor $\mathcal{D}$ (*right panel*) on the viewing angle θ and the intrinsic speed β.

(Lind & Blandford, 1985). One can find that for a smooth jet,

$$\frac{S_1}{S_2} = \left(\frac{1+\beta'\cos\theta}{1-\beta'\cos\theta}\right)^{2-\alpha}. \tag{1.45}$$

For one-sided radio galaxies, such as 3C 111, one can only state an upper limit to the counter jet flux. After all, one still remains with two unknowns, β' and θ. For estimating the viewing angle, one has to assume an intrinsic speed or Lorentz factor. As these systems are highly relativistic, the viewing angle of the observer has to be transformed to the jet rest frame with

$$\cos\theta' = \frac{\cos\theta - \beta}{1-\beta\cos\theta} \tag{1.46}$$

(Lyutikov et al., 2005; Wardle, 2013). For a viewing angle of $\theta = 1/\Gamma$, the intrinsic viewing angle is exactly 90°. This transformation is in particular useful to interpret the polarized emission of magnetized jets and to infer the intrinsic orientation of the field. For planar shocks, one expects any magnetic field configuration to be compressed in the plane of the shock front (Laing, 1980), which results in an effective toroidal field. Figure 7 of Lyutikov et al. (2005) demonstrates that the degree of polarization strongly depends on $\theta^{'}$ and also on the pitch angle of the helix.

1.2.5.3.4 The broad-band spectral appearance of radio-loud AGN

In AGN, thermal and non-thermal emission processes are known to emit a broad spectrum from the radio up to the X-rays (see Fig. 1.13 for a typical SED of Seyfert galaxies). For blazars, non-thermal radiation processes dominate the entire electromagnetic spectrum and reliably reach energies up to the γ-rays (see Fig. 1.23). Blazar SEDs consist of two smooth humps, one at lower and one at higher energies. The origin of the first is well known as being due to synchrotron emission of relativistic electrons (or protons as studied by Mücke & Protheroe 2001). It is often superimposed with thermal blackbody emission from the host galaxy in the optical and infrared or the accretion disk in the UV (BBB) as we show in Krauß et al. (2014) and Krauß et al. (2016). In contrast, a number of theories exist to explain the origin of the hump at higher energies. Corresponding models can be divided into leptonic (e.g., Finke et al., 2008; Sikora et al., 2009) and hadronic ones (e.g., Mannheim & Biermann, 1992; Mücke & Protheroe, 2001), i.e., models that describe jets that entrain free leptons or hadrons. See also the review by Böttcher (2007). In reality, both processes may play a role as indicated by mutual degeneracies (e.g., Abdo et al., 2011; Böttcher et al., 2013). This led to the formulation of hybrid models (e.g., Weidinger & Spanier, 2015).

In leptonic models, the high energy emission is explained with a photon field that gets inverse-

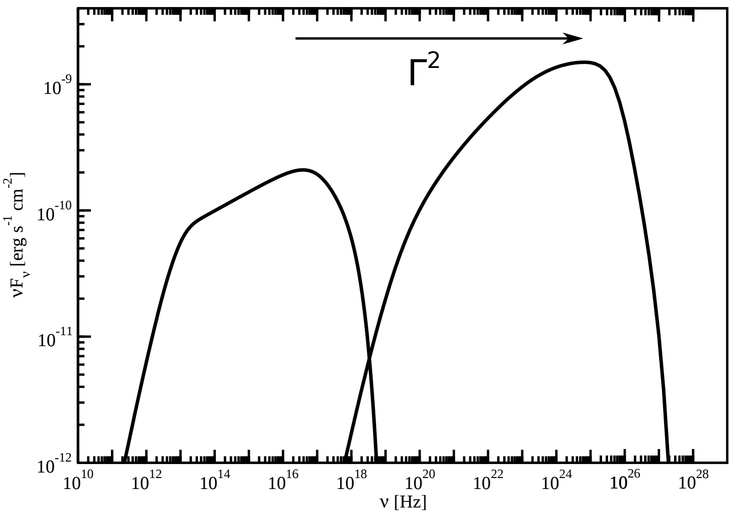

Figure 1.23. Example broad-band SED of a BL Lac as adapted from Finke et al. (2008). The sketch shows a SSC scenario in which the synchrotron hump at lower energies is upscattered by the same relativistic electron population that emits the synchrotron spectrum to form the hump at higher energies.

Compton upscattered by leptons that are accelerated to relativistic energies inside the jet. These upscattered seed photons can either be the synchrotron photons themselves, i.e., synchrotron self Comptonization (SSC, Ghisellini et al., 1985; Ghisellini & Madau, 1996), or external photons from the BLR, torus or accretion disk (EC, Dermer & Schlickeiser, 1993; Sikora et al., 1994; Błażejowski et al., 2000; León-Tavares et al., 2011). As indicated in Fig. 1.23, the energy of the seed photon field is boosted by the factor Γ^2, where Γ is the Lorentz factor of the relativistic leptons. In this context, the peak frequency of the synchrotron hump is determined by the energy of the relativistic electrons and therefore the seed photon field, which regulates the electron energies, i.e., it can be used to classify blazars as is has been done with the “blazar sequence” (Fossati et al., 1998; Ghisellini et al., 1998; Meyer et al., 2011; Krauß et al., 2016).

Hadronic models explain the high energy hump with secondary photons produced in photo-pion processes. An independent method to identify the need of hadrons in the jet and to break model degeneracies is given by the detection of neutrinos, which has become a popular field in research (e.g., Krauß et al., 2014; Kadler et al., 2016) since the firm detection of extragalactic PeV neutrinos (Aartsen et al., 2013, 2014).

1.2.5.3.5 Polarimetry as a tool to study parsec-scale jet physics

Superluminal features observed in parsec-scale jets are found to be bright in total and polarized flux (Hogbom, 1979; Blandford & Rees, 1978) at polarization levels of a few percent in the core region, increasing to higher levels as propagating down the jet (e.g., Homan, 2005; Lister et al., 2009a, for a survey at centimeter wavelengths with the MOJAVE program). The polarization signatures of jets reflect their underlying (shocked) magnetic field structure, which has been a strongly debated issue ever since.

The Stokes formalism describes the polarized synchrotron emission with the four Stokes parameters I, Q, U, V. These parameters can be measured with radio polarimeters that are sensitive to left- and right-hand circular polarized signals ($E_\mathrm{l}, E_\mathrm{r}$) using circular feeds. As it is described in Beuchert (2013), one finds the derived quantities

$$p = \frac{I_\mathrm{pol}}{I} = \frac{\sqrt{Q^2+U^2+V^2}}{I} \quad \text{and} \quad \chi = \frac{1}{2}\arctan\left(\frac{U}{Q}\right) \tag{1.47}$$

where I_pol is the polarized flux, p the fractional polarization and χ the electric vector position angle (EVPA). For a gyrating mono-energetic electron, the maximum degree of polarization is 75%, for a distribution of energies, this value will be lower (69% for a power-law distribution with index two). AGN jets can show degrees of up to 20–40% with exceptions of ∼70% (Bridle et al., 1994). On average, however, jets are only measured with reduced values of $\lesssim 10\%$ (e.g., Homan, 2005) due to Faraday or beam depolarization as well as non-homogeneous magnetic fields.

Due to the opaqueness of the jet upstream of the frequency-dependent $\tau = 1$ region, observations at increasingly high frequencies from millimeter radio waves to the optical bands are indispensable. This jet region close to is launching pad is assumed to be threaded by highly ordered magnetic fields, therefore strongly polarized, and is often referred to as the AC region (see Sect. 1.2.5.2). Sample studies of blazars at optical wavelengths (e.g., Blinov et al., 2016) show that the observed electric vectors rotate over time with a large dynamic range, reaching more than 180° on comparatively short time scales. Prominent examples are BL Lac (Marscher et al., 2008), PKS 1510−089 (Marscher et al., 2010), and 3C 279 (Larionov et al., 2008; Abdo et al., 2010; Kiehlmann et al., 2016). These optical EVPA swings may be interpreted as the geometrical projected rotation of plasma flowing along helical trajectories inside the ordered helical field of the AC zone (Meier, 2013, and references therein), which itself propagates with the jet flow. This effect is only observable for shallow rest-frame viewing angles. On the other hand, light-travel time effects can equally explain such large swings on short time-scales (Zhang et al., 2014). The bridge between the upstream zone dominated by optical polarized emission and the downstream radio jet is crossed by observations of mutual correlations of their polarization properties (Lister & Smith, 2000; D'Arcangelo et al., 2007; D'arcangelo et al., 2009; Jorstad et al., 2010; Kiehlmann et al., 2016) and flux (Marscher et al., 2008; Arshakian et al., 2010).

It is not yet clear whether the radio core coincides with the initial recollimation of an AC zone around the FMSS, whether equipartition is in fact reached at this point (Porth et al., 2011) and how the jet continues further downstream. There are indications that radio jets are still significantly magnetized with an ordered (toroidally dominated) field configuration. Acceleration has been shown to be effective up to tens of parsecs in de-projected distance (Homan et al., 2015), similar to what is proposed by Vlahakis & Königl (2004) and Komissarov et al. (2007).

Radio studies of large samples of unresolved blazars confirm a quasi-bimodal distribution of EVPAs (Bridle, 1984). The majority of VLBI knots in BL Lac objects show aligned EVPAs at a range of frequencies. This picture is not as clear for quasars (Gabuzda et al., 1994, 2000; Lister & Smith, 2000; Lister & Homan, 2005; Pollack et al., 2003). Wardle (1998), Wardle (2013), and Homan (2005) emphasize a non-negligible fraction of oblique EVPA orientations, i.e., "local anomalies", especially for quasars as opposed to clear bimodal orientations. For the simplified case of an underlying axisymmetric and helical magnetic field (Lyutikov et al., 2005), these results imply a dominance of toroidally dominated fields in the inner jet of BL Lac objects and a range of field directions in quasars, where oblique or even transverse shocks (e.g., Hughes et al., 2011) may be one explanation (e.g., Lister, 2001; Marscher et al., 2002; Lister & Homan, 2005; Jorstad et al., 2005).

For many transversely resolved parsec scale jets, the EVPAs of the outer envelopes are perpendicular to the jet, while those on top of the spine are aligned with the jet. Those are for example the blazar 1055+18 (Attridge et al., 1999), the head-tail radio galaxy NGC 1265 (O'Dea & Owen, 1986), Mrk 501 (Giroletti et al., 2004) and a number of other sources (Pushkarev et al., 2005). In the spine/sheath scenario, a planar shock propagating through the spine would result in the observed EVPAs indicating a compressed, toroidally dominated magnetic field. Interactions of the boundary sheath layer with the ambient would result in a sheared longitudinal magnetic field and therefore explain the observed EVPAs in the surroundings (Laing, 1980, 1981; Hughes et al., 1985; Cawthorne et al., 1993a; Laing, 1996; Wardle, 1998; Urpin, 2002). These observations could, however, be equally well explained with a resolved and hollow helical magnetic field (Lyutikov et al., 2005).

Studying the polarization properties of jets for large samples has revealed important characteristics and facilitated to isolate class-specific properties. Despite bimodal EVPA distributions that one observes mainly in unresolved jets, the exception of more complex oblique orientations proves the rule. Dedicated single-source studies of the dynamics of spatially resolved polarized parsec-scale jets are invaluable to gain more insight into the complex processes inherent to these systems.

Such studies involve in particular a monitoring of the EVPA evolution over time. In contrast to the optical bands, large and smooth rotations of more than 90° are rare in the radio (e.g., Altschuler, 1980; Aller et al., 2016, for the University of Michigan variability program) and only found in a few sources (e.g., Aller et al., 1981; Homan, 2005; Myserlis et al., 2016, for BL Lac, 0727−115, PKS 1510−089, and OJ 287). Marscher et al. (2010) explain the large EVPA swing in PKS 1510−089 with a projected, geometrical rotation in presence of an ordered, helical field observed at a shallow angle (Larionov et al., 2008; Nalewajko, 2010). Myserlis et al. (2016), on the other hand, propose transitions between an optically thin and thick state of the polarized ejecta. As Homan et al. (2002) show, the EVPA swings of the majority of 12 selected blazars are overall limited by 90°, consistent with changes of the underlying magnetic field from toroidally dominated to poloidally dominated or vice versa. These observations already demonstrate the ambiguity when attempting to interpret polarimetric data.

One natural explanation for large EVPA swings is given by a source-intrinsic or an external Faraday screen. The rotation measure

$$\mathrm{RM}\,[\mathrm{rad\,m^{-2}}] = 812 \int_0^L n_\mathrm{e} B \, dl \tag{1.48}$$

is proportional to the amount of EVPA rotation in units of rad/m^2 that is induced by both the projected magnetic field B in units of µG along the line of sight L and the electron density n_e in units of cm^{-3}. The observed EVPAs change with respect to the intrinsic ones as

$$\chi_\mathrm{obs} = \chi_\mathrm{int} + \lambda^2 \mathrm{RM}, \tag{1.49}$$

where λ is the observing wavelength. It has been shown that a RM gradient contributes significantly to the observed EVPA rotation in 3C 120 (Gómez et al., 2008), where the depolarizing effect of the Faraday screen was also observed.

Also, the polarized radio emission of spatially resolved recollimation shocks is supposed to reveal complex EVPA patterns: Cawthorne (2006) for example simulates the polarized emission of conical recollimation shocks, which introduce antisymmetric and oblique EVPA orientations. This result is confirmed by observations of the blazar core in S5 1803+784 (Cawthorne et al., 2013) as well as a downstream feature in 3C 120 (Agudo et al., 2012). Also, RMHD simulations predict the polarized radio emission of steady state jets forming a series of recollimations (Roca-Sogorb et al., 2009; Gómez et al., 2016).

Still, there is a lack of numerical (G)RMHD simulations with full radiative output that can predict the EVPA evolution for an interaction of a propagating shock with a stationary recollimation. Such a shock-shock interaction has been observed for example by Fromm et al. (2016) in CTA 102. Existing simulations that try to assess such an interaction, use cells of random magnetic field orientations featuring a turbulent plasma that are propagated inside a pressure-matched jet (Myserlis et al., 2016) or onto a recollimation shock (TEMZ model by Marscher, 2014). In Sect. 4.1, I will discuss the complex EVPA evolution of shocks in interaction with a recollimation for the peculiar radio galaxy 3C 111.

1.2.5.3.6 Morphology and classes of radio-loud AGN

In Sect. 1.2.5.2, I have introduced the inner parsecs of jets. Here, I shortly introduce jets on larger, kiloparsec scales and their interaction with the ISM.

Radio galaxies can be classified based on their radio spectrum. It is flat at their cores, which

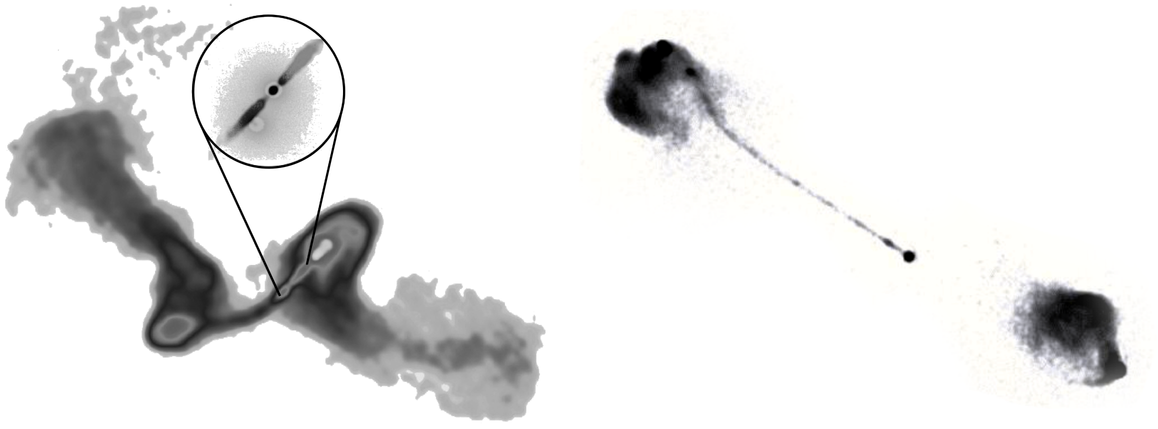

Figure 1.24. VLA radio maps of two prominent radio galaxies. *Left:* NGC 326 (FR I) at 1.4 GHz with a restoring beam of $4''$ FWHM (Murgia et al., 2001); *right:* 3C 175 (FR II) at 4.9 GHz with a restoring beam of $0.4''$ FWHM (Bridle et al., 1994); image courtesy of NRAO.

makes them appear bright at a range of frequencies. More extended jet features are characterized by steep spectra. They are brightest at lower frequencies and become fainter at higher frequencies. Depending on the resolution of the imaging instrument, the compact inner jet will appear as a part of the flat-spectrum core.

Fanaroff & Riley (1974) proposed a morphological classification with the Fanaroff-Riley (FR) sub-classes I and II. The basic criterion is the separation of regions of largest intensity. This separation is larger for the bright hot spots observed in FR II galaxies. Hot spots mark regions of violent interaction with the ambient medium at the downstream end of the collimated jets. In contrast, FR I galaxies show neither signs of strong collimation nor hot spots and appear to interact with the environment already close after the launching site. Prominent examples of FR I galaxies are Cen A (e.g., Burns et al., 1983; Condon et al., 1996; Feain et al., 2011), 3C 31 (e.g., Laing et al., 2008), M87 (e.g., Turland, 1975; Forster et al., 1978) and NGC 326 (e.g., Murgia et al., 2001). The FR II classification is met for example by 3C 270 (e.g., Kolokythas et al., 2015), 3C 111 (e.g., Linfield & Perley, 1984; Jaegers, 1987; Leahy et al., 1997), 3C 353 (e.g., Swain et al., 1998) and 3C 175 (e.g., Bridle et al., 1994). In Fig. 1.24, I show the total intensity images of two prominent sources, one of each class. Both galaxies are viewed nearly edge-on. The collimated jet of 3C 175, however, appears one sided due to beaming in direction of the observer, i.e., arguing for a deviation from a edge-on inclination (Eq. 1.45). The hot spots of FR II galaxies have zero bulk speed and are therefore visible for a wide range of viewing angles.

The question arises, if both classes just reflect different appearances of the large-scale exhaust of one and the same underlying compact source. Arguments against this scenario are provided by studies that imply fundamentally different physics for both classes, as for example different host galaxy properties (e.g., Heckman et al., 1986; Baldi & Capetti, 2008). Also, FR II jets stand out against FR I jets by their overall power: they evidently remain collimated and supersonic on kiloparsec scales as opposed to FR I jets. It has been argued that the accretion rate and/or black-hole spin may be larger in FR II nuclei. Also, FR II types show stronger optical line emission than FR I types, which means that in FR II, nuclear photoionization is more relevant. Baum et al. (1995) first suggested that these differences have to arise because of intrinsic differences of the AGN and not because of differences in the interaction with the environment (De Young, 1993). FSRQs as the most luminous quasars are therefore said to be good candidates for the parent population of FR IIs. The BL Lac sub-class of blazars, on the other hand, may be related to FR Is.

Meier (2013) follows up on this notion and proposes a paradigm in which processes inside the parsec-scale jet may decide on the jet physics on kiloparsec scales. This goes back to issues related with jet acceleration (Sect. 1.2.5.2). Meier (2013) argues that the jets of FR IIs may be Poynting-flux dominated and therefore remain collimated until punching into the ambient medium. FR I jets, on the other hand, reach equipartition early and are therefore prone to destructive interactions with the external medium. Sikora et al. (2005), however, argue against Poynting-flux dominance far at large distances to the black hole.

Polarimetric observations show that jets are strongly magnetized on parsec scales. If jets remain Poynting flux dominated on kiloparsec scales, the jet would have to be dominated by a toroidal field ($\propto r^{-1}$) as compared to the poloidal component ($\propto r^{-2}$). The EVPAs in FR IIs, however, are in general found to be oriented perpendicular to the jet (Bridle, 1984; Cawthorne et al., 1993b; Bridle et al., 1994; Lister & Smith, 2000), indicating a strong axial field. This can, just like on parsec scales, be explained with a spine/sheath configuration.

In a few AGN, the non-vanishing jet inclination of radio galaxies facilitates dedicated studies of both the radio jets and the nuclear properties. Examples are the FR II galaxy 3C 111 (see Sects. 4.2, 4.1 of this work) and the FR I galaxy Cen A. In Cen A we detected a significant Fe K α line in the X-ray spectrum that is normally dominated by non-thermal Comptonized continuum emission (Fürst et al., 2016). We even detected a redshifted neutral Fe K α line in the unusual blazar PMN J1603−4904 (Müller et al., 2015), which challenges its classification as BL Lac and suggests a significant jet inclination.

1.3 The bigger picture of AGN

Now as I have introduced the intrinsic mechanisms that we believe form the various appearances of core- or jet-dominated AGN, I briefly introduce how these various faces of AGN could possibly fit into the global context of compact accreting objects.

AGN and their broad-band spectral information are particularly suited to study the cosmological evolution of black holes (e.g., King et al., 2008) and their evident interaction with the environment (e.g., Merloni & Heinz, 2008; Fiore et al., 2017). Cosmological simulations by Di Matteo et al. (2005, 2007) and DeGraf et al. (2015) underpin that AGN and their black holes are well entangled with their environment. This mutual interaction is imprinted in the M_{BH}-σ relation (King, 2003, 2010), which links the black-hole mass with the velocity dispersion of the surrounding matter as part of the host galaxy (Ferrarese & Merritt, 2000; Gebhardt et al., 2000; Hopkins et al., 2007b, for observational evidence). Also, gas accretion on the most compact scales is found to be directly related to feedback on larger scales (see also Silk & Rees, 1998; Di Matteo et al., 2008; Alexander & Hickox, 2012; Hopkins et al., 2016).

Also, the question arises if compact accreting objects are similar across a range of black-hole mass, i.e., AGN as compared to galactic X-ray binaries with accreting stellar-sized black holes. The fundamental plane of black-hole accretion describes a tight correlation between the X-ray and radio emission of X-ray binaries, i.e., between their accretion and exhaust processes (Merloni et al., 2003; Falcke et al., 2004; Körding et al., 2006). This relation has been found to also hold for SMBHs in AGN, which may indicate the universality of accretion and exhaust processes over a range of mass and luminosity (Plotkin et al., 2012). Still, no direct observational evidence yet exists for AGN to follow the same evolutionary scheme as stellar-sized black-hole binaries. In contrast to AGN, the latter are observed to cycle between disk- and jet-dominated states multiple times. These cycles can be observed in near-real time within a human life.

What has been inferred from surveys of AGN is that they appear to be dominated by heavy SF at high redshifts, that is, during early evolutionary stages, where dust is prevalent and emits reprocessed radiation in the IR (e.g., Bell et al., 2006; Lotz, 2007; Rujopakarn et al., 2010). Related classes of AGN are Ultraluminous Infrared Galaxies (ULIRG, Veilleux, 2008), those at lower luminosities (LIRGs, Sanders & Mirabel, 1996) as well as Submillimeter Galaxies (SMG, Hickox et al., 2012; Smolčić et al., 2017). Eventually AGN are observed to switch from an accretion-dominated "quasar mode" in the earlier universe, to a feedback-dominated "radio mode" during later evolutionary stages (Hopkins et al., 2007a; Peng et al., 2010, 2012, 2014). The quasar mode is characterized by high accretion and black-hole growth rates (Steffen et al., 2006; Lusso & Risaliti, 2016; Aird et al., 2016, see also Di Matteo et al. 2005 and Merloni & Heinz 2008). Buchner et al. (2015) show that the bulk of obscured AGN at higher z are also found at higher luminosities (see also Georgantopoulos et al., 2011). This result underpins the prospect of an era, where increased AGN activity results in material to be blown into the line of sight. Mainieri et al. (2011) find that strong quasar outflows also explain the decreasing SF rate at that times and therefore the lower stellar masses of galaxies (Smolčić et al., 2009). During the radio mode, the stellar mass further decreases (Borch et al., 2006; Wolf et al., 2003) and so does the accretion rate. Here, AGN are interpreted to switch their main dynamic feedback channel from winds to strong and collimated radio jets (Smolčić et al., 2009; Smolčić, 2009). Galaxies in that mode govern the so-called "red sequence" (Bell et al., 2004; Faber et al., 2007). Observations of an increased number of radio-loud AGN at lower redshifts together with an anticorrelation of the black-hole mass with the accretion rate (Ho, 2002; Elitzur, 2007) strengthen this evolutionary scheme and so does the millennium simulation (Croton et al., 2006). Also, the AGN fraction appears to be a function of redshift decreasing from ∼24% during the early and violent universe to only a few percent in the present universe (Wang et al., 2016). The high accretion efficiency during the quasar mode is usually explained with radiatively efficient, geometrically thin α-disks (Shakura & Sunyaev, 1973). These flows may switch to radiatively inefficient, blown-up, and optically thin ADAFs that could favor the formation of collimated jets (Smolčić et al., 2009; Smolčić, 2009), although related GRMHD simulations are yet missing. These authors also suggest that the dichotomy in excitation states (HERGs and LERGs, see Sect. 1.1) can be explained with the evolutionary dichotomy in accretion efficiency. On top, these changing modes may be reflected by the distinct radio morphologies of Fanaroff-Riley galaxies on large scales (e.g., Smolčić, 2009; Chandola & Saikia, 2017) with all consequences for the accretion physics (Tchekhovskoy, 2015).

Having in mind this bigger picture, I provide compprehensive and dedicated studies of a denumerable sample of prominent AGN with the aim of unveiling the physics inherent to these supermassive accretors. Those are the radio-quiet Seyfert galaxies NGC 3227 and NGC 4151, the radio-loud galaxy 3C 111 as well as the young radio galaxy PKS 1718−649.

CHAPTER 2

METHODS

For being able to conduct research on the topics that I have introduced, I make use of both archival and proposed data of various ground- and space-based observatories. This chapter provides the necessary background related to their operation and the analysis of the provided data. In Sect. 2.1, I outline the basics of radio interferometry. Section 2.2 contains detailed information on the interferometers and telescopes used. Section 2.3 explains the basics of X-ray astronomy with an emphasis on focusing and non-focusing X-ray instruments onboard of various observatories in space.

2.1 THE TECHNIQUE OF RADIO INTERFEROMETRY

Radio interferometry is an inevitable tool to resolve the inner part of collimated radio-emitting jets, which is directly linked to the accreting environment and therefore most important for understanding jet physics close to their launching pad. The use of long baselines as part of VLBI enables one to reach milliarcsecond resolution, which translates to sub-parsec scales. This section is strongly based on Burke & Graham-Smith (2009) and the Whitebook titled "Synthesis Imaging in Radio Astronomy II" with the particular proceedings papers from Napier (1999), Fomalont & Perley (1999), Cotton (1999), Briggs et al. (1999) and Wrobel & Walker (1999).

The concept of radio interferometry is best introduced with a two-element interferometer consisting of two radio telescopes that receive a monochromatic signal with the frequency ν at different times,

$$\begin{aligned} x_1(t) &= a_1 \cos(2\pi\nu t) \\ x_2(t) &= a_2 \cos(2\pi\nu\,(t-\tau_\mathrm{g})), \end{aligned} \tag{2.1}$$

where τ_g is the geometric time delay given by the pointing direction of the antennas (see Fig. 2.1). While one measures the total power by forming the autocorrelation of the recorded signals for a single telescope, one has to correlate the signals received by individual antennas for an interferometer, i.e.,

$$R(\tau_\mathrm{g}) = \int x_1(t)x_2(t-\tau)dt \approx \cos\left(\frac{2\pi Dl}{\lambda}\right) \tag{2.2}$$

with $\tau_\mathrm{g} = D\sin(\theta_0)/c = \boldsymbol{D}\boldsymbol{s}_0/c = \boldsymbol{D}_\lambda\boldsymbol{s}_0$. Here, the angle θ_0 is measured from the zenith to the source and goes with $l = \sin(\theta_0)$. The angle θ_0 is equivalent to the vector $\boldsymbol{s}_0$, which is pointing to the source. The baseline vector, i.e., the vector connecting pair of antennas, is given in units of wavelengths and defined as $\boldsymbol{D}_\lambda = \boldsymbol{D}/\lambda$. When measuring signals within a bandpass, one has to integrate Eq. 2.2 over frequency. Assuming a rectangular bandpass, one finds

$$R(\tau_\mathrm{g}) = \cos(2\pi\boldsymbol{D}_\lambda\boldsymbol{s}_0)\,\mathrm{sinc}\,(\tau_\mathrm{g}\Delta\nu\,\pi)\,. \tag{2.3}$$

The fringe pattern defined with the cosine on the left hand side is attenuated with the envelope

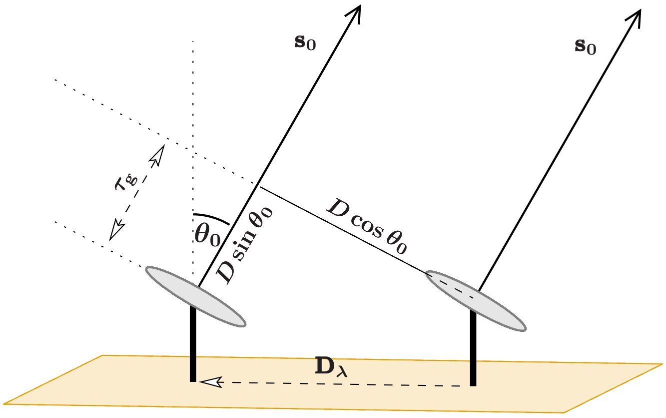

Figure 2.1. Interferometer with two dishes spaced by the baseline vector $\boldsymbol{D}_\lambda$, which is expressed in units of wavelengths. The pointing vector $\boldsymbol{s}_0$ of both telescopes is inclined by θ_0 with respect to the zenith. Signals arrive delayed with the time difference τ_{g}.

of a sinc function that depends on a combination of the geometric delay and the bandwidth $\mathcal{B} = \Delta\nu$. As soon as the delay approaches the inverse bandwidth, the fringes are attenuated, which is known as "bandwidth loss" and results from a loss of coherence. The larger $\mathcal{B}^{-1}$, i.e., the smaller the bandpass $\mathcal{B}$, the larger the delay can get without loosing a coherent signal.

To prevent this from happening, one can introduce an instrumental delay time τ_{i} to compensate the geometrical delay time τ_{g}, i.e., one replaces τ_{g} with $\tau = \tau_{\mathrm{g}} - \tau_{\mathrm{i}}$. Ideally, it is achieved that $\tau \to 0$ and therefore $\mathrm{sinc}\,(\tau_{\mathrm{g}}\Delta\nu\,\pi) \approx 1$.

By now, I only considered a point source under the zenith angle θ_0. Extended sources, however, also emit under angles of $\theta_0 + \Delta\theta$ or, translated to pointing vectors, $\boldsymbol{s}_0 + \boldsymbol{\sigma}$. For astronomical distances, one can approximate with small angles and get the fringe pattern

$$R(\tau_{\mathrm{g}}) \sim R(l) \approx \cos\,(2\pi u l) \tag{2.4}$$

with $u = D\cos(\theta_0)/\lambda$ and $l = \sin(\Delta\theta)$. The coordinate l describes the intensity distribution in the source frame (here, in one dimension).

For a single dish, the total power of a source with the intensity distribution $I(l,\nu)$ is received by an antenna with the reception characteristic $\mathcal{A}(l,\nu)$ under the solid angle $d\Omega$ and can be expressed as

$$P = \int x(t)^2 dt = \int\int \mathcal{A}(l,\nu) I(l,\nu)\, d\Omega\, dl, \tag{2.5}$$

where the power is immediately measured by the autocorrelation of the received signal $x(t)$. $\mathcal{A}(l,\nu)$ can be derived as the far-field Fourier transformation of a two-dimensional circular aperture that is completely covered with radio emitting dipoles. It is therefore also called the three dimensional power beaming pattern of the antenna.

The received power of an interferometer is similar to the convolution of the fringe pattern from Eq. 2.4 with the antenna characteristic $\mathcal{A}(l,\nu)$ and gives

$$R(u) = \int_{l'} \cos\,(2\pi u(l - l'))\, \mathcal{A}(l',\nu) I(l',\nu)\, dl'. \tag{2.6}$$

By using source vectors instead of angles and going over to the complex equivalent, Eq. 2.6 translates to the complex visibility

$$\mathcal{V} = \int_{4\pi} e^{[i2\pi(\boldsymbol{D}_\lambda(\boldsymbol{s}_0+\boldsymbol{\sigma})-\nu\tau_{\mathrm{i}})]} \mathcal{A}(\boldsymbol{\sigma},\nu) I(\boldsymbol{\sigma},\nu)\, d\Omega, \tag{2.7}$$

which is the Fourier transform of the modified intensity $\mathcal{A}(\boldsymbol{\sigma},\nu)I(\boldsymbol{\sigma},\nu)$, and can be measured with the interferometer. One observable, the phase, corresponds to the vector distance $\boldsymbol{\sigma}$ from the phase tracking center, which is itself defined to have zero phase, if the instrumental delay is

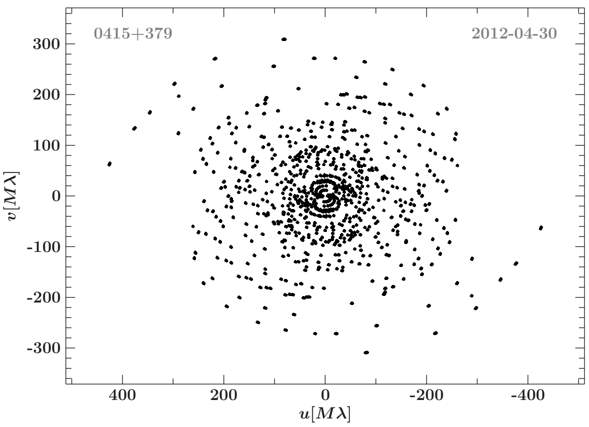

Figure 2.2. Plot of the *uv*-coverage of the VLBA array at 15 GHz during an observation of 3C 111 in the MOJAVE epoch 2012-04-29. Each point in the plane corresponds to the baseline distance between two individual telescopes in units of Mλ and is point-symmetric with respect to the center. The effect of Earth rotation becomes apparent as a displacement of baseline positions along arcs in the plane.

applied correctly with $\mathcal{V}(\boldsymbol{\sigma}=0)=\mathcal{A}(\boldsymbol{s}_0,\nu)I(\boldsymbol{s}_0,\nu)$. The second observable is the amplitude of the visibility.

Similar to Eq. 2.4, one usually uses the coordinates (u,v,w) to define a plane in the frame of the interferometer that lies tangential to all telescopes. The coordinates (l,m) describe the intensity distribution $I(\boldsymbol{\sigma},\nu)$ in the source frame as it is projected on the celestial plane. By Fourier transforming the visibility

$$\mathcal{V}(u,v,w)=\int_{4\pi}\mathcal{A}(l,m)I(l,m)e^{-i2\pi(ul+vm+wn)}\,d\Omega, \tag{2.8}$$

one can therefore switch between the observers and the source frame. For sources on astronomical distance scales, the coordinate w and therefore the curvature of the Earth can be neglected, if the maximal baseline distance is significantly smaller than the Earth diameter. Note that this does not hold for space-VLBI experiments (Kardashev et al., 2013).

A real interferometer can only sample the continuous visibility $\mathcal{V}$ with a discrete number of baselines (or antenna pairs) using the sampling function $S(u,v)$, i.e.,

$$\mathcal{V}(u_k,v_k)=\mathcal{V}(u,v)S(u,v) \quad \text{with} \quad S(u,v)\sim\sum_k\delta(u-u_k)\delta(v-v_k) \tag{2.9}$$

and $k=1\ldots N(N-1)/2$ for N single antennas. When taking into account the rotation of the Earth, one can increase the number of sampling points in the visibility plane. The Figs. 2.2 and 2.3 show the so-called *uv*-coverage for the VLBA interferometer.

Crane & Napier (1989), Walker (1995), and Wrobel & Walker (1999) derived the sensitivity of an interferometer. For N antennas, it is given by

$$\sigma_\mathrm{S}=\frac{\mathrm{SEFD}}{\eta_\mathrm{a}\sqrt{N(N-1)\Delta\nu\, t_\mathrm{int}}} \tag{2.10}$$

where η_a is the system efficiency and includes loss terms of receiver and electronics, the bandwidth $\mathcal{B}=\Delta\nu$, the integration time t_int and where the system equivalent flux density (SEFD) is

$$\mathrm{SEFD}=S_\mathrm{sys}(\nu)/\eta_\mathrm{a}=2k_\mathrm{B}T_\mathrm{sys}/A_\mathrm{eff}\eta_\mathrm{a}. \tag{2.11}$$

The SEFD is the flux density equivalent for the thermal power that a receiver receives without pointing to a source. It depends on the system temperature T_sys, which includes various noise terms from the receiver and the local environment. It also takes into account the antenna efficiency η_a. The sensitivity given in Eq. 2.10 assumes that the SEFD is the same for all antennas. It equals the sensitivity of a single dish with the total collecting area NA_eff.

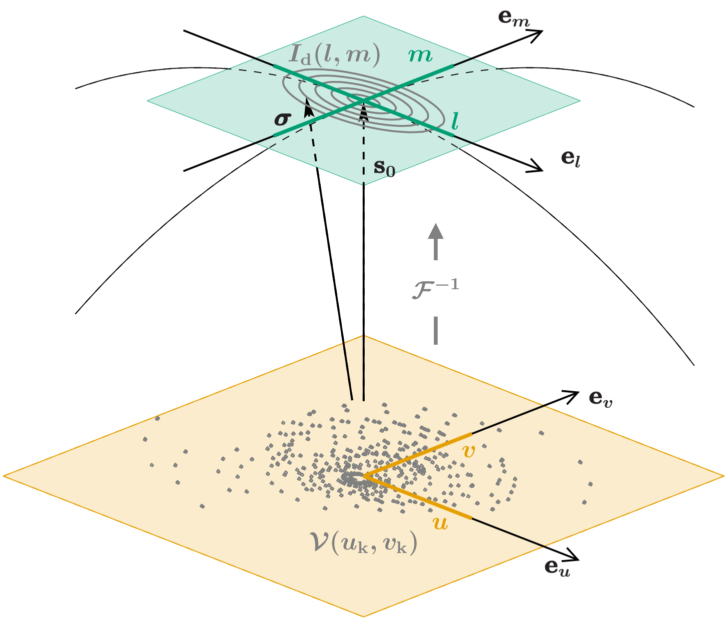

Figure 2.3. Visualization of the Earth- and sky-based coordinate systems related to VLBI imaging. The uv-coverage that characterizes the interferometer is displayed in gray and samples the complex visibilities $\mathcal{V}(u, v)$. When Fourier transforming the measurement $\mathcal{V}(u_\mathrm{k}, v_\mathrm{k})$, one can reconstruct a best guess of the source intensity distribution. This dirty image ($I_\mathrm{d}(l, m)$, gray contours) appears projected on the lm-plane on the sky (blue/green) parallel to the uv-plane. The vectors $\boldsymbol{s}_0$ and $\boldsymbol{\sigma}$ define the phase tracking center and a position on the source.

The VLBA also measures polarized signals via pairs of feeds that are sensitive to orthogonal circular polarized signals (left- and right-handed). The Stokes parameters that are measured by a single antenna are defined as the linear combinations of the autocorrelations of the orthogonal signals (Stokes I and Q) as well as of cross-correlations of these signals (Stokes U and V). I present the details in Beuchert (2013). For an interferometer one has to also correlate the signals of all antennas. This gives the so-called Stokes visibilities for pairs of antennas, which can be treated just like the total intensity visibility data (Thompson et al., 2004). The sensitivity of the corresponding maps of the channels Q, U, and V is $\sigma_\mathrm{S}/\sqrt{2}$.

The sampled visibility data can now be used to infer the best-guess of the source intensity distribution. A first and brute-force approach is to use the discrete Fourier transform, which returns the so-called "dirty image"

$$I_\mathrm{d}(l, m) = \sum_k \mathcal{V}\left(u_k, v_k\right) e^{-2\pi(u_k l + v_k m)}. \tag{2.12}$$

Figure 2.3 illustrates this mechanism. One can also derive the dirty image by convolving the true brightness distribution $I(l, m)$ with the synthesized or "dirty beam", i.e., the Fourier transform of the sampling function $S(u, v)$. As a significant part of the array is not covered by antennas, this is giving rise to sidelobes of the dirty beam. In that sense, a single dish antenna can be seen as a perfect interferometer. The width of the maximum of the dirty beam is a measure for the spatial resolution of the array, while the largest beam of the contributing dishes defines the field of view. For reaching highest resolution, VLBI makes use of antennas that are distributed around the globe with large baselines.

In general, the dirty map will improve the better the sampling of the uv-plane gets. A large density of small baselines or small spatial frequencies, i.e., points with short distance to the center of the uv-plane will be most sensitive to large-scale structures of $I(l, m)$, while small-scale structures are best resolved with larger baselines. As the Earth rotates, uv-points cluster close to the center of the interferometer. When all points in the map are weighted equally (natural weighting), one will be most sensitive to weak emission. On the other hand, details can be better resolved when applying a weighting factor proportional to the inverse of the uv-density (uniform weighting). The VLBA data taken in the framework of the MOJAVE program are naturally weighted.

Assume a dataset of visibilities that are already calibrated against sources of known flux and phase information. The dirty map is distorted by convolving the measured visibility data with the dirty beam (which is the same as building the Fourier transform of the sampled visibility data). The final task is to de-convolve Eq. 2.8. In practice, this is done by finding a good model description for the sampled visibility data. Two methods allow one to infer the clean image from these data, which are both implemented in the tool `difmap` (Shepherd, 1997):

1. With the CLEAN algorithm (Högbom, 1974; Schwarz, 1978), one identifies the point of maximum intensity in the dirty map and assumes the main contributor to be a point source convolved with the dirty beam, which is subtracted from the map. One repeats this iteratively, until the residual map is well balanced and smooth to the largest possible extent.

   The a priori calibration, however, is uncertain for reasons that involve a different setup at different observatories including deviations from an absolute time standard, varying atmospheric conditions and more. The *uv*-data that one uses for cleaning have therefore been adapted during "hybrid imaging". This method uses additional degrees of freedom (dof) given for the visibility phases between groups of three antennas (the "closure phases", see for example Rogers et al. 1974). After each CLEAN-step, one can use the current model that consists of one or more δ-components and transform this model back to infer visibility data that explain this model. These inferred "model visibilities" differ from the observed visibilities both in amplitude and phase. Under the premise that the current model is a good representation of the source, one can adapt the phases of the observed visibilities within the degrees of freedom. This procedure is also called "self-calibration" (Cornwell & Wilkinson, 1981; Cornwell & Fomalont, 1999). This method requires a compact and strong reference component, which is mostly given by the most upstream radio core of AGN jets. When transforming the adapted visibilities back, one can continue working on the phase-calibrated dirty image and add further δ-components. For an overview of the cleaned and self-calibrated images of the entire MOJAVE sample as well as further details on the data analysis of the data used in this work, see Lister et al. (2009a).

   The power of the CLEAN algorithm is that a complex intensity distribution can be reconstructed to highest precision by exploiting the full range of degrees of freedom inherent to the data. The final model will be composed of a number of δ-components.

2. The visibility data that are provided by the MOJAVE collaboration are already calibrated. I am therefore able to quickly reconstructed the sky images by fitting a number of Gaussian model components with varying widths and fluxes instead of a much larger number of δ-components.

Eventually, I fold the final model with the so-called "clean beam", which is a Gaussian approximation of the dirty beam. That way, the side lobes can be attenuated. One can reach a similar effect with a better sampling of the sparse *uv*-coverage. When the model gets folded with the clean beam, the resulting "clean image"[1] has a significantly reduced noise level.

2.2 SINGLE-DISH RADIO TELESCOPES AND INTERFEROMETERS

Now as I have introduced the technique of VLBI, I provide some additional information on the interferometers and radio telescopes that I use in this thesis, i.e., the SMA, VLBA and IRAM 30-m telescope.

---

[1] The clean image carries the units of Jansky/beam, where 1 Jansky corresponds to $10^{-26}\,\mathrm{W\,m^{-2}\,Hz^{-1}}$.

2.2.1 SMA

The 230 GHz and 350 GHz flux density data were obtained at the Submillimeter Array (SMA) near the summit of Mauna Kea (Hawaii). 3C 111 is included in an ongoing monitoring program at the SMA to determine flux densities of compact extragalactic radio sources that are used as calibrators at millimeter wavelengths (Gurwell et al., 2007). Observations of available potential calibrators are from time to time observed for 3 to 5 minutes, and the measured source signal strength calibrated against known standards, typically solar system objects (Titan, Uranus, Neptune, or Callisto). Data from this program are updated regularly and are available at the SMA website[2].

2.2.2 MOJAVE

The MOJAVE program makes use of the Very Long Baseline Array (VLBA) and uses the technique of VLBI, which I described in Sect. 2.1. The details related to the analysis of MOJAVE data are entirely provided in Sect. 4.1.2.

2.2.3 IRAM 30-M

I use data at 86 GHz and 230 GHz that were recorded with the correlation polarimeter XPOL (Thum et al., 2008) of the 30-m Institute for Radio Astronomy in the Millimeter Range (IRAM) telescope on Pico Veleta (Spain). Details on the instrumentation and observing technique are provided by Agudo et al. (2014). The data shown here are measured using the on-off technique with a wobbler of $\sim 45''$. The data were taken in the framework of the Polarimetric Monitoring of AGN at Millimeter Wavelengths (POLAMI) program (Agudo et al. 2017a,b, MNRAS, in prep.; Thum et al. 2017, MNRAS, in prep.). The half-power beam widths are $28''$ and $11''$, respectively. The observations of the monitoring are spaced on the time scale of weeks.

2.3 X-RAY SPECTROSCOPY WITH SPACE-BASED OBSERVATORIES

The compact scales of AGN produce highly energetic radiation and can be probed in the X-rays. To accomplish this, the absorption of the atmosphere requires us to use observatories in space, which have been launched into space since the 1970s and greatly improved in sensitivity until today.

There are several methods to detect X-rays. Here, I provide an overview of focusing (Sect. 2.3.1) and coded-mask instruments (Sect. 2.3.2). The effective area of focusing instruments is largest between 0.1 keV and 10 keV. Prominent examples are the X-ray observatories *Swift* (Gehrels et al., 2004), *XMM-Newton* (Lumb et al., 1996), *Suzaku* (Mitsuda et al., 2007)[3] and *Chandra* (Weisskopf et al., 2000). Recently, the usable energy range was extended up to 80 keV with help of the expendable mast of *NuSTAR* (Harrison et al., 2013), which enables an outstanding focal length of 10 m in contrast to 3.8 m for *XMM-Newton*.

The basic relation

$$c(i) = \int_0^\infty R(i,E)A(E)F(E)dE \tag{2.13}$$

(Davis, 2001; Arnaud et al., 2011) describes how the detector response translates between the counts c detected by the instrument per time with the energy channel i, and the actual source photon flux $F(E)$ in units of Photons $\mathrm{s^{-1}\,cm^{-2}\,keV^{-1}}$. The response divides into the auxiliary response file (ARF) and the redistribution matrix function (RMF). The ARF carries the units

---

[2] `http://sma1.sma.hawaii.edu/callist/callist.html`

[3] Note that *Suzaku* experienced major power issues in 2015 and was switched off in September 2015.

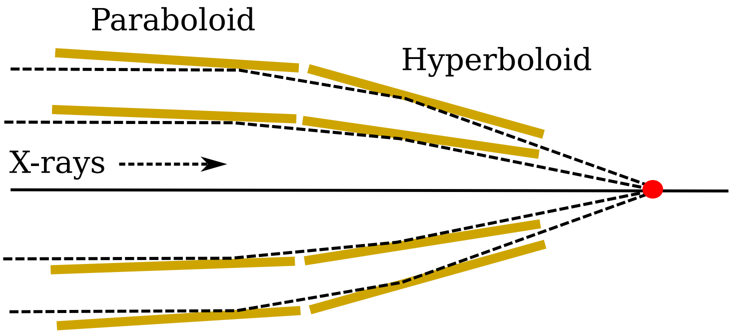

Figure 2.4. Illustration of the nested-shell assembly of a Wolter telescope. The mirror shells divide into a parabolic and a hyperbolic section and focus incoming X-rays onto the focal plane via total reflection.

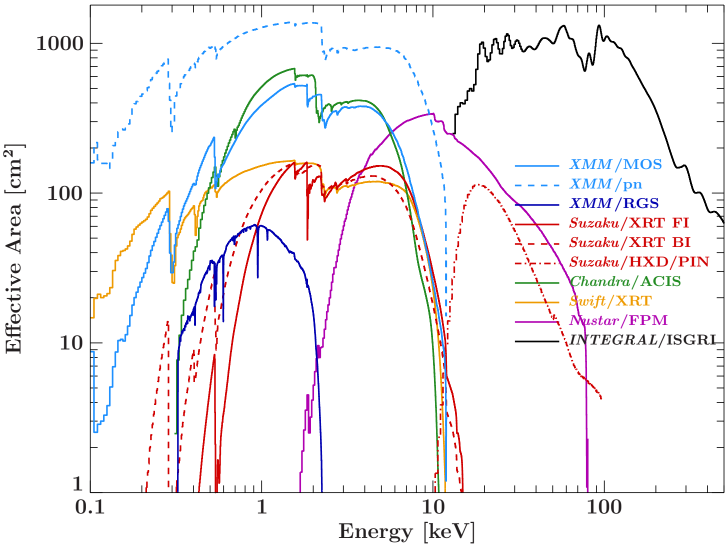

Figure 2.5. Overview of the effective areas of the used X-ray instruments.

of [cm^{-2}] and describes the area-reducing effects of filters in front of the detector, the limiting quantum efficiency as well as downgrading effects of the mirror shells themselves. The RMF operates in the frame of the detector. It redistributes photons of certain energy E into the channels of the detector described by the energy E' as

$$R(i,E) = \int_{E'_i}^{E'_{i+1}} dE' \widetilde{R}(E',E). \tag{2.14}$$

The RMF therefore describes in particular effects related to the excited charge clouds and escape peaks. In an ideal detector, this matrix is diagonal.

2.3.1 FOCUSING X-RAY INSTRUMENTS

In the following, I outline details on the spectral analysis using the above mentioned observatories. The descriptions are strongly related to and taken partly verbatim from Beuchert et al. (2015) and Beuchert et al. (2017). Focusing X-ray instruments make use of a large number of nested mirror shells that are coated with thin high-purity gold layers to increase the effective area. Due to the high energies of X-rays, one needs a geometry as shown in Fig. 2.4 in order to allow total reflection for the incoming photons.

2.3.1.1 XMM-NEWTON

I use all instruments on board of the European Space Agency's Xray Multi-Mirror mission (*XMM-Newton*). Those are the European Photon Imaging Camera (EPIC; Villa et al., 1996), which splits into two EPIC-MOS (Holland et al., 1996; Turner et al., 2001) and one EPIC-pn (Meidinger et al., 1996; Strüder et al., 2001) CCD-cameras, as well as the Reflection Grating Spectrometer (RGS; den Herder et al., 2000) and the Optical Monitor (OM; Mason et al., 2001). While the EPIC camera features a large effective area peaking at $\gtrsim 1000\,\mathrm{cm}^{-2}$ between 0.5 keV and 10 keV, the RGS reaches superb spectral resolution at soft energies $\lesssim 2\,\mathrm{keV}$. The total collecting area of the three equal Wolter telescopes of *XMM-Newton* lies around $1500\,\mathrm{cm}^{-2}$. The maximum effective area as shown in Fig. 2.5 is, however, somewhat lower due to the effects related to the mirrors and the detector as described above. The gratings are placed inside the beam of two of the telescopes.

I follow the standard guidelines for extracting EPIC data with the use of the to date latest versions of the Science Analysis Software (`SAS`) and the calibration database. First, I filter the event lists for hot and bad pixels. I exclude events that are caused by particle flaring and filter those between 10–12 keV for EPIC-pn and above 10 keV for EPIC-MOS. Here, the threshold is set to a maximal rate of 0.4 counts/s for EPIC-pn and 0.35 counts/s for EPIC-MOS. From the filtered events I only consider single and double events for EPIC-pn[4]. For EPIC-MOS, I also allow quadruple patterns. The events are further filtered by the location at which they hit the detector. Here, I consider two regions: one enclosing the source and one the background. AGN are point sources for *XMM-Newton* with a spatial resolution of only $\sim 6''$. If not stated otherwise, I choose the extraction regions to have at least $40''$ in radius, which encloses more than 90% of the encircled energy of the point-spread function (PSF). I use the tool `epatplot` to detect pile-up[5]. In case of a significant excess of double events above the expected rate, the central part of the extraction region should be avoided, where the count-rate is highest. I extract the background from a region off source, which is as large as possible to guarantee the best possible statistics of the background spectrum.

From the RGS gratings data, I extract both diffraction orders with the task `rgsproc`. For each, I combine the resulting spectra of both instruments (RGS 1 and RGS 2) with the task `rgscombine`.

2.3.1.2 SUZAKU

I use both the X-ray Imaging Spectrometer (XIS; Koyama et al., 2007) operating at energies of ~0.5–10 keV and the Hard X-ray Detector (HXD; Takahashi et al., 2007), which extends the probable energies up to a few hundred keVs. Each of the four XIS detectors (XIS 2 is not operational any more) is illuminated by a separate X-ray Telescope (XRT, Burrows et al., 2005; Serlemitsos et al., 2007). The XRTs are constructed in a similar way to those of *XMM-Newton*. The spatial resolution, however, is worse with $\sim 2'$ as opposed to $6''$. The total effective area of the three functional XIS detectors (two back-illuminated and one front-illuminated) adds to $570\,\mathrm{cm}^{-2}$. The HXD detector is a non-imaging instrument with a large field of view of $34' \times 34'$. I use data from the HXD/PIN silicon photodiodes to probe energies above ~10 keV and below ~60 keV. In contrast to the decent energy resolution of the CCD XIS detectors with 130 eV at 6 keV, the resolution of the PIN diodes is only 4.5 keV.

I consider data for the front (XIS 0,3) and back-illuminated (XIS 1) chips in the 3×3 and 5×5 telemetry modes. While applying the latest calibration available, I reprocess and screen the unfiltered event lists with default parameters. Due to the uncertain attitude, the events have to be corrected for changes of the pointing direction using `aeattcor2`. I merge the resulting spectra of the 3×3 and 5×5 telemetry modes using `mathpha` or `phaadd` for each XIS to increase the

---

[4] Double events are those, where the charge cloud that is produced by the incident X-ray photon spreads over two neighboring pixels.

[5] Pile-up occurs, when two or more photons hit the same CCD pixel at times that are close enough to be considered as a single photon with larger energy by the readout process.

count statistics. Based on similar arguments as those given in Sect. 2.3.1.1, the circular extraction regions have a $\sim 90''$ radius and are centered on the point source. I exclude pixels that exceed a threshold of 4% pile-up as estimated with the tool `pileest`. I also exclude events between 1.72 keV and 1.88 keV as well as 2.19 keV and 2.37 keV due to known calibration uncertainties (Nowak et al., 2011). The extraction of the non-imaging HXD/PIN data is straight-forward and all events can be extracted for the whole $34' \times 34'$ field of view. Similar to the imaging instruments, I screen and extract events for the whole field of view.

2.3.1.3 SWIFT

The XRT on board *Swift* (Burrows et al., 2005) provides imaging and spectroscopic capabilities for the energy range 0.5–10 keV. The Burst Alert Telescope (BAT, Krimm et al., 2013) uses the coded mask technique to monitor the hard X-ray sky within 15–50 keV.

Swift/XRT is by design a flexible instrument with a relatively low effective area. It can be used to rapidly react to ToO requests. The strategy of *Swift* therefore makes frequent observations of AGN affordable. Observatories with focusing instruments of larger effective area, on the other hand, are used for deeper observations resulting in spectra of better count statistics.

The two common observation modes of *Swift*/XRT are the photon counting (PC) for fluxes below 1 mCrab and the windowed-timing (WT) mode with faster readout time for higher fluxes. I filter the events for occurrences of certain event patterns on the CCD, also called "grades". For the PC mode, I use grade IDs from 0–12, while I consider only grade 0 events for the WT mode. To sample the entire PSF with a half-power diameter of $\sim 20''$, I extract events from within $30''$–$70''$ around the pointing center depending on the count rate. I extract the background from circular regions of at least $60''$ radius on a position on the chip, which is free of sources.

This paragraph is taken mostly verbatim from Beuchert et al. (2015). The Ultraviolet/Optical Telescope (UVOT; Roming et al., 2005) on board *Swift* can be operated using up to six filters (UVW2, UVM2, UVW1, U, B, and V; Roming et al., 2005). The UVOT image data are summed up using `uvotimsum` (V. 24Jan2014_V6.15.1). I use circular region of $5''$ radius around the source position for the extraction of counts of the core component. I define the background as an annulus around the source with $13''$ and $25''$ inner and outer radius to minimize contributions from the host galaxy. Eventually, I convert the resulting files into pha files using the task `uvot2pha` and de-redden the data as discussed in Sect. 3.1.3.4.

2.3.1.4 NUSTAR

This paragraph follows mostly verbatim Beuchert et al. (2017). *NuSTAR* (Harrison et al., 2013) is the first instrument to focus hard X-rays between 3 keV and 78 keV. Here, X-rays are focused on the two focal-plane modules (FPMs) FPM A and FPM B. For extracting the raw data, I filter events using the tools `nupipeline` and `nuproducts` of the standard *NuSTAR* Data Analysis Software `NuSTARDAS-v.1.5.1`, which is part of `HEASOFT-v.6.18`. The high flux of NGC 4151 in particular forced me to extract source counts from within a relatively large region of $90''$ radius on both chips FPM A and FPM B, and background counts from a region of the same size located $\sim 340''$ off-source. I choose the background region to be close enough not to introduce significant bias due to the spatial dependence of the background (Wik et al., 2014). Due to irregularities in the cross-calibration between *XMM-Newton*, *Suzaku*, and *NuSTAR*, I only consider *NuSTAR* data above 5 keV in Sect. 3.2.

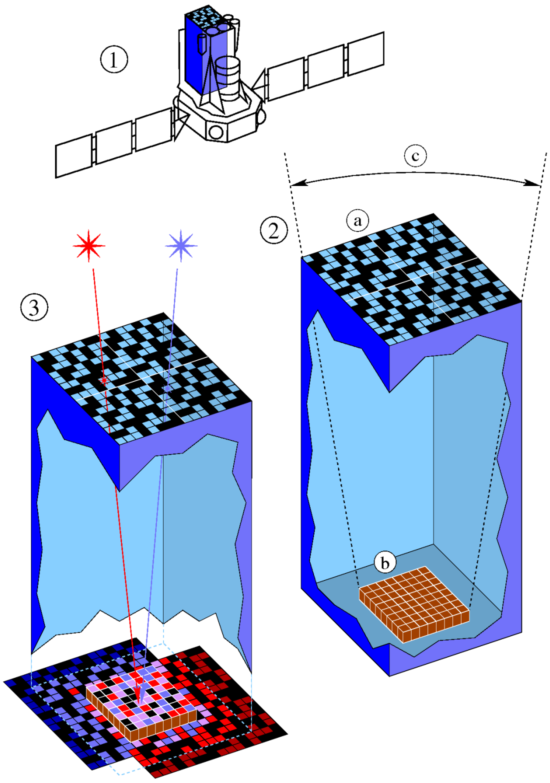

Figure 2.6. Illustration of the IBIS coded-mask imaging system onboard of *INTEGRAL* (1). The sketch (2) shows the coded mask on the top (a) through which the detector array (b) is illuminated. The angle (c) defines the fully-coded field of view (FCFOV, 8° × 8°). The partially-coded field of view (PCFOV, 19° × 19°) includes angles under which only parts of the detector are illuminated, while the total zero-coded field of view (ZCFOV, 29° × 29°) includes the entire field down to zero sensitivity. The sketch on the left (3) shows the overlapping of two mask patterns that are projected onto the detector under different angles. Credits: ISDC/M. Türler

2.3.2 THE CODED-MASK INSTRUMENT INTEGRAL

NuSTAR, *Swift*/BAT, and *Suzaku*/HXD are well suited instruments to cover energies above 10 keV and below ∼80 keV. Above these energies, it is no longer possible to focus X-rays with Wolter telescopes that have a feasible focal length. Instead, *INTEGRAL* and *Swift*/BAT use the technique of coded-mask imaging and spectroscopy. *INTEGRAL* carries a number of instruments (Winkler et al., 2003). I will concentrate on the imager IBIS (Ubertini et al., 2003) that allows one to probe the energy range from ∼15 keV to ∼1 MeV with an angular resolution of $\sim 12'$. All observed AGN therefore appear as point sources. It consists of a coded aperture mask forming the top layer of the instrument and a 128 × 128 CdTe detector array below forming the *INTEGRAL* Soft Gamma-Ray Imager (ISGRI; Lebrun et al., 2003). The total and nominal collecting area of $\sim 2600\,\mathrm{cm}^{-2}$ is directly related to the detector size in contrast to focusing instruments, where the collecting area is given by the mirror size. Degrading effects related to the detector are described by the effective area. For *INTEGRAL*/IBIS/ISGRI, it lies around $\sim 1000\,\mathrm{cm}^{-2}$ as shown in Fig. 2.5. In contrast to *Swift*/BAT, a monitoring detector that is hardware-wise comparable to *INTEGRAL*/IBIS/ISGRI, *INTEGRAL* is performing pointed observations with foregoing announcements of opportunity. The observing strategy of *INTEGRAL* includes dithering patterns[6] that reduce bias given by time and spatial background variability. With the large field of view of IBIS, these patterns quickly sample large fractions of the sky. *INTEGRAL* therefore provides a large archive of deep observations for most sources, which is an additional reason why it outperforms *Swift*/BAT in terms of sensitivity. The way one can use such a detector for imaging and spectroscopy is briefly outlined in the following.

Figure 2.6 shows the principle of the “Modified Uniformly Redundant Array” (MURA; Gottesman & Fenimore, 1989), the coded mask on board of *INTEGRAL*. The detector image is a shadowgram, which is superposed by multiple mask projections depending on the location of point sources in the field of view and the dither patterns. In mathematical terms, the resulting shadowgram is the two dimensional convolution of the mask pattern with the sky map, which

---

[6] http://integral.esac.esa.int/AO14/AO-14_Overview_Policies_Procedures.pdf

can either consist of extended sources or a number of point sources. The following formalism closely follows Goldwurm et al. (2003). The spatial count distribution on the detector plane can be expressed as

$$C = S * M + B, \tag{2.15}$$

where S is the sky map, M describes the mask pattern and B the background distribution. Note that the background will always dominate the source spectra for coded-mask instruments, as the source flux can not be focused with mirrors. For the mask M one can find a "decoding function" D, which is designed to fulfill $S * D = \delta$. There are several methods to reconstruct the initial sky map. One is to use the decoding function as an inverse array, i.e.,

$$S' = C * D = S * M * D + B * D = S * \delta + B * D. \tag{2.16}$$

In other words, if one knows the exact inverse array, the sky map can be reconstructed by simply adding a constant background on top of individual point sources that can be approximated with delta functions. As opposed to focusing instruments it is impossible for coded-mask instruments to directly extract events for certain sources from the detector plane. Instead, the image has to be reconstructed from the entire shadowgram via deconvolution of the mask pattern. For *INTEGRAL*/IBIS, one uses inverse arrays in an iterative way: the reconstructed sky image $S' = C * D$ is fitted with the PSF of the instrument. This PSF also includes a number of secondary "ghost" peaks, which are spread around the primary peak in a regular pattern. As a next step, the shadowgram of this model is computed by convolving it with the mask pattern M and subtracted from the observed shadowgram. This algorithm is iterated until all contributing sources are identified and properly modeled with the detector PSF.

My primary focus lies on AGN, which are point sources for *INTEGRAL* and are weak in flux. For galactic X-ray binaries, the above steps can be conducted for a large number of energy bins and spectra can be studied in detail. For AGN, I use as large energy bins as possible (mostly 20–200 keV) for collecting a sufficient number of counts and to facilitate the image reconstruction. Here, I consider data (provided as "science windows" or "scws") where the target is located at a maximum distance of 14° off the pointing center. One scw usually combines 20-40 minutes of exposure, while the telescope pointing performs certain dither patterns (Courvoisier et al., 2003) for each scw. I exclude data that are taken in the performance verification phase before March 24, 2003. I have used the to date most recent version of the Off-Line Scientific Analysis (`OSA`) with the version number `v.10.1` after 2015 February 11 and `v.10.2` after 2016 February 02. For being able to detect AGN with fluxes around the sensitivity limit or below, I combined a number of scws and calculated stacked mosaic maps.

Note that the image reconstruction of individual scws (using the tool `ibis_science_analysis`) becomes increasingly challenging the more sources are located in the field of view and the weaker the source of interest is. For that reason, peaks in the decoded maps below $6\,\sigma$ above the background may not be trustworthy[7].

For the case of a solid detection, I fit a Gaussian to the corresponding source position and extract the count rate with the tool `mosaic_spec`. Eventually, I wrote a tool with the Interactive Spectral Interpretation System (`ISIS`) to calculate the source flux for the power-law $E^{-\Gamma}$ from the count rate of the channel i, which is given by

$$c(i) = A \int_{E_1}^{E_2} E\, E^{-\Gamma} A(E) R(i,E)\, dE. \tag{2.17}$$

The response matrix $R(i,E)$ can be replaced with unity for a single energy bin or must be re-binned according to the *INTEGRAL* user handbook[8]. The resulting differential energy flux

---

[7] Note, however, a possible exception for known sources as outlined in Sect. 4.3 and in 't Zand et al. (1994).

[8] `http://www.isdc.unige.ch/integral/download/osa/doc`

carries units of keV×Photons/cm^2/s/keV, which can be translated to Janskies (keV/s/cm^2/Hz). For SEDs, one usually uses units of νF_ν, which one can achieve by multiplying with the centroid bin energy, i.e., yielding units of keV/cm^2/s $= 1.602 \times 10^{-9}$ ergs/cm^2/s.

The detection significance is given with the signal-to-noise ratio (S/N) in units of the standard deviation of the background with

$$SN = \frac{C_\mathrm{S}}{\sqrt{C_\mathrm{S} + C_\mathrm{B}}}. \tag{2.18}$$

This relation holds for the Fully Coded Field of View (FCFOV), where the variance is roughly constant and equal to the total number of counts (Skinner et al., 1987; Skinner, 2008).

If no detection can be achieved, I state an upper limit. An upper limit should also include systematics in addition to the photon statistics that are given by the square root of the variance. The systematics on the photon statistics can be described by an additional factor given by the root mean squared (RMS) of the significance map, which always exceeds 1 for *INTEGRAL*. The best choice for the RMS is a region around the source of interest with a homogeneous exposure distribution and the lack of strong sources in the field. The systematics therefore strongly depend on the position on the map. The main contributors are: (1) coding noise due to uncertainties in the image reconstruction, (2) a non-homogeneous instrumental background, (3) diffuse emission that is not removed with the background for maps containing bright images, and (4) uncertainties in the energy calibration. For example, a $5\,\sigma$ upper limit is thus given by $\sqrt{\mathrm{VAR}} \times 5 \times \mathrm{RMS(bkg\_sig)}$, where VAR is the variance of the source and RMS(bkg_sig) the RMS of the significance map in absence of sources.

CHAPTER 3

UNVEILING THE HIDDEN

X-RAY STUDIES OF VARIABLE ABSORPTION IN RADIO-QUIET SEYFERT GALAXIES

The following chapter contain work that I have conducted with collaborators. We use time-resolved spectroscopy and the study of time-dependent line-of-sight absorption to shed light onto the compact environment in close vicinity of accreting black holes – an environment that has not yet been able to be spatially resolved. In the past, similar methods have already revealed a number of absorption events for Seyfert galaxies including also NGC 3227 and NGC 4151 at different time-scales and column densities. Note that studying reverberation time-delays between changes of the irradiating source and the reflecting environment (e.g., Uttley et al., 2014) is also a very powerful tool to assess the interior of AGN and will be used to cross-check our results. This chapter is structured as follows: our work on the prominent Seyfert galaxies NGC 3227 and NGC 4151 is contained in the Sects. 3.1 and 3.2. A study of the environment of the presumably young and absorbed radio galaxy PKS 1718−649 is provided in Sect. 3.3.

3.1 A VARIABLE-DENSITY ABSORPTION EVENT IN NGC 3227

3.1.1 INTRODUCTORY REMARKS

Here, I present work on the Seyfert 1.5 AGN NGC 3227 that we published in Beuchert T., Markowitz A.G., Krauß F., et al., 2015, A&A, 584, A82. The majority of this chapter including these introductory remarks are taken in verbatim from this publication, which is indicated accordingly for the individual sections. NGC 3227 was subjected to sustained monitoring with *RXTE* from 1999-Jan-02 to 2005-Dec-04 (Uttley & McHardy, 2005). The monitoring revealed two eclipse events: an ~80-day event in 2000/2001 (Lamer et al., 2003) and a 2–7 day event in 2002 (Markowitz et al., 2014). The estimated distances from the central engine are tens of light days (lds). Given the estimated location of the BLR from the SMBH, at 2–19 ld (Peterson et al., 2004; Landt et al., 2008), and the inner edge of the IR-emitting torus as determined by reverberation mapping, ~ 20 ld (Suganuma et al., 2006), these clouds are likely located in the inner dusty torus or at least the outermost BLR.

For our study. we use the systemic redshift of $z = 0.00386$ (de Vaucouleurs et al., 1991) and a Galactic equivalent hydrogen column of $N_{\mathrm{H}} = 1.99 \times 10^{20}\,\mathrm{cm}^{-2}$ (Kalberla et al., 2005). The black-hole mass is assumed to be $1.75 \times 10^{7}\,M_{\odot}$, which is the average of a set of measurements collected at the AGN Black-Hole Mass Database[1]. Luminosities are calculated using a luminosity

---

[1] `http://www.astro.gsu.edu/AGNmass/`

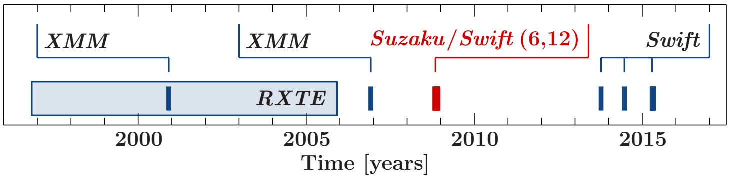

Figure 3.1. Time line including all observations of NGC 3227 discussed here. The blue region shows the time range of sustained *RXTE* monitoring from 1999-Jan-02 to 2005-Dec-04 (Uttley & McHardy, 2005). The observations by *Suzaku* and *Swift* from the 2008 campaign are marked in red; the times of the *XMM-Newton* and recent *Swift* observations are shown in blue.

distance of 20.3 Mpc (Mould et al., 2000). We perform the K-correction according to Ghisellini et al. (2009). Neutral absorption is modeled with `tbnew`. Ionized absorption is modeled using the `zxipcf` model, which is based on pre-calculated `xstar` tables (Kallman & Bautista, 2001).

Here, we study an additional, intriguing, absorption event in NGC 3227 found in quasi-simultaneous *Suzaku* and *Swift* data from 2008. The column density profile turns out to be highly irregular. In Sect. 3.1.2 we present the data reduction, while Sect. 3.1.3 revisits the two already published *XMM-Newton* observations to define a model that we use to simultaneously fit the archival *Suzaku* observations. The X-ray and UV data provided by *Swift* are analyzed in Sect. 3.1.4 together with data in the IR and optical. In Sect. 3.1.5 we discuss the properties and location of the absorbing cloud and its possible origin in light of these observations, while Sect. 3.1.6 provides the results of a follow-up study with *Swift*. We conclude on our results in Sect. 3.1.7.

3.1.2 OBSERVATIONS AND DATA REDUCTION

The following two paragraphs are taken in verbatim from Beuchert et al. (2015) except of deviations in the descriptions of the individual observatories. Figure 3.1 provides an overview of all of the archival observations of NGC 3227 that we consider. NGC 3227 was the subject of a 35 d long *Suzaku* and *Swift* monitoring campaign between 2008 October 2 and 2008 December 03. The campaign consists of six *Suzaku* and 12 nearly simultaneous *Swift* observations (Table 3.1). Outside of this campaign, further archival data with good soft X-ray coverage are provided by two *XMM-Newton* observations, one from 2000 November 28–29 at the onset of the 2000/2001 absorption event (obsid: 0101040301, exposure time post screening 32 ks; Lamer et al., 2003), and a 97 ks observation on 2006 December 3–4 (obsid: 0400270101; Markowitz et al., 2009) during a state with intrinsically high flux and relatively low absorption. The observation from 2006 yielded RGS data of sufficient S/N for a detailed analysis of the absorbers. Recent *Swift* pointings, from 2013 October 20 until 2015 May 02, are also included in our analysis.

For the reduction of these data, we used `HEASOFT` v. 6.15.1 and *XMM-Newton* `sas` v. 13.5.0 and closely follow the tasks that are introduced in Sect. 2.3. Exceptions and additional information are stated below. Throughout, I show uncertainties corresponding to the 90% confidence level.

XMM-Newton— Both *XMM-Newton* observations were taken in the full-frame mode of the EPIC-pn camera. As no pileup is evident, we extract 0.3–10 keV spectra from all counts within 40″ of the central source position of NGC 3227. The same angular radius of the extraction region is used to extract the background from a position ∼6′off-source on the same CCD-chip. The observation with the ID 0101040301 is binned to a minimum S/N of 10, the observation 0400270101 to a S/N of 35.

Suzaku— We extract both the data of the detectors XIS and HXD. Spectra are extracted from circular regions of ∼93″ radius and centered on the point source. We normalize all fluxes with respect to XIS0. Our fits find that the flux normalization of the XIS1 and XIS3 spectra deviates by about 5% from that of the XIS0 spectrum, consistent with the *Suzaku*

Table 3.1. *Suzaku* and *Swift* observations in 2008 with their screened exposure times. Counts listed are in the energy bands given in Sect. 3.1.2. The check-symbol (√) denotes observations that are used in the data analysis, while observations labeled with a cross (✗) are excluded (see Sect. 2.3.1.3 for details).

Suzaku XIS							*Swift* XRT						
abbrv.	obsid	det	time	exp [ks]	cnts [$\times10^4$]		abbrv.	obsid	mode	date	exp [ks]	cnts	
Suz 1	703022010	XIS 0	2008-10-28	58.9	7.8	√	Sw 1a	00037586001	pc	2008-10-28	1.0	543	√
		XIS 1			8.6	√	Sw 1b	00037586002	pc	2008-10-29	2.0	2386	✗
		XIS 3			8.0	√							
		HXD		47.9	3.4	√							
Suz 2	703022020	XIS 0	2008-11-04	53.7	2.2	√	Sw 2a	00031280001	wt	2008-11-04	1.0	255	√
		XIS 1			2.2	√	Sw 2b	00031280002	wt	2008-11-05	2.2	497	√
		XIS 3			2.2	√							
		HXD		46.4	3.1	√							
Suz 3	703022030	XIS 0	2008-11-12	56.6	3.3	√	Sw 3a	00031280003	wt	2008-11-12	1.0	291	√
		XIS 1			3.4	√	Sw 3b	00031280004	pc	2008-11-13	2.2	702	√
		XIS 3			3.4	√							
		HXD		46.6	3.2	√							
Suz 4	703022040	XIS 0	2008-11-20	64.6	1.5	√	Sw 4a	00031280005	pc	2008-11-21	2.1	280	√
		XIS 1			1.8	√	Sw 4b	00031280006	pc	2008-11-22	1.9	256	√
		XIS 3			1.5	√							
		HXD		43.4	2.9	√							
Suz 5	703022050	XIS 0	2008-11-27	79.4	3.7	√	Sw 5a	00031280007	pc	2008-11-25	2.0	429	√
		XIS 1			3.8	√	Sw 5b	00031280008	pc	2008-11-27	1.9	252	√
		XIS 3			3.7	√							
		HXD		37.2	2.6	√							
Suz 6	703022060	XIS 0	2008-12-02	51.4	1.7	√	Sw 6a	00031280009	pc	2008-12-02	0.3	50	✗
		XIS 1			1.8	√	Sw 6b	00031280010	pc	2008-12-03	1.7	264	√
		XIS 3			1.7	√							
		HXD		36.5	2.3	√							

ABC guide (`http://heasarc.gsfc.nasa.gov/docs/suzaku/analysis/abc/`), version 5.0. We perform simultaneous fits of observations Suz 2–Suz 6 using the SimFit routines of `ISIS` (Kühnel et al., 2015), and rebin their spectra to a combined minimum S/N of 25. Observation Suz 1 is fitted separately and binned to a minimum S/N of 18. In both cases, the binning does not exceed the energy resolution of the XIS detectors of 150 eV at ~6 keV in 2008[2]. Based on the exclusion intervals 1.72–1.88 keV and 2.19–2.37 keV, the first interval is extended to 1.5–1.88 keV because of further insufficient calibration just above 1.5 keV.

For a list of total counts and good exposure times of the extracted HXD data, see Table 3.1. The flux normalization of the HXD with respect to XIS0 suffers large uncertainties because of the low S/N of the HXD data, but is consistent with what we expect for the current calibration release from 2014-10-01. In order to reduce degeneracies, we therefore fix the HXD flux normalization constant to its nominal value of 1.16.

Swift— Except for observations Sw 2a,b and Sw 3a, which were taken in WT mode, all observations were performed in PC mode. For the low count-rates of NGC 3227 it is sufficient to extract source counts only within 30″ of the source position. We exclude observation Sw 1b from our analysis because of an excess above 7 keV of unknown origin. Observation Sw 6a was also ignored because of an insufficient number of detected counts.

3.1.3 X-RAY SPECTRAL ANALYSIS

This section is mainly taken in verbatim from Beuchert et al. (2015). The main focus of the data analysis lies on the simultaneous *Suzaku* and *Swift* data describing an additional absorption event. In the following, we first build up a spectral baseline model using the *Suzaku* data. With help of this model, we revisit the two archival *XMM-Newton* observations and finally model each set of *Suzaku* and *Swift* observations simultaneously.

---

[2] `https://heasarc.gsfc.nasa.gov/docs/astroe/prop_tools/suzaku_td/node10.html`

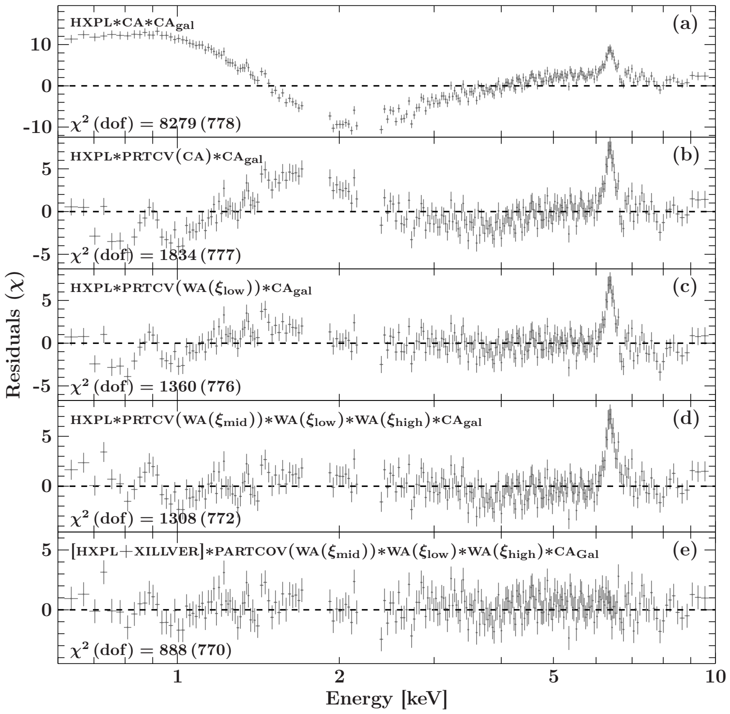

Figure 3.2. Example of the steps followed to find the best-fit baseline model on the *Suzaku* spectra (we use observation Suz 3 in this example). **a)** Fit to the spectrum with a single power law absorbed by neutral gas. **b)** The neutral absorber is partially covering the incident power law. **c)** As a result of characteristic residuals, we replace the solely neutral absorber by an ionized absorber, and **d)** two more warm absorbers leading to a stratified composite of differently ionized absorbers. **e)** The remaining residuals in the soft band and around 6.4 keV are flattened when finally adding a reflected power law in panel.

3.1.3.1 A BASELINE MODEL BASED ON SUZAKU DATA

Before we start to develop a baseline spectral model for NGC 3227, we briefly review the previous attempts to describe the spectrum. Lamer et al. (2003) describe the 2000 *XMM-Newton* observation with a power law absorbed by material with neutral or low ionization (hereafter WA_1) and an unabsorbed power law. The slope of the absorbed power law was difficult to constrain. As shown by Lamer et al. (2003), this model is highly degenerate in ξ (two orders of magnitude) and N_{H}. We find that a lower degree of degeneracy can be obtained by assuming a partial covering scenario, which yields comparable statistics. The lack of sufficient RGS data and the low S/N did not allow Lamer et al. (2003) to constrain more absorbers.

In contrast, the 2006 *XMM-Newton* observation caught the source in a typical hard X-ray flux and spectral state, that is, unabsorbed by moderately Compton-thick gas. The high soft X-ray flux and the long exposure time allowed Markowitz et al. (2009) to obtain a high S/N RGS spectrum. They constrained two layers of ionized absorption, one absorber that is moderately ionized, $\log\xi \sim 1.45$, and one absorber that is highly ionized, $\log\xi \sim 2.93$. We call these WA_2 and WA_3 in the following. Markowitz et al. (2009) also detected an absorber with a small neutral column, which is similar to WA_1 seen in 2000 by Lamer et al. (2003).

We use the high S/N *Suzaku* data to derive the baseline model. We assume from now on that WA_1, WA_2, and WA_3 are present in all *XMM-Newton*, *Suzaku*, and *Swift* observations. We assume these absorbers to represent physically distinct absorbing media with different levels of ionization. The assumption that WA1, WA2, and WA3 are present in all observations and stable over durations of years is a simplifying one; a given absorber may not always be statistically required, particularly, if the column densities of the other absorbers dominate the spectral shape. In addition, as demonstrated below, we observe a wide range of column densities in WA1 and WA2 across spectra taken several years apart. A simple assumption is that each absorber remains present in all observations, and has varied primarily in column density and not ionization state. However, we cannot exclude the possibility of some observations capturing an additional physically distinct absorber with similar ionization level moving into the line of sight.

Figure 3.2 shows the steps followed to find the best-fit baseline model on the 2008 *Suzaku* spectra motivated by Lamer et al. (2003) and Markowitz et al. (2009). We use observation

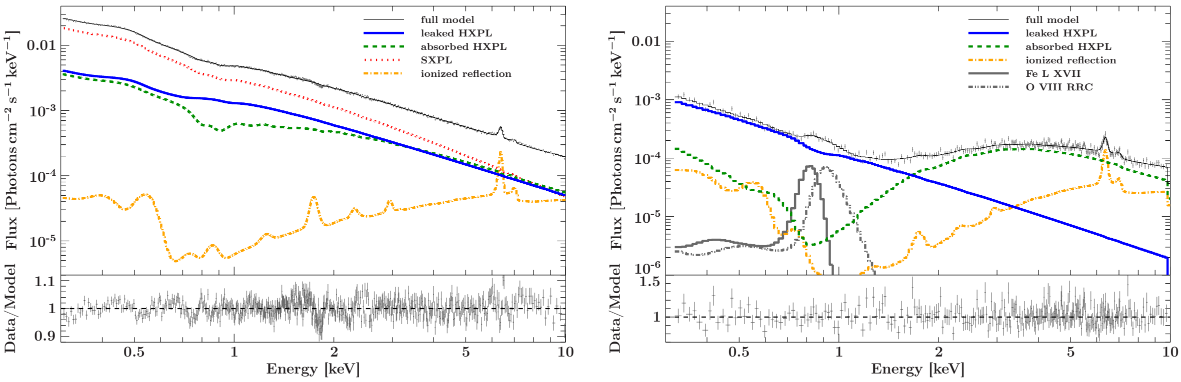

Figure 3.3. The 2006 (*left*) and 2000 (*right*) *XMM-Newton* spectra, the best-fit model components, and the complete model shown with thick and thin solid lines, respectively. Both spectra are described by the baseline model that comprises a high-energy X-ray power law with a reflection component and absorption by three layers of low-, moderate- and high-ionization gas as well as the Galactic column. The source is partially covered by WA$_2$ for the 2006 and by WA$_1$ for the 2000 observation. The data from 2006 also require a steep soft excess. The sharp residuals at $\sim$1.85 keV are likely due to calibration uncertainties around the Si K edge.

Suz 3 in this example, which has the best combination of count rate and strong absorbing column density. The χ^2 of each fit is labeled in the figure and shows the gradual improvement of the model. In Fig. 3.2a the high-energy X-ray power law (HXPL) absorbed by one layer of cold/neutral absorption (CA). Apart from the prominent Fe Kα line around 6.4 keV, the strong residuals below 4 keV suggest a partial covering scenario similar to that seen in the 2000 *XMM-Newton* data. Assuming partial absorption by a neutral medium results in the residuals shown in Fig. 3.2b. The residuals still show strong positive and negative excesses below 3 keV. Replacing the neutral absorber by a warm absorbing layer of low ionization results in substantially flattened residuals (Fig. 3.2c). We identify this component with WA$_1$.

While this model describes the smooth turnover of the partial coverer, some residuals remain. Based on the 2006 *XMM-Newton* observation, we model these residuals by including two additional layers of ionized absorption, WA$_2$ and WA$_3$ (Fig. 3.2d). Here, following the RGS analysis of Markowitz et al. (2009), the absolute redshift of WA$_3$ is fixed at -0.00302. The fit requires the moderately-ionized absorber WA$_2$ ($\log \xi \sim 0.5$) to be dominant and partially covering.

Leftover residuals in the final continuum fit are line-like features in the soft band around 0.9 keV, which are most likely due to Ne IX emission and the strong signature of a Fe Kα/Fe Kβ complex between 6.4 and 7.1 keV. These soft and hard components can either be modeled individually using empirical emission lines, or by adding ionized reflection (modeled with `xillver`; García et al., 2013), where we require that the reflected continuum has the same shape as the primary continuum. Both approaches describe all of the excess components equally well and without appreciably changing the continuum parameters. Because of the unique physical interpretation and the smaller number of free parameters, we continue the modeling with `xillver`. The resulting model describes the data well (Fig. 3.2e).

3.1.3.2 Revisiting the XMM-Newton spectra with the baseline model

We now test whether the baseline model also describes the *XMM-Newton* observations that have been used to motivate this model and its absorbers. The spectra and model components of the 2000 and 2006 *XMM-Newton* observations are shown in Fig. 3.3. The continuum is described by an absorbed high-energy power law, leaked emission, and unblurred ionized reflection components. The Tables 3.2 and 3.3 list the best-fit parameters.

[POW+XILLVER]*
ZXIPCF(WA$_1$)*ZXIPCF(WA$_2$)*ZXIPCF(WA$_3$)*TBNEW__SIMPLE(LOCAL)

mod. comp.	parameter	value ± uncert.
0400270101: χ^2 (dof) = 1341.1 (953)		
SXPL	norm	$\left(4.1^{+0.5}_{-0.6}\right) \times 10^{-3}$
	Γ	1.57^{*}
HXPL	norm	$\left(6.2^{+0.7}_{-0.5}\right) \times 10^{-3}$
	Γ	$2.099^{+0.041}_{-0.021}$
Ion. Refl.	norm	$\left(2.670^{+0.004}_{-0.757}\right) \times 10^{-4}$
	$\log\xi\,(\mathrm{erg\,cm\,s^{-1}})$	$0.17^{+0.16}_{-0.17}$
	Z_{Fe}	$0.50^{+0.04}_{-0.00}$
	z (absolute)	0.00386^{*}
WA 1	$N_{\mathrm{H}}\,(10^{22}\mathrm{cm^{-2}})$	$0.1391^{+0.0006}_{-0.0013}$
	$\log\xi\,(\mathrm{erg\,cm\,s^{-1}})$	$-0.521^{+0.018}_{-0.017}$
	$\mathrm{f_{cvr}}$	1^{*}
	z (absolute)	0.00386^{*}
WA 2	$N_{\mathrm{H}}\,(10^{22}\mathrm{cm^{-2}})$	2.75 ± 0.29
	$\log\xi\,(\mathrm{erg\,cm\,s^{-1}})$	$2.01^{+0.06}_{-0.10}$
	$\mathrm{f_{cvr}}$	$0.533^{+0.023}_{-0.045}$
	z (absolute)	0.00386^{*}
WA 3	$N_{\mathrm{H}}\,(10^{22}\mathrm{cm^{-2}})$	$0.11^{+0.22}_{-0.07}$
	$\log\xi\,(\mathrm{erg\,cm\,s^{-1}})$	$3.10^{+0.23}_{-0.30}$
	$\mathrm{f_{cvr}}$	1^{*}
	z (absolute)	-0.00302^{*}
CA	$N_{\mathrm{H,Gal}}\,(10^{22}\mathrm{cm^{-2}})$	0.0199

Table 3.2. Continuum parameters of the spectral fit of the baseline model to the relatively unabsorbed 2006 *XMM-Newton* observation. Fixed parameters are marked with an asterisk. We assume that the incident HXPL of the ionized reflection and the continuum power law are identical. To reduce model degeneracies, we freeze the photon index to the value found by Markowitz et al. (2009), who find WA$_3$ to be outflowing. We therefore also freeze the absolute redshift of WA$_3$ to the according value in our model. The soft excess is modeled by a power law (SXPL).

[POW+XILLVER]*
ZXIPCF(WA$_1$)*ZXIPCF(WA$_2$)*ZXIPCF(WA$_3$)*TBNEW__SIMPLE(LOCAL)

mod. comp.	parameter	value ± uncert.
0101040301: χ^2 (dof) = 305 (261)		
HXPL	norm	$\left(3.6^{+1.6}_{-0.8}\right) \times 10^{-3}$
	Γ	1.89 ± 0.20
Ion. Refl.	norm	$\left(2.1^{+1.3}_{-1.8}\right) \times 10^{-4}$
	$\log\xi\,(\mathrm{erg\,cm\,s^{-1}})$	$0.06^{+0.68}_{-0.07}$
	Z_{Fe}	$0.60^{+0.37}_{-0.10}$
WA$_1$	$N_{\mathrm{H,int}}\,(10^{22}\mathrm{cm^{-2}})$	$6.6^{+0.6}_{-0.5} \times 10^{22}$
	$\log\xi\,(\mathrm{erg\,cm\,s^{-1}})$	$0.4^{+0.4}_{-0.5}$
	f_{cvr}	$0.959^{+0.012}_{-0.021}$
	z (absolute)	0.003859^{*}
WA$_2$	$N_{\mathrm{H}}\,(10^{22}\mathrm{cm^{-2}})$	$0.5^{+1.0}_{-0.5}$
	$\log\xi\,(\mathrm{erg\,cm\,s^{-1}})$	$2.01^{*,\dagger}$
	f_{cvr}	1^{*}
	z (absolute)	0.003859^{*}
WA$_3$	$N_{\mathrm{H}}\,(10^{22}\mathrm{cm^{-2}})$	$0.2 \times 10^{22*}$
	$\log\xi\,(\mathrm{erg\,cm\,s^{-1}})$	3.10^{*}
	f_{cvr}	1^{*}
	z (absolute)	-0.00302^{*}
Gauss	norm	$\left(3.2^{+1.8}_{-2.0}\right) \times 10^{-4}$
	Energy (keV)	0.83^{*}
	σ (keV)	0^{*}
	z (absolute)	0.00386^{*}
Rec. Edge	norm	$\left(4.7^{+2.8}_{-2.3}\right) \times 10^{-4}$
	Energy (keV)	0.87^{*}
	kT (keV)	$0.07^{+0.05}_{-0.04}$

Table 3.3. Continuum parameters of the spectral fit of the derived baseline model to the absorbed 2000 *XMM-Newton* observation. Fixed parameters are marked with an asterisk, parameters adopted from the fit to the 2006 *XMM-Newton* observation with †. The photon index of the reflection component is tied to that of the high-energy power law. The model also includes an unresolved Gaussian line at $E_{\mathrm{c}} = 0.826\,\mathrm{keV}$ identified as Fe L XVII and a O VIII radiative recombination continuum (RRC) with an edge energy of 0.871 keV.

Because of the inability to constrain the covering fraction of the absorbers with low (WA$_1$) and high (WA$_3$) ionization, we always require them to fully cover the compact source. Their column densities and ionization parameters are all left free to vary.

The continuum as well as the Fe K α/β lines of the 2006 *XMM-Newton* observation are well fitted with a combination of an incident power law and the ionized reflection component `xillver`. The two modest absorption dips, at around 0.75 keV and 0.9 keV, require WA$_2$ to have $\log\xi \sim 2$ and to cover the X-ray source by ∼50%. Figure 3.4 shows the 0.5–2.3 keV unfolded spectra of both the Suz 1 observation from 2008 and the *XMM-Newton* observation from 2006. The two absorption features enclosed by the gray shaded region are found at about the same energy in both spectra, arguing for WA$_2$ as a common origin. The similar spectral shape prefers WA$_2$ to be partial covering in both observations. In contrast to the 2000 data, a steep soft excess is seen

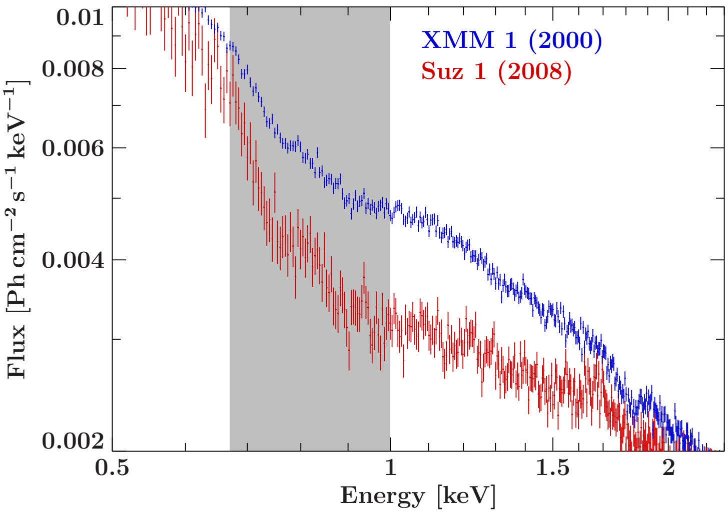

Figure 3.4. Comparison of the 2006 *XMM-Newton* and Suz 1 observations in the 0.5–2.3 keV range. The gray area marks the energy range comprising two modest absorption features that are due to an absorber of similar ξ, i.e., WA$_2$.

in 2006, which we describe by a soft-energy X-ray power law (SXPL), consistent with the results of Markowitz et al. (2009). The fit converges to a statistic of $\chi^2/\mathrm{dof} = 1851/1542$.

While the data from 2006 are described well with the partially covering absorber WA$_2$, the 2000 data require a dominant partial covering column of low-ionization gas (WA$_1$). Given the strong X-ray absorption, it is not clear if a soft excess is present in the spectrum. If our partial-covering model is correct and the continuum below ∼2 keV is dominated by leaked emission, then the soft excess ($\Gamma \sim 3$) must have had a negligible presence. Given the low S/N of the data, with the exception of the column of WA$_2$, the parameters of the two highest ionized absorbers, WA$_2$ and WA$_3$, cannot be constrained and are assumed to be equal to those found in the 2006 data. The emission feature at ∼0.88 keV is described by a narrow unresolved Gaussian for Fe L XVII at 0.826 keV and an O VIII radiative recombination continuum (RCC) at 0.871 keV. We find the best-fit statistic to be $\chi^2/\mathrm{dof} = 901/847$, which is consistent with that found by Lamer et al. (2003).

We conclude that the *XMM-Newton* data of both the absorbed (2000) and relatively unabsorbed (2006) observations of NGC 3227 can be described with our baseline model regarding the absorber structure and unblurred reflection. The spectral variability between both is dominated by the absorption component WA$_1$ with low ionization.

3.1.3.3 SIMULTANEOUS FIT TO ALL SUZAKU SPECTRA

The success of the baseline model in describing both the individual *Suzaku* data and the *XMM-Newton* data suggests that we can use it to model all 2008 *Suzaku* spectra simultaneously. The fit results indicate that the parameters of WA$_1$ and WA$_3$ stay constant during the 2008 observational campaign, while the spectral variability is dominated by WA2. We have to model Suz 1 separately, as it does not share some of the time-independent parameters. Table 3.4 lists the results of the fit.

In more detail, the time-independent parameters include the detector constants, the iron abundance Z_Fe of the ionized reflector (a simultaneous fit of Suz 2 to 6 yields $Z_\mathrm{Fe} = 2.81 \pm 0.17$) and all parameters of the non-varying ionized absorbers WA$_1$ and WA$_3$. The absorbers WA$_1$ and WA$_3$ with low- and high-ionization are assumed to fully cover the central source. The absorber WA$_1$ has a relatively low column density of $0.137^{+0.009}_{-0.006} \times 10^{22}\,\mathrm{cm}^{-2}$ of low-ionization ($\log\xi = -0.29^{+0.09}_{-0.13}$) gas for Suz 1 and $0.068^{+0.025}_{-0.014} \times 10^{22}\,\mathrm{cm}^{-2}$ ($\log\xi = -0.9 \pm 0.6$) for the later five observations. While both $\log\xi$ are consistent with each other, the column found in Suz 1 is slightly higher. For WA$_3$ the column densities are consistently around $\sim 4 \times 10^{22}\,\mathrm{cm}^{-2}$, while the ionization parameter differs between the single fit of Suz 1 ($\log\xi = 3.44^{+0.07}_{-0.05}$) and the other

Table 3.4. List of parameters for the simultaneous fit of observations Suz 2 to Suz 6 and the individual fit of the observation Suz 1. We use the same model for both fits. The simultaneous fit consists of time-dependent parameters that are equal for a group comprising XIS and HXD data of one observation, and time-independent parameters that are equal for all data, denoted with quotation marks. Frozen parameters are denoted by the symbol †, $*$ denotes parameters adopted from the simultaneous fit. The redshift is frozen to the systemic value of $z = 0.003859$ (de Vaucouleurs et al., 1991). All spectra are additionally absorbed by the Galactic column. Normalizations are given in units of ph keV^{-1} cm^{-2} s^{-1} at 1 keV.

`detconst(1)*(cutoffpl(%)+xillver(%))*((1-constant(%))+constant(%)*zxipcfTB(2+%))*zxipcfTB(1)*zxipcfTB(2)*tbnew_simple(1)`

		Suz 1	Suz 2	Suz 3	Suz 4	Suz 5	Suz 6	
PL	norm ($\times 10^{-2}$)	1.01 ± 0.04	$0.62^{+0.04}_{-0.06}$	$0.76^{+0.05}_{-0.04}$	$0.345^{+0.046}_{-0.026}$	$0.82^{+0.09}_{-0.05}$	$0.70^{+0.11}_{-0.08}$	time dependent
	Γ	1.658 ± 0.017	$1.592^{+0.026}_{-0.036}$	$1.653^{+0.031}_{-0.025}$	$1.62^{+0.05}_{-0.04}$	$1.694^{+0.041}_{-0.029}$	$1.72^{+0.06}_{-0.05}$	
Ion. Refl.	norm ($\times 10^{-5}$)	$0.31^{+0.51}_{-0.11}$	0.24 ± 0.05	$0.192^{+0.179}_{-0.024}$	$0.29^{+0.18}_{-0.05}$	$0.37^{+0.43}_{-0.13}$	$0.60^{+15.5}_{-0.40}$	
	$\log \xi$ (erg cm s^{-1})	$1.73^{+0.19}_{-0.44}$	$2.05^{+0.09}_{-0.05}$	$2.03^{+0.04}_{-0.29}$	$2.01^{+0.04}_{-0.25}$	$1.69^{+0.17}_{-0.37}$	$1.4^{+0.4}_{-1.4}$	
WA$_2$	N_H (10^{22}cm^{-2})	$4.75^{+0.32}_{-0.29}$	$16.0^{+1.0}_{-0.8}$	6.2 ± 0.5	$15.9^{+1.6}_{-1.5}$	10.8 ± 0.7	$13.4^{+1.0}_{-0.9}$	
	$\log \xi$ (erg cm s^{-1})	2.04 ± 0.04	$1.27^{+0.12}_{-0.08}$	$0.71^{+0.29}_{-0.23}$	$0.08^{+0.19}_{-0.17}$	1.21 ± 0.04	$1.11^{+0.07}_{-0.16}$	
	f_{cvr}	$0.735^{+0.024}_{-0.025}$	$0.873^{+0.007}_{-0.012}$	0.905 ± 0.006	$0.833^{+0.016}_{-0.013}$	0.929 ± 0.007	0.930 ± 0.009	
Detconst	XIS 0	$1^{\dagger}$	$1^{\dagger}$	"	"	"	"	time-independent
	XIS 1	$1.058^{+0.010}_{-0.008}$	1.096 ± 0.007	"	"	"	"	
	XIS 3	$1.054^{+0.009}_{-0.011}$	1.036 ± 0.006	"	"	"	"	
	HXD	$1.16^{\dagger}$	$1.16^{\dagger}$	"	"	"	"	
Ion. Refl.	Z_{Fe}	2.81^{*}	2.81 ± 0.17	"	"	"	"	
WA$_1$	N_H (10^{22}cm^{-2})	$0.137^{+0.009}_{-0.006}$	$0.068^{+0.025}_{-0.014}$	"	"	"	"	
	$\log \xi$ (erg cm s^{-1})	$-0.29^{+0.09}_{-0.13}$	-0.9 ± 0.6	"	"	"	"	
	f_{cvr}	$1.00^{\dagger}$	$1.00^{\dagger}$	"	"	"	"	
WA$_3$	N_H (10^{22}cm^{-2})	$3.0^{+0.8}_{-1.3}$	$4.1^{+4.1}_{-2.1}$	"	"	"	"	
	$\log \xi$ (erg cm s^{-1})	$3.44^{+0.07}_{-0.05}$	$4.17^{+0.16}_{-0.22}$	"	"	"	"	
	f_{cvr}	$1.00^{\dagger}$	$1.00^{\dagger}$	"	"	"	"	
$L^{ion}_{0.0136-13.6\,keV}$ (10^{42}erg s^{-1})		7.6 ± 0.03	7.4 ± 0.05	7.3 ± 0.04	5.6 ± 0.05	6.7 ± 0.04	5.6 ± 0.04	
$L^{X}_{0.6-10\,keV}$ (10^{42}erg s^{-1})		2.60 ± 0.03	1.80 ± 0.05	2.09 ± 0.04	9.82 ± 0.05	2.15 ± 0.04	1.80 ± 0.04	

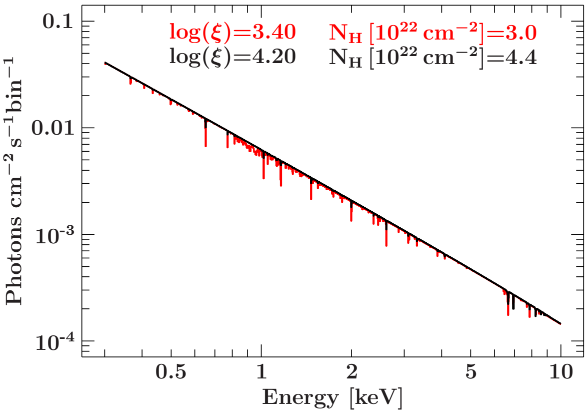

Figure 3.5. Effect of WA$_3$ if it were to fully cover the background power law. The warm absorber of observation Suz 1 is shown in red; black shows the effect of the absorber found in the remaining *Suzaku* observations.

observations, which have ($\log \xi = 4.17^{+0.16}_{-0.22}$). Figure 3.5 shows how both instances of WA$_3$ affect the high-energy power law. The model with $\log \xi \sim 3.4$ for Suz 1 imprints a clear absorption feature around 0.9–1.0 keV due to Ne IX and Ne X. A column of comparable ionization was also constrained by Markowitz et al. (2009) but disappears in Suz 2 to Suz 6. It may, however, still be intrinsically present but undetected because of degeneracies within the model description. The highly-ionized absorber WA$_3$ ($\log \xi \sim 4$) shows weak absorption lines from the highly-ionized species of ion (Fig. 3.5). These are difficult to constrain in a single *Suzaku* observation but are consistent with the detailed study of Suz 1–Suz 3 by Gofford et al. (2013), who show the existence of absorption lines due to He-like and H-like Fe.

The time-dependent group parameters of the model represent the effects of variability. In particular we mention the variability of the moderately ionized and partially covering absorber WA$_2$. Simultaneous fitting isolates WA$_2$ as the only variable layer of absorption within the

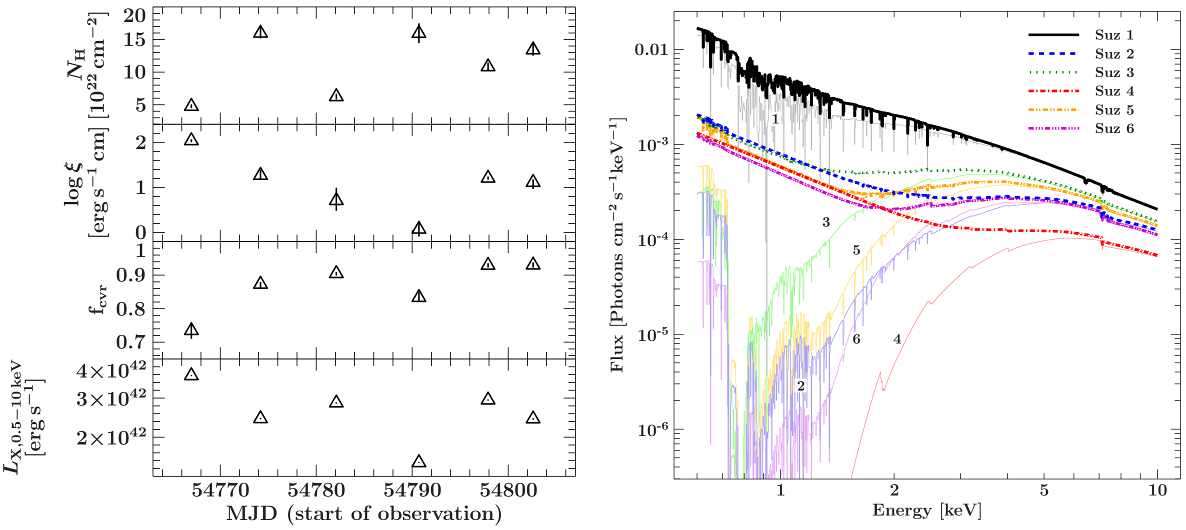

Figure 3.6. *Left:* Temporal evolution of the parameters describing the variable moderately ionized absorber WA$_2$ and the luminosity in the 0.6–10 keV X-ray band for the six *Suzaku* observations; *right:* effect of the partial coverer WA$_2$ onto a power law (thick lines with line styles given in the figure) as part of the best-fit model (Fig. 3.7). The thin and solid lines of lighter color show the effect the coverer would have if it were to fully cover the source.

complex interaction of the three absorbers contained in the model. Figure 3.6 (left) shows the time evolution of the fit parameters N_H, $\log\xi$, f_cvr and the X-ray luminosity L_X. The covering fraction scatters around ∼0.9. Only Suz 1 shows a lower value of ∼0.74. The column density peaks in a complex fashion between 5 and $18\times10^{22}\,\mathrm{cm}^{22}$ across all six observations. The ionization parameter first decreases from $\log\xi\sim2$ to nearly zero and then increases again to values of $\log\xi\sim1$ for the last two observations. In Fig. 3.6 (right) we illustrate the effect of WA$_2$ onto the power-law continuum if this absorber had a covering fraction of unity (cf. Fig. 3.7). In this representation of the model, we can identify the most prominent contributing absorption features below 1 keV, which are mainly due to the He-like and H-like ions O VII, O VIII, Ne IX, and Ne X[3].

Other variable parameters are the photon-index Γ that scatters between ∼1.6 and ∼1.7. We also find moderate ionization states of the reflecting and absorbing material ranging from $\log\xi\sim0.8$ up to ∼2.

The results of the fits are shown in Figure 3.7. We show the XIS and HXD spectra of all observations including the best-fit models. The residual panels suggest a fit that describes the continuum well with adequate statistics. Figure 3.8 gives an overview of all *Suzaku* spectra shown together with the full model and the best-fit model components. Above the power law in the energy range covered by *Suzaku*/HXD/PIN, excess emission becomes apparent, which is most likely due to the Compton hump peaking around 30 keV. The 6.4 keV Fe Kα line is self-consistently modeled by reflection off Compton-thick gas (`xillver`), as is the extra emission below 1 keV. Figure 3.8 illustrates that the reflection parameters are mainly derived from that soft emission and the iron line complex as dominant features. The HXD/PIN data quality is good enough to constrain the normalization of `xillver`. No extra soft emission component is needed in contrast to the 2006 *XMM-Newton* observation. Although we cannot rule out its presence, the soft X-rays are well modeled by a combination of ionized reflection and leaked coronal emission described by the HXPL. The (narrow) Fe Kα line has an equivalent width of

---

[3] Note that because in reality the warm absorber is only partly covering the source, the fit is not particularly sensitive to these narrow features and mainly driven by the characteristic curvature below 2 keV caused by the moderate ionization of WA$_2$.

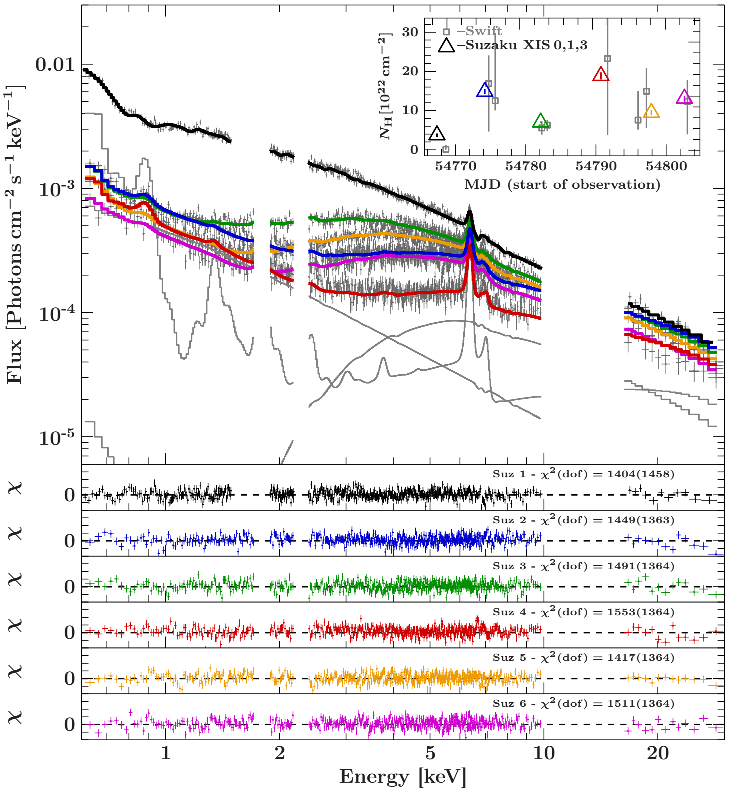

Figure 3.7. Spectra and residuals for fits of the baseline model to the *Suzaku* spectra of the 2008 campaign (Table 3.4). A single fit is performed for the high state observation (Suz 1). The remaining observations (Suz 2–Suz 6) are fitted as part of one simultaneous fit with tied time-independent parameters. The residual panels also include the statistics of each fit. The inset shows the time evolution of the column density with colorized triangles for *Suzaku* and with gray squares for *Swift*. The plot additionally shows the model components of absorbed, leaked and reflected emission in gray. This plot is modified from Beuchert et al. (2015).

EW $\sim 130\,\mathrm{eV}$ and is well described by `xillver`. No further line emission is required, indicating that the line is fully described by reflection off Compton-thick material.

The complexity of our model leads us to study possible degeneracies. The $\Delta\chi^2$ contours for all pairs of time-dependent parameters show that the simultaneous fit is remarkably robust. Figure 3.9 shows the contours of Suz 2. The overall correlations are similar for the other observations but differ in extent depending on the data S/N. A mild degeneracy between the covering factor with both the normalization and the photon index of the high-energy power law is present. We find modest degeneracies between the ionization state and the column density of the WA_2 as well as the photon index and the normalization of the power law. The contours of `xillver` show an overall degeneracy with most other parameters, which can be removed by assuming that photon index is a time-independent parameter. Finally, turning to the time variability of the absorber, Fig. 3.10 shows the contours of all time-dependent parameters related to N_H for all observations and in particular reveals a clear variability in column density across the observations. Note that the contours, including the normalization and ionization of the unblurred reflection component `xillver,` reveal no significant variability.

3.1.3.4 ANALYSIS OF THE SWIFT/XRT DATA

For each *Suzaku* observation the archive contains two simultaneous *Swift* observations, which we model simultaneously with the same baseline spectral model but independently of the simultaneous fit of the *Suzaku* data. The *Swift* data are consistent with the *Suzaku* data and do not contribute additional information due to the lower effective area. We therefore impose constraints gained with *Suzaku* for certain parameters that can neither be constrained with *Swift* nor identified as variable with *Suzaku*. The resulting parameters are listed in Table 3.5. When additionally considering the simultaneous data provided in the UV with the UVOT instrument, we can, however, make effective use of *Swift*.

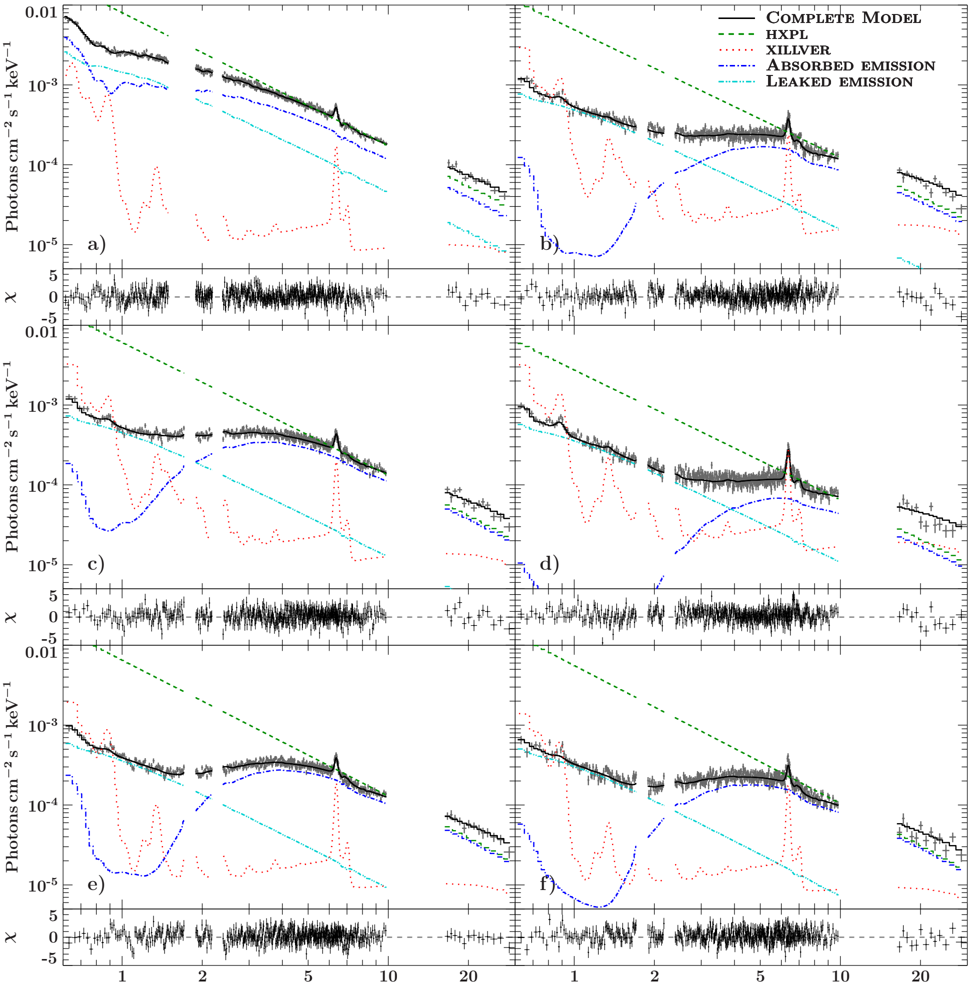

Figure 3.8. Spectra and model components of all *Suzaku* observations. We show the complete model (black solid line) with residuals, the hard X-ray power law (dark green dashed line), the ionized reflection component (red dotted line), the emission absorbed by the variable partially covering column (blue dotted-dashed line) and the leaked emission (cyan double dotted-dashed line).

3.1.4 MULTIWAVELENGTH DATA ANALYSIS

3.1.4.1 NIR–X-RAY SED AND REDDENING

SEDs as a powerful tool — Broad-band studies with SEDs are an indispensable tool to probe complex processes hidden in the compact and unresolved AGN core. Considering data from other wavebands is particularly useful to also break degeneracies of multi-temperature disk models that attempt to describe the hidden part of the spectrum in the (E)UV. See in that regard the review of Koratkar & Blaes (1999) and the PhD thesis of Harrison (2004).

In early studies, for example Malkan & Filippenko (1983) composed broad-band spectra of Seyfert galaxies from the IR to the UV using data of ground-based telescopes. They fitted these data with a simple combination of a thermal black-body component and a non-thermal high-energy component. The authors also emphasize the considerable contribution of the stellar light, which makes up nearly three-fourth of the visible continuum for NGC 3227 given a 10″ aperture.

Prieto et al. (2010) provide a number of high spatial resolution SEDs for the inner 10 parsecs of Seyfert galaxies with data ranging from the radio at $\sim 10^8$ Hz to the X-rays at $\sim 10^{18}$ Hz. The authors demonstrate the basic features of radio-quiet SEDs, that is, non-thermal Comptonization

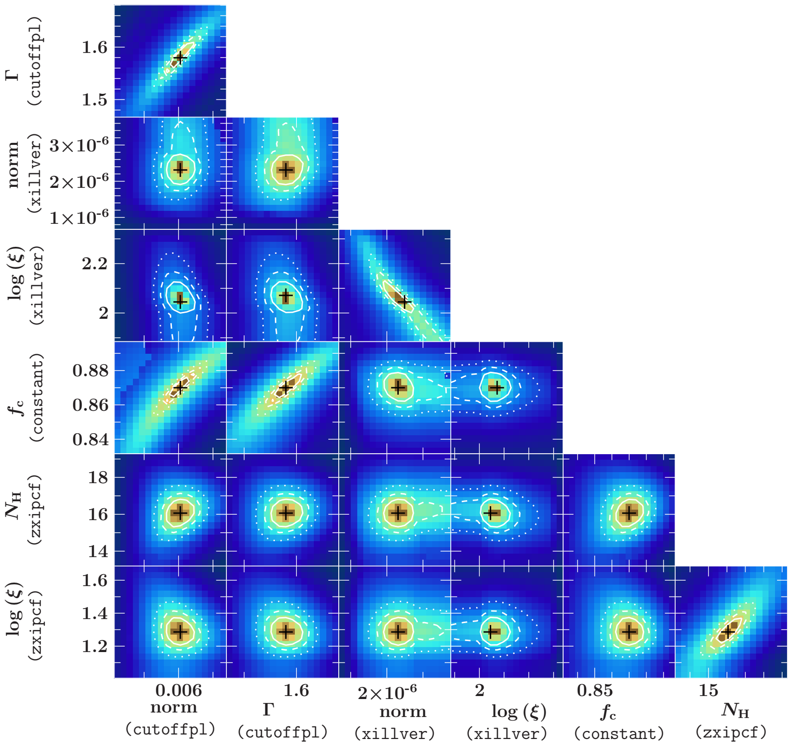

Figure 3.9. Color-coded $\Delta\chi^2$ contours for relevant spectral parameters of Suz 2. The 68.27%, 90%, and 99% contours correspond to the solid, dashed, and dotted lines. The color code ranges from brown (small $\Delta\chi^2$) up to dark blue (large $\Delta\chi^2$).

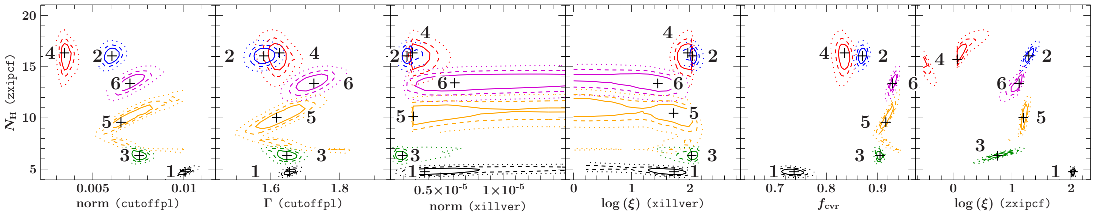

Figure 3.10. Contours relating all time-dependent parameters of all observations to N_H of WA$_2$. The solid, dashed, and dotted lines represent the 68%, 90%, and 99% confidence contours. Observations Suz 1 to Suz 6 are both marked with numbers and color-coded in black, blue, green, red, orange, and purple, respectively.

processes and power-law emission in the X-rays and thermal disk emission in the UV forming the BBB. Parts of the EUV and soft X-rays that become extinct by dust get re-emitted in the IR, forming a prominent bump. Contributions of the host galaxy star light at compact spatial scales are also discussed.

Scott & Stewart (2014) extended the involved data and increased the number of sources to over 700 type-1 quasars. They investigate in particular physical parameters of the sample such as the distribution of bolometric luminosities ($L_{\rm bol}$), the strength of the BBB and other quantities, suggesting a positive correlation of the accretion rate and the inner disk temperature. One major result is that the shape of the SEDs of AGN are similar despite of obvious differences between obscured and unobscured sources. These differences change the strength of the UV/X-ray primary emission as well as the IR reprocessed emission. For type-1 quasars, the only difference between the SEDs of radio-loud and radio-quiet quasars is in fact the dominance of the jet in the radio bands, which strengthens the unifying paradigm. Also, their Fig. 5 shows remarkable similarities of averaged SEDs with respect to different samples of radio-quiet quasars (see also Elvis et al., 1994; Richards et al., 2006a; Shang et al., 2011; Lusso et al., 2012; Elvis et al., 2012).

By making use of the space-based observatory *XMM-Newton* with the optical/UV monitor OM, the hard X-ray detector BAT on board of *Swift* (Vasudevan & Fabian, 2009), as well as UV data from *Swift*/UVOT and reprocessed IR data, Vasudevan & Fabian (2009) study over 60 AGN and

Table 3.5. List of parameters for the simultaneous fit of all *Swift* observations. The model equals that fitted to the *Suzaku* data. The simultaneous fit consists of time-dependent parameters individually fitted to each observation, and time-independent parameters that are equal for all observations, denoted with quotation marks. The symbol $*$ marks parameters adopted from the simultaneous fit of the *Suzaku* observations. The redshift is frozen to the systemic value of $z = 0.003859$ (de Vaucouleurs et al., 1991). All spectra are additionally absorbed by the Galactic column density. Normalizations are given in units of $\mathrm{ph\,keV^{-1}\,cm^{-2}\,s^{-1}}$ at 1 keV.

		Sw 1a	Sw 2a	Sw 2b	Sw 3a	Sw 3b	
PL	norm	$\left(0.84^{+0.14}_{-0.20}\right) \times 10^{-2}$	$0.008^{+0.010}_{-0.004}$	$\left(3.5^{+1.5}_{-1.7}\right) \times 10^{-3}$	$\left(0.78^{+0.16}_{-0.20}\right) \times 10^{-2}$	$\left(0.69^{+0.10}_{-0.11}\right) \times 10^{-2}$	time dep.
Ion. Refl.	norm	$\left(0.28^{+0.93}_{-0.28}\right) \times 10^{-5}$	$\left(0.5^{+1.3}_{-0.5}\right) \times 10^{-5}$	$\left(0.9^{+0.6}_{-0.7}\right) \times 10^{-5}$	$\left(0.24^{+1.02}_{-0.25}\right) \times 10^{-5}$	$\leq 0.6 \times 10^{-5}$	
$\mathrm{WA_2}$	$N_\mathrm{H}\,(10^{22}\mathrm{cm^{-2}})$	$6.8^{+6.6}_{-2.8}$	27^{+25}_{-8}	15^{+8}_{-11}	$8.3^{+4.3}_{-2.9}$	$7.0^{+2.4}_{-1.5}$	
	f_cvr	$0.80^{+0.14}_{-0.09}$	$0.90^{+0.06}_{-0.07}$	$0.79^{+0.05}_{-0.13}$	$0.86^{+0.08}_{-0.06}$	$0.93^{+0.05}_{-0.04}$	
		Sw 4a	Sw 4b	Sw 5a	Sw 5b	Sw 6b	
PL	norm	$\left(0.36^{+0.40}_{-0.25}\right) \times 10^{-2}$	$0.007^{+0.011}_{-0.006}$	$\left(0.62^{+0.12}_{-0.21}\right) \times 10^{-2}$	$\left(0.39^{+0.13}_{-0.17}\right) \times 10^{-2}$	$\left(3.6^{+1.4}_{-0.9}\right) \times 10^{-3}$	time dep.
Ion. Refl.	norm	$\left(1.1^{+0.7}_{-0.9}\right) \times 10^{-5}$	$\leq 1.2 \times 10^{-5}$	$\left(0.19^{+0.68}_{-0.19}\right) \times 10^{-5}$	$\left(0.017^{+0.533}_{-0.017}\right) \times 10^{-5}$	$\left(0.26^{+0.54}_{-0.27}\right) \times 10^{-5}$	
$\mathrm{WA_2}$	$N_\mathrm{H}\,(10^{22}\mathrm{cm^{-2}})$	42^{+22}_{-30}	54^{+45}_{-38}	15^{+4}_{-6}	15^{+6}_{-8}	$8.2^{+5.5}_{-2.5}$	
	f_cvr	$0.85^{+0.08}_{-0.25}$	$0.903^{+0.015}_{-0.404}$	$0.911^{+0.023}_{-0.037}$	$0.90^{+0.04}_{-0.07}$	$0.93^{+0.07}_{-0.04}$	
PL	Γ	1.50 ± 0.04	"	"	"	"	time-independent
Ion. Refl.	$\log\xi\,(\mathrm{erg\,cm\,s^{-1}})$	1.84 ± 0.15	"	"	"	"	
	Z_Fe	2.81^{*}	"	"	"	"	
$\mathrm{WA_2}$	$\log\xi\,(\mathrm{erg\,cm\,s^{-1}})$	1.44 ± 0.12	"	"	"	"	
$\mathrm{WA_1}$	$N_\mathrm{H}\,(10^{22}\mathrm{cm^{-2}})$	$0.066^{+0.018}_{-0.017}$	"	"	"	"	
	$\log\xi\,(\mathrm{erg\,cm\,s^{-1}})$	-0.89^{*}	"	"	"	"	
	f_cvr	1^{*}	"	"	"	"	
$\mathrm{WA_3}$	$N_\mathrm{H}\,(10^{22}\mathrm{cm^{-2}})$	4.12^{*}	"	"	"	"	
	$\log\xi\,(\mathrm{erg\,cm\,s^{-1}})$	4.17^{*}	"	"	"	"	
	f_cvr	1^{*}	"	"	"	"	

their physical properties with strong emphasis also on the non-thermal contribution. Their sample also includes NGC 3227. They provide a catalog comprising Eddington luminosities, Eddington ratios and κ-correction factors for the IR and X-rays to infer the bolometric luminosities, which we will make use of in the remainder of the present study of NGC 3227.

Data pool for the SED of NGC 3227[4] — The broadband SED (Fig. 3.11) is based on *Swift*/UVOT data from the observation Sw 4a and allows us to estimate the amount of reddening due to dust in the line of sight and to draw conclusions on the dust content of the X-ray absorbing cloud. For reducing model degeneracies, we also include data from other wavebands. These include photometric data from space- and ground-based facilities of different spatial resolutions and apertures: *WISE* (Wright et al., 2010) and 2MASS (Skrutskie et al., 2006) data from the All-Sky Source Catalogs, data (Ramos Almeida et al., 2011) from the NASA 3 m IRTF telescope (NSFCam at L-band), the 3.8 m UKIRT telescope (IRCAM3 at M-band), the Gemini-South telescope (T-ReCs, N-band) as well as *HST* NICMOS data in the filters F160W and F222M (Quillen et al., 1999), *HST* FGS data at F550W (Bentz et al., 2009a), and *HST* ACS data at 3300Å (Muñoz Marín et al., 2007). This last data point, taken in 2002, is roughly consistent with the UVOT flux taking the different spatial resolution into account as well as likely long-term source variability[5]. Note that Muñoz Marín et al. (2007) give ST magnitudes for different regions of the *HST* image. Those are 14.46 mag, 14.27 mag, and 14.05 mag for regions within 0.3″, 1″, and the entire galaxy, respectively. Using the relation $\mathrm{mag_{ST}} = -2.5 \log F_\text{Å} - 21.1$, those magnitudes translate to the fluxes of 2.17 Jy, 2.58 Jy and 3.16 Jy. As a result, we can extract one flux value for the nuclear region with 2.17 Jy ($1.97 \times 10^{-11}\,\mathrm{erg\,s^{-1}\,cm^{-2}}$) and one for the stellar

---

[4] These paragraphs deviate in some parts from Beuchert et al. (2015) but contain verbatim parts.

[5] The extended flag in the ALLWISE catalog introduces problems with the profile-fit photometry, which is why we add 10% systematic uncertainties to 2MASS and *WISE* data as well as 5% for UVOT, which has a similar PSF.

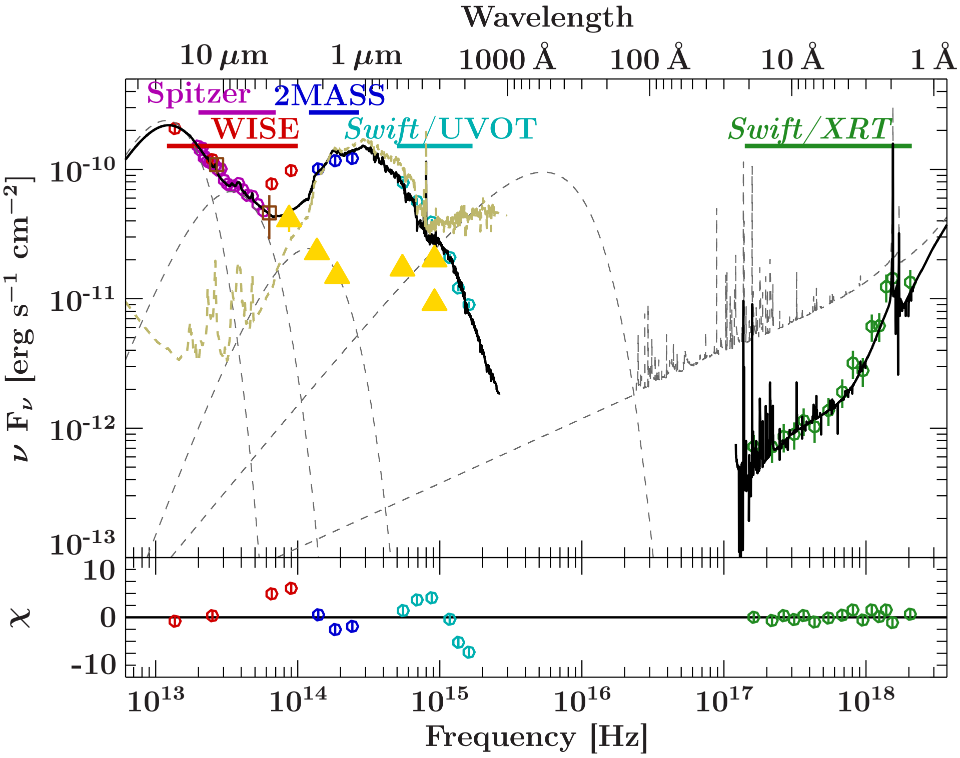

Figure 3.11. Example spectral energy distribution (SED) of NGC 3227 illustrating the coverage from the MIR (WISE: red circles; *Spitzer*: purple circles; and *HST*: orange triangles) over the NIR (ground-based data: brown squares), the optical (2MASS: blue circles; *HST*) and UV (*Swift*/UVOT: turquoise circles) to the X-ray band up to 10 keV (*Swift*/XRT: green circles). The UV and X-ray data were simultaneously measured at 2008-11-21, while the 2MASS and WISE data are archival catalog data. The *HST* data are taken at 1.60 μm, 2.22 μm, 5550Å and 3300Å; more information on the instruments are contained in the main text. At 3300Å, we plot two data points: the lower one marks the stellar, the upper one the nuclear contribution (cf. Muñoz Marín et al. 2007). The *Spitzer* data are simulated data based on the AGN contribution (Hernán-Caballero et al., 2015). Other data are non-simultaneous photometric measurements from the literature. The dashed lines correspond to the unabsorbed and unreddened model components, the thick solid line to the overall reddened and absorbed model. Here, we show three single black bodies to model the dust emission from the FIR to the NIR, the host galaxy contribution shown in brown/gray with contributions from the FIR to the UV, a multi-temperature disk blackbody dominating in the EUV to soft X-rays as well as the X-ray model as derived before.

host contribution with $3.16 - 2.17 \approx 1$ Jy ($0.9 \times 10^{-11}\,\mathrm{erg\,s^{-1}\,cm^{-2}}$).

In the MIR, we make use of archival observations with *Spitzer*/IRS (Hernán-Caballero et al., 2015, see also Gallimore et al. (2010) for data of all instruments). In contrast to most of the ground-based telescopes, *Spitzer* has a relatively large PSF of ∼3.6″ (∼320 pc). It is therefore impossible to spatially resolve any component inside the AGN. Hernán-Caballero et al. (2015), however, are able to decompose the high-quality *Spitzer*/IRS spectra of individual sources into contributions of the compact AGN core and the large-scale host galaxy. We use their resulting AGN template and simulate corresponding *Spitzer* data for the core component.

For finding a descriptive model for the SED, we only take into account data with PSFs comparable to those of *Swift*/UVOT, i.e., *WISE*, 2MASS data with PSFs of 5″–10″radius, as well as *Swift*/XRT data. Systematic effects and model degeneracies due to aperture effects of the instruments and a lack of simultaneous data lead us to abstain from performing a statistical χ^2 minimization at energies lower than X-rays. Instead, we use sub-arcsec *Spitzer*, *HST*, and the ground-based data, which are only sensitive to the AGN core, to constrain the AGN-related model components, that is, the dusty torus and the accretion disk emission in the IR and

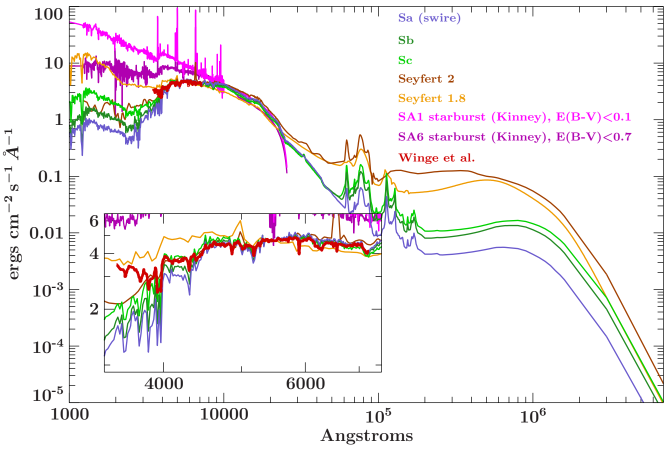

Figure 3.12. Collection of SWIRE spectral templates for Sa, Sb and Sc host galaxies (purple, dark green, light green, respectively) as well as two SWIRE templates for the active types Sy 2 and Sy 1.8 (brown and orange). Two additional starburst templates by Kinney et al. (1996) are shown in magenta. The dark red spectrum corresponds to a stellar template by Winge et al. (1995).

UV, respectively. The X-ray band turns out to be the only band with strong variability. The IR–UV bands, in contrast, show only minor variability up to 25% on the timescales monitored by *Swift*/UVOT. In the following, we describe our best-matching model for data below the X-rays, for which we find $\chi^2/\mathrm{dof} = 125/23$.

Determining the best-fitting model description[6] — The reprocessed MIR/NIR emission probed by *Spitzer*, ground-based and *HST* data at 1550Å and 2300Å have been fitted previously with clumpy torus models by, e.g., Ramos Almeida et al. (2011) or Alonso-Herrero et al. (2011). We instead use a phenomenological description of three blackbodies from 145 K up to 1480 K, which is supported by Calderone et al. (2012). Two *HST* data points at 1.60 μm and 2.22 μm set the upper limit for the nuclear torus with contributions from warm dust in the FIR.

The host galaxy starlight can be modeled using a Spitzer Wide-Area Infrared Extragalactic Survey (SWIRE) [7] template (Fig 3.12) for a Sa spiral galaxy, which matches well the stellar template spectrum of NGC 3227 by Winge et al. (1995) within the range 3500–7000Å. We normalize the Sa template to the flux of the stellar template at 5500Å. The inlay of Fig. 3.12 indicates that extra emission with respect to the Sa template is measured below 4000Å for NGC 3227. This is confirmed in Fig. 3.13 (left): we find a best-matching description with a template normalization of ∼4, which may be caused by systematics in the derivation of the stellar template and aperture effects. We do not expect this host galaxy component to be variable over time. As a reference, we also plot the stellar template for a normalization of one, that is, corresponding to the stellar flux measured by Winge et al. (1995) in their setup. For the best-matching model in Fig. 3.13 (left), UVOT measures emission in excess above the combined model. This excess can neither be explained by the Sa host galaxy template, nor the accretion disk emission. Figure 3.13 (right) shows the identical setup except that we model the (E)UV excess emission by extending the SWIRE template with a starburst template by Kinney et al. (1996) below 4000Å. The starburst component is justified from independent detections. Those are for example Rodríguez-Ardila & Viegas (2003), who report evidence for a starburst within the inner 2″(180 pc), and Davies et al. (2006), who can constrain this region even to the central 30 pc by measuring the remainders of starburst emission accounting for 20% to 60% of the galaxy's bolometric luminosity. Reminiscent of starburst activity is also that we observe evidence for strong dust-extinction (Siebenmorgen et al., 2004) and a central galactic bar (Hunt & Malkan, 1999; Roussel et al., 2001) in NGC 3227 Bentz et al. (2009a).

The extra component below 4000Å may be independently justified by a measurement of the starlight by *HST* at 3300Å (lower triangle in Fig. 3.11), which perfectly matches the combined template for a normalization of one (compare the right panel of Fig. 3.13 with the left panel, where this extra emission component is missing). Yet another indication for this starburst

---

[6] These paragraphs contain additional information beyond those published by Beuchert et al. (2015).

[7] `http://www.iasf-milano.inaf.it/~polletta/templates/swire_templates.html`

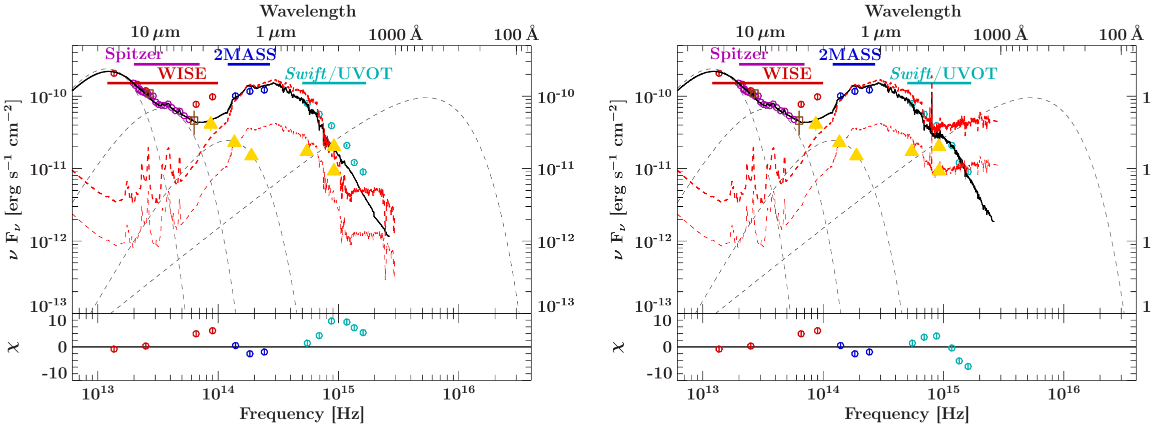

Figure 3.13. Same as Fig. 3.11 with the emphasized wavelength range from the FIR to the EUV. *Left:* the SWIRE Sa template is emphasized in red with two realizations: the upper one with the best-matching normalization of 4 and for reference, the lower one with a normalization of unity, for which it matches the stellar template of Winge et al. (1995); *right:* same as *left* showing the effect of the additional starburst component of Kinney et al. (1996) below 4000Å. See the text for more details.

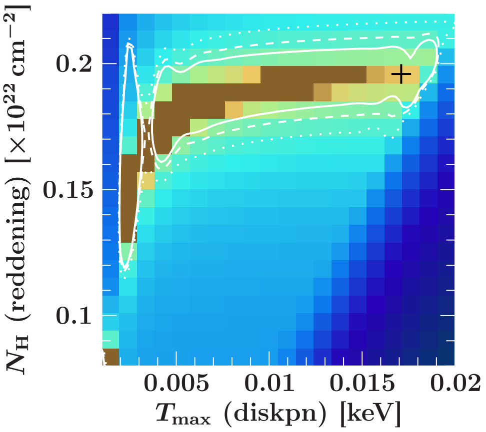

Figure 3.14. Color-coded $\Delta\chi^2$ contours indicating a strong degeneracy between the reddening column N_H and the inner disk temperature T_mas for a stellar template normalization of one (including the extra starburst component) and a configuration of four single back bodies from the FIR to the optical bands. We consider data from *Spitzer*, 2MASS, *Swift*/UVOT and *Swift*/XRT for the fit. The 68.27%, 90%, and 99% contours correspond to the solid, dashed, and dotted lines. The color code ranges from brown (small $\Delta\chi^2$) up to dark blue (large $\Delta\chi^2$).

component is given by the detection of strong Polycyclic Aromatic Hydrocarbon (PAH) features in the *Spitzer*/IRS data shown here and the inner tens of parsec of NGC 3227 (Hönig et al., 2010b).

The accretion disk emission is described with a multi-temperature disk blackbody (`diskpn` Gierliński et al., 1999) and forms the BBB. The inner disk temperature T_max determines the high energy tail of the multi-temperature disk spectrum, which usually extends up to the EUV–soft X-rays. Constraining this component is challenging due to the lack of data in this energy range, which is obscured due to the effects of Galactic, intrinsic and interstellar and dust extinction (see also Lee et al., 2013, for a comprehensive SED of IRAS 13349+2438). Statistical constraints come from observations of samples of luminous and strongly redshifted quasars, where the high-energy tail of the disk spectrum falls into the observable part of the spectrum (Koratkar & Blaes, 1999; Lee et al., 2013).

As a result, we observe strong degeneracies between the two competing parameters T_max and the equivalent hydrogen column density N_H due to dust extinction (Fig. 3.14). For an extremely high inner disk temperature, the spectral disk component dominates the host galaxy and extends all the way to the soft X-rays at $\sim 4 \times 10^{16}$ Hz. When integrating over the SED, the bolometric luminosity reaches $L_\mathrm{bol} \sim 10^{45}\,\mathrm{erg\,s^{-1}}$, which exceeds the value found by Vasudevan et al. (2010) by a factor of ∼30 and approaching the Eddington limit of $L_\mathrm{Edd} = 2.4 \times 10^{45}\,\mathrm{erg\,s^{-1}}$.

The following two paragraphs follow, mostly verbatim, Beuchert et al. (2015). The exact value of T_{max} is therefore largely unknown for nearby Seyferts such as NGC 3227 and needs to be inferred otherwise. One approach is to accurately model the extincted UV spectrum with the correct reddening curve for NGC 3227 (Crenshaw et al., 2001, and Sect. 1.2.4.1). In another, independent method, we use *HST* and its small PSF to constrain the compact emission at 5550Å and 3300Å, which has to be disk-dominated. Note that the lower data point at 3300Å contains only starlight (cf. Fig. 3.11). The data were taken two years apart from each other, which can explain their scatter around the inferred disk-model. Overall, they seem to follow the rising wing of the `diskpn` component. After an investigation of the parameter space under consideration of the above constraints, we can reduce the degeneracies on the inner disk temperature significantly and determine $T_{\text{max}} \sim 1 \times 10^5\,\text{K}$ at the inner side of the disk ($r_{\text{in}} = 6\,r_{\text{g}}$), which is reddened with a column of $0.12 \times 10^{22}\,\text{cm}^{-2}$ or $A_{\text{V}} \sim 0.45\,\text{mag}$. Our value of T_{max} is consistent with sample studies of quasars with minimal extinction (Koratkar & Blaes, 1999) as well as the expected inner disk temperature of a thin α-disk.

The large reddening column that we infer is in agreement with Komossa & Fink (1997), Kraemer et al. (2000), and Crenshaw et al. (2001). Their column of $\sim 0.2 \times 10^{22}\,\text{cm}^{-2}$ is claimed to be consistent with a persistent, dusty, “lukewarm” absorber at $\sim 100\,\text{pc}$ distance. *Swift* observations from 2013–2015 likely measure the same distant absorber but with only half the column, which is consistent with the reddening found in our model, and possibly also by Winge et al. (1995).

The amount of UV extinction is associated with a column that is still ~ 70 times smaller than the X-ray column. Even for larger reddening and therefore larger inner disk temperatures, the severe mismatch persists and has recently been confirmed as being inclination dependent by Burtscher et al. (2016) for a sample of Seyfert galaxies. Such a mismatch is unexpected if both the X-ray and UV absorber were of the same origin, although it has been found that higher ionized X-ray absorbers can coexist with UV absorbers (e.g., Krolik & Kriss, 1995; Morales & Fabian, 2002; Couto et al., 2016, and references therein).

Caveats — Varying apertures of the different space- and ground-based instruments and observatories represent the main systematic uncertainty that complicates the search for a descriptive model of these data. We use a $5''$ extraction region for *Swift*/UVOT, which is comparable with the apertures of 2MASS and *WISE* but contrasts with the PSF of *Spitzer* with $\sim 3.6''$ ($\sim 320\,\text{pc}$) and *HST* of $\sim 0.2''$($\sim 18\,\text{pc}$). In Fig. 3.11, we therefore applied a cross-calibration factor between *WISE* and *Spitzer* of 1.6, which is consistent with flux calibration uncertainties and aperture effects (Hernán-Caballero et al., 2015). While the 2MASS and *WISE* data likely include large amounts of extended host-galaxy emission, we have used *HST* to constrain spatially compact emission components such as the dusty torus or the accretion disk. Here, the magnitude of the AGN is given by the peak of the *HST* surface brightness profile (Bentz et al., 2009a), which coincides with the PSF. We also need to consider some additional uncertainty, as the PSF likely also contains emission from the inner bulge or the bar of NGC 3227.

In addition to the observed magnitudes, Bentz et al. (2009a) also provide color-corrected fluxes using the extinction law of Cardelli et al. (1989). I abstain of using these luminosities due to strong ambiguities related to the choice of the extinction law (compare Fig. 1.14).

We also need to be cautious when interpreting the stellar spectrum by Winge et al. (1995) that is used to normalize the host-galaxy. This spectrum was recorded with a $5'' \times 10''$ slit oriented along a position angle (PA) of 90°. The authors find a flux of $6 \times 10^{-11}\,\text{erg}\,\text{s}^{-1}$ at 5100Å. This flux changes depending on the size and PA of the slit: using a slit of $1.5'' \times 4.0''$ (PA=25°), Salamanca et al. (1994) measure nearly twice the flux of Winge et al. (1995). These systematics therefore prevent a direct comparison with instruments of comparable aperture. As a result, we expect significant systematics for the normalization of the host-galaxy template.

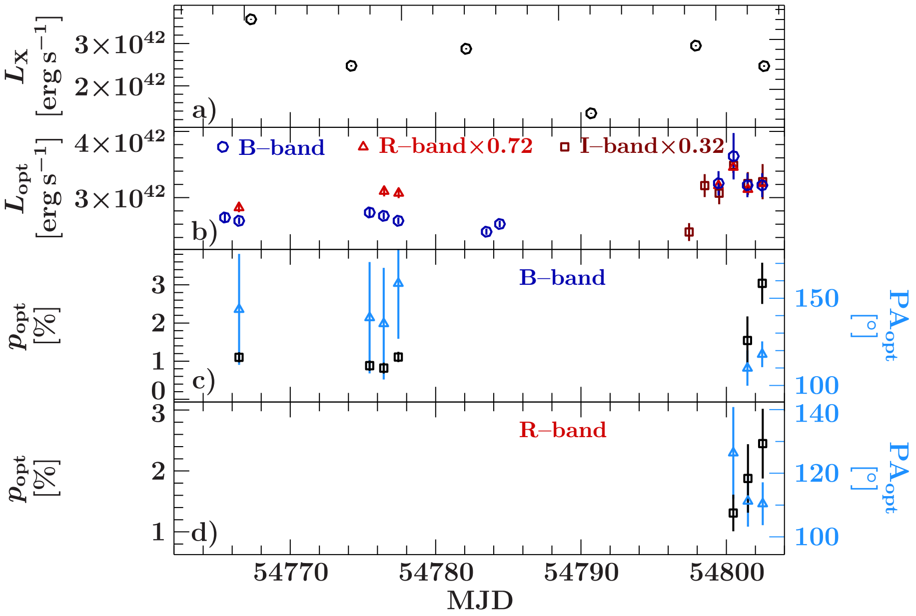

Figure 3.15. **a)** Light curve of the unabsorbed X-ray luminosity in the 0.6–10 keV band; **b)** light curve of monochromatic luminosities in the B-band (blue circles), R-band (red triangles), and I-band (brown squares) for the 84 cm and 1.5 m SPM telescopes; the R-band and I-band luminosities are normalized to the weighted mean of the B-band with relative factors of 0.72 and 0.32, respectively; **c/d)** degree of optical polarization p_{opt} (black squares) and the electric vector (EVPA$_{\mathrm{opt}}$, blue triangles) for the B/R-filters. The I-filter did not provide polarimetry data. The central wavelength of the B/R/I filters are given as 0.438/0.641/0.798 µm by Bessell et al. (1998).

3.1.4.2 OPTICAL POLARIMETRY

This section is taken in verbatim from Beuchert et al. (2015). A portion of the optical AGN emission undergoes scattering into our line of sight, resulting in a few percent of linear polarization. Investigations prefer the scenario of polar scattering for NGC 3227 (Smith et al., 2004). This result implies an intermediate inclination of the nucleus toward the line of sight, similar to what is predicted by clumpy torus models that are tested for NGC 3227 in Sect. 3.1.5.5. We therefore investigate additional optical polarimetric data coincident to the 2008 *Swift*/*Suzaku* campaign that have been taken between 2008 October 26 and 2008 December 03 with the 84 cm and 1.5 m telescopes of the San Pedro Mártir Observatory (SPM) in Mexico. The data were taken with the B filter (Johnson system) as well as R and I filters (Cousins system), according to the standard photometric system (Bessell, 2005). For the magnitude-flux conversion we use the zero-point magnitudes from Bessell et al. (1998).

We compare the optical photometric luminosities with the X-ray luminosities in Fig. 3.15. The sparse sampling pattern precludes a detailed cross-correlation analysis between the X-ray and optical light curves. The two bottom panels show polarimetry data for the B- and R-band. The degree of polarization p and the EVPA scatter around a few percent and 100°–150°, respectively, which is roughly consistent with the results from Smith et al. (2004). They find that the PA is constant over wavelength with a value of PA $\sim$ 135°. In contrast we observe different weighted averages between the B-band (PA $\sim$ 140°) and R-band (PA $\sim$ 119°). Mundell et al. (1995a) find both signatures for a narrow line region in high-excitation O III emission lines (PA $\sim$ 30°) and two compact radio cores along a PA of $\sim$170°. Mundell et al. (1995b) identify a much more extended radio source with PA $\sim$ 158°, which shows a rotating disk-like structure on scales of a typical host galaxy with an inclination of $\sim$56°; any connection to the AGN on much smaller scales is not immediately obvious, especially given the uncertainty regarding the AGN system inclination. We support the suggestion of Mundell et al. (1995a) and Smith et al. (2004) that

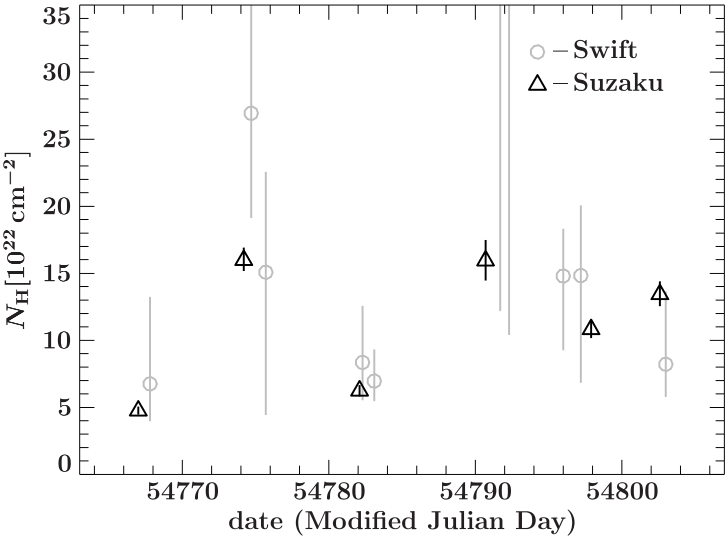

Figure 3.16. Evolution of the column density N_H of WA$_2$ over time as found in the *Suzaku* (black triangles) and *Swift* (gray circles) data. We plot uncertainties according to the 90% confidence level. The two data points derived by *Swift* that are cut off by the plotting window have the values $N_\mathrm{H} = 42^{+22}_{-30} \times 10^{22}\mathrm{cm}^{-2}$ and $54^{+45}_{-38} \times 10^{22}\mathrm{cm}^{-2}$.

the cone of excited O III gas may be oriented along the symmetry axis of the AGN. The angle enclosed between the cone and the measured average PA in the B-band is therefore ∼102°, which is close to a PA of 90°. Along with the degree of polarization we therefore find the optical emission in NGC 3227 to be consistent with polar scattering, similar to that suggested by Smith et al. (2004).

When facing additional systematic uncertainties in the polarimetry data we cannot conclude any significant variability. The optical luminosities, in contrast, show less than 40% variability with systematics most likely affecting the I-band data point at MJD 54796.7.

3.1.5 THE PROPERTIES AND ORIGIN OF THE ABSORBING GAS

3.1.5.1 SUMMARY OF OBSERVATIONAL RESULTS

This and the following subsections of Sect. 3.1.5 are taken in verbatim from Beuchert et al. (2015). The 6.9 years of sustained *RXTE* monitoring from 1999 Jan to 2005 Dec (Rivers et al., 2011b) caught two discrete eclipses. The first ∼80 d long event in 2000 was analyzed by Lamer et al. (2003) and is dominated by a low-ionization absorption component ($\log\xi \sim 0.4$; WA$_1$ in our model). The second event lasted 2–7 days and was also dominated by low-ionization or, at most, moderate-ionization gas (Markowitz et al., 2014). Based on this monitoring, the observation by *XMM-Newton* in 2006, and recent *Swift* observations from 2013–2015, NGC 3227 was usually relatively unobscured before 2006 and after 2013. Thanks to these previous observations and in particular the 2008 *Suzaku*/*Swift* campaign, we draw a clearer picture of the behavior of the variable absorption components in NGC 3227 over the last 15 years and also address the properties and origin of the absorber during the 2008 campaign.

During the 2008 campaign, the observed spectral variability was dominated by absorption due to moderately-ionized gas[8] ($\log\xi \sim 1$; WA$_2$ in our baseline model) with a time-variable, complex and irregular density profile, and columns spanning $\sim$5–16 $\times 10^{22}\,\mathrm{cm}^{-2}$ (Fig. 3.16). The column densities derived by *Swift* are mostly consistent with those from *Suzaku* within $2\,\sigma$. The event duration is ≥ 35 days. As a result of the lack of concurrent *RXTE* monitoring in 2008, we have no firm information on cloud ingress or egress.

---

[8] We caution that WA$_2$ as modeled during the 2008 campaign and WA$_2$ as measured during the 2006 XMM observation may represent different components: the ionization parameters may be similar but the column densities differ by more than a factor of 50.

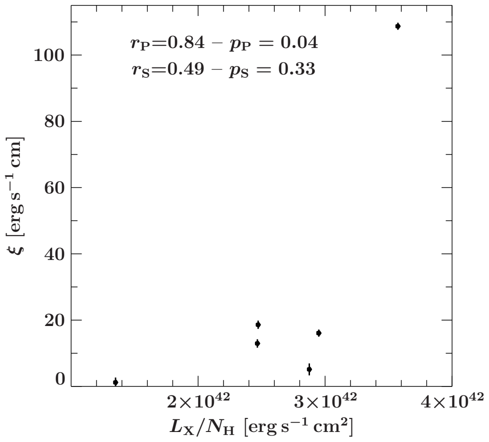

Figure 3.17. Correlation between the ionization parameter ξ and the X-ray luminosity L_X as a proxy for the ionizing luminosity. The numbers give the Pearson and Spearman rank correlation coefficients as well as null hypothesis probabilities.

3.1.5.2 LUMINOSITY AND IONIZATION

We now proceed to study further the nature and properties of WA$_2$ by testing if there is any relation between its ionization state and the measured source properties.

Because of Eq. (1.23), we expect a linear relation between ξ and the ionizing luminosity. We first assume that the measured X-ray continuum is a direct proxy for the variation of the ionizing continuum, i.e., we assume that the measured X-ray luminosity by *Suzaku*, taken here from 0.6 keV to 10 keV, is directly proportional to the overall ionizing luminosity L_ion. Figure 3.17 shows that there may be a trend in the data that higher luminosities also imply larger ξ. The Pearson correlation coefficient for ξ as a function of L_X is $r_\mathrm{P,X} = 0.70$ with a null hypothesis probability of $P_\mathrm{P,X} = 0.12$. However, the Pearson correlation coefficient is sensitive to extreme outliers, i.e., the data from Suz 4. As a second check we also calculate the Spearman rank correlation coefficient, which is less sensitive to extreme outlying points than the Pearson coefficient. We find $r_\mathrm{S,X} = 0.71$ ($P_\mathrm{S,X} = 0.11$). The data thus do not allow us to claim a direct relation between ξ and L_X; any correlation is tentative at best. More observations, especially at lower luminosity states, are needed.

3.1.5.3 THE LOCATION OF THE ABSORBER

Here we provide estimates of the distance of the variable absorber detected in the 2008 campaign from the SMBH. Throughout this section we make the simplified assumption that the mapped column density profile is due to a single spherical cloud of uniform density, illuminated by a central source and therefore ionized. For the ionization state and column density we use the average fit parameters from the *Suzaku* campaign, that is, $\log\xi \sim 1.1$ and $N_\mathrm{H} \sim 11.2 \times 10^{22}\,\mathrm{cm}^{-2}$.

Many of the properties of the cloud also depend on the ionizing luminosity, L_ion. As we showed above, there is only a tentative relation between the ionization parameter and the X-ray luminosity as proxy for the ionizing luminosity, i.e., the ionization state of the absorber is mainly determined by the source behavior in the UV, which is inaccessible to our measurements, and hidden in model degeneracies. We can place a constraint on the source's UV emission from the measured SED shown in Fig. 3.11.

To derive the ionizing luminosity between 13.6 eV and 13.6 keV (1–1000 Ryd), we assume that the UVOT data are non-variable within the 2008 campaign. We find $L_\mathrm{ion} = 8.9 \times 10^{42}\,\mathrm{erg\,s}^{-1}$ for the sum of the non-variable disk blackbody and the average of the X-ray power laws of all observations. The average bolometric luminosity is measured as $L_\mathrm{bol} = 1.3 \times 10^{43}\,\mathrm{erg\,s}^{-1}$. Using the assumed black-hole mass, we find an Eddington ratio of $\lambda_\mathrm{Edd} \sim 0.005$.

The measured value of L_ion is highly model dependent. We therefore compare our results with those of Vasudevan & Fabian (2009) and Vasudevan et al. (2010), who present strong sample studies for estimating the energy output of AGN but lack extended data coverage. They show that the ratio of the UV luminosity below 100 eV to the bolometric luminosity, $L^{\mathrm{ion}}_{0.0136-0.1\,\mathrm{keV}}/L_{\mathrm{Bol}} = 0.21 \ldots 0.59$ for values of the Eddington ratio $\lambda_{\mathrm{Edd}} = L_{\mathrm{Bol}}/L_{\mathrm{Edd}}$ ranging from 0.01 to 0.61. In contrast to our study, Vasudevan et al. (2010) include nuclear IR emission in the bolometric luminosity $L_{\mathrm{Bol}} = 10^{43.5}\,\mathrm{erg\,s^{-1}}$ for NGC 3227. Their lower black-hole mass results in a higher Eddington ratio of $\lambda_{\mathrm{Edd}} = 0.039$. We find via linear interpolation that $L^{\mathrm{ion}}_{0.0136-0.1\,\mathrm{keV}} \sim 0.23\,L_{\mathrm{Bol}} \sim 10^{42.9}\,\mathrm{erg\,s^{-1}}$, which results in $L^{\mathrm{ion}}_{0.0136-13.6\,\mathrm{keV}} \sim 1 \times 10^{43}\,\mathrm{erg\,s^{-1}}$ using our measured X-ray data. Considering the uncertainties of this method, this value is consistent with our result from a more complete SED in a single source study.

Constraints from the ionization parameter — We assume that the illuminated cloud is in photoionization equilibrium with the radiation field. Using the definition of ξ in Eq. (1.23) and estimating the particle density from the radial extent, ΔR ($\leq R$), of the cloud, $n_{\mathrm{H}} = N_{\mathrm{H}}/\Delta R$, we find

$$R \leq \frac{L_{\mathrm{ion}}}{\xi\, N_{\mathrm{H}}}. \tag{3.1}$$

This yields an upper limit for the distance of the cloud of 2.2 pc (2938 ld) when using the average measured parameters.

Constraints from the photoionization equilibrium — Following Reynolds & Fabian (1995), we now combine the information we gain from Eq. (3.1) with requirements for the recombination timescale. As we assume that the absorber is in photoionization equilibrium with the radiation field, the recombination timescale of the plasma must be much smaller than the timescale of variations of the ionizing continuum. A direct test of this assumption would be measurements of a positive correlation between $\log\xi$ and L_{ion} or L_{X}. Figure 3.17 indeed shows a positive trend, but the correlation is weak. This can be explained with the assumption of a spherical cloud, which may be an oversimplification. Any variations of the extent or number density of the cloud can distort a direct correlation. Also, the ionizing luminosity cannot be measured directly, as the gap between the FUV and soft X-rays is not observable. If the cloud reaches ionization equilibrium, the recombination timescale is given by (Blustin et al., 2005; Krolik, 1999)

$$t_{\mathrm{rec}} \sim (n_{\mathrm{e}}\alpha_{\mathrm{rec}})^{-1} \sim 2 \times 10^4 Z^{-2} T_5^{1/2} n_9^{-1}\,\mathrm{s}, \tag{3.2}$$

where $n_9 = n_{\mathrm{e}}/10^9\,\mathrm{cm^{-3}}$ with n_{e} is the electron particle density, and where α_{rec} is the recombination rate coefficient, Z the atomic number of the ion, and $T_5 = T/10^5\,\mathrm{K} \sim 1$, a representative value corresponding to gas with the ionization parameter $\log\xi \gtrsim 1$ (Reynolds & Fabian, 1995; Krolik & Kriss, 2001; Chakravorty et al., 2009). We use $Z = 9$ to represent the likely dominant ions for WA$_2$, O VIII, and Ne IX (Kallman & Bautista, 2001). In their study of warm absorber properties, Chakravorty et al. (2009) find that for typical AGN SEDs the $\log\xi/T$-$\log T$ stability curves are independent of the hydrogen number density for $10^5 \leq n_{\mathrm{H}} \leq 10^{10}\,\mathrm{cm^{-3}}$. Assuming solar abundances, $n_{\mathrm{e}} = 1.2 n_{\mathrm{H}}$. Using these assumptions we find $t_{\mathrm{rec}} \sim 370\, n_9^{-1}\,\mathrm{s}$, suggesting recombination timescales easily less than hours to days for most densities of relevance here.

A further constraint on the density can be obtained from the observed variability of the absorber. The shortest timescales over which we can reliably measure changes in the illuminating flux and ionization in NGC 3227 is 7 days. The *RXTE* light curves indicate that NGC 3227's X-ray flux typically varies by factors of a few tens of percent on timescales of 7 days and less (Uttley & McHardy, 2005), which makes the assumption of photoionization balance a reasonable assumption. The weekly spaced *Suzaku* observations confirm this finding, while no variability is found within each of the observations with exception of Suz 1. The overall low variability is consistent with the assumption of photoionization balance, such that $t_{\mathrm{rec}} \leq t_{\mathrm{var}} = 7\,\mathrm{d}$. This

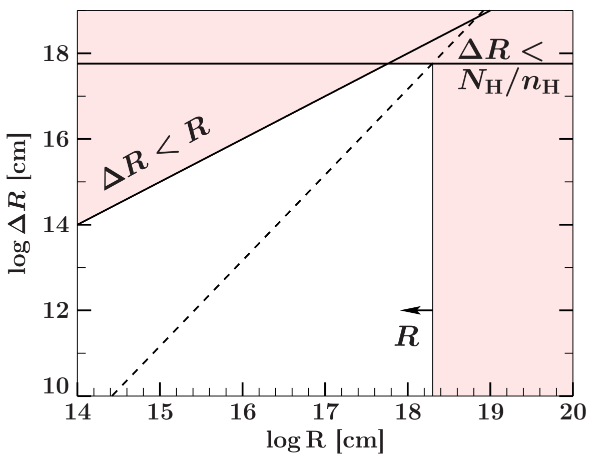

Figure 3.18. Constraints on the radial distance R of the ionized absorbing material from the central engine visualized in the $\log R - \log \Delta R$ plane, where ΔR resembles the diameter of the intrinsic absorber. The regions filled with light red can be excluded based on spectral results of *Suzaku* and the relations denoted along the border lines. The dashed line follows the relation $\Delta R = N_\mathrm{H} R^2 \xi / L_\mathrm{ion}$ with the appropriate average parameters derived from spectral fits to all *Suzaku* observations. The intersecting points with lines where $\Delta R < N_\mathrm{H}/n_\mathrm{H}$ marks the upper limit on R.

requirement can be translated to find a lower limit on the hydrogen number density from Eq. (3.2),

$$n_\mathrm{H} > \frac{2 \times 10^4}{1.2\, Z^2\, t_\mathrm{var}} \sim 1.94 \times 10^5\,\mathrm{cm}^{-3}, \tag{3.3}$$

which, in turn, sets an upper limit on the thickness of the absorbing layer,

$$\Delta R < \frac{N_\mathrm{H}}{n_\mathrm{H}}. \tag{3.4}$$

Figure 3.18 helps us find an appropriate upper limit on the distance R of the absorber by considering the variation of $\log \Delta R$ against $\log R$ (see also Reynolds & Fabian, 1995). We can exclude three regions in the $\log R$-$\log \Delta R$ space (Fig. 3.18, light-red region). The first region is obtained using Eq. (3.4) with the assumed average N_H of the absorbing cloud and the minimum hydrogen number density necessary to obtain ionization balance. In addition, we can also exclude a region where the basic assumption $\Delta R < R$ is violated. Since

$$\Delta R = \frac{N_\mathrm{H} R^2 \xi}{L_\mathrm{ion}} \tag{3.5}$$

and because $N_\mathrm{H} = n_\mathrm{H} \Delta R$, we can also find an upper limit for R. Inserting the average N_H, ionization state, and luminosity measured with *Suzaku* gives the dashed line in Fig. 3.18. An upper limit for R can be derived from the intersecting point of Eq. (3.4) and Eq. (3.5). As a result, the blank region includes all values of ΔR and R that come into consideration based on our spectral analysis, that is, $R \lesssim 10^{18.3}\,\mathrm{cm} = 0.65\,\mathrm{pc} = 770\,\mathrm{ld}$ (blue upper limit in Fig. 3.19), consistent with the dusty torus following Suganuma et al. (2006), Ramos Almeida et al. (2011), and our geometrical considerations in Eq. (3.1).

Constraints from a putative orbiting cloud — In this section we additionally consider the Keplerian orbital motion of an obscuring cloud that is illuminated by the central source while passing the line of sight in $\geq$35 d, equal to the duration of the campaign. We again use the average parameters N_H, $\log \xi$, and L_ion. With these assumptions we can estimate the distance of this kind of cloud.

The first rough estimate is based on Risaliti et al. (2007, 2009a,b) and Lohfink et al. (2012), who discuss a spherical cloud that passes the line of sight. It is able to fully cover the central X-ray source, if it is larger than the diameter of the X-ray emitting corona $\sim$10 r_g (Morgan et al., 2012) to five times this arbitrarily chosen value. This results in a lower limit for the distance of this kind of cloud of $R \gtrsim 0.1\,\mathrm{pc}$, marked as green lower limit in Fig. 3.19. Because of the complex shape of the N_H profile, the underlying assumptions are probably too simple. The limit is also highly sensitive to the choice of the size of the X-ray emitting region.

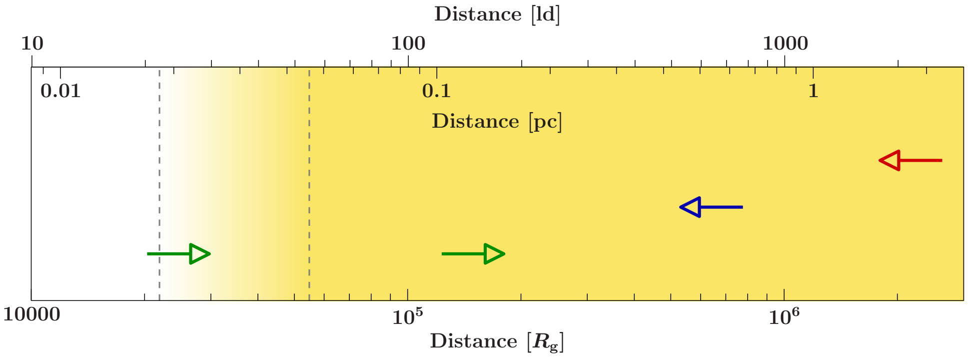

Figure 3.19. Radial distribution of clumps that can potentially exist below and beyond the dust sublimation zone, that is, $0.4\,R_\mathrm{d}$–R_d (dashed lines). The distance limits from Sect. 3.1.5.3 are marked with colored arrows. For all estimates we use the average measured parameters of WA_2 plus the average ionizing luminosity. The red upper limit from Sect. 3.1.5.3 uses the definition of the ionization parameter, while the blue upper limit from Sect. 3.1.5.3 is determined from geometrical constraints on a spherical homogeneous cloud in photoionization balance. The Keplerian orbital motion of this hypothetical cloud passing the line of sight is additionally included to form the lower limit in green (Sect. 3.1.5.3) while the second, larger lower limit in green is determined for an orbiting cloud neglecting the information on its ionization or column density.

This rough estimate of the distance can be improved when adding information about the average irradiating luminosity as well as column density and ionization state of the putative cloud. Writing the Kepler velocity as $v = \sqrt{G\,M_\mathrm{BH}/R} = \Delta R/\Delta t = N_\mathrm{H}/\left(n_\mathrm{H}\,\Delta t\right)$ and expressing n_H with the ionization parameter gives (Lamer et al., 2003)

$$R \geq 4\times 10^{16}\,\mathrm{cm}\,M_7^{1/5}\left(\frac{L_\mathrm{ion}\,\Delta t_\mathrm{days}}{N_{22}\,\xi}\right)^{2/5}. \tag{3.6}$$

With $M_7 = M_\mathrm{BH}/10^7\,M_\odot = 0.76$, $L_{42} = L/10^{42}\,\mathrm{erg\,s^{-1}} = 8.9$, $N_{22} = N_\mathrm{H}/10^{22}\,\mathrm{cm^{-2}} = 11.18$, and $\Delta t \geq 35\,\mathrm{d}$, we find $R \geq 0.017\,\mathrm{pc} = 20.7\,\mathrm{ld}$. This lower limit is shown as additional green lower limit in Fig. 3.19.

Finally, we estimate the size ΔR of the assumed spherical cloud. Equating the Keplerian velocity with $\Delta R/\Delta t = N_\mathrm{H}/n_\mathrm{H}\,\Delta t$, we find

$$n_\mathrm{H} = \frac{N_\mathrm{H}}{\Delta t}\sqrt{\frac{R}{G\,M_\mathrm{BH}}}. \tag{3.7}$$

Our distance estimates of 0.017–0.65 pc and the campaign-average value for N_H, then yield number densities of $n_\mathrm{H} \sim 2.7\times 10^8$–$1.7\times 10^9\,\mathrm{cm^{-3}}$, consistent with the lower limit found from the recombination timescale analysis. This result translates to a range in the size of the absorbers of $\Delta R \sim 6.6\times 10^{13}$–$4.1\times 10^{14}$ cm. Note that the column density profile has no defined ingress or egress. If we assume that the absorption by the cloud takes $\lesssim 2$ years, i.e., the time interval between the absorbed observations and the 2006 unabsorbed *XMM-Newton* observation, the density would be about one order of magnitude less and its size accordingly larger.

3.1.5.4 A DUST-FREE CLOUD LOCATED IN THE BLR?

The range of 0.017–0.65 pc found in the previous section means the possible location for the cloud spans radial distances both inside and outside the dust sublimation zone. Here, we define the dust sublimation zone to range from $0.4\,R_\mathrm{d}$–R_d, with the dust sublimation radius (Barvainis, 1987; Suganuma et al., 2006),

$$R_\mathrm{d} = 0.4\,\mathrm{pc} \cdot \left(\frac{L_\mathrm{bol}}{10^{45}\,\mathrm{erg\,s^{-1}}}\right)^{0.5} \left(\frac{T_\mathrm{d}}{1500\,\mathrm{K}}\right)^{-2.6} \sim 0.05\,\mathrm{pc}, \tag{3.8}$$

with an assumed bolometric luminosity of $1.3 \times 10^{43}\,\mathrm{erg\,s^{-1}}$ and a dust temperature of $T_\mathrm{d} = 1500\,\mathrm{K}$ (Barvainis, 1987; Nenkova et al., 2008b).

The result is consistent with Blustin et al. (2005), who determine the minimum and maximum distance of the absorbing gas solely based on geometrical considerations for a sample of 23 Seyfert galaxies of intermediate classification. Blustin et al. find that most low-velocity absorbers are consistent with the inner edge of the torus. Similarly, Risaliti et al. (2002) explain the column density variations of a large fraction of their Seyfert 2 sample sources with clouds at the inner edge of the dust sublimation zone.

We can test the dust content of the cloud using the reddening derived in Sect. 3.1.4.1. If the Galactic dust-to-gas ratio is applicable, the X-ray absorbing gas columns predict that we should see roughly $A_\mathrm{V} \sim 20$–$60\,\mathrm{mag}$ of optical extinction. During the strong 2008 absorption event, however, we only measure a reddening of $A_\mathrm{V} \sim 0.45\,\mathrm{mag} \sim 1.2 \times 10^{21}\,\mathrm{cm^{-2}}$.

There are potential reasons for the lack of a strong dust component in the variable X-ray column density. First we consider a scenario where a cloud inside the line of sight to the X-ray source may indeed contain dust, but does not cover the line of sight to the UV continuum source. The diameter of a spherical cloud on a Keplerian orbit was determined in Sect. 3.1.5.3 to be $\sim 6.6 \times 10^{13}$–$4.1 \times 10^{14}\,\mathrm{cm}$. We now estimate the diameter of the UV emitting part of the accretion disk for comparison. The radial temperature profile of a standard thin disk is

$$T(R) \sim 2 \times 10^5\,\mathrm{K} \left(\frac{M}{10^8\,M_\odot}\right)^{1/4} \left(\frac{\dot{M}}{\dot{M}_\mathrm{Edd}}\right)^{1/4} \left(\frac{R}{10^{14}\,\mathrm{cm}}\right)^{-3/4}, \tag{3.9}$$

with the derived Eddington ratio $\lambda_\mathrm{Edd} = L_\mathrm{bol}/L_\mathrm{Edd} = \dot{M}/\dot{M}_\mathrm{Edd} \sim 0.004$, the black-hole mass, and the radius of the UV emitting region. To solve the equation for R, we estimate the temperature at the outer UV emitting disk using the Wien displacement law and the longest wavelength *Swift*/UVOT filter. We find a radius of $1.1 \times 10^{15}\,\mathrm{cm}$, that is, larger than the estimated diameter range of a spherical, homogeneous X-ray absorbing cloud. In addition, McHardy et al. (2014), studying the inter-band time lags in NGC 5548, inferred that UV-emitting regions can extend slightly further than expected from standard α-disk theory, at least in that object. Consequently, based on our results, which assume a simple spherical cloud, we cannot rule out that the weak reddening is due to an X-ray absorbing cloud that fully covers the X-ray corona but not the entire UV-emitting disk.

A second possible reason for the low reddening is that the cloud does indeed contain dust but at a high gas-to-dust ratio. With the results above, we find a gas-to-dust ratio of $N_\mathrm{H}/A_\mathrm{V} \sim 2.5 \times 10^{23}\,\mathrm{cm^{-2}\,mag^{-1}}$, which is about a factor 100 higher than the assumed Galactic gas-to-dust ratio.

Finally, the low level of variability that we infer for the reddening supports the notion that the reddening matter has an origin, which is distinct from the much more strongly variable X-ray column. It is consistent with the distant, dusty, "lukewarm" absorber identified by Kraemer et al. (2000) and Crenshaw et al. (2001) as well as recent *Swift* observations. They therefore conclude that the X-ray absorbing gas is likely dust-free, which is supported by Sect. 3.1.5.3. We find that the absorber is consistent with a BLR cloud that orbits the black hole well below the dust sublimation radius. The hydrogen number density range of 2.5×10^8–$1.5 \times 10^9\,\mathrm{cm^{-3}}$ is consistent with the typical density of $\gtrsim 10^9\,\mathrm{cm^{-3}}$ expected for BLR clouds (Baldwin et al., 2003; Osterbrock, 1989).

3.1.5.5 THE MORPHOLOGY AND SPATIAL DISTRIBUTION OF THE PUTATIVE CLOUDY ABSORBER

We now investigate the possibility for the detected absorber to be part of an overall clumpy medium. According to the clumpy torus model of Nenkova et al. (2008a,b), the average number clouds along a line of sight with inclination i with respect to the system symmetry axis, N_C, is given by

$$N_\mathrm{C} = N_0 \exp\left[-\left(\frac{90-i}{\sigma}\right)^2\right], \tag{3.10}$$

where N_0 is the number of clouds along a ray in the equatorial plane between the R_d and $Y\,R_\mathrm{d}$. The radial distribution of the clouds follows a power law r^{-q}. This model has observational support from extensive time-resolved X-ray spectroscopy (Markowitz et al., 2014) and Bayesian model fits (Asensio Ramos & Ramos Almeida, 2009) to IR SEDs (Ramos Almeida et al., 2011; Alonso-Herrero et al., 2011).

Elitzur (2007) and Gaskell et al. (2008) claim that clouds can exist both in the BLR below, and in the dusty torus beyond R_d, all as part of a common structure. We therefore assume for simplicity that the power-law index q is the same for both the BLR and torus clouds, which yield a successively growing number of clouds toward the center. We assume the following mode values for the clumpy torus parameters from the posterior probability distributions of Alonso-Herrero et al. (2011): $N_0 = 15$, $Y = 15$, $q = 0.1$, $\sigma = 44°$ and $i = 30°$. They use IR photometry and additionally spectroscopic data around 10 μm. These values result in ~16 clouds in the equatorial plane between 0.4 and $15R_\mathrm{d}$. The lower limit equals the derived minimal distance of the absorber in NGC 3227. We call this number $N_0^\mathrm{X+IR}$, as it includes both dusty clouds detected in the IR and also dust-free clouds that additionally absorb X-rays. The number of clouds at the given inclination angle and width of the Gaussian cloud distribution then equals $N_\mathrm{C}^\mathrm{X+IR} = 2.5$ (Eq. (3.10)).

For comparison one can estimate the average number of clouds on the line of sight based on 6.9 years of sustained *RXTE* monitoring, the 2006 *XMM-Newton* observation, and the 35 days of *Suzaku* and *Swift* monitoring in 2008. During that time NGC 3227 was in an obscured state for a total of at least ~114 days. Based on the given data, NGC 3227 spends 4.4% of the observed time in eclipse.

Assuming Poisson statistics, the time averaged escape probability for photons without undergoing strong absorption by an average of $N_\mathrm{C}^\mathrm{X+IR}$ clouds in the line of sight is given by

$$P \sim \exp\left(-N_\mathrm{C}^\mathrm{X+IR}\,\tau_\lambda\right), \tag{3.11}$$

where the monochromatic optical depth of one cloud, $\tau_\lambda \gtrsim 1$ to be able to obscure the line of sight as observed during eclipses. With a 4.4% probability of obscuration, the integrated escape probability equals ~95.5%, i.e., $N_\mathrm{C}^\mathrm{X+IR} \sim 0.045$. This value is lower than the average of 2.5 clouds estimated above.

One can still find consistency when considering severe degeneracies between different attempts of clumpy tori fits. Ramos Almeida et al. (2011), for example, only use IR photometry between 1–40 μm. They find much larger uncertainties and different mode values of $N_0 = 2$, $Y = 19$, $q = 0.6$, $\sigma = 33°$ and $i = 66°$. Based on these values we find $N_0^\mathrm{X+IR} = 2.3$ between 0.4 to $30\,R_\mathrm{d}$; $N_\mathrm{C}^\mathrm{X+IR}$ is consequently equal to 1.4. When inserting not only the mode values, but other values of high probability within the posterior probability distributions of the parameters, we can find consistency with the observed number of 0.045 clouds along the line of sight. If the inclination angle is even more face on, the number of clouds $N_\mathrm{C}^\mathrm{X+IR}$ on the line of sight is also reduced. Marin (2014) provides an overview of different methods and inclination angles measured so far. Hicks & Malkan (2008) and Fischer et al. (2013) indeed find a value of $i \sim 16°$ using

NIR spectroscopy consistent with Fischer et al. (2013), although results from optical polarimetry (Sect. 3.1.4.2) are more consistent with the intermediate inclinations derived from IR SED fitting.

We note that the larger number of clouds that we find in the line of sight from extending the clumpy torus model than required from historical eclipse events is not inconsistent with the spectral results. Markowitz et al. (2009) show that even in a relatively unabsorbed state, ionized absorbers are present in the line of sight. Those could explain the determined excess of clouds.

3.1.5.6 The origin of the absorber

Here, we discuss the implications of the measured variable density profile of the absorber. Besides the highly variable column density over time, the covering fraction remains roughly constant for the latter five out of six *Suzaku* observations. This argues against two distinct clouds as an explanation for the two overdensities, but for a potential filament with a variable internal density structure that enters the line of sight. As a test, we can estimate the limiting size of one cloud, which is confined by its own magnetic field or the external pressure of the intercloud medium, not to get tidally sheared by the central force of gravity, to

$$r_\mathrm{cl} \leq 10^{16} \frac{N_{23} R_\mathrm{pc}^3}{M_7}\,\mathrm{cm}, \tag{3.12}$$

(Elitzur & Shlosman, 2006) where $N_{23} = N_\mathrm{H}/10^{22}\,\mathrm{cm}^{-2}$, $R_\mathrm{pc} = R/1\,\mathrm{pc}$ is the distance of the cloud to the central engine, and where $M_7 = M_\mathrm{BH}/10^7\,M_\odot$. Inserting the average column density N_H from the 2008 event and $R_\mathrm{pc} \sim 0.017$–0.65, we find $r_\mathrm{cl} \leq 3.3 \times 10^{10} - 1.8 \times 10^{15}\,\mathrm{cm}$. For comparison, the estimated diameter of a spherical cloud on a Keplerian orbit was $6.6 \times 10^{13}\,\mathrm{cm}$–$4.1 \times 10^{14}\,\mathrm{cm}$. Both ranges are consistent. Note, however, that the limiting size of the absorber, r_cl, is strongly dependent on its distance. We can argue for a distance R_pc of the absorbing cloud toward the lower limit of allowed ranges when considering the weak reddened, implying a location inside the dust sublimation radius. In this case we would have to assume an extended and filamentary medium in contrast to the simplified picture of spherically symmetric clouds bound by self-gravity.

Mechanisms that are thought to be able to lead to these structures include MHD-driven winds that are launched from the accretion disk, for example, via magnetocentrifugal acceleration (Blandford & Payne, 1982; Contopoulos & Lovelace, 1994; Königl & Kartje, 1994a). We find consistency between the measured ionization structure and column density of the absorber and the range of values simulated for MHD winds by Fukumura et al. (2010).

The absorber is also qualitatively consistent with the turbulent, dusty disk wind proposed by Czerny & Hryniewicz (2011). In this model, dusty clouds from the low-ionization part of the BLR can rise from the disk, e.g., driven by MHD forces, and get irradiated and heated sufficiently such that dust sublimates. Eventually clouds may fall back toward the disk when the gravitational force prevails over the driving forces. In this context, the absorbing cloud from 2008 may be just recently sublimated and temporarily situated at a height intercepting our line of sight.

The question remains how these driven clouds can get stretched out to filamentary structures of internal overdensities, which seem to best explain the observations. A potential mechanism is described by Emmering et al. (1992) in the context of MHD winds. As a wind or cloud forms, the material initially contains a high amount of dust, which is a good coolant via IR thermal emission. Once the clouds are driven away from the accretion disk they are heating up to $\sim 10^4\,\mathrm{K}$ as the dust sublimes. After a cloud is photoionized, its internal pressure increases and expands at roughly its internal sound speed until its pressure decreases to roughly that exerted by the external magnetic field. Rees (1987) shows that the polodial magnetic field of the disk together with the internal field of magnetized BLR clouds can cause the expanded clouds to stretch out along the magnetic field, which is frozen in the disk.

Additionally we mention radiative driving of accretion disk winds. Dorodnitsyn & Kallman (2012) provide detailed simulations of how the X-ray radiation from the hot corona can be transferred to the IR by exerting pressure on dust and allowing clumpy or filamentary structures to arise. Again, the cloud or filament can be ionized by the nuclear radiation when reaching a certain height matching the observables of the absorber.

The 2008 absorption event might not be unique. Similar to the long-term obscurations of $\sim$80 d and ≥ 35 d of NGC 3227 in 2000/2001 and 2008, respectively, NGC 5548 is continuously obscured for years (Kaastra et al., 2014). These phenomena may thus be typical to Seyfert galaxies, although the probability to observe them is low.

3.1.6 A FOLLOW-UP STUDY WITH SWIFT

The event that I have studied is intriguing in many ways. Resolving such profiles over time with a time resolution shorter than the event duration has so far been possible only for a few sources, mainly with long events, e.g., Cen A (170 d), NGC 3227 ($\sim$80 d Lamer et al., 2003), and NGC 3783 ($\sim$15 d Markowitz et al., 2014). Time-resolved spectroscopy of Cen A and NGC 3227 revealed column density profiles that indicated centrally-peaked clouds. NGC 1365 and Swift J2127.4+5654 are the only objects where a comprehensive study allowed to also resolve the internal density structure of short-term events with time. With help of the $\sim$35 d long N_H-profile measured by the *Swift*/*Suzaku* campaign, we derived valuable information on the nature of the absorbing gas. Measuring additional profiles of this kind would consolidate our results, which led me and a number of co-investigators to propose a follow-up study to the *XMM-Newton* Time Allocation Committee (TAC).

As part of this proposal, we estimated a significant trigger probability for an additional absorbing event based on all available archival observations. Assuming that single clouds are responsible for the observed event, we can use the clumpy-torus model of Nenkova et al. (2008b) and argue that the observed N_H is caused by the superposition of N_cld clouds on the line of sight. Together with the foregoing *RXTE* monitoring, we (Beuchert et al., 2015) show that obscuration events occurred during 4.4% of NGC 3227's monitored time. The 96% escape probability of photons is equal to $\exp(-N_\mathrm{cld}\,\tau)$ where τ is the optical depth of a single cloud. IR spectroscopy studies (e.g., by Asensio Ramos & Ramos Almeida, 2009) find $N_\mathrm{cld} \sim 1$–3 clouds on the line of sight. In our picture, single clouds have columns of $\sim 10^{22}\,\mathrm{cm}^{-2}$, which we separated from the time-average of $\sim 0.3 \times 10^{22}\,\mathrm{cm}^{-2}$ that we measure for the bulk of the 6.9 year long *RXTE* monitoring.

The few obscuration events that have been reported for NGC 3227 during the entire monitoring of *RXTE* between 1999 and 2005 may therefore just be the "tip of the iceberg". *RXTE*'s lack of soft X-ray coverage made it insensitive to ionized, partially-covering eclipse events with $N_\mathrm{H} \lesssim 10^{22.5}\,\mathrm{cm}^{-2}$. We therefore proposed for a monitoring with the observatory *Swift*, which allows for flexible scheduling and still provides sufficient effective area to discern single clouds. We defined a threshold of $2 \times 10^{22}\,\mathrm{cm}^{-2}$ above which we will trigger a series of observations with *XMM-Newton*. Our successful proposal lead to an extensive *Swift* monitoring campaign in 2015.

Figure 3.20 (left) shows the parameter evolution for the fit of all *Swift* spectra with a partial coverer, which is statistically required. The two *XMM-Newton* visibility windows are denoted as blue-shaded areas. The choice of the trigger level for these observations is well justified by the measured column densities. The N_H level, however, peaked once above the campaign-average of $N_\mathrm{H} = 1.14 \times 10^{22}\,\mathrm{cm}^{-2}$ just at the end of the *XMM-Newton* visibility window. A trigger of *XMM-Newton* would have been justified but was no longer feasible. During the second part of the monitoring in the end of 2015, both parameters N_H and f_cvr remained below the limit. In Fig 3.20 (right) we find that N_H and f_cvr seem to follow each other vaguely with a Pearson rank coefficient of 0.43 and a p-value of only 4%, i.e., the probability that both are mutually

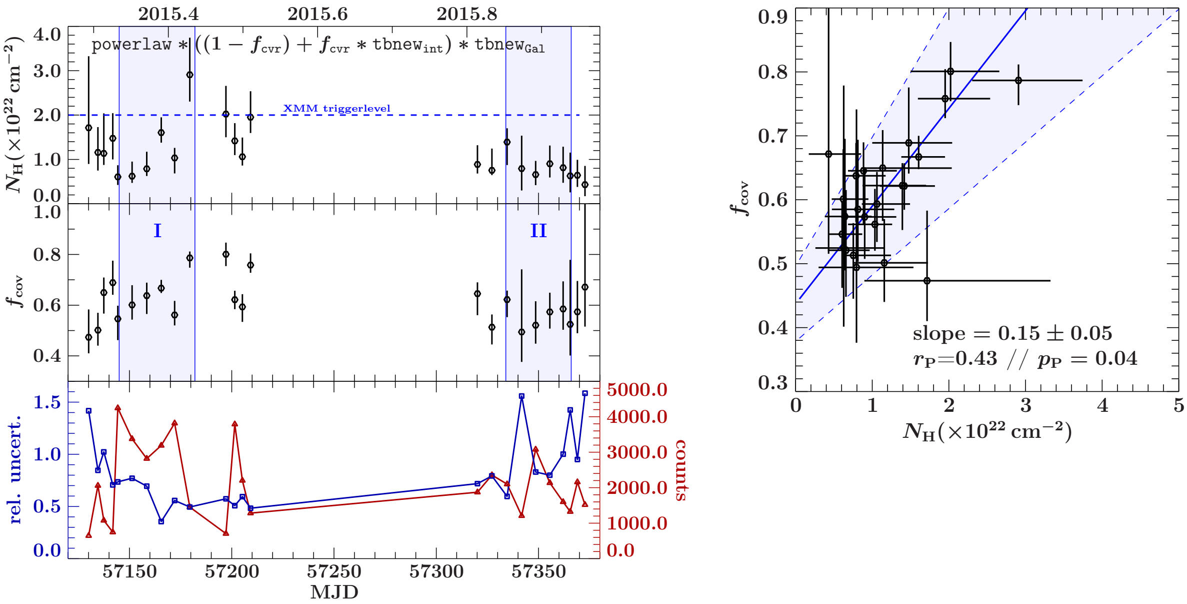

Figure 3.20. *Left:* evolution of N_H and f_cvr over time for a partial covering absorber modeled to the 2015 *Swift* monitoring of NGC 3227. The lowest panel shows the relative uncertainty of the column density (blue) together with the total counts collected by the individual pointings; *right:* study of the correlated variability of N_H and f_cvr.

independent.

Based on these results, we tentatively propose the detection of an absorption event during the first part of the campaign. The observations meet our expectations from above for the passage of a single cloud of no more than a few $\times 10^{22}\,\mathrm{cm}^{-2}$. Complementary *XMM-Newton* observations are still required to study the physics of the transiting absorbing structure.

3.1.7 SUMMARY AND CONCLUSIONS

This section is taken mainly in verbatim from Beuchert et al. (2015). We have studied data from a five-week-long *Suzaku* and *Swift* X-ray and UV monitoring campaign on the Sy 1.5 NGC 3227 in late 2008, which caught the source in an absorbed state. We performed time-resolved X-ray spectroscopy to untangle the various emission components, that is, the coronal power law and ionized reflection as well as multiple ionized absorption components, and to isolate the time-dependent behavior of the dominant absorber in 2008. Past *RXTE* monitoring reveals NGC 3227 to be usually unabsorbed, except for eclipses in 2000/2001 (Lamer et al., 2003) and 2002 (Markowitz et al., 2014). The ultimate aim of this study is to understand the properties of the X-ray absorber.

1. We used two archival and previously published *XMM-Newton* spectra to derive a baseline model that we fit simultaneously to six *Suzaku* and 12 *Swift* observations from 2008. An extensive exploration of the parameter space reveals only minor degeneracies. The two *XMM-Newton* spectra allowed us to identify three differently ionized absorbers, called WA_1 (low ionization), WA_2 (moderate ionization), and WA_3 (high ionization). We conclude that the detected absorption variability in 2008 is solely due to WA_2, while WA1 and WA_3 remain constant.

2. We resolved the column density and covering fraction of WA_2 to be variable with time. The covering fraction rises from ∼70% for the first *Suzaku* observation to ∼90% for the

remaining five observations. The column density varies from ∼5 to $\sim 18 \times 10^{22}\,\mathrm{cm}^{-1}$ in a double-peaked density profile. The ionizing luminosity L_{ion} and the ionization state ξ of WA_2 are seen to vary by factors of 1.3 and 104, respectively. A correlation analysis shows a tentative dependence between ξ and L_{ion} as a proxy for L_{ion}.

3. We used the average parameters of WA_2 ($\langle N_{\mathrm{H}} \rangle \sim 11.2 \times 10^{22}\,\mathrm{cm}^{-2}$, $\langle \log \xi \rangle \sim 1.1$, $\langle L_{\mathrm{ion}} \rangle \sim 8.9 \times 10^{42}\,\mathrm{erg\,s}^{-1}$) during the $\geq$35 d long absorption event to estimate that the distance of the absorbing medium is between 0.017 and 0.65 pc from the central SMBH. Here we made use of all available information, which comprise the ionization state, column density, and minimal duration of the event as well as the incident irradiation. The underlying, simplified assumption is that of a spherical cloud on a Keplerian orbit around the illuminating source.

4. For the derived distance range we inferred the hydrogen number density of the spherical cloud to be $\sim 2.7 \times 10^{8} - 1.7 \times 10^{9}\,\mathrm{cm}^{-3}$. The cloud therefore has a diameter of $\Delta R \sim 6.6 \times 10^{13} - 4.1 \times 10^{14}\,\mathrm{cm}$. We conclude that the absorber may be located in the outermost dust free BLR or the inner dusty torus.

5. We found only moderate reddening in the *Swift* UVOT data, which is due to a column density of $N_{\mathrm{H}} \sim 1.2 \times 10^{21}\,\mathrm{cm}^{-2}$. In contrast, we measured X-ray-absorbing column densities at about a factor of 100 larger. We conclude based on Sect. 3.1.5 that the X-ray absorber responsible for the variability in 2008 and the absorber responsible for extinction are distinct. The first seems to comprise a high gas-to-dust ratio due to its vicinity to the SMBH. A location in the BLR is consistent with our results. The latter is consistent with the distant (100 pc) lukewarm absorber proposed by Kraemer et al. (2000) and Crenshaw et al. (2001), which still seems to be present in recent *Swift* observations.

6. We also investigated the measured absorber in the context of the clumpy absorber model of Nenkova et al. (2008a,b). The inferred distribution of clouds is consistent with the eclipses observed for NGC 3227. The result that the absorber is likely located in the BLR leads us to extend the distribution of clouds down to $0.4R_{\mathrm{d}}$. The consistency of the model with past observations and the 2008 event is in particular reached for small inclination angles ($\lesssim$ 20–30°) of the putative clumpy torus that are measured by independent methods and can explain the predominant lack of absorption in NGC 3227 during past observations.

7. A spherical cloud situated below the dust sublimation zone can most likely not withstand tidal shearing by the central source of gravity. Several mechanisms, including MHD driving, are able to lift an initially dusty cloud from the disk where it is getting exposed to nuclear radiation and therefore ionized. Pressure gradients potentially stretch the cloud preferably along the magnetic field lines frozen to the disk.

8. A follow-up study of NGC 3227 with *Swift* reveals indications for an additional absorption event. Observations with an instrument of larger effective area such as *XMM-Newton* are needed to extract the physical properties of this absorbing structure.

In that context, the observing campaign represents a series of snapshots of parts of a cloud or filament whose properties (size, density distribution) may be evolving over time. The density profile of this event contrasts with that of the 2000/2001 event, which showed a centrally symmetric profile and clear ingress and egress. We therefore conclude that NGC 3227 is a rare laboratory to study the range of physical processes that lead to the formation of a range of shapes of absorbing structures from dense and distinct clouds to extended filaments.

3.2 A SUZAKU, NUSTAR, AND XMM-NEWTON VIEW ON VARIABLE ABSORPTION AND RELATIVISTIC REFLECTION IN NGC 4151

Here, I present work on the peculiar Seyfert 1.5 galaxy NGC 4151, which is known to show pronounced absorption variability in conjunction with signs for relativistic reflection off the inner parts of the accreting flow. The presented work is contained in and taken mainly in verbatim from Beuchert T., Markowitz A.G., Dauser T., et al., 2017, A&A, in press (arXiv:1703.10856).

3.2.1 INTRODUCTORY REMARKS

As I have outlined in Sect. 1.2.3.2, spectra that are blurred by the effects of strong gravity are ubiquitous features for unabsorbed Seyfert galaxies. Only a few intermediate-class Seyferts such as NGC 1365 are known to show variable cold absorption (Risaliti et al., 2005, 2007, 2009b; Maiolino et al., 2010) in conjunction with clear evidence for relativistic reflection (Risaliti et al., 2009a, 2013; Brenneman et al., 2013; Walton et al., 2013, 2014). The inclination of the symmetry axis of NGC 1365 to our line of sight was estimated as $\sim 60°$ (Walton et al., 2013). For this source, Risaliti et al. (2009a) are able to disentangle a partial covering absorber with low covering fraction from a component of blurred reflection, both of which produce similar spectral signatures. Mrk 766 may be an additional example, while a relativistically broadened iron line is still subject of debate (Miller et al., 2007; Patrick et al., 2012). Variability in line of sight absorption is in general a common feature of Seyfert galaxies at a wide range of time-scales and implies the passage of discrete clouds or more complex structures across the line of sight (see for example the results on NGC 3227 and the references provided in the previous section and Beuchert et al. 2015).

NGC 4151 is a close by ($z = 0.003319$; de Vaucouleurs et al. 1991) and well-studied Seyfert 1.5 galaxy. Complex and variable line-of-sight absorption has been reported for this source from X-ray spectra for over three decades (e.g., Holt et al., 1980; Yaqoob et al., 1989; Fiore et al., 1990). The absorption has been modeled in a variety of ways across various X-ray missions; successful models have typically incorporated combinations of $\sim$ two absorbers with cold and/or warm components. Having at least one component be partial covering (covering fraction typically $\sim$ 30–70%) is common. Variability absorption has been observed across a wide range of time-scales. Identifying the responsible component(s), however, remains difficult (de Rosa et al., 2007; Puccetti et al., 2007; Wang et al., 2010).

Similar to NGC 1365, Keck et al. (2015) provide solid evidence for relativistic inner-disk reflection in harmony with absorption variability in NGC 4151. Note that in contrast to NGC 1365, the inclination angle of NGC 4151 is still uncertain with estimates around $i < 30°$ from reverberation studies (Cackett et al., 2014), consistent with the estimate $i < 19°$ by Yaqoob et al. (1995) using the `diskline` model (Fabian et al., 1989) or $i \sim 30°$ from fits of the convolution model `kdblur2` (Nandra et al., 2007). Measuring the inclination angle is evidently highly model dependent.

The goal of this work is to revisit the spectral modeling of NGC 4151 and to pursue a physically-motivated model of its broadband X-ray spectrum and spectral variability. We consider multiple datasets with high count statistics, which allows us to constrain the complex model `relxillCp_lp` for relativistic reflection with a primary LP source of Comptonized X-rays. The choice of this model is strongly motivated by the detection of non-relativistic radio jets at a velocity of $\sim 0.05\,c$ (Wilson & Ulvestad, 1982; Mundell et al., 2003; Ulvestad et al., 2005) and by related Comptonization models in the jet-base of X-ray binaries (Markoff & Nowak, 2004; Markoff et al., 2005). When additionally applying complex absorption models, we remain mindful of potential degeneracies with the model for relativistic reflection. In Sect. 3.2.2 we provide an overview of the observations we consider for the data analysis, which we present in Sect. 3.2.3.

abbrv.	obsid	det	time	exp [ks]	cnts [$\times 10^4$]	
(XMM)	657840101	pn	2011-05-11			✗
		MOS 1				✗
		MOS 2				✗
XMM 1	657840201	pn	2011-06-12	2.3	1.4	√
		MOS 1		0.2	0.07	✗
		MOS 2		0.1	0.04	✗
XMM 2	657840301	pn	2011-11-25	5.7	2.8	√
		MOS 1		6.9	1.3	√
		MOS 2		7.1	1.3	√
XMM 3	657840401	pn	2011-12-09	6.6	3.0	√
		MOS 1		8.8	1.5	√
		MOS 2		9.0	1.5	√
XMM 4	679780101	pn	2012-05-13	6.3	2.6	√
		MOS 1		8.6	1.3	√
		MOS 2		8.7	1.3	√
XMM 5	679780201	pn	2012-06-10	8.7	1.6	√
		MOS 1		12.5	0.9	√
		MOS 2		12.5	0.9	√
XMM 6	679780301	pn	2012-11-14	3.8	2.4	√
		MOS 1		1.8	0.2	√
		MOS 2		2.0	0.3	√
XMM 7	679780401	pn	2012-12-10	6.6	2.7	√
		MOS 1		9.5	0.5	√
		MOS 2		9.6	1.4	√
(XMM)	679780501	pn	2012-12-10			✗
		MOS 1				✗
		MOS 2				✗
Suz 1	906006010	XIS 0	2011-11-17	61.7	18.5	√
		XIS 1		61.7	17.7	√
		XIS 3		61.7	19.0	√
		HXD		54.6	8.1	√
Suz 2	906006020	XIS 0	2011-12-18	55.1	21.1	√
		XIS 1		55.1	21.3	√
		XIS 3		55.1	23.4	√
		HXD		32.1	7.3	√
Suz 3	707024010	XIS 0	2012-11-11	150.2	32.5	√
		XIS 1		150.2	32.8	√
		XIS 3		150.2	35.2	√
		HXD		139.9	18.9	√
$\mathrm{Nu}_{\mathrm{Suz}}$	60001111002/3/5	FPM A	2012-11-12/14	106.1	71.3	√
		FPM B		106.2	67.4	√

Table 3.6. *XMM-Newton* and *Suzaku* observations in 2011/2012 with screened exposure times. Listed are the satellite, the observation ID of the observation, the date when the observation started, the exposure time after screening, and the number of counts detected. The check-symbol (√) denote observations that we consider for the data analysis. We exclude observations that are labeled with a cross (✗). The observation $\mathrm{Nu}_{\mathrm{Suz}}$ only contains data that are fully simultaneous to Suz 3.

For the analysis, we carefully motivate a baseline model, which we then apply to all observations. We also investigate the inherent spectral variability as well as the sensitive parameters of the relativistic reflection components. The soft X-rays are separately investigated. The results and implications are discussed in Sect. 3.2.4 and concluded in Sect. 3.2.5.

3.2.2 OBSERVATIONS AND DATA REDUCTION

This section is taken mostly verbatim from Beuchert et al. (2017). The observing log in Table 3.6 lists all examined *XMM-Newton*, *Suzaku*, and *NuSTAR* observations. They divide into the long-look *Suzaku* observation Suz 3 with the simultaneous long-look *NuSTAR* observation $\mathrm{Nu}_{\mathrm{Suz}}$. We complement these observations with two additional *Suzaku* observations of significant exposure, Suz 1 and Suz 2, from roughly one and two years before the joint *Suzaku*/*NuSTAR* campaign. We also add a number of shorter *XMM-Newton* observations to probe spectral variability on time-scales from months to years. The data extraction is done according to Sect. 2.3. Additional remarks are listed below.

Suzaku — For extracting *Suzaku* data, we make use of the calibration releases 2015-10-05 for Suz 1 and Suz 2 and the later version from 2016-02-04 for Suz 3. A previous investigation of Suz 3 by Keck et al. (2015) has shown discrepancies between the unfolded spectra among the different XIS detectors below 2.5 keV. With the calibration from 2016-02-04, this effect seems to be reduced. We therefore consider data in the full range between 0.6 and 10 keV. We find identical event files with both releases. For *Suzaku*/HXD, we use the latest calibration release

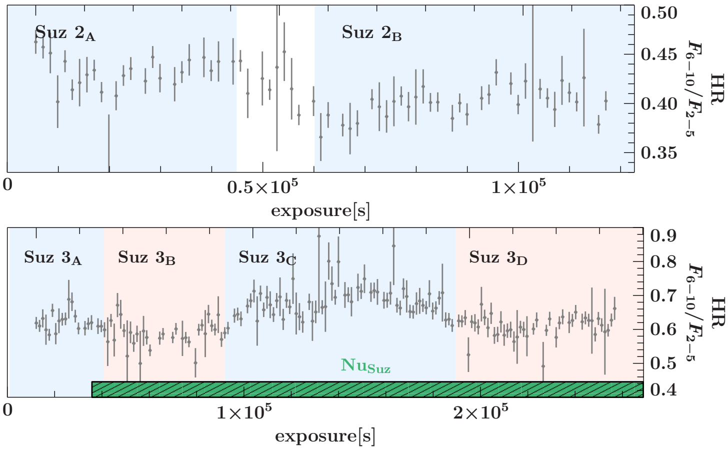

Figure 3.21. Hardness ratio of the 55 ks and 150 ks *Suzaku* observations Suz 2 (top) and Suz 3 (bottom) given by the ratio of count-rate light curves extracted between 6 and 10 keV and 2–5 keV. The shaded regions divide the observation in different parts for a time-resolved spectroscopy and are derived using a Bayesian block analysis. The green-shaded and striped region in the bottom panel indicates the relative observation time of $\mathrm{Nu}_{\mathrm{Suz}}$.

from 2011-09-15. All spectra are binned to a minimal S/N of 10 but at least 11 channels per bin in presence of spectral lines and at least 20 channels per bin for the continuum. The size of each bin is larger than the resolution of the response grid at ∼6 keV[9].

Figure 3.21 shows the hardness ratio evolution for the 55 ks and 150 ks observations Suz 2 and Suz 3, respectively, revealing significant variability. We use a Bayesian block analysis (Scargle, 1998; Scargle et al., 2013) to divide both observations Suz 2 and Suz 3 into single sub-spectra (Suz 2_{A}, Suz 2_{B} and Suz 3_{A}–Suz 3_{D}) that are highlighted in color in the figure. This method uses Bayesian statistics to identify time intervals that are, given the Poisson likelihood, compatible with constant hardness ratio. We extract observations from these blocks with the same procedures as described above. The exposures divide into 25.0, 25.6, 55.9, and 43.7 ks for the observations Suz 3_{A}–Suz 3_{D} resulting in 27.3×10^4, 19.0×10^4, 33.3×10^4 and 30.9×10^4 counts for the combination (XIS 0+XIS 1+XIS 3). Similarly, we find 23.0 and 32.1 ks for the observations Suz 2_{A} and Suz 2_{B} with 23.1×10^4 and 37.2×10^4 counts.

We bin the HXD data to a minimum S/N of 40 and a S/N of 20 for resolved sub-spectra. Where simultaneous *NuSTAR* data are present, cross calibration constants are fitted relative to FPMA (Madsen et al., 2015), otherwise spectra are normalized relative to XIS0[10].

NuSTAR — We explicitly extract *NuSTAR* data from time intervals that are fully simultaneous to Suz 3 ($\mathrm{Nu}_{\mathrm{Suz}}$) and Suz 3_{A}–Suz 3_{D} ($\mathrm{Nu}_{\mathrm{Suz,A}}$–$\mathrm{Nu}_{\mathrm{Suz,D}}$) with exposures of 106 ks, 2.5 ks, 25.8 ks, 50.2 ks, and 27.6 ks, respectively. This translates to a range of 3–62 × 10^4 counts for the observations $\mathrm{Nu}_{\mathrm{Suz,A}}$ to $\mathrm{Nu}_{\mathrm{Suz,D}}$. Spectra are binned to a minimum S/N of 100 for the integrated spectrum and to 20 for the four individual spectra, which only leaves data below 50 keV. Due to irregularities in the cross-calibration between *XMM-Newton*, *Suzaku*, and *NuSTAR* we take into account only *NuSTAR* data taken above 5 keV.

XMM-Newton — There exist nine observations of NGC 4151 with the EPIC camera between 2011-05-11 and 2012-12-10. We need to exclude the *XMM-Newton* observation 679780501 due to bad data quality. To prevent photon pile-up for this exceptionally bright source, *XMM-Newton* observed in small-window mode, which comes with faster readout. We use the `SAS v.14` with the most recent calibration files to date and extract all counts within a maximum possible radius of 40–43″ for EPIC-pn, and within ∼120″ for EPIC-MOS. While the region size is physically limited by the chip border for EPIC-pn, we are able to extract counts from nearly 100% of the encircled energy fraction of the on-axis PSF for EPIC-MOS. Background counts are extracted from an off-source spot on the chip within 45″ and 89″ for EPIC-pn and EPIC-MOS, respectively. We detect significant pileup in all three cameras. For the MOS we exclude the central pixels within 20″ of the source position. For the EPIC-pn, we exclude data from the inner 15″ for

---

[9] `https://heasarc.gsfc.nasa.gov/docs/astroe/prop_tools/suzaku_td/node10.html`

[10] http://heasarc.gsfc.nasa.gov/docs/suzaku/analysis/abc/

all observations, except for `0679780201`, where $17.5''$ needed to be excluded due to the higher count-rate of 8.7 cnts s^{-1}. The EPIC-pn data are binned by a factor of 2 between 0.5 and 1.0 keV, 4 between 1 and 5 keV, 6 between 5 and 8 keV, and 10 above that. The EPIC-MOS data are binned to a minimum S/N of 10, with additional geometrical of 3, 5, and 12 channels/bin in the 0.5–1.0, 1.0–3.0, and 3.0–10 keV bands. This choice guarantees at least 20–25 cnts bin^{-1} and provides an optimal trade-off between a decently binned continuum and sufficient data bins around line features in the spectrum. The first *XMM-Newton* observation, XMM 1, will not be further used due to strong particle flaring. For XMM 2, we exclude the EPIC-MOS data due to the small amount of net-exposure after filtering the event-files.

When fitting the RGS data, we simultaneously include both orders and all considered observations. We choose a geometrical binning of a factor of 3 for individual spectra to limit the oversampling of the theoretical RGS energy resolution as suggested by Kaastra & Bleeker (2016). Given the lack of sufficient counts per bin, we choose Cash-statistics for the further data analysis. Due to the low effective area at short wavelengths, we consider only data below 1.3 keV (9.5Å).

3.2.3 X-RAY SPECTRAL ANALYSIS

This section is entirely based on and taken in verbatim from Beuchert et al. (2017). In the following we examine all *XMM-Newton*, *Suzaku* and *NuSTAR* observations. These observations were taken during a span of more than one year. We provide a detailed investigation of the spectral components as well as their variability. We apply the Galactic column of $N_{\mathrm{H,Gal}} = 2.3 \times 10^{20}\,\mathrm{cm}^{-2}$ (Kalberla et al., 2005) in all cases. In Fig. 3.22, we show the spectra of all observations in the top panel. The data imply a lack of obvious variability of the soft X-rays below ~1 keV. The source is moderately variable above 6 keV within the range of $1\text{–}1.5 \times 10^{-3}$ Photons $\mathrm{cm}^{-2}\,\mathrm{s}^{-1}\,\mathrm{keV}^{-1}$ at 10 keV with XMM 5 catching the source in an exceptional low flux state. Strong spectral variability, in contrast, is apparent for the range between ~1 and 6 keV, both in spectral shape and normalization. This argues strongly against a physical partial coverer to explain the continuum including the soft emission below ~1 keV (see earlier work by Holt et al., 1980; Perola et al., 1986; Fiore et al., 1990) but in favor of diffuse emission from optically thin and ionized gas on larger spatial scales (e.g., Wang et al., 2011a, and references therein).

3.2.3.1 MOTIVATION FOR A BLURRED-REFLECTION COMPONENT

As a first approach to model the X-ray data, we simultaneously fit all *XMM-Newton* and *Suzaku* spectra with an incident and reflected power law using `xillver` that is absorbed by near-neutral intrinsic material (`zxipcf`) and Galactic foreground gas (`tbnew`). We fit the diffuse emission below 1 keV phenomenologically with a partial-covering version of `zxipcf` with a covering fraction of ~98%. We emphasize that the partial coverer has no physical meaning in this case and reflects the combination of a fully absorbed with an attenuated power law, both of identical slope. A physical interpretation of the latter is nuclear emission scattered off distant and large-scale gas. Figure 3.22 shows the spectra with corresponding fits. The modeling confirms a strongly changing column density ranging between 2.6 and $14.0 \times 10^{22}\,\mathrm{cm}^{-2}$ as well as a variable power-law flux. The ionization states of the reflecting material lie between $\log \xi \sim -3$ and 1.1.

For simplicity, we freeze the cutoff energy of the incident continuum to $E_{\mathrm{cut}} = 300\,\mathrm{keV}$ and the inclination angle to $i = 30°$. The Galactic column is considered as foreground absorption in all spectral fits. The residuals indicate decent fits to the continua of the individual observations and the ionized reflection component accounts well for a narrow Fe Kα and Fe Kβ line contribution but leaves line-like residuals below 2 keV, strengthening the notion of line-emitting plasma. Broad line-like residuals between ~5 and 6.4 keV, and a hard excess above 8 keV are reminiscent of an additional component of blurred reflection (see also Fig. 3.23).

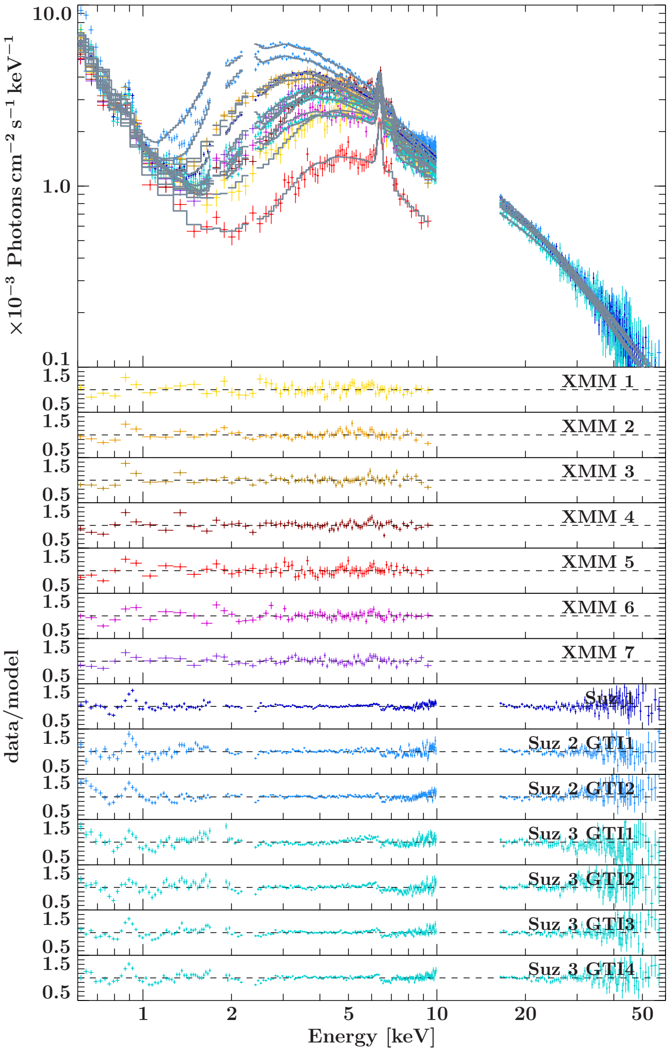

Figure 3.22. Fit to the *XMM-Newton* and *Suzaku* data. The model consists of a power law that is partially covered by near-neutral intrinsic material as well as fully covered by Galactic foreground gas. A `xillver`-component of ionized, unblurred reflection is used to model the narrow iron line and potential soft-line emission.

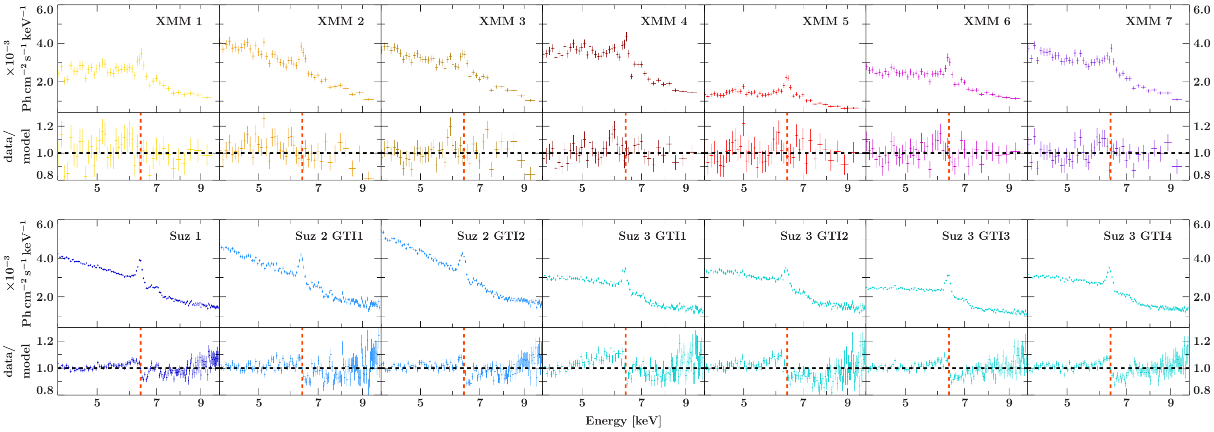

Figure 3.23. Zoom-in into the iron-line region of the complete set of observations of *XMM-Newton* and *Suzaku* with the same model applied as shown in Fig. 3.22. We mark the centroid energy of the Fe Kα line with a red, dashed line in the residual panels.

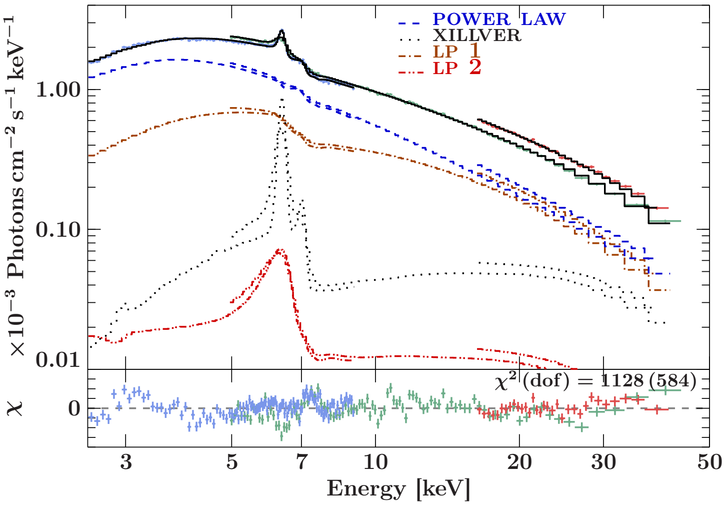

Figure 3.24. Application of the two-LP model of Keck et al. (2015) to the Suz 3 and $\mathrm{Nu}_{\mathrm{Suz}}$ data. All model components shown here are fully absorbed with the column reported by Keck et al. (2015). The incident continuum is plotted in blue, the unblurred component in black and the blurred reflection components with a low and high primary source in brown and red, respectively. The residuals indicate the *Suzaku*/XIS, *Suzaku*/HXD and *NuSTAR* data in blue, green and red, respectively.

3.2.3.2 BUILDING ON A RECENT INVESTIGATION OF THE SUZAKU DATA: APPLICATION OF AN IMPROVED MODEL FOR RELATIVISTIC REFLECTION

Keck et al. (2015) have presented a detailed study of the joint *Suzaku*/*NuSTAR* campaign (Suz 3/$\mathrm{Nu}_{\mathrm{Suz}}$) for data above 2.5 keV. They discuss two possible models: (1) their best-fit model dominated by relativistic inner-disk reflection and (2) an entirely absorption-dominated model. The first is given by a convolution of the unblurred and initially angle-resolved reflection continuum `xillver` with the relativistic code `relconv` describing reflection off the inner parts of an accretion disk. The authors also test for the more self-consistent model `relxill` (García et al., 2013). This model is a great improvement in that it links the relativistic transfer-function and the angle-resolved disk-reflection spectrum `xillver` at each point of the disk. It therefore accounts for the inconsistency of previous convolution codes. These codes averaged over photons that reach the observer under various disk emission angles, which must not be equal to the inclination angle of the system due to the effects of light bending. Although García et al. (2013) predict deviations of up to 20% for parameters of `relconv` and `relxill`, Keck et al. (2015) find a negligible statistical difference. They attempt to fit for a LP geometry with the convolution code `relconv_lp` and require two distinct LP components at different heights ($\sim 1.3\,r_{\mathrm{EH}}$ and $\sim 14\,r_{\mathrm{EH}}$, where r_{EH} is the radius of the EH). The authors, however, find significant S-shaped residuals between 3 and 5 keV and therefore reject this solution on statistical grounds. The immediate aim of our study is to investigate this model description using a LP geometry that is physically motivated not only by steep inner disk-emissivities (Svoboda et al., 2012) but also by independent reverberation studies (e.g., Kara et al., 2013, and references therein). As a first improvement, we replace the convolution model with the fully angle-resolved version `relxillCp_lp`. In this model, the fraction of reflected photons is self-consistently calculated via ray tracing in the lamp-post geometry. Also, it takes into account the Comptonization continuum `nthcomp` as primary continuum irradiating the disk (Zdziarski et al., 1996). We adopt the parameters found by Keck et al. (2015) using `relconv_lp`. In Fig. 3.24, we show this model evaluated for the data of Suz 3 and $\mathrm{Nu}_{\mathrm{Suz}}$ in the same energy range considered by Keck et al. (2015). We find similar statistics and residuals as compared to the convolution model. The S-shaped residuals around the turnover of the absorber between 3 and 5 keV imply a yet unmodeled partial coverer, which the authors investigated as part of their independent model (2).

This model combines two partial coverers, one with a column of $\sim 6 \times 10^{23}\,\mathrm{cm}^{-2}$ and low covering fraction (~40%) and a second one with $\sim 1.3 \times 10^{23}\,\mathrm{cm}^{-2}$ and a near-maximum covering fraction (~94%). The model provides a decent description of the continuum above 2.5 keV,

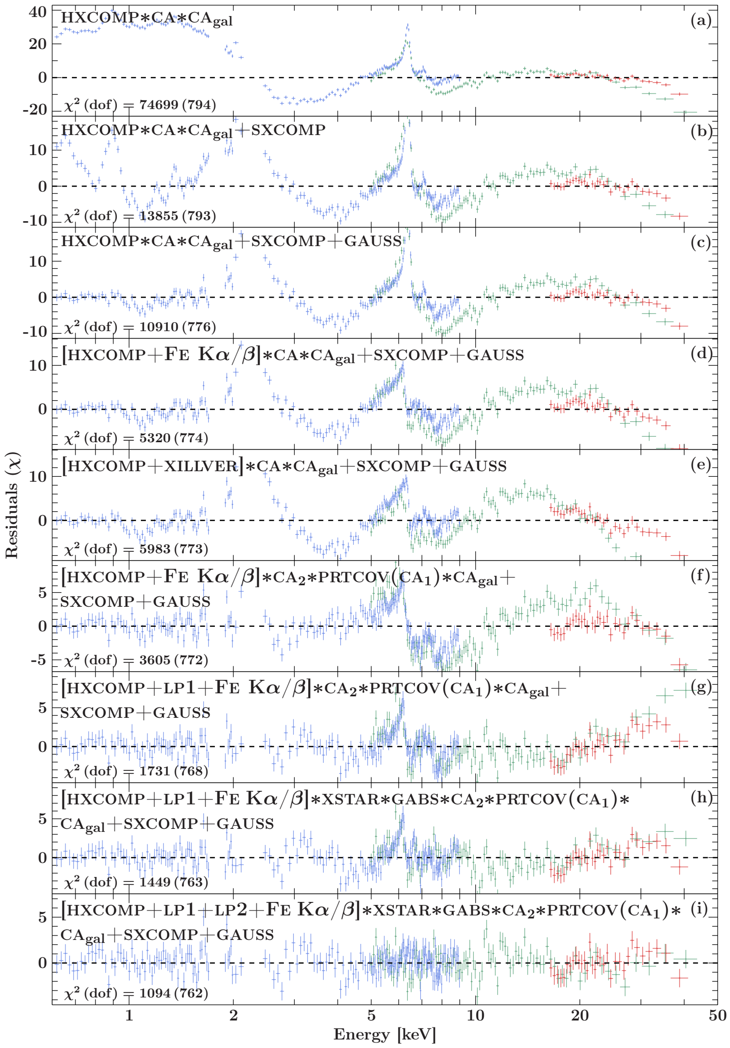

Figure 3.25. Residuals (χ) for a bottom-up approach towards the best-fit of Suz3. The statistics of each step are shown on the bottom left. *NuSTAR* residuals below 5 keV are excluded from the plot due to deviations of the cross-calibration between *Suzaku* and *NuSTAR*. The ranges of the residual axes are adapted to show the full dynamic range.

but leaves residuals reminiscent of a broad iron line and is statistically less preferred. This demonstrates that modeling the complex spectrum of NGC 4151 is not straightforward but combined with degeneracies between these two solutions.

We build a baseline model using the long-look 150 ks Suz 3 and simultaneous Nu$_{\text{Suz}}$ observations. We extend the work by Keck et al. (2015) by considering the entire energy range covered by the instruments. For flattening the S-shaped residuals in our broad-band X-ray continuum, we combine their models (1) and (2) and apply the latest self-consistent relativistic reflection code `relxillCp_lp`. We fix the seed photon temperature to 50 eV, which is used to calculate the `xillver` tables.

3.2.3.3 A re-investigation of the 150 ks simultaneous Suzaku and NuStar observations with `relxillCp_lp`

Derivation of a baseline model — The residuals at each step are shown in Fig. 3.25. First, we fit the data with the Comptonization continuum `nthcomp`, hereafter referred to as HXCOMP. It provides a more physically motivated primary continuum with an intrinsic cutoff as opposed to a power law with external cutoff (García et al., 2015). This continuum is absorbed by fully-covering neutral gas (CA, `tbnew_simple_z`). The residuals are shown in Fig. 3.25a and in particular indicate an unmodeled soft continuum.

In previous studies using *Chandra* data Ogle et al. (2000) and Wang et al. (2011a) accounted

Table 3.7. Best-fit parameters of the blend of Gaussian lines for Suz 3. All Gaussian lines are fitted with zero width. Centroid energies marked with ∞ are adopted from Schurch et al. (2004), Ogle et al. (2000), and Vainshtein & Safronova (1978), line blends marked with † from the *Chandra*/ACIS study of Wang et al. (2011a). Frozen parameters are denoted with an asterisk ($*$). When marked with the symbol $\between$, the line identification is uncertain and can be confused with an instrumental edge. The lines are consistent with the study on *XMM-Newton*/RGS data in this work. Note that the O VII line falls outside the sensitive energy range of *Suzaku*/XIS. For the possible line-blends Ne IX RRC / Mg XI r and Si XIII (r/f), we additionally fit for the centroid energies, because of unclear line identifications. Also, we require two narrow Gaussians with zero width at 1.58 keV and 1.72 keV, which may be due to intrinsic Si I Kα and Mg XI $1s3p-1s^2$ or due to calibration effects at the instrumental Al K and Si K edges.

Line	E* [keV] / λ^* [Å]	flux [$\mathrm{Ph\,s^{-1}\,cm^{-2}}$]
O VII (r,i,f) †	0.57 / 21.8	$(1.09 \pm 0.29) \times 10^{-3}$
O VIII Ly α^{∞}	0.65 / 18.97	$(2.67 \pm 0.19) \times 10^{-4}$
O VII RRC $^{\infty}$	0.74 / 16.77	$(9.4 \pm 1.0) \times 10^{-5}$
O VIII RRC $^{\infty}$	0.87 / 14.23	$\left(7.6^{+0.7}_{-1.0}\right) \times 10^{-5}$
Ne IX (r,i,f) †	0.91 / 13.55	$(1.02 \pm 0.09) \times 10^{-4}$
Ne X Ly $\alpha^\dagger$	1.03 / 12.04	$(1.8 \pm 0.4) \times 10^{-5}$
Ne IX RRC / Ne X Ly $\beta^\dagger$	1.2 / 10.33	$(3.0 \pm 0.4) \times 10^{-5}$
Ne X RRC / Mg XI (r) $^{\infty}$	$1.351^{+0.004}_{-0.005}$ / 9.18 ± 0.03	$(4.39 \pm 0.29) \times 10^{-5}$
Mg VII Ly α^{∞}	1.47 / 8.43	$(2.15 \pm 0.26) \times 10^{-5}$
Mg XI $1s3p - 1s^{2\,\infty}$ $\between$	1.58 / 7.85	$(2.8 \pm 0.4) \times 10^{-5}$
Si I Kα^{∞} $\between$	$1.7200^{+0.0017}_{-0.0000}$ / $7.2084^{+0.0000}_{-0.0071}$	$(3.6 \pm 0.4) \times 10^{-5}$
Si XIII (r,f) $^{\infty}$	$1.8473^{+0.0008}_{-0.0013}$ / $6.712^{+0.005}_{-0.003}$	$(4.4 \pm 0.4) \times 10^{-5}$
Si XIV Ly α^{∞}	2.0 / 6.20	$(2.3 \pm 0.4) \times 10^{-5}$
Continuum	Γ	norm [$\mathrm{Ph\,keV^{-1}\,s^{-1}\,cm^{-2}}$]
	1.72*	$(1.33 \pm 0.05) \times 10^{-3\,*}$

for the soft continuum with a bremsstrahlung component. The latter authors, however, emphasize their lack of a physical motivation for this component. We therefore consider a simple scenario, in which the nuclear Comptonized continuum is scattered off distant and large-scale gas and model this component with an unabsorbed soft Comptonization continuum (SXCOMP, Fig. 3.25b). Here, we adopt the same parameters of the HXCOMP but leave the normalization free to vary. This way of modeling introduces a minimal set of additional degrees of freedom. Also, at CCD energy resolution and given the blend of emission lines present (see below), we cannot constrain the exact form of the soft continuum, so fits using Comptonization or bremsstrahlung continua yield statistically identical fits.

On top of the soft continuum, a number of lines appear in the residuals, reminiscent of emission from the ionized large-scale gas component that has been extensively studied by, e.g., Wang et al. (2011a) using *Chandra* and physical emission codes. We focus mainly on the nuclear properties of the X-ray spectrum and instead fit this emission with a phenomenological blend of Gaussians in Fig. 3.25c. The centroid energies are adopted from those lines that are significantly detected in gratings data of *XMM-Newton*/RGS (Schurch et al., 2004) and *Chandra*/LETG (Ogle et al., 2000, see also Vainshtein & Safronova 1978), or as line-blends by *Chandra*/ACIS (Wang et al., 2011a). Table 3.7 lists the parameters of all fitted lines with their ion identification, line flux and centroid energies. For deriving the final photon line fluxes and their uncertainties, we freeze all continuum parameters including the SXCOMP normalization to the best-fit value found in the final step. This also reduces degeneracies between the line-blend and the continuum. The remaining residuals show a yet unmodeled swing in the continuum around 2 keV, strong and broad emission forming an iron-line complex around 6 keV and extra curvature above 10 keV.

Narrow emission components at the centroid energies of the Fe Kα (β) lines at ~6.4 (7.1) keV are modeled with either two narrow Gaussians (Warwick et al., 1989; Zdziarski et al., 2002; Schurch et al., 2003; Wang et al., 2010) with a frozen flux-ratio of 12% (Fig. 3.25d) or a component of distant reflection (`xillver`) in Fig. 3.25e. Both options leave a broad emission feature between

5 keV and 6 keV, as previously seen by Wang et al. (1999), as well as equal continuum residuals. We are therefore not able to confirm a strong statistical need for a distant reflection component. We remain with using two Gaussian components as a phenomenological description of the iron line emission that likely originates from Compton-thin gas. This way, we only add a minimal set of additional degrees of freedom to the model.

Due to the use of a full-covering neutral absorber, there still remain S-shaped residuals below 5 keV, similar to what Keck et al. (2015) found. We replace the fully covering absorber with the combination of a partially covering absorber (CA_1) and a fully covering absorber (CA_2), both neutral (see Fig. 3.25f). CA_1 requires a covering fraction of ~40–50%. A similar dual neutral absorber has been frequently applied before (e.g., Wang et al., 2010; Keck et al., 2015, and references therein).

The broad pattern just below 6 keV remains, even after flattening the continuum below 5 keV. It likely features the red wing of an extremely blurred Fe Kα line (e.g., Dauser et al., 2010). We attempt to flatten this feature with the previously introduced model `relxillCp_lp`, that is, inner-disk reflection in a self-consistent LP geometry. We call this component LP_1. Its height hits the lower limit at $\sim 1.1\,r_{\mathrm{EH}}$, which corresponds to $1.2\,r_{\mathrm{g}}$ for the spin fixed at its maximum value. Note that we fit the incident and reflected continua independently at this point. Due to the lack of data above 50 keV, we are unable to constrain the cutoff energy (expressed via the electron temperature in our model) and freeze it at $kT_{\mathrm{e}} = 399$ keV or $E_{\mathrm{cut}} \approx 1000$ keV. We note, however, that Malizia et al. (2014) find $E_{\mathrm{cut}} = 196^{+47}_{-32}$ keV with *INTEGRAL*, *Swift* and *XMM-Newton* data between 2 and 100 keV. We expect significant bias for their measurement of the cutoff because of the lack of soft X-rays (García et al., 2015), the use of a lower photon index of Γ ~1.63 and the background dominance of *INTEGRAL* as opposed to the *NuSTAR* data used in this work. We emphasize that for primary sources close to the black hole, one has to correct the cutoff energy for the gravitational redshift as outlined by Niedźwiecki et al. (2016). The resulting residuals (Fig. 3.25g) illustrate that the underlying broad feature as well as parts of the Compton hump above 10 keV are successfully fitted by LP_1.

Dips around 7 keV suggest an additional column of highly ionized absorption. We can greatly improve the fit using a `xstar` absorption component with $\log\xi \sim 2.8$. Warm absorber components with similar ionization have previously been found by Weaver et al. (1994b), Schurch & Warwick (2002), and Keck et al. (2015). The `xstar` model removes line-like residuals close to the centroid energies of Fe XXV He α, Fe XXVI Ly α and Fe XXV He β, at zero velocity offset relative to systemic. There remain narrow absorption-like residuals around 8 keV; they can be modeled with a broad Gaussian absorption component that has an energy centroid of $8.17^{+0.11}_{-0.09}$ keV (rest frame). We identify this feature as a blueshifted Fe XXV He α or Fe XXVI Ly α line, although the possibility of unmodeled contributions from Fe XXVI Ly β (8.25 keV rest frame) associated with the systemic warm absorber cannot be ruled out. The implied velocities are $0.22^{+0.02}_{-0.01}$ c for He-like Fe or $0.17^{+0.02}_{-0.01}$ c for H-like Fe, suggesting an ultra-fast outflow (UFO), as previously constrained with `xstar` modeling by Tombesi et al. (2011, 2013a). Figure 3.25h shows the flattened residuals.

An excess around ~6 keV implies a still broad iron line with a much less smeared red wing. We therefore add a second LP component (LP_2) with a primary source at the larger height of $\sim 17\,r_{\mathrm{EH}}$, which also takes care of remaining excess residuals above 20 keV. While both components LP_1 and LP_2 already describe the entire Compton hump above 10 keV, further tests can exclude the need for a third, distant reflection component to model also the narrow iron line. We find a best-fitting baseline model with $\chi^2/\mathrm{dof} = 1094/762$ and overall flat residuals in Fig. 3.25i.

The best-fit baseline model — We found a solid model for the broad continuum from the soft to the hard X-rays, which we will later apply to the remaining observations. This baseline model combines a set of four complex absorbers with a physical description of blurred reflection as part of the self-consistent LP geometry. We fit both LP components with a tied slab-ionization

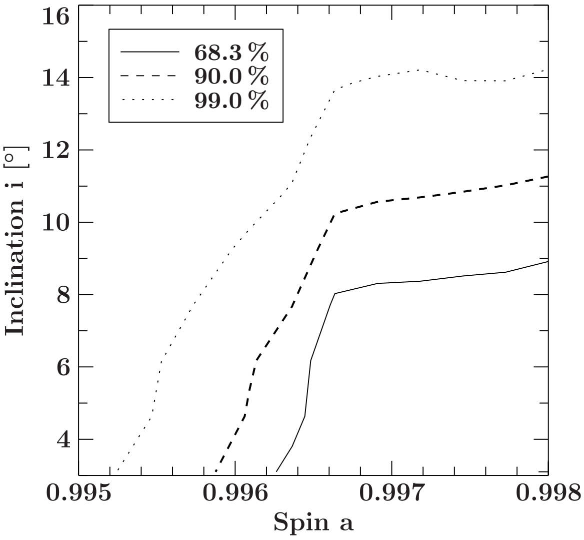

Figure 3.26. Contours between the spin and inclination of both LP reflection components for a fit with free spin. We show 68.3%, 90% and 99% confidence levels.

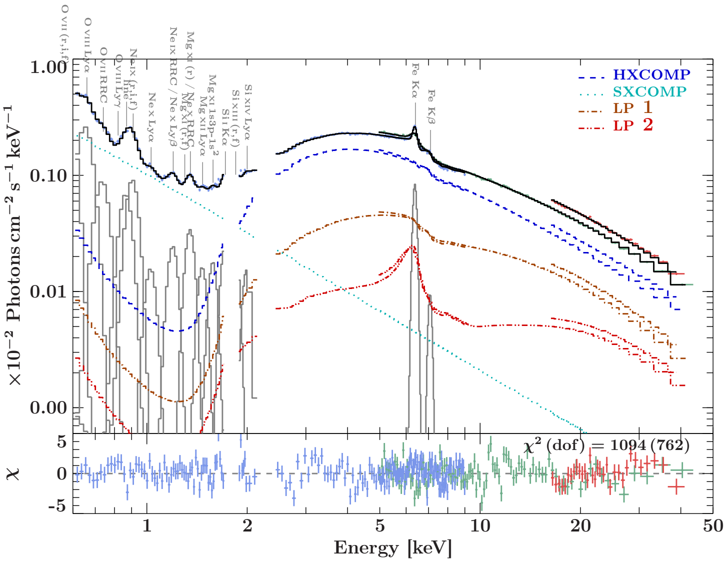

Figure 3.27. Model components together with the data and residuals of the 150 ks long observation Suz 3. The incident HXCOMP continuum (dashed blue line) and both LP models (LP_1: dotted-dashed brown line, LP_2: double-dotted-dashed red line) are shown as absorbed components, the SXCOMP (dotted cyan line) as unabsorbed component. The soft emission lines (gray) required for the best-fit are labeled with their line identifiers and listed in Table 3.7. The residuals of *Suzaku*/XIS, *Suzaku*/HXD as well as *NuSTAR*/FPM are drawn in blue, red, and green, respectively.

and find a common value of $\log \xi \sim 2.8$. The fit is hitting the lower-limit for the inclination of 3.1° with 90% uncertainties allowing values as high as 10° (see the contours between disk inclination and spin in Fig. 3.26 where we unfroze the spin parameter). The wide range originates in the $\cos i$-dependence of the model. This inclination is consistent with the constraint of $\theta < 30°$ that Cackett et al. (2014) found with reflection-component reverberation mapping. We find no obvious correlation with the spin parameter and fix the spin at its maximum value. The relatively flat turnover between 3 and 6 keV is well described by the dual neutral absorber rather than a single full-covering absorber. The column densities of the two neutral absorbers are $N_{\mathrm{H},1} \sim 21 \times 10^{22}\,\mathrm{cm}^{-2}$ with $f_{\mathrm{cov}} = 0.46$ and $N_{\mathrm{H},2} \sim 9 \times 10^{22}\,\mathrm{cm}^{-2}$ for the full-covering absorber. The HXCOMP photon index is well constrained to $\Gamma = 1.72 \pm 0.01$ for the long-look observation. We will therefore keep it fixed for the remaining observations of lower count statistics to reduce degeneracies within the complex model composite.

We list the best-fit parameters and their uncertainties in Table 3.8 and show all model components in Fig. 3.27. The flat turnover between 3 and 6 keV is well described by the dual neutral absorber as compared to a single full-covering absorber.

We test for degeneracies inherent to the complex continuum for Suz 3 and study the resulting contours in $\Delta\chi^2$-space (Fig. 3.28). The contours and derived uncertainties suggest that we are able to constrain and separate between both LP continua with primary sources at different

Table 3.8. Best-fit parameters of the baseline model for the simultaneous 150 ks data of Suz 3 and $\mathrm{Nu_{Suz}}$. The black-hole spin of both LP components is set to its maximum value of $a = 0.998$. The radii of the inner and outer disk are kept at the default values of $1\,r_{\mathrm{EH}}$ and $499\,r_{\mathrm{g}}$, respectively. Parameters marked with the symbol † are tied amongst each other, those marked with an asterisk ($*$) are frozen. The reflection fraction is no free parameter here, as the incident continuum (`nthcomp`) and both reflection continua ($\mathrm{LP_1}$, $\mathrm{LP_2}$) are fitted independently (`refl_frac=-1`). The normalization of `nthcomp` is defined at unity for a norm of 1 at 1 keV. The normalization of `xillver` and `relxill` is defined in the Appendix of Dauser et al. (2016).

Model component	Parameter	Value
707024010: $\chi^2\,(\mathrm{dof}) = 1147.78\,(789)$		
Detconst	XIS 0	0.998 ± 0.005
	XIS 1	0.954 ± 0.005
	XIS 3	1.012 ± 0.005
	HXD	1.215 ± 0.009
	FPMA$*$	1
	FPMB	1.030 ± 0.004
$\mathrm{CA_{Gal}}$	$N^*_{\mathrm{H,Gal}}$ $[10^{22}\,\mathrm{cm^{-2}}]$	0.023
XSTAR 1	N_{H} $[10^{22}\,\mathrm{cm^{-2}}]$	1.2 ± 0.3
	$\log\xi$ $[\mathrm{erg\,cm\,s^{-1}}]$	$2.82^{+0.10}_{-0.11}$
$\mathrm{CA_1}$	$N_{\mathrm{H,int}}$ $[10^{22}\,\mathrm{cm^{-2}}]$	21^{+4}_{-2}
cov. factor	$\mathrm{f_{cvr}}$	$0.46^{+0.06}_{-0.05}$
$\mathrm{CA_2}$	$N_{\mathrm{H,int}}$ $[10^{22}\mathrm{cm^{-2}}]$	$8.8^{+0.5}_{-0.6}$
Abs. line	E [keV]	$8.17^{+0.11}_{-0.09}$
	σ [keV]	$0.34^{+0.14}_{-0.07}$
	Depth $[2\pi\,\sigma\,\tau_{\mathrm{line}}]$	$0.0339^{+0.0124}_{-0.0020}$
HXCOMP	norm	0.047 ± 0.002
	Γ^*	1.72
	$\mathrm{k}\,T^*_{\mathrm{e}}$ [keV]	399
	$\mathrm{k}\,T^*_{\mathrm{bb}}$ [keV]	0.05
Fe Kα	norm $[\mathrm{Ph\,s^{-1}\,cm^{-2}}]$	$\left(2.27^{+0.13}_{-0.14}\right) \times 10^{-4}$
	E [keV]	$6.394^{+0.005}_{-0.006}$
Fe Kβ	norm $[\mathrm{Ph\,s^{-1}\,cm^{-2}}]^*$	$0.12 \times \mathrm{norm_{Fe\,K\alpha}}$
	E^* [keV]	7.1
$\mathrm{LP_1}$	norm	$6.9^{+1.2}_{-4.9}$
	height $[r_{\mathrm{EH}}]$	$1.1000^{+0.0013}_{-0.0000}$
	$i^\dagger$	3^{+6}_{-0}
	Γ^*	1.72
	$\log\xi$ $[\mathrm{erg\,cm\,s^{-1}}]$	$2.835^{+0.016}_{-0.048}$
	$Z^\dagger_{\mathrm{Fe}}$	$2.5^{+0.6}_{-0.5}$
	$\mathrm{k}\,T^*_{\mathrm{e}}$ [keV]	399
$\mathrm{LP_2}$	norm	$(8 \pm 2) \times 10^{-4}$
	height $[r_{\mathrm{EH}}]$	$14.1^{+3.8}_{-1.9}$
	$i^\dagger$	3^{+6}_{-0}
	Γ^*	1.72
	$\log\xi^\dagger$ $[\mathrm{erg\,cm\,s^{-1}}]$	2.84
	$Z^\dagger_{\mathrm{Fe}}$	$2.5^{+0.6}_{-0.5}$
	$\mathrm{k}\,T^*_{\mathrm{e}}$ [keV]	399
SXCOMP	norm	$(1.33 \pm 0.05) \times 10^{-3}$
	Γ^*	1.72
	$\mathrm{k}\,T^*_{\mathrm{e}}$ [keV]	399
	$\mathrm{k}\,T^*_{\mathrm{bb}}$ [keV]	0.05

heights and a two-fold absorber, composed of a partial-covering and full-covering neutral column. We only observe a tentative correlation between the $\mathrm{LP_2}$-normalization and the column density of $\mathrm{CA_1}$. This correlation is likely not physical but caused by both models describing a similar spectral shape around 6 keV. The additional absorber of highly ionized gas, in contrast, is free of degeneracies with the continuum and can be kept separate throughout the analysis.

The reflection fraction and reflection strength — In our best-fit baseline model for Suz 3, we fit the primary continuum independently from the reflection continua $\mathrm{LP_1}$ and $\mathrm{LP_2}$. The normalizations of the reflection continua have no geometrical interpretation in this case. In other words, this does not allow us to infer the reflection fraction R_{f}, which is defined intrinsically to the LP geometry and corresponds to the ratio of coronal photons incident on the disk to those escaping the system towards the observer (Dauser et al., 2014, 2016). The reflection fraction therefore mainly depends on the effect of light-bending, which is stronger for primary LP sources

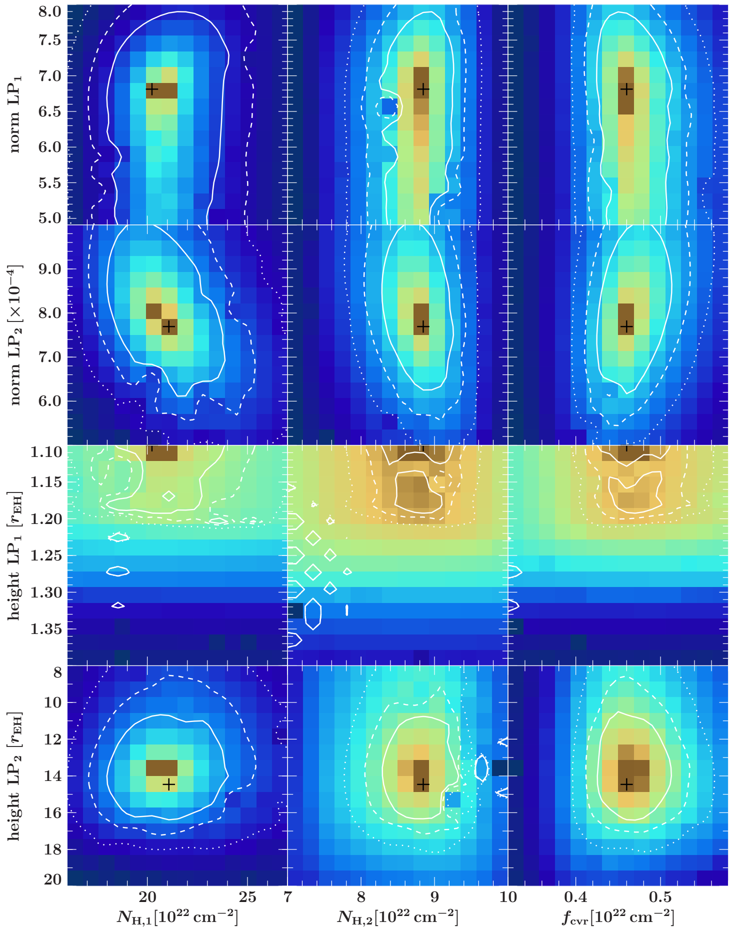

Figure 3.28. $\Delta\chi^2$-maps relating the parameters of the cold absorbers CA$_1$ (partial covering) and CA$_2$ with those of the blurred reflection components LP$_1$ and LP$_2$. We show three contour levels of 68.27%, 90%, and 99% (solid, dashed, and dotted lines).

close to the disk, i.e., predicting larger values of reflection fraction R_{f} (Miniutti et al., 2004). In the following, we use a workaround to find access to the intrinsic reflection fraction for both LP$_1$ and LP$_2$. We re-define the baseline model, remove the independent HXCOMP continuum and thaw R_{f} with `refl_frac`> 0. This model describes the same spectral components but now provides two primary continua instead of one that are intrinsically linked to the reflected continua via the LP geometry, i.e., it allows us to directly fit for R_{f} as a more meaningful parameter.

If we fit for both primary continua and both reflection fractions at a time, we find strong degeneracies and large uncertainties with $N_{\mathrm{LP}_1} = 0.5^{+6.6}_{-0.4}$ and $N_{\mathrm{LP}_2} = \left(1.68^{+0.11}_{-0.84}\right) \times 10^{-3}$ as well as $R_{\mathrm{f}}^{\mathrm{LP}_1} = 14^{+36}_{-13}$ and $R_{\mathrm{f}}^{\mathrm{LP}_2} = 0.43^{+49.58}_{-0.05}$. For that reason, we mutually freeze the reflection fraction of one component to the value predicted for the emission of a point source at the previously determined height above the disk (`fixReflFrac=2`) and fit for the reflection fraction of the other component as well as both normalizations of the primary continua. The results are shown in Table 3.9. In the left column, LP$_2$ is fixed to a predicted reflection fraction of 1.2 for the given height of $h_{\mathrm{LP}_2} = 14.1\,r_{\mathrm{EH}} = 15.0\,r_{\mathrm{g}}$. A fit of the reflection fraction of LP$_1$ is now well constrained as $R_{\mathrm{f}}^{\mathrm{LP}_1} = 1.50 \pm 0.06$, which is rather low with respect to its low height of $h_{\mathrm{LP}_1} = 1.1\,r_{\mathrm{EH}}$ and the therefore predicted fraction of 22.5. This is absorbed by a much larger normalization of LP$_1$ as opposed to LP$_2$, owing to strong degeneracies between these parameters. In the second case, we set the reflection fraction of LP$_1$ to $R_{\mathrm{f}}^{\mathrm{LP}_1} = 22.5$ as predicted for its height $h_{\mathrm{LP}_1} = 1.1\,r_{\mathrm{EH}} = 1.17\,r_{\mathrm{g}}$ and freely fit $R_{\mathrm{f}}^{\mathrm{LP}_2}$. We find a reasonably low reflection fraction of $R_{\mathrm{f}}^{\mathrm{LP}_2} = 0.437 \pm 0.023$ as expected for a primary LP source at larger height. Also, the LP-normalizations do not diverge as strongly as in the case before. We can still demonstrate that degeneracies make it challenging to interpret the reflection fraction as a probe of the LP geometry for the two interacting LP sources.

	free LP_1	free LP_2
norm LP_1	4.59 ± 0.13	0.306 ± 0.011
norm LP_2	$(6.6 \pm 0.4) \times 10^{-4}$	$(1.822 \pm 0.019) \times 10^{-3}$
$R_\mathrm{f}^{\mathrm{LP}_1}$	1.50 ± 0.06	22.5*
$R_\mathrm{f}^{\mathrm{LP}_2}$	1.2*	0.437 ± 0.023
$R_\mathrm{s}^{\mathrm{LP}_1}$	0.69	10.5*
$R_\mathrm{s}^{\mathrm{LP}_2}$	0.64*	0.24
$R_\mathrm{s}^{\mathrm{LP}_2+\mathrm{LP}_2}$		0.68

Table 3.9. Values obtained for reflection fraction R_f, the reflection strength R_s and normalization of the two LP components LP_1 and LP_2. Frozen parameters are denoted by an asterisk (∗).

The reflection fraction cannot simply be inferred from the observed spectra without knowledge of the geometry (Dauser et al., 2014, 2016). In contrast, the reflection strength R_s is defined as the strength of the Compton hump of the reflection model with respect to the primary continuum, that is, the flux-ratio of the reflected to the incident continuum in the 20–40 keV energy band. The derived numbers in Table 3.9 imply a behavior similar to that observed for the reflection fraction. The reflected LP_1-spectrum seems to be too weak with $R_\mathrm{s}^{\mathrm{LP}_1} = 0.69$ compared to the value of 10.5 as predicted by the geometry of a point source very close to the black hole, which is again accounted for by degeneracies between the reflection fraction and the LP-normalizations. In contrast, we find a reasonable value of $R_\mathrm{s}^{\mathrm{LP}_2} = 0.24$ at larger height, featuring a weak Compton hump close to the predicted value of 0.64, predicted for a point source at the given height. The reflection strength of the combination of both LP components is 0.68.

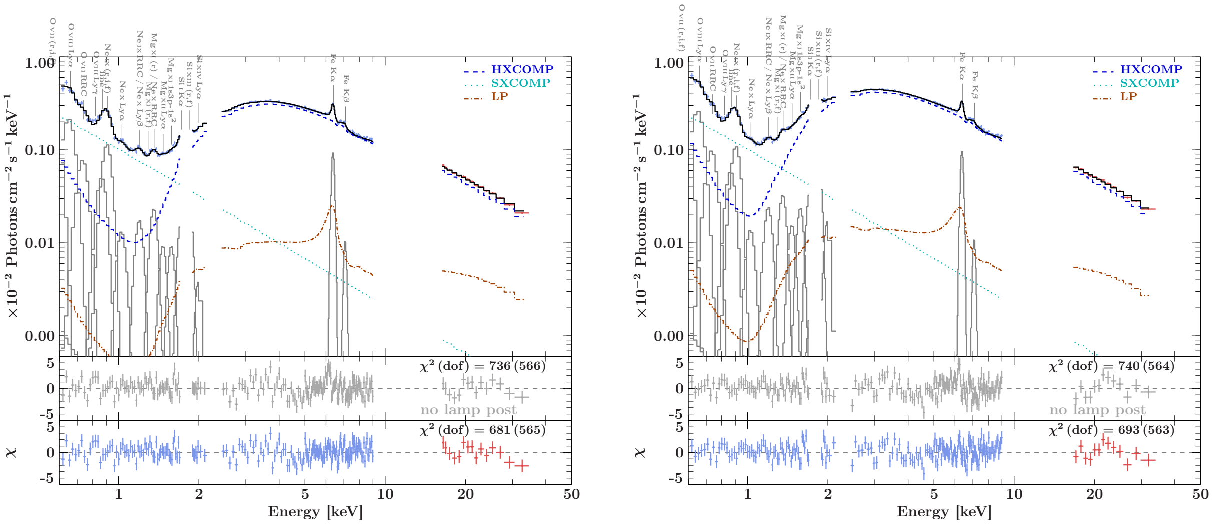

Figure 3.29. Model component plots for Suz 1 *(left)* and Suz 2 *(right)* with the single LP component drawn as brown dotted-dashed line. We also show the absorbed HXCOMP (blue dashed line) and the unabsorbed SXCOMP (cyan dotted line). The soft emission lines (gray) are labeled with their line identifiers. The residuals of *Suzaku*/XIS and *Suzaku*/HXD are drawn in blue and red, respectively.

3.2.3.4 TEST FOR RELATIVISTIC REFLECTION IN OTHER SUZAKU AND XMM-NEWTON OBSERVATIONS

We now have derived a robust baseline model based on the average 150 ks observation by *Suzaku* (Suz 3) and *NuSTAR* (Nu_Suz) that can be applied also to the remaining observations of *Suzaku* and *XMM-Newton*. We again use the original model description with one primary continuum (HXCOMP) that is fitted independently of the reflection continua (see Table 3.8). We re-fit the observations Suz 1 and Suz 2 and freeze all parameters except of the two absorbers CA_1 and

CA_2 and the normalizations of the incident continuum and the narrow Fe Kα and Kβ lines. This approach yields overall good fits except for broad excess residuals in the iron band, indicating deviations from the Suz 3-model and therefore potential variability of the reflection components. A re-fit of the normalizations of the LP continua results in strong degeneracies. When fitting with both LP components switched off, we find the gray residuals shown in Fig. 3.29, arguing for the presence of blurred reflection features via broad features in the iron band. We can, however, demonstrate that the data of Suz 1 and Suz 2 do not allow us to disentangle two emitting sources at different heights.

Given the comparatively large amount of counts for Suz 1 and Suz 2 we attempt to constrain a single LP component with variable height. We find overall good fits (Fig. 3.29, bottom panels). The statistics improve compared to the model lacking relativistic reflection with $\Delta\chi^2 = 55\,(1)$ for Suz 1 and with $\Delta\chi^2 = 47\,(1)$ for Suz 2. The LP heights are fitted with $24^{+7}_{-9}\,r_\mathrm{EH}$ for Suz 1 and $14^{+4}_{-6}\,r_\mathrm{EH}$ for Suz 2. Due to parameter degeneracies we can neither state variability of this single LP-component between Suz 1 and Suz 2, nor between the time-resolved spectra of Suz 2. A direct comparison with the complex and well constrained double-LP source in Suz 3 is not possible either. We suggest, however, that the single component fitted to Suz 1 and Suz 2 may likely be a blend of these components LP_1 and LP_2.

Similar to the *Suzaku* data, the *XMM-Newton* data reveal visible broad features in the iron-band residuals of a fit using the unblurred `xillver` model (Fig. 3.23). Due to the strong degeneracies arising for a free LP height in the models of Suz 1 and Suz 2, we freeze the heights of both LP components to those derived for Suz 3 and only fit the normalizations. Table 3.10 shows that LP_1 is undetected by *XMM-Newton* in contrast to LP_2, where we can constrain its normalization to within ~12–60% with the exception of a very good constraint of ~4% for XMM 5. Together with the *XMM-Newton* data, we report significant variability in normalization for LP_2 over time with a minimum time-scale of 20–30 d. These results demonstrate the need for a decent amount of counts to properly constrain one or even multiple components of relativistically blurred reflection. Else, it is challenging to simultaneously probe the stability of both reflection components, LP_1 and LP_2, over time.

3.2.3.5 SPECTRAL VARIABILITY PROBED WITH SUZAKU AND XMM-NEWTON

Table 3.10. Summary of all *XMM-Newton*-related model parameter that are free to vary. The normalization of the Comptonized continua HXCOMP and SXCOMP are defined as unity if the norm equals to one at 1 keV. Parameters that are marked with an asterisk (∗) are frozen to the parameters found for the long-look observation Suz 3.

		XMM 1	XMM 2	XMM 3	XMM 4	XMM 5	XMM 6	XMM 7
Detconst	pn	1*	1*	1*	1*	1*	1*	1*
	MOS 1	–	1.29 ± 0.02	1.24 ± 0.02	1.27 ± 0.03	1.27 ± 0.03	1.27 ± 0.06	$1.43^{+0.05}_{-0.04}$
	MOS 2	–	1.28 ± 0.02	1.28 ± 0.02	1.29 ± 0.03	1.33 ± 0.04	1.32 ± 0.06	$1.32^{+0.03}_{-0.02}$
HXCOMP	norm	$0.037^{+0.006}_{-0.007}$	0.0645 ± 0.0007	$0.061^{+0.004}_{-0.005}$	$0.077^{+0.005}_{-0.007}$	$0.035^{+0.003}_{-0.006}$	$0.055^{+0.007}_{-0.014}$	$0.059^{+0.004}_{-0.005}$
SXCOMP	norm	$\left(1.34^{+0.16}_{-0.24}\right) \times 10^{-3}$	$\left(1.42^{+0.06}_{-0.32}\right) \times 10^{-3}$	$(9.3 \pm 3.0) \times 10^{-4}$	$\left(1.36^{+0.10}_{-0.27}\right) \times 10^{-3}$	$\left(1.10^{+0.07}_{-0.04}\right) \times 10^{-3}$	$\left(1.3^{+0.2}_{-0.4}\right) \times 10^{-3}$	$\left(1.15^{+0.00}_{-0.05}\right) \times 10^{-3}$
LP 1	norm	≤ 10	≤ 0.4	≤ 2	≤ 3	≤ 3	≤ 6	≤ 2
	height [r_{EH}]	1.1*	"	"	"	"	"	"
LP 2	norm	$\left(1.6^{+1.1}_{-0.9}\right) \times 10^{-3}$	$(1.06 \pm 0.13) \times 10^{-3}$	$(1.1 \pm 0.5) \times 10^{-3}$	$(2.2 \pm 0.6) \times 10^{-3}$	$\left(6.7^{+3.6}_{-1.0}\right) \times 10^{-4}$	$(9 \pm 7) \times 10^{-4}$	$\left(1.85^{+0.42}_{-0.13}\right) \times 10^{-3}$
	height [r_{EH}]	14.1*	"	"	"	"	"	"
CA_1	$N_{\mathrm{H,int}}$ [$10^{22}\,\mathrm{cm}^{-2}$]	25^{+12}_{-8}	$11.8^{+0.8}_{-0.7}$	14 ± 2	17 ± 4	$25.3^{+1.9}_{-5.1}$	26^{+10}_{-7}	$12.3^{+1.4}_{-2.4}$
	$\mathrm{f}_{\mathrm{cvr}}$	0.46*	"	"	"	"	"	"
CA_2	$N_{\mathrm{H,int}}$ [$10^{22}\,\mathrm{cm}^{-2}$]	$12.4^{+1.6}_{-0.8}$	$6.80^{+0.11}_{-0.26}$	5.9 ± 0.3	$12.8^{+0.5}_{-0.6}$	$15.6^{+0.4}_{-0.7}$	$9.2^{+0.6}_{-0.7}$	$9.05^{+0.17}_{-0.35}$
Fe Kα	norm [$\mathrm{Ph\,s^{-1}\,cm^{-2}}$]	$\left(2.4^{+0.7}_{-0.8}\right) \times 10^{-4}$	$\left(2.0^{+0.6}_{-0.4}\right) \times 10^{-4}$	$(2.5 \pm 0.6) \times 10^{-4}$	$\left(2.3^{+0.8}_{-0.7}\right) \times 10^{-4}$	$\left(2.8^{+0.2}_{-0.4}\right) \times 10^{-4}$	$\left(2.7^{+0.4}_{-0.9}\right) \times 10^{-4}$	$\left(1.650^{+0.621}_{-0.005}\right) \times 10^{-4}$
	E [keV]	6.4*	"	"	"	"	"	"
XSTAR 1	N_{H} [$10^{22}\,\mathrm{cm}^{-2}$]	$\left(6^{+34}_{-6}\right) \times 10^{21}$	$(1.2 \pm 0.7) \times 10^{22}$	$\left(1.2^{+1.4}_{-1.2}\right) \times 10^{22}$	$\left(3.2^{+2.6}_{-1.8}\right) \times 10^{22}$	$\leq 8.5 \times 10^{21}$	$\left(1.9^{+2.8}_{-1.8}\right) \times 10^{22}$	$\leq 9.5 \times 10^{21}$

Table 3.11. Summary of all *Suzaku*-related model parameter that are left free to vary. The normalization of the Comptonized continua HXCOMP and SXCOMP are defined as unity if the norm equals to one at 1 keV. Parameters that are marked with an asterisk (∗) are frozen to the parameters found for the long-look observation Suz 3.

		Suz 1	Suz 2	Suz 2-1	Suz 2-2	Suz 3	Suz 3-1	Suz 3-2	Suz 3-3	Suz 3-4
Detconst	XIS 0	1*	1*	1*	1*	0.998 ± 0.005	$1.076^{+0.019}_{-0.018}$	1.010 ± 0.010	$0.961^{+0.008}_{-0.007}$	0.957 ± 0.008
Detconst	XIS 1	1.017 ± 0.006	1.032 ± 0.006	0.949 ± 0.009	1.047 ± 0.006	0.954 ± 0.005	$1.043^{+0.019}_{-0.017}$	1.000 ± 0.011	0.910 ± 0.007	0.923 ± 0.008
	XIS 3	0.995 ± 0.006	0.975 ± 0.006	0.977 ± 0.009	$0.986^{+0.006}_{-0.005}$	1.012 ± 0.005	$1.113^{+0.020}_{-0.018}$	1.053 ± 0.011	0.997 ± 0.008	$0.993^{+0.009}_{-0.008}$
	HXD	1.30 ± 0.02	1.29 ± 0.02	1.32 ± 0.03	1.09 ± 0.04	1.215 ± 0.009	1.35 ± 0.03	$1.239^{+0.019}_{-0.018}$	1.186 ± 0.013	1.197 ± 0.014
	FPMA	–	–	–	–	1*	1*	1*	1*	1*
	FPMB	–	–	–	–	1.030 ± 0.004	1.05 ± 0.02	0.998 ± 0.007	1.039 ± 0.005	1.039 ± 0.007
HXCOMP	norm	0.0698 ± 0.0013	0.0726 ± 0.0012	0.072 ± 0.002	$0.055^{+0.007}_{-0.004}$	0.047 ± 0.002	$0.0406^{+0.0012}_{-0.0010}$	0.0481 ± 0.0005	0.0445 ± 0.0004	0.0509 ± 0.0005
SXCOMP	norm	1.33×10^{-3} *	"	"	"	$(1.33 \pm 0.05) \times 10^{-3}$	"	"	"	"
LP_1	norm	$\left(5.3^{+1.4}_{-1.2}\right) \times 10^{-4}$	$\left(7.1^{+2.8}_{-1.9}\right) \times 10^{-4}$	$\left(6^{+4}_{-3}\right) \times 10^{-4}$	$0.4^{+0.4}_{-0.3}$	$6.9^{+1.2}_{-4.9}$	"	"	"	"
	height [r_{EH}]	24^{+9}_{-7}	14^{+6}_{-4}	14^{+10}_{-6}	$1.53^{+6.31}_{-0.15}$	$1.1000^{+0.0013}_{-0.0000}$	"	"	"	"
LP_2	norm	–	–	–	–	$(8 \pm 2) \times 10^{-4}$	"	"	"	"
	height [r_{EH}]	–	–	–	–	$14.1^{+3.8}_{-1.9}$	"	"	"	"
CA_1	$N_{\mathrm{H,int}}$ [$10^{22}\,\mathrm{cm}^{-2}$]	13^{+3}_{-2}	$9.2^{+1.5}_{-1.1}$	12^{+6}_{-4}	$5.6^{+1.6}_{-0.9}$	21^{+4}_{-3}	$13.7^{+4.8}_{-1.8}$	$12.2^{+2.3}_{-1.4}$	$24.2^{+1.9}_{-1.7}$	$15.7^{+2.1}_{-1.4}$
	$\mathrm{f}_{\mathrm{cvr}}$	$0.46^{+0.11}_{-0.10}$	0.45 ± 0.06	$0.33^{+0.13}_{-0.08}$	$0.49^{+0.09}_{-0.10}$	$0.46^{+0.06}_{-0.05}$	$0.57^{+0.13}_{-0.18}$	0.57 ± 0.14	0.51 ± 0.04	0.57 ± 0.09
CA_2	$N_{\mathrm{H,int}}$ [$10^{22}\,\mathrm{cm}^{-2}$]	$6.9^{+0.7}_{-0.8}$	4.4 ± 0.3	$5.3^{+0.4}_{-0.6}$	3.9 ± 0.3	$8.8^{+0.5}_{-0.6}$	$7.7^{+1.6}_{-1.3}$	$7.3^{+1.2}_{-1.4}$	$9.1^{+0.5}_{-0.6}$	$7.7^{+0.9}_{-1.0}$
Fe Kα	norm [$\mathrm{Ph\,s^{-1}\,cm^{-2}}$]	$(2.4 \pm 0.2) \times 10^{-4}$	$(2.5 \pm 0.2) \times 10^{-4}$	$(2.8 \pm 0.3) \times 10^{-4}$	$\left(2.70^{+0.16}_{-0.14}\right) \times 10^{-4}$	$\left(2.27^{+0.13}_{-0.14}\right) \times 10^{-4}$	$\left(2.00^{+0.22}_{-0.18}\right) \times 10^{-4}$	$\left(1.75^{+0.16}_{-0.11}\right) \times 10^{-4}$	$\left(2.35^{+0.16}_{-0.09}\right) \times 10^{-4}$	$(2.31 \pm 0.14) \times 10^{-4}$
	E [keV]	6.394*	"	"	"	$6.394^{+0.005}_{-0.006}$	"	"	"	"
XSTAR 1	N_{H} [$10^{22}\,\mathrm{cm}^{-2}$]	1.22×10^{22}	"	"	"	$(1.2 \pm 0.3) \times 10^{22}$	"	"	"	"

As

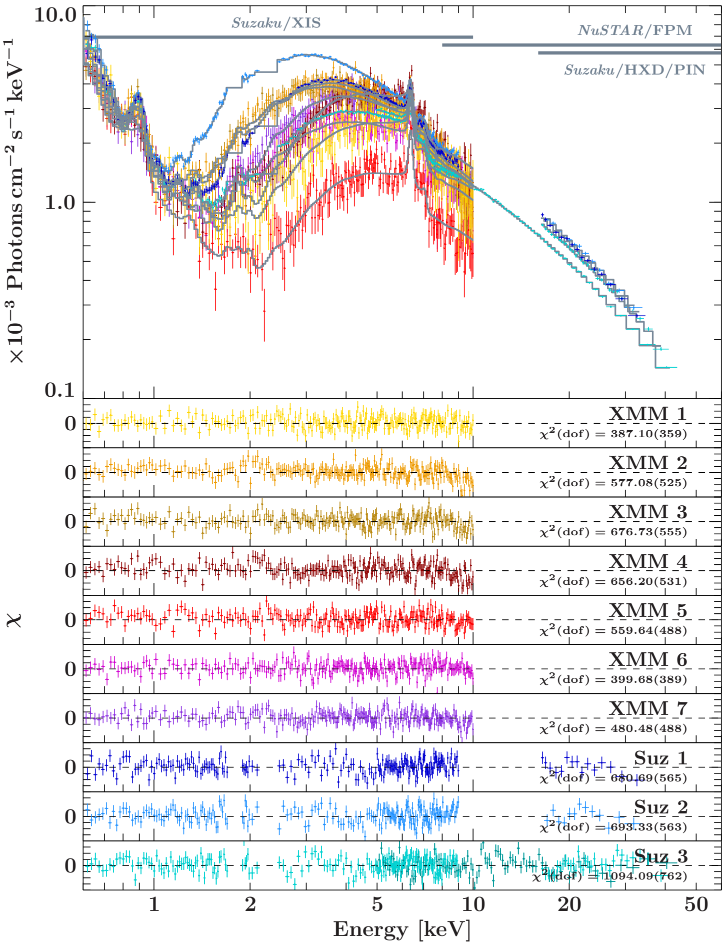

Figure 3.30. Composite of all *XMM-Newton* and *Suzaku* spectra as well as one *NuSTAR* spectrum simultaneous to Suz 3 with the applied best-fit baseline model and residuals. The statistics of each fit are listed in the residual panels. The minor residual ticmarks are separated by 0.1.

we have shown in Sect. 3.2.3, NGC 4151 shows significant spectral variability between 1 and 6 keV, which we will focus on in the following. We consider all *XMM-Newton*, *Suzaku*, and *NuSTAR* observations between 2011 and 2012 including the time-resolved observations Suz $2_{\mathrm{A,B}}$ as well as Suz $3_{\mathrm{A-D}}$ and $\mathrm{Nu}_{\mathrm{Suz,A-D}}$. To address the variability of the spectral components, we apply the baseline model and allow only a few parameters to vary. Besides the cross-normalizing detector constants and the flux normalizations of the model components, these are $N_{\mathrm{H},1}$, $N_{\mathrm{H},2}$, and the covering fraction f_{cvr} of CA 1. We detect strong degeneracies between $N_{\mathrm{H},1}$ and f_{cvr} for *XMM-Newton* data and therefore fix the covering fraction to the weighted mean with respect to the observations Suz 1, Suz 2, and Suz 3, which all lie very closely to $f_{\mathrm{cvr}} = 0.46$. Note that the SXCOMP normalization is kept frozen to the value derived for Suz 3 for all *Suzaku* observations but allowed to vary for *XMM-Newton*. The derived values are, however, consistent with the frozen value.

The baseline model fits well to all observations with only the few above mentioned free parameters. All parameters and uncertainties are listed in the Tables 3.10 and 3.11. Figure 3.30 shows all spectra with overlaid fits in the top panel and residuals in the bottom panels. Most previous studies have found the X-ray emission below ∼1–2 keV to be non-variable (e.g., Yang et al., 2001; de Rosa et al., 2007); Landt et al. (2015) report on weakly-variable coronal O VII emission. In contrast, Wang et al. (2010) find evidence for significant variability of the soft continuum. Our multiple observations yield 0.6–1.0 keV fluxes that remain within ∼6% of each[11] but underlie large uncertainties. This range contrasts with ∼20% variability for the 7–10 keV flux of the incident HXCOMP continuum. We find no direct correlation between the SXCOMP and HXCOMP variability. We can also exclude correlated variability between the Ne IX emission

---

[11] The amount of variability is calculated as the standard deviation over the average.

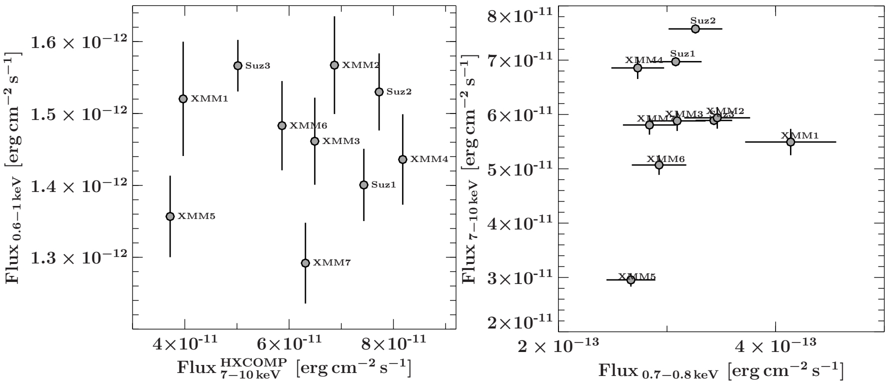

Figure 3.31. *Left:* Soft X-ray 0.6–1 keV energy flux over the 7–10 keV unabsorbed energy flux of the HXCOMP. *Right:* Hard X-ray 7–10 keV energy flux over the 0.7–0.8 keV energy flux enclosing Ne IX emission.

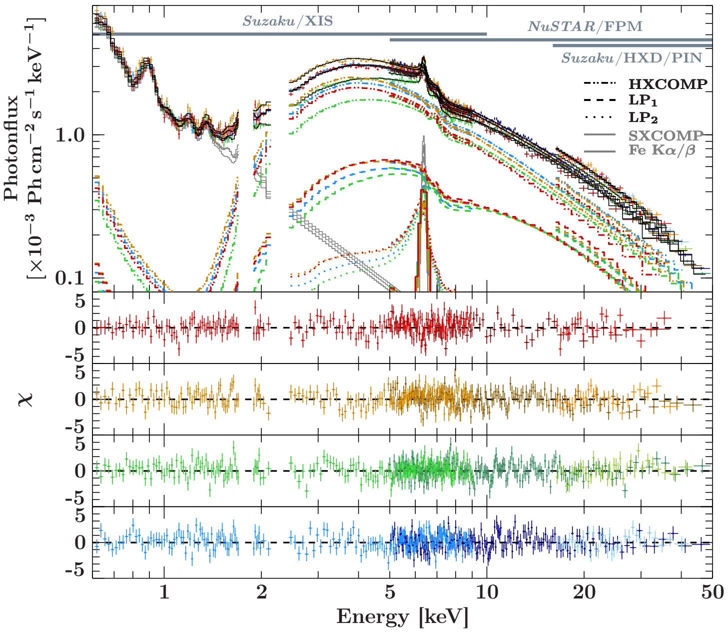

Figure 3.32. Time-resolved spectra of Suz 3_{A}–Suz 3_{D} / $\mathrm{Nu}_{\mathrm{Suz,A}}$–$\mathrm{Nu}_{\mathrm{Suz,D}}$ with the best-fit model components HXCOMP (double-dotted dashed line), LP_1 (dashed line), LP_2 (dotted line) and SXCOMP (solid line). The spectra A–D are drawn in red, orange, green and blue, respectively.

line and the incident 7–10 keV flux (see Fig. 3.31). Within the statistical uncertainties, the Ne IX line flux remains constant over the probed timescale. Due to the CCD resolution of our spectra and the blend of emission lines, it is not clear if the weak flux variability within 0.6 and 1.0 keV is due to soft continuum, the Ne IX flux, or both. The narrow Fe Kα/β line, in contrast, is stable over the monitored time interval.

We find significant absorption variability with column density changes of a maximum of 50% for CA_1 and 20% for CA_2. Spectral variability is not only found between single observations but also within the 150 ks-long observation Suz 3 as we show in Fig. 3.32. This figure shows the time-resolved spectra for the four individual observations Suz $3_{\mathrm{A-D}}$ with the absorbed continuum model components HXCOMP, SXCOMP, LP_1, LP_2, and the Fe Kα/β lines.

The evolution of the parameters of both neutral absorbers and the incident HXCOMP is shown in Fig. 3.33. We find overall larger columns $N_{\mathrm{H},1}$ but smaller uncertainties for the partial coverer than for the full-covering column $N_{\mathrm{H},2}$. Both columns $N_{\mathrm{H},1}$ ($N_{\mathrm{H},2}$) seem to show correlated variability over time with an initial decline around MJD 55900 followed by an increase between MJD 56080 and MJD 56200 and a subsequent decline after MJD 56240 back down to a baseline-level of $N_{\mathrm{H},1}$ ($N_{\mathrm{H},2}$) $\sim 12\,(9) \times 10^{22}\,\mathrm{cm}^{-2}$. The normalizations of the primary continuum (HXCOMP) can be shown to be variable down to a time-scale of ∼20 d over a normalization range of ~ 0.03–$0.08\,\mathrm{Photons\,cm^{-2}\,s^{-1}}$ at 1 keV. The time-resolved measurements for Suz 2 and Suz 3 strengthen the presence of variability of these parameters on time-scales as short as days. This remains true even though the uncertainties of the parameters found for Suz $2_{\mathrm{A,B}}$ are larger

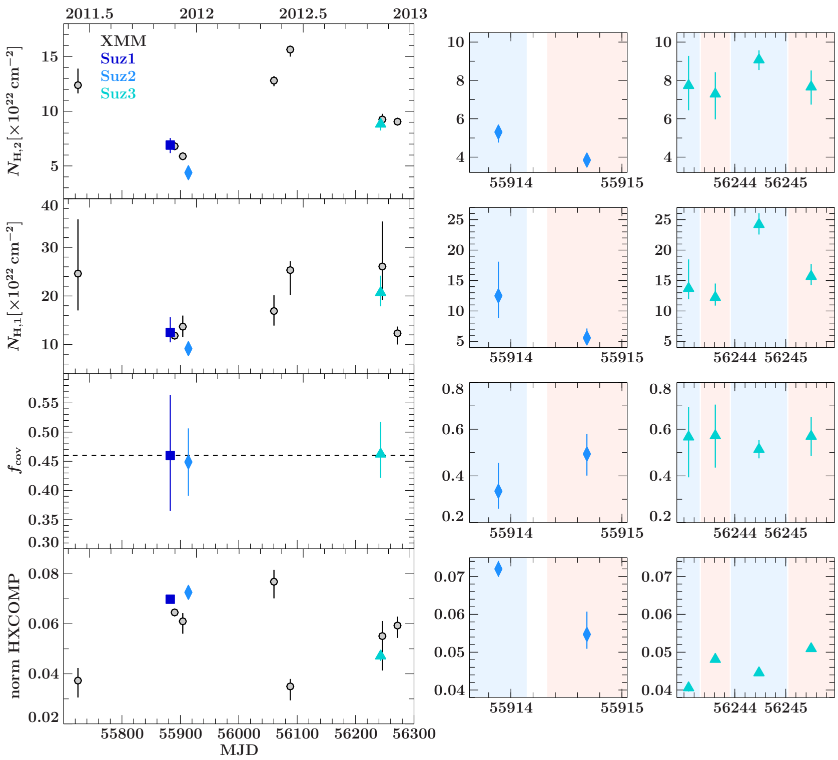

Figure 3.33. *Left:* Evolution of the free parameters related to the two absorbers and the normalization of the HXCOMP continuum. We show parameters fitted to *XMM-Newton* (gray) and the average *Suzaku* spectra Suz 1, Suz 2, and Suz 3 (blue, light-blue, and turquoise). *Right:* parameter evolution of the time-resolved spectra of the *Suzaku* observations Suz 2 (light-blue) and Suz 3 (turquoise). The shaded regions correspond to those from Fig. 3.21.

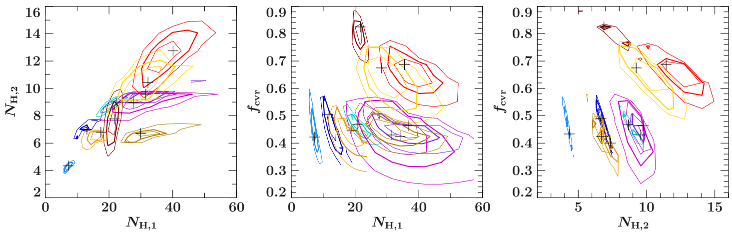

Figure 3.34. Contours related to the two absorbers CA_1 and CA_2. The colors are the same used in Fig. 3.22 and Fig. 3.30 and correspond to the different observations. The best-fit parameters are indicated as black crosses.

compared to those inferred from the spectra Suz $3_{\mathrm{A-D}}$. The covering fraction is constant within the uncertainties. The same applies to the time-resolved results of Suz $3_{\mathrm{A-D}}$, where we find covering fractions scattering around 0.55. This value is slightly larger than that derived for the total observation Suz 3, which can be attributed to model degeneracies. The columns $N_{\mathrm{H},1}$ and $N_{\mathrm{H},2}$ peak during the observation Suz 3_{D} and cover a dynamic range of $N_{\mathrm{H},1}$ ($N_{\mathrm{H},2}$) $\sim$ 13–25 (6–10) $\times\,10^{22}\,\mathrm{cm}^{-2}$. The primary continuum, in contrast, shows a more complex variability pattern with normalizations between $0.04\,\mathrm{Ph\,keV^{-1}\,s^{-1}\,cm^{-2}}$ and $0.05\,\mathrm{Ph\,keV^{-1}\,s^{-1}\,cm^{-2}}$.

The correlated variability between CA_1 and CA_2 on all probed time-scales can likely be attributed to degeneracies arising between both absorbers (Fig. 3.34) that cover similar columns. We probably also observe systematics related to the complexity of the dual absorber and to the assumptions made for the baseline model. According to these results, we can therefore not claim the observed variability to be inherent in one or the other absorber. In contrast, both contributing absorbers are likely well separated by the single 150 ks-long observation Suz 3 (see Fig. 3.28). We further observe an anticorrelation between the 7 and 10 keV flux of the pre-absorbed HXCOMP continuum and both columns $N_{\mathrm{H},1}$ and $N_{\mathrm{H},2}$, which is highlighted in Fig. 3.35. This relation is stronger for CA_1 with the Pearson correlation coefficient $r_{\mathrm{P,CA_1}} = 77\%$ and a low p-value of $P_{\mathrm{P,CA_1}} = 0.8\%$ as compared to CA_2 with $r_{\mathrm{P,CA_2}} = 60\%$ and $P_{\mathrm{P,CA_2}} = 7.2\%$.

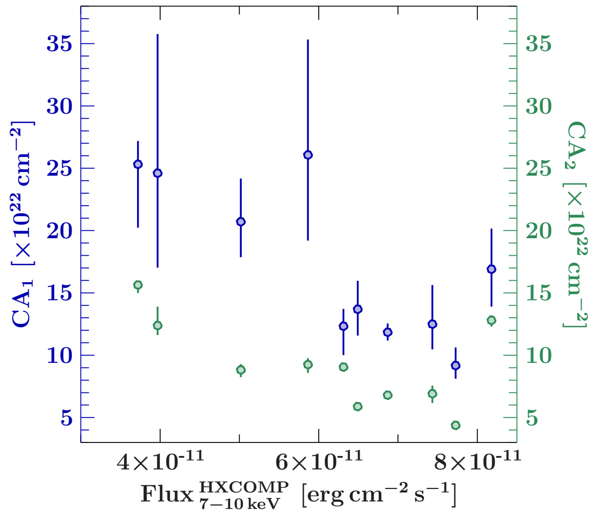

Figure 3.35. Anticorrelation of the normalization of the irradiating flux (HXCOMP) with the column densities of the absorbers CA$_1$ (blue) and CA$_2$ (green).

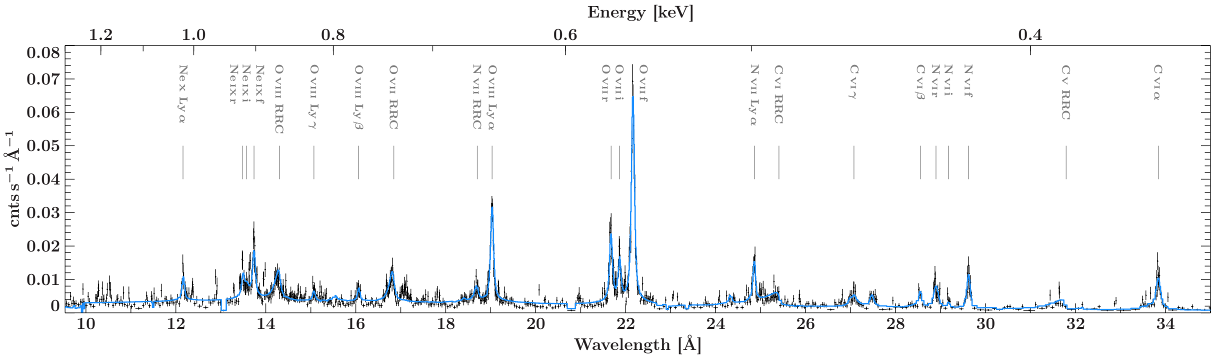

Figure 3.36. Combined count spectrum including all *XMM-Newton*/RGS observations, each with two diffraction orders for each of the two RGS detectors RGS1 and RGS2. The line model is overlaid in blue, the residuals are shown in the bottom panel. The identifiers of the fitted emission lines are shown on top of vertical lines at the corresponding wavelengths.

3.2.3.6 THE SOFT X-RAYS AND THE NLR

NGC 4151 and its ionized environment have been the subject of a number of studies that combine high spectral and spatial resolution (e.g., Wang et al., 2011a, and references therein). In Sect. 3.2.3.3, we motivate the description of the soft X-rays below 2 keV with the SXCOMP continuum, which is complemented with a blend of Gaussian emission lines that have been measured to persist over decades (see also Ogle et al., 2000; Yang et al., 2001; Schurch et al., 2004; Wang et al., 2011a). While Perola et al. (1986), Weaver et al. (1994a), Weaver et al. (1994b), Warwick et al. (1995) and Wang et al. (2010) detect no signs of major variability in the soft X-rays, we find tentative signs of variability at a low dynamic range in Sect. 3.2.3.5. As the S/N of individual RGS spectra are too low for measuring line fluxes over time, we combine the *XMM-Newton*/RGS data of all observations ranging over more than 1.5 years. The resulting spectrum reveals a series of highly significant emission lines, dominated by the H-like and He-like ions O VIII, O VII, and Ne IX (Fig. 3.36) on top of the weak SXCOMP continuum. The emission lines are modeled with Voigt profiles. Whenever the S/N of a line-feature is too low to constrain its centroid energy, we use the values from Vainshtein & Safronova (1978) as starting parameters. Additional radiative recombination continua (RRC) are described with the `redge` model[12]. The model is simultaneously fitted to all observations with the resulting parameters listed in Table 3.12. The centroid energies of all fitted lines are consistent with

---

[12] `https://heasarc.gsfc.nasa.gov/xanadu/xspec/manual/`

Table 3.12. Line parameters of Voigt profiles fitted to the combined RGS data of all *XMM-Newton* observations as part of the monitoring. Where the S/N of the data is not sufficient to fit for the line energy, we adopt the centroid energies from Schurch et al. (2004), Ogle et al. (2000) and Vainshtein & Safronova (1978) when marked with an asterisk (∗).

Line	E [keV]	FWHM [keV]	$k_\mathrm{B}\,T$ [keV]	flux [Ph s^{-1} cm^{-2}]
C VI α	0.36637 ± 0.00008	$\left(4.3^{+1.8}_{-1.5}\right) \times 10^{-3}$	–	$\left(2.65^{+0.30}_{-0.28}\right) \times 10^{-4}$
C V RRC	$0.3901^{+0.0004}_{-0.0005}$	–	$\left(4.4^{+1.4}_{-1.0}\right) \times 10^{-3}$	$\left(1.92^{+0.29}_{-0.26}\right) \times 10^{-4}$
N VI f	0.41855 ± 0.00009	$\leq 1.5 \times 10^{-3}$	–	$\left(1.35^{+0.16}_{-0.15}\right) \times 10^{-4}$
N VI i	0.4250 ± 0.0004	$\leq 6 \times 10^{-3}$	–	$\left(2.4^{+3.3}_{-2.4}\right) \times 10^{-5}$
N VI r	0.42909 ± 0.00015	$\left(8^{+30}_{-8}\right) \times 10^{-4}$	–	$\left(9.6^{+1.6}_{-1.5}\right) \times 10^{-5}$
C VI β	0.43423 ± 0.00020	$\left(7^{+50}_{-7}\right) \times 10^{-4}$	–	$\left(3.6^{+1.4}_{-3.6}\right) \times 10^{-5}$
C VI γ	$0.45796^{+0.00026}_{-0.00021}$	$\leq 4.8 \times 10^{-2}$	–	$\left(3.5^{+0.5}_{-3.5}\right) \times 10^{-6}$
C VI RRC	$0.4875^{+0.0005}_{-0.0006}$	–	$0.010^{+0.000}_{-0.005}$	$\left(1.53^{+0.20}_{-0.41}\right) \times 10^{-4}$
N VII Ly α	$0.49874^{+0.00015}_{-0.00008}$	$\leq 2.1 \times 10^{-2}$	–	$\left(1.6^{+0.5}_{-1.6}\right) \times 10^{-3}$
O vii f	0.55946	2.5×10^{-3}	–	4.5×10^{-4}
O vii i	0.56702	2.7×10^{-3}	–	7.9×10^{-5}
O vii r	0.57200	2.6×10^{-3}	–	1.3×10^{-4}
O VIII Ly α	$0.65158^{+0.00013}_{-0.00011}$	$\left(3.4^{+2.1}_{-1.8}\right) \times 10^{-3}$	–	$\left(1.58^{+0.11}_{-0.12}\right) \times 10^{-4}$
N VII RRC	$0.6629^{+0.0004}_{-0.0007}$	–	$\left(10^{+1.2}_{-0}\right) \times 10^{-3}$	$\left(2.5^{+0.6}_{-0.5}\right) \times 10^{-5}$
O VII RRC	0.7366 ± 0.0005	–	$\left(3.0^{+0.8}_{-0.7}\right) \times 10^{-3}$	$(5.5 \pm 0.7) \times 10^{-5}$
O VIII Ly β	0.7723 ± 0.0006	$\leq 4.5 \times 10^{-3}$	–	$\left(1.6^{+0.5}_{-0.4}\right) \times 10^{-5}$
O VIII Ly γ	0.8228 ± 0.0008	$\leq 6.3 \times 10^{-2}$	–	$0.094^{+0.007}_{-0.094}$
O VIII RRC	$0.8677^{+0.0008}_{-0.0010}$	–	$\left(4.0^{+1.9}_{-1.4}\right) \times 10^{-3}$	$\left(4.2^{+0.7}_{-0.6}\right) \times 10^{-5}$
Ne ix f	0.9024	$\leq 6 \times 10^{-3}$	–	5.8×10^{-5}
Ne ix i	0.9132	0.041	–	2.2×10^{-5}
Ne ix r	0.9191	$\leq 9 \times 10^{-3}$	–	2.4×10^{-5}
Ne X Ly α	1.0192 ± 0.0006	$\leq 9 \times 10^{-3}$	–	$\left(2.7^{+0.5}_{-1.1}\right) \times 10^{-5}$
Continuum	Γ	norm [Ph keV^{-1} s^{-1} cm^{-2}]		
	1.72^{*}	$(1.33 \pm 0.05) \times 10^{-3\,*}$		

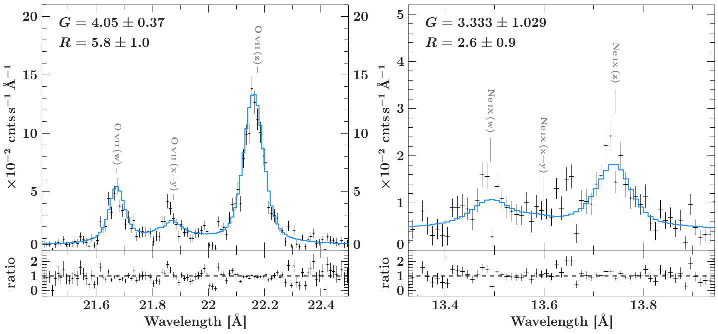

Figure 3.37. Enlarged view onto the bands of the He-like triplets of the ions O VII (*left*) and Ne IX (*right*). For both, we show unbinned data from the first diffraction order combined out of all observations. The model corresponds to the parameters listed in Tables 3.12 and 3.13.

those derived earlier, e.g., by Ogle et al. (2000) or Schurch et al. (2004). The poor constraints on the width and the turbulent velocities arise at the cost of the choice of the Voigt profile as physically motivated description of the emission lines, coming along with more free parameters than a Gaussian approximation. Despite these increased uncertainties, the Voigt profile shape is statistically required by the most prominent lines. In contrast, we can roughly constrain the plasma temperatures of the prominent RRC features.

The data also show prominent O VII and Ne IX triplets at ∼0.56 keV (22 Å) and ∼0.91 keV (13.5 Å), respectively (Fig. 3.37). Both are statistically best described by Voigt profiles. We list the parameter constraints in Table 3.13. In addition to the statistical uncertainties, we also assume non-vanishing systematical uncertainties for the fit of the hardly detected resonance and intercombination lines of Ne IX.

Both triplets consist of a resonance (w), an intercombination ($x + y$) and a forbidden line (z), while the intercombination line is a blend of the two individual lines x and y. Relating the

Line	E [keV]	FWHM [keV]	flux [$\mathrm{Ph\,s^{-1}\,cm^{-2}}$]
O VII w	$0.57200^{+0.00013}_{-0.00006}$	$\left(2.6^{+0.5}_{-1.1}\right) \times 10^{-3}$	$\left(1.30^{+0.13}_{-0.10}\right) \times 10^{-4}$
O VII x+y	$0.56702^{+0.00022}_{-0.00007}$	$\left(2.7^{+1.7}_{-0.8}\right) \times 10^{-3}$	$\left(7.9^{+1.8}_{-0.7}\right) \times 10^{-5}$
O VII z	$0.55946^{+0.00005}_{-0.00006}$	$\left(2.5^{+0.6}_{-0.5}\right) \times 10^{-3}$	$\left(4.51^{+0.15}_{-0.13}\right) \times 10^{-4}$
Ne IX w	$0.9191^{+0.0007}_{-0.0006}$	$\leq 9 \times 10^{-3}$	$\left(2.4^{+0.5}_{-0.9}\right) \times 10^{-5}$
Ne IX x+y	$0.9132^{+0.0013}_{-0.0015}$	≤ 0.041	$\left(2.2^{+0.8}_{-0.7}\right) \times 10^{-5}$
Ne IX z	0.9024 ± 0.0004	$\leq 6 \times 10^{-3}$	$(5.8 \pm 0.6) \times 10^{-5}$

Table 3.13. Triplet line parameters of the ions O VII and Ne IX. Both lines are described with Voigt profiles. The thermal velocities are unconstrained and not listed in the table. The continuum parameters are frozen to those of the SXCOMP.

strengths of these lines can be used as a powerful diagnostic for the density and temperature of the emitting gas (Gabriel & Jordan, 1969; Porquet & Dubau, 2000; Bautista & Kallman, 2000). The ratio $R = z/(x + y)$ is sensitive to the gas density in that the rate of collisions increases with n^2 and therefore suppressing the forbidden line emission. The ratio $G = (z + x + y)/w$, in turn, is sensitive to the temperature, which positions the gas between being dominated by collisions or recombination. A hot plasma gives rise to collisions and therefore a strong resonance line, that is, small values of G. For larger values of $G \gtrsim 4$, the plasma is dominated by recombination and the triplet levels with the intercombination and forbidden line have large statistical weight, therefore featuring a plasma dominated by photoionization. For both He-like ions the ratios are well consistent with those derived using *XMM-Newton*/RGS by Armentrout et al. (2007). For O VII the ratios ($G = 4.05 \pm 0.37$ and $R = 5.8 \pm 1.0$) indicate gas dominated by photoionization. These ratios imply a low gas temperature of $T_\mathrm{e} \lesssim 10^5\,\mathrm{K}$, which is consistent with that obtained from the narrow RRC features. In contrast to Schurch et al. (2004), who find a moderate R-ratio of 3.9, our value is more consistent with that measured by Landt et al. (2015), arguing for a gas of low density with $n_\mathrm{e} \sim 10^3\,\mathrm{cm}^{-3}$. We detect a strong resonance line for Ne IX, resulting in a low G-ratio of 3.333 ± 1.029 and R-ratio of 2.6 ± 0.9. This result implies a hybrid plasma (e.g., Porquet & Dubau, 2000; Bautista & Kallman, 2000), likely in pressure equilibrium with a collisionally ionization gas phase (Wang et al., 2011a). The temperature ($\sim 10^6\,K$) and density (a few $\times 10^{11}\,\mathrm{cm}^{-3}$) are estimated to be significantly higher compared to the O VII gas. Again, the results are overall consistent with earlier work (Schurch et al., 2004; Armentrout et al., 2007; Ogle et al., 2000; Wang et al., 2011a). The suppression of the forbidden line of Ne IX and therefore the R-ratio can alternatively arise from a strong UV field, where photoionization is still dominant (Mewe & Schrijver, 1978).

3.2.4 DISCUSSION

This section is taken in verbatim from Beuchert et al. (2017). Extending earlier work by Keck et al. (2015) by including soft X-ray data, here we re-investigated data from the joint *Suzaku*/*NuSTAR* campaign of NGC 4151. The resulting broad energy coverage and the use of the LP model `relxillCP_lp` allowed us to disentangle complex and variable absorption from blurred disk reflection originating in the regime of strong gravity. We described the blurred reflection with two LP components at different heights, while the bulk of the 1–6 keV continuum absorption was attributed to an absorber consisting of partial- and full-absorbing components. We also detected narrow absorption features that can be modeled with a highly ionized ($\log \xi \sim 2.8$) warm absorber and an additional absorption line indicating an UFO. The soft emission was modeled with a SXCOMP scattering continuum and a number of emission lines that are identified with *XMM-Newton*/RGS.

3.2.4.1 Size of the corona and pair production

Our baseline model encompasses two point-like primary LP sources at the heights of $1.2\,r_\mathrm{g}$ and $15.0\,r_\mathrm{g}$, which result in strongly and moderately blurred spectral reflection components (see also Keck et al., 2015). Individual studies, e.g., by Dauser et al. (2012), Parker et al. (2014), and Fink et al. (2017, in prep.) apply the model `relxill_lp` and confirm the need for low source heights between ∼2 and $4 r_\mathrm{g}$ and compact coronae to explain the observed spectra. This has been independently confirmed by simulations of Svoboda et al. (2012) as well as reverberation studies (Fabian et al., 2009; Zoghbi et al., 2010, for 1H 0707−495). In the following we discuss the implications and limitations of this solution.

For the moment, we assume two distinct emission regions as they result from our modeling. As outlined in Sect. 1.2.3.2, Dovčiak & Done (2016) provide estimates on the spatial extent of spherical coronae depending on their height above the BH for an observed luminosity of $L_\mathrm{X,obs}^{0.3-10\,\mathrm{keV}} = 0.001\,L_\mathrm{Edd}$ and a photon index of $\Gamma = 2$. The models fitted to the *XMM-Newton*, *Suzaku* and *NuSTAR* data examined in this work imply the incident power law to have a mean observed luminosity of $L_\mathrm{X,obs}^{0.3-10\,\mathrm{keV}}/L_\mathrm{Edd} = 0.001$–$0.002$, which is comparable to the luminosity assumed by Dovčiak & Done (2016). We therefore adopt a coronal radius of $1\,r_\mathrm{g}$ for our components. If the corona of LP_1 was in fact situated at $1.2\,r_\mathrm{g}$ above the BH, its radius would have to be even smaller in order not to interfere with the event horizon.

The compactness of a corona with radius d can be expressed as

$$\ell = 4\pi\,\frac{m_\mathrm{p}\,L_\mathrm{int}}{d\,m_\mathrm{e}\,L_\mathrm{Edd}} \tag{3.13}$$

where L_int is the intrinsically emitted luminosity, $L_\mathrm{Edd} \sim 1.5 \times 10^{38}\,(M/M_\odot)\,\mathrm{erg\,s^{-1}} = 4.5 \times 10^{45}\,\mathrm{erg\,s^{-1}}$ is the Eddington luminosity[13] and d the radius of a simplified spherical corona in units of r_g. The compactness can be interpreted as the optical depth of the corona with respect to pair production and has been extensively discussed by Lightman & Zdziarski (1987), Svensson (1987), Dove et al. (1997a) and Dove et al. (1997b). A useful parameter in that regard is $\Theta = k\,T_\mathrm{e}/m_\mathrm{e}\,c^2 \sim E_\mathrm{cut}/2\,m_\mathrm{e}\,c^2$ (García et al., 2015), where E_cut is the high-energy cutoff of the Comptonized continuum. The cross-section for electron/positron pair production per photon peaks between $E = m_\mathrm{e}\,c^2 = 511\,\mathrm{keV}$ and ∼1 MeV. We therefore evaluate the intrinsic luminosity for the model of each observation both in the range 0.1–200 keV (the energy range used by Fabian et al. 2015) and 0.1–1000 keV, which includes the peak of the cross-section.

If we replace the model description of our best-fit baseline model (Table 3.8) with two separate incident continua and fit for both normalizations (N_{LP_1}, N_{LP_2}) and reflection fractions ($R_\mathrm{f}^{\mathrm{LP}_1}$, $R_\mathrm{f}^{\mathrm{LP}_2}$), these four parameters are strongly degenerate (see Sect. 3.2.3.3 for the numbers). The dynamic range of the normalizations comprises also the solutions of Table 3.9 and therefore provides the full range of allowed values in a conservative way. The observed source luminosities therefore range between $3.2 \times 10^{41}\,\mathrm{erg\,s^{-1}} \lesssim L^{\mathrm{LP}_1}_{\mathrm{obs},0.1-200\,\mathrm{keV}} \lesssim 2.54 \times 10^{43}\,\mathrm{erg\,s^{-1}}$ and $1.17 \times 10^{43}\,\mathrm{erg\,s^{-1}} \lesssim L^{\mathrm{LP}_2}_{\mathrm{obs},0.1-200\,\mathrm{keV}} \lesssim 2.50 \times 10^{43}\,\mathrm{erg\,s^{-1}}$. Especially for LP_1, where the corona must be situated deep inside the gravitational potential, we need to transform the observed luminosities into the intrinsic frame of the corona. The conversion factor $(1+z_\mathrm{g})^\Gamma$ depends on the gravitational redshift $z_\mathrm{g} = (1/\sqrt{1-2\,h/(h^2+a^2)}) - 1$ between the corona and the observer as well as the photon index Γ. Fixing the spin at $a = 0.998$, we find that the conversion factor increases quickly from ∼1.14 ($z_\mathrm{g} \sim 0.08$) at $h \sim 15.0\,r_\mathrm{g}$ to ∼37 ($z_\mathrm{g} \sim 7.2$) at $h \sim 1.2\,r_\mathrm{g}$. In addition, for LP_1 we also need to apply a correction factor to account for photon trapping. Due to strong light-bending, at the height of $1.2\,r_\mathrm{g}$ only ∼1% of the photons of an isotropically emitting primary source reach the observer, while a significant fraction of the photons (∼13%) reach the accretion disk, leading to a reflection fraction of $R_\mathrm{f}^{\mathrm{LP}_1} = 22$ for LP_1 (see also Table 3.9). At this reflection

---

[13] The Eddington luminosity is calculated with the black-hole mass $M_\mathrm{BH} = 3 \times 10^7\,M_\odot$ (Hicks & Malkan, 2008).

fraction the corresponding luminosity becomes $L^{\mathrm{LP}_1}_{\mathrm{int},0.1-200\,\mathrm{keV}} = 0.4L_{\mathrm{Edd}}$. Leaving R_f free, the incident continuum can reach observed luminosities as large as $2.54 \times 10^{43}\,\mathrm{erg\,s^{-1}}$. For this value, the corona intrinsically exceeds L_{Edd} by a factor of ten.

The full range of allowed luminosities translates into a compactness-range of $2500 \lesssim \ell_{\mathrm{LP}_1} \lesssim 200000$ and $5 \lesssim \ell_{\mathrm{LP}_2} \lesssim 11$. With these constraints, we can show that the compactness parameter ℓ covers well the parameter space below the limits for pair production (Stern et al., 1995; Dove et al., 1997a,b; Fabian et al., 2015) for LP_2. It would, however, exceed this limit in some extreme representations of LP_1. Here, we also have to correct the parameter Θ and the cutoff energy for the gravitational energy shift arising between the compact source and the observer. For LP_1, this shifts the primary source above the pair limit for all compactness values independent of the value for E_{cut}. As a result, the corona is entirely optically thick for photons with energies $E > 511\,\mathrm{keV}$ with respect to pair production.

Such extremely compact coronae have not been found in the sample of AGN and XRBs studied by Fabian et al. (2015). Also, the limitations that we outline above and that also are mentioned by Niedźwiecki et al. (2016) challenge the interpretation of LP_1 as distinct component. The component LP_1 can therefore only be interpreted in combination with LP_2. Although the superposition of the two distinct LP components LP_1 and LP_2 serves well to describe our data, we hesitate to claim the two point sources to represent a realistic description of the corona. Also, the strong degeneracies between the uncertain normalizations of both LP components argues against two extremely compact and distinct coronae. A continuous structure enclosing both components seems more likely. The detected spectral signatures of strongly blurred reflection yet indicate in a model-independent way that at least a part of the corona must lie close to the black hole. The low reflection fraction measured for LP_1 particularly points towards a vertically extended structure (Keck et al., 2015). It may be reflected by outflows (see also King et al., 2017) that have been detected for NGC 4151 (Kraemer et al., 2005; Tombesi et al., 2010, 2011), where relativistic aberration (Beloborodov, 1999; Malzac et al., 2001) can effectively reduce the observed fraction of reflected photons. These outflows together with its non-relativistic jets (e.g., Pedlar et al., 1993; Ulvestad et al., 2005) fit well in this picture and may provide a natural environment for the source of primary X-ray photons (Markoff & Nowak, 2004; Markoff et al., 2005; Wilkins & Gallo, 2015; King et al., 2017).

Reverberation studies have independently suggested horizontally (Wilkins & Fabian, 2012) and, in particular, vertically extended primary sources above the black hole for Ark 564 (Zoghbi et al., 2010), Mrk 335 (Kara et al., 2013), IRAS 13224−3809 (Wilkins & Gallo, 2015), and also for NGC 4151 (Zoghbi et al., 2012; Cackett et al., 2014). The latter authors come up with a primary source at ~5–10 r_g distance from the black hole. This may, in conjunction with the high-quality spectral information of the long-look *Suzaku* and *NuSTAR* data, be well in agreement with a jet-base geometry, which can still be radially compact. Magnetic fields (e.g., Baczko et al., 2016, in the extreme radio galaxy NGC 1052) make this region an efficient emitter of synchrotron photons (e.g., Merloni et al., 2000; Markoff et al., 2005), which can act as additional seed photons for Comptonization processes in the corona and therefore at least reduce its transverse extent (Dovčiak & Done, 2016) close to or below the value of $1\,r_\mathrm{g}$, which we have previously assumed for our estimates of the compactness.

3.2.4.2 COMPLEX ABSORPTION VARIABILITY

We model four layers of absorption: two neutral layers, one partially covering the nucleus with $f_{\mathrm{cvr}} \sim 0.5$ ($\mathrm{CA}_1/N_{\mathrm{H},1}$) and one full-covering absorber ($\mathrm{CA}_2/N_{\mathrm{H},2}$), a warm absorber with $\log \xi \sim 2.8$ as well as an additional broad absorption line around 8 keV that can either be formed by a Fe XXVI Ly β line that is unmodeled by the warm absorber or, more likely, a blueshifted Fe XXV He α or Fe XXVI Ly α line, indicative of an UFO at a speed of ~0.16–0.24 c.

We showed that one or both of the absorbers CA_1 or CA_2 account for the bulk of the spectral variability between 1 and 6 keV on time-scales from days to years. This agrees with Puccetti et al. (2007) and de Rosa et al. (2007) for a similar set of absorbers. The partial-covering column $N_{\mathrm{H},1}$ ranges between 10 and $25 \times 10^{-22}\,\mathrm{cm}^{-2}$. Its covering fraction averages 46% across the *Suzaku* observations. The full-covering column $N_{\mathrm{H},2}$, on the other hand, ranges between 5 and $15 \times 10^{-22}\,\mathrm{cm}^{-2}$. The columns $N_{\mathrm{H},1}$ and $N_{\mathrm{H},2}$ seem to track each other well; given the data quality and the comparable values of both columns, we can explain this model-dependent result as due to degeneracies between $N_{\mathrm{H},1}$ and $N_{\mathrm{H},2}$. In agreement with earlier analyses using *BeppoSAX* (Puccetti et al., 2007; de Rosa et al., 2007) and *Chandra* (Wang et al., 2010), we can therefore not tell if one or the other column dominates the variability. A separation of both neutral absorbers from the inner-disk reflection component is equally challenging, as both describe similar spectral features at the flat turnover. We have shown that disentangling both is indeed possible with the high count statistics and broad spectral coverage of the long-look *Suzaku* and *NuSTAR* observations as well as the variable nature of the absorbers. The latter also has been demonstrated by Risaliti et al. (2009a) and Risaliti et al. (2013) for NGC 1365, which is similar to NGC 4151 in that regard.

The shortest variability time-scale of 2 d has been measured with the time-resolved analysis of Suz 3 (see Fig. 3.33). The circumnuclear gas in NGC 4151 may be continuous yet non-homogeneous and/or containing (or consisting of) a discrete number of localized clouds. Such scenarios have been explored for this source in the past by Holt et al. (1980), Yaqoob & Warwick (1991), Zdziarski et al. (2002), and Puccetti et al. (2007).

Where the variable absorber consists solely of clouds, variability either by N_{H} or the covering fraction may be associated with single clouds entering or exiting the line-of-sight. We cannot exclude variability of the covering fraction due to inherent degeneracies that lead us to fix this parameter. The model by Nenkova et al. (2008b) attempts to explain line-of-sight variability for all inclinations with a Poissonian distribution of clouds that decrease in number density further out. This model has been successfully fitted to IR SEDs by Alonso-Herrero et al. (2011) and is able to explain absorption events observed in the X-rays (Markowitz et al., 2014; Beuchert et al., 2015). On average, these studies predict only a few clouds on the line-of-sight for inclinations similar to the one we measure for NGC 4151. This is consistent with independent estimates for NGC 4151 by Holt et al. (1980), Yaqoob & Warwick (1991), and Zdziarski et al. (2002).

Regardless of whether the variable absorber is CA_1 or CA_2, we can use the observed variability time-scales of N_{H} to estimate the location of potential clouds that are moving on Keplerian orbits (Risaliti et al., 2002; Puccetti et al., 2007) with

$$R = 3.6 \times 10^{17}\,\frac{M_{\mathrm{BH}}}{10^7\,M_\odot}\left(\frac{n_{\mathrm{H}}}{10^9\,\mathrm{cm}^{-3}}\right)^2\left(\frac{\Delta t}{2\,\mathrm{d}}\right)^2\left(\frac{N_{\mathrm{H}}}{10^{22}\,\mathrm{cm}^{-2}}\right)^{-2}\,\mathrm{cm} \tag{3.14}$$

where M_{BH} is the black-hole mass and where n_{H} and N_{H} are the cloud number density and column density, respectively. For Δt we use the shortest variability time-scale of 2 d. The column density is set to the maximum modeled value of $N_{\mathrm{H},1} \sim 25 \times 10^{22}\,\mathrm{cm}^{-2}$. The number density is unknown. If we assume number densities for BLR clouds of $n_{\mathrm{H}} = 10^{9-10}\,\mathrm{cm}^{-3}$ (Netzer, 1990; Kaspi & Netzer, 1999; Netzer, 2008), we obtain a distance range of $R \sim 5.6 \times 10^{-4}$–$5.6 \times 10^{-2}$ pc or 3.9×10^2–$3.9 \times 10^4\,r_{\mathrm{g}}$. These distances are consistent with those inferred by Puccetti et al. (2007) and with the distance of the BLR ($\sim 8 \times 10^{-3}$ pc, Maoz et al., 1991). Note that for the inclination of NGC 4151, the average number of clouds on our line-of-sight stays approximately the same even if we extrapolate the clumpy torus model down to the BLR. In contradiction to this theoretical consideration, Arav et al. (1998) find no signs of distinct BLR clouds in high-resolution optical Keck spectra. This result favors an interpretation of our data with irregular and dynamic absorbing structures. In theory, dust must be entirely or at least partially sublimated at the inferred distances with the dust sublimation radius

$$R_\mathrm{d} = 0.13\,\mathrm{pc}\left(\frac{L_\mathrm{bol}}{10^{44}\,\mathrm{erg\,s^{-1}}}\right)^{0.5}\left(\frac{T_\mathrm{d}}{1500\,\mathrm{K}}\right)^{-2.6} \tag{3.15}$$

(Nenkova et al., 2008b). We find $R_\mathrm{d} \sim 0.13\,\mathrm{pc} = 8.9 \times 10^4\,r_\mathrm{g}$ with the assumed bolometric luminosity $L_\mathrm{bol} = 10^{44}\,\mathrm{erg\,s^{-1}}$ (Vasudevan & Fabian, 2009) and the dust evaporation temperature of $T_\mathrm{d} = 1500\,\mathrm{K}$ (Barvainis, 1987). When the inner range of the torus is estimated independently, slightly smaller distances are found: using the 5100Å line luminosity (Kaspi et al., 2005), the outer BLR of NGC 4151 could be constrained to a distance of $\sim 6 \times 10^3$–$6 \times 10^4\,r_\mathrm{g}$, the inner rim of the torus to $\sim$0.04 pc using thermal dust reverberation studies by Minezaki et al. (2004) and Burtscher et al. (2009). Schnülle et al. (2015), however, find no signs of dust sublimation in their data and explain this with large graphite dust grains that sublimate at much higher temperatures. If we assumed clouds at the distance of $R = R_\mathrm{d}$, the cloud density required by the observed N_H variability pattern would be on the order of $\sim 6 \times 10^{10}\,\mathrm{cm^{-3}}$, which Elitzur (2007) can exclude for a dusty torus.

On the other hand, we also detect variability over longer time-scales of approximately one year that may indicate clouds at larger distances. If we assume, for example, number densities of $10^{7-8}\,\mathrm{cm^{-3}}$, which are typical for the dusty torus (Miniutti et al., 2014; Markowitz et al., 2014), we find $R \sim 2 \times 10^{-3}$–2×10^{-1} pc or 1.3×10^3–$1.3 \times 10^5\,r_\mathrm{g}$. These values put the clouds into the outer BLR or at the inner side of the dusty torus, which is a common result of Markowitz et al. (2014) for similar time-scales. Much larger distances of clouds from well inside the torus require unrealistically large number densities and are therefore unlikely.

Recently, Couto et al. (2016) published a study that investigates X-ray absorbers with archival long-look *Chandra* observations. They find a highly ionized column similar to our `xstar` component as well as an outflowing near-neutral absorber[14] with the speed $\sim 500\,\mathrm{km\,s^{-1}}$. Couto et al. fit these absorbers to a number of seven archival *Chandra* observations with two additional observations by *XMM-Newton* in 2000 and *Suzaku* in 2006. They conclude that the bulk of the spectral variability over 14 years is caused by a change in the ionization state of both absorbers as response to changes in the irradiating luminosity rather than the observed variations in N_H. Similar to the absorbers used by Couto et al. (2016), we find the columns of both neutral absorbers, CA_1 and CA_2, to be anticorrelated with the incident photon flux of the HXCOMP component. A portion of either of these is likely consistent with the component D+Ea. Its outward motion forms a consistent picture with the observed anticorrelation of the incident flux with the column density, in which a still dusty, radiatively driven wind (e.g., Czerny & Hryniewicz, 2011; Dorodnitsyn & Kallman, 2012) causes a decrease of the line-of-sight absorption for stronger radiative driving. We, however, emphasize that the interpretation of the data analyzed in this work strongly depends on the way of modeling. Both the interpretation with orbiting clouds or with an outflowing near-neutral absorber represent structural changes in the absorber. We do not favor one over the other. In a yet different scenario, the ionization state of the absorber can change with varying irradiation, resulting in changes of the equivalent column density. We, however, are not sensitive to this effect with the available count statistics.

On larger scales, Ruiz et al. (2003) and Radomski et al. (2003) detect dusty extended gas in NIR/MIR data, which is fully covering the nucleus similar to dust that has been found within $\sim$4 pc using the Gemini NIR integral field spectrograph Riffel et al. (2009). This dusty component may therefore make up a non-variable portion of our CA.

---

[14] This neutral absorber goes back to absorption line features in *HST*/GHRS/STIS data first mentioned by Weymann et al. (1997) and referred to as the kinematic component “D+Ea” in Table 1 of Kraemer et al. (2001); see also Kraemer et al. (2006) for further usage.

3.2.4.3 THE SOFT X-RAYS

We model the soft X-rays of all observations with a SXCOMP with the photon index tied to that of the HXCOMP as well as a blend of Gaussian lines that are motivated from high-resolution grating observations of *XMM-Newton*/RGS and *Chandra*/HETG. We have shown that the soft flux below 1 keV is, contrary to the hard flux, only mildly variable at a low dynamic range of ~6% at most. The origin of the variability (continuum, emission line(s), or both) is unclear. If we calculate the ratio of the SXCOMP and HXCOMP normalization, we can, on average, infer a low optical depth of the soft emitting gas of $\tau \sim 0.023$.

Due to the comparatively large PSFs of *XMM-Newton* and *Suzaku*, we are unable to spatially resolve the line-emitting gas. In contrast, a number of authors have been using *Chandra* for this purpose, which is both powerful in spatial and spectral resolution. Ogle et al. (2000) and Wang et al. (2011a) show that a considerable part of the soft X-rays is due to distant, extended gas that is spatially coincident with a bi-conical gas distribution (see Storchi-Bergmann et al., 2010, for integral field spectroscopy of [O III]) and the NLR (Bianchi et al., 2006; Guainazzi & Bianchi, 2007a). A spatially resolved modeling of the extended gas with `Cloudy` allows Wang et al. (2011a) to conclude a two-phase photoionized medium of intermediate ($\log \xi \sim 1.7$) and high ($\log \xi \sim 2.7$) ionization (see also Armentrout et al., 2007, for similar modeling using `Cloudy` with *XMM-Newton*/RGS data) next to the collisionally ionized phase. The higher ionized line-emitting gas phase detected using `Cloudy` may also be consistent with the highly ionized warm absorber of similar ionization ($\log \xi \sim 2.8$) that we model with `xstar`.

To infer the values of $\log \xi$ from the published ones of $\log U$, we use the double-broken powerlaw proposed by Kraemer et al. (2005) and find a conversion factor of $f = \xi/U \approx 87$. The spectral model can be described with $N(E) \sim E^{-\Gamma} = E^{\alpha}$ ($\Gamma = 1 - \alpha$), where

$$\begin{aligned} \Gamma &= 1.0 & E &< 13.6\,\mathrm{eV} \\ \Gamma &= 1.3 & 13.6\,\mathrm{eV} < E &< 0.5\,\mathrm{keV} \\ \Gamma &= 0.5 & E &> 0.5\,\mathrm{keV} \end{aligned} \tag{3.16}$$

To cross-check the results of Wang et al. (2011a), I extend on the work of Beuchert et al. (2017) and calculate a stability curve for the same input SED that they used for NGC 4151 (Eq. 3.16). This curve is shown as blue dashed line in Fig. 1.16 and confirms multiple stable gas phases, each in an isobaric environment, that is, $\xi/T = \mathrm{const.}$ I can confirm that the two ionization states that Wang et al. (2011a) find via spectral fits using a `Cloudy` model, are not in pressure equilibrium with each other. Both ionization states are, however, found to be consistent with stable gas states, i.e., positive slopes of the stability curve.

The evidence for a thermal, collisionally ionized gas phase may point towards a contribution of a bremsstrahlung continuum to the soft X-rays, which we, for simplicity, model with a SXCOMP continuum, that is, scattered nuclear Comptonized emission. We are unable to favor either of both options with our data, but provide a short discussion on the implications of our chosen model. In this picture, the observed that highly ionized phase, which we refer to as a “warm mirror” (Guainazzi et al., 2005; Guainazzi & Bianchi, 2007a,b) can act as scattering medium for the nuclear emission. This scenario would justify our SXCOMP component to be a long-term average with respect to the variable nuclear HXCOMP (see also Pounds et al., 1986; Yang et al., 2001; Wang et al., 2011b). The low degree of flux-variability that we measure between 0.6 and 1.0 keV may be explained with portions of this warm mirror that are located close enough to the nuclear source to respond to its variability. In fact, around 30%[15] of the soft X-rays originate in a region that is unresolved by *Chandra* (Ogle et al., 2000). The response of this mirror at various distances from the source can explain the lack of correlated variability between the soft

---

[15] This number can only be approximate due to the recent improvements on the *Chandra* PSF.

and hard bands. A correlation of the HXCOMP variations with the prominent O VII and Ne IX line fluxes can neither be claimed nor excluded with respect to the large uncertainties at CCD resolution. Also, we can neither report in favor for or against correlated variability of these lines with the column density of the absorbers. This would be expected if the clumpy absorber would temporarily block the nuclear irradiation onto the diffuse gas and promote the gas to recombine.

Other than the warm mirror, an intrinsic soft excess may also explain the soft emission, which has phenomenologically been modeled with a steep soft power-law (Yang et al., 2001; Wang et al., 2010, e.g.,). This also involves a fit with an extra bremsstrahlung component (e.g., Warwick et al., 1995). In a more self-consistent picture, the soft excess emission is provided by a combination of blurred and unblurred ionized disk reflection, i.e., by the model components `relxillCp_lp` and `xillver`, which we use to describe the relativistic features inherent in the continuum. Although this works decently well for the soft continuum at CCD resolution, `xillver` is unable to model the highly ionized species of the H-like and He-like ions O VII/O VIII and Ne IX, which we observe with *XMM-Newton*/RGS. In addition, `xillver` predicts a number of strong lines from Mg, Si, and S rather than O or Ne, which are not observed with *XMM-Newton*/RGS. We therefore prefer an independent soft continuum due to extended gas on larger scales.

3.2.5 Conclusions and Outlook

These conclusions are mostly taken in verbatim from Beuchert et al. (2017). The unique Seyfert galaxy NGC 4151 allowed us to both probe the circumnuclear absorber and its dynamics together with the effects of strong gravity close to the BH via imprints on the reflection spectrum. As part of this work, we conducted a follow-up study based on Keck et al. (2015) and apply the improved model `relxillCp_lp` that describes blurred reflection in a physically motivated and self-consistent LP geometry together with the complex set of neutral absorbers that has been frequently reported in the literature. We applied the resulting baseline model to a large set of *Suzaku*, *XMM-Newton*, and *NuSTAR* spectra that cover time scales from days to years. We performed a time-resolved spectral analysis of the neutral absorbers CA_1 and CA_2 that are variable on time-scales from days to years. We find the soft X-rays below 1 keV to be only mildly variable within a maximum of ∼6% as opposed to ∼20% for the HXCOMP. Strong spectral variability is apparent between 1 and 6 keV. As a result from our dedicated modeling we come up with the following conclusions:

1. We identified two separate point-like LP components LP_1 and LP_2 in simultaneous long-look *Suzaku* and *NuSTAR* spectra at the heights of $h \sim 1.2\,r_\mathrm{g}$ and $h \sim 15.0\,r_\mathrm{g}$, respectively. We applied the most recent model `relxillCp_lp` that combines the reflection spectrum off each point on an ionized disk (`xillver`) with the appropriate relativistic transfer function. The normalizations and reflection fractions of both LP components are highly degenerate. In particular we measured a low reflection fraction for LP_1 and find that runaway pair production dominates for such a single and compact corona as close to the BH. Based on these results, we propose a vertically extended and potentially outflowing corona as opposed to two distinct and compact coronae. Our results possibly reflect Comptonization processes in a jet-base and we emphasize the presence of non-relativistic jets in NGC 4151 in that regard. We point to the presence of magnetic fields in such a jet-base and that additional synchrotron seed photons may lead to a corona that is compact in horizontal direction. The relevance of magnetic fields for coronae close to the BH is strongly implied and needs to be carefully investigated in the future.

2. Thanks to the high count statistics provided by the long-look *Suzaku*/*NuSTAR* campaign, we were able to constrain a complex system of four separate layers of absorption. Those are two neutral absorbers, one of which is partially covering the nucleus with only 40%–50%

(CA_1) and one fully covering the same (CA_2), a third layer of highly ionized absorption ($\log\xi \sim 2.8$) as constrained with absorption features of Fe XXV and Fe XXVI, as well as an UFO with an outflow velocity of ~0.16–0.24 c from a broad absorption feature around ~8 keV. We did also show that we are able to distinguish the flat turnover of the neutral partial coverer between 3 and 6 keV from the broad and blurred reflection components, which both describe a similar spectral shape in this energy range.

3. We observed both columns CA_1 and CA_2 to be strongly variable both on short time-scales of 2 d (probed with the long-look *Suzaku* observation) and long time-scales of approximately one year (probed with two additional *Suzaku* observations as well as a *XMM-Newton* monitoring). Both absorbers are responsible for the bulk of the spectral variability observed between 1 and 6 keV. Their variability patterns are similar at all time-scales, which is likely caused by the observed degeneracies between both columns. We are therefore unable to tell from our modeling, if one or even both absorbers are intrinsically variable. We interpreted the observed column density evolution with a clumpy absorber, where one or more single clouds transit the line-of-sight at a distance as close as the BLR up to the inner side of the torus. While no BLR clouds have yet been detected in the BLR of NGC 4151, a clumpy nature of the inner dusty torus may still be a valid explanation. On the other hand, the anticorrelation of the irradiating photon flux with the column densities $N_{\mathrm{H},1}$ and $N_{\mathrm{H},2}$ offers the alternate explanation of a radiatively driven dusty wind or changes of the ionization degree of the near-neutral absorber.

4. The soft X-rays below 1 keV are only mildly variable. They likely originate in extended NLR gas, which is included by the large PSF of *Suzaku* and *XMM-Newton*. We observed a blend of unresolved emission lines in the CCD spectra together with a weak continuum that we model with the SXCOMP. We analyzed the combined *XMM-Newton*/RGS spectrum of all seven *XMM-Newton* pointings to precisely identify the underlying soft emission lines. Line-ratio diagnostics on the dominant He-like triplets O VII and Ne IX result that the gas must primarily be photoionized with a minor contribution of a collisionally ionized phase. Related to the choice of the SXCOMP as underlying continuum, we discussed the extended and highly ionized gas with a “warm mirror”, scattering nuclear Comptonized continuum emission into our line of sight. We outlined observational evidence for this gas phase, that is, the $\log\xi \sim 2.8$ warm absorber and the soft line emission. The mild degree of variability in the soft X-rays may originate in gas that is located close enough to the nucleus to be able to respond to changes in the hard X-ray continuum within the probed time-scale. We can exclude intrinsic soft excess emission due to blurred, ionized reflection.

5. It can be shown that the spatially extended X-ray line emission from the NLR coincides with the [O III] cone Wang et al. (2011a). Because this gas is so extended, it can be observed independently of the orientation of the AGN. The emitted lines in both the X-rays and optical therefore act as isotropic tracers for classifying AGN in large surveys (e.g., Schneider et al., 2010).

3.3 AGN IN THEIR CRADLE: STUDYING ABSORPTION PROCESSES IN THE YOUNG RADIO GALAXY PKS 1718−649

Gigahertz-peaked spectrum (GPS) radio galaxies form a peculiar class of AGN. Associated sources show compact (parsec-scale) symmetric radio morphology, which may be a down-scaled version of the gigantic radio plumes and lobes on kiloparsec scales in radio galaxies. GPS sources are also characterized by a low degree of variability in the radio bands as opposed to the rapid flaring observed for sources with beamed jet emission and flat radio spectra. GPS sources

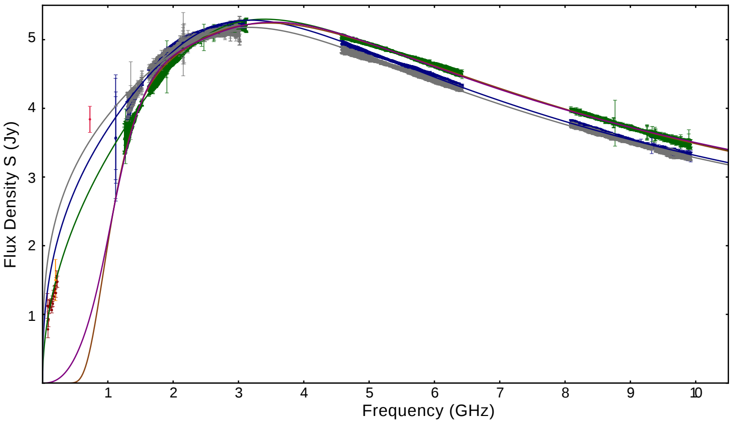

Figure 3.38. Multi-epoch ATCA data measured with the broad spectral coverage of the updated Compact Array Broadband Backend (CABB Wilson et al., 2011). Data from February 2012, February 2013 and December 2013 are shown in green, blue and gray, respectively. Free-free absorption fits by Bicknell et al. (1997) considering an inhomogeneous ISM are indicated with solid lines in the corresponding colors. The data from February 2012 are further fitted with a homogeneous SSA and free-free model as shown in purple and brown. The figure is adapted from Tingay et al. (2015) and complemented with data from the GLEAM survey at 72 MHz and 231 MHz by Wayth et al. 2015. (Joseph Callingham, ASTRON, priv. comm.).

meanwhile do not show flat spectra but instead a rising branch with ν^α ($\alpha < 0$) as well as a turnover towards lower frequencies at a few GHz. Those with a spectral turnover below 1 GHz are also called Compact Steep Spectrum Sources (CSSs). Whenever the radio morphology of two symmetric jets can be identified, these sources are named Compact Symmetric Objects (CSOs).

3.3.1 THE YOUNG RADIO GALAXY PKS-1718−649

PKS 1718−649 is a prominent CSO (Tingay et al., 1997) with an embedded AGN. The high measured brightness temperature of $> 10^{10}$ K (Jauncey et al., 1998) points towards synchrotron processes to cause the observed radio emission. The authors also note that no strong beaming can be detected in this source, which, together with the paradigm of unification, suggests a nearly edge-on inclination of the AGN. Recent observations of the emitted radio spectrum show a prominent turnover at observable radio frequencies (Fig. 3.38). One can describe this turnover either with free-free absorption (FFA) or SSA. PKS 1718−649 as a GPS or CSO does not show signs of the morphology of compact jet emission but is supposed to be entirely contained in, and absorbed by the NLR of the AGN (O'Dea, 1998). Observations at highest angular resolution with TANAMI[16] (Fig. 3.39) reveal compact parsec-scale radio emitting lobes forming a dense environment and thus confirm the classification as CSO (see also Müller et al., 2014, for the prominent CSO PMN J1603−4904). The core is self-absorbed at radio frequencies higher than 8 GHz with a positive spectral index in contrast to the compact lobes that can be probed with the Australia Telescope Compact Array (ATCA) on larger scales (Fig. 3.38). Tingay et al. (1997) further find evidence that this source is very young – a typical feature of CSOs – and reflect an AGN in its cradle. In contrast, Sadler (2016) argue against the evolutionary scenario, in which the still compact radio jets of CSOs would eventually pierce their cocoon of gas and dust and evolve to jets that could be classified as FR Is or FR IIs during later stages of evolution.

One key question that will facilitate to unveil the nature of the absorbing environment is whether the spectral turnover in the radio is caused by SSA, i.e., the electron plasma in the synchrotron source, or FFA, i.e., foreground ionized material covering the line of sight to the

---

[16] The TANAMI (Tracking Active Galactic Nuclei with Austral Milliarcsecond Interferometry) multiwavelength monitoring program (Ojha et al., 2010) uses the Australian Long Baseline Array (LBA) at 8.4 GHz and 22.3 GHz.

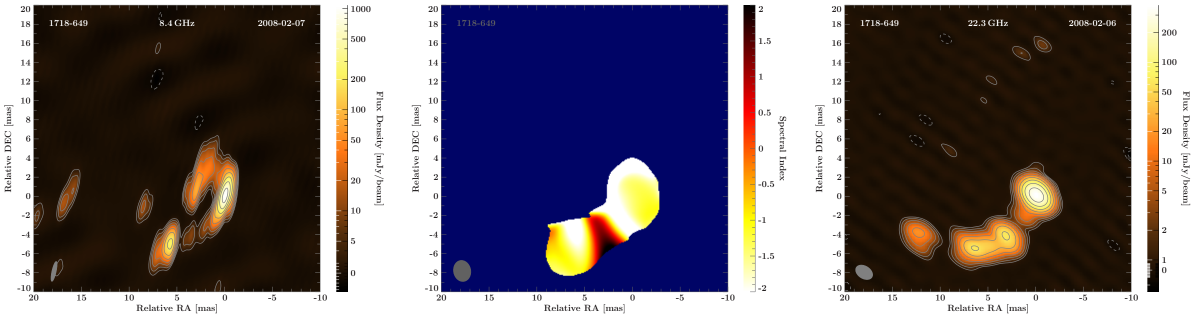

Figure 3.39. TANAMI VLBI maps showing the compact symmetric morphology of the CSO source PKS 1718−649 at 8.4 GHz (*left panel*) and 22.3 GHz (*right panel*). The central panel shows the spectral index map between both frequencies (image courtesy: R. Schulz).

nucleus processes. Tingay & de Kool (2003) have extensively studied an earlier ATCA spectrum and attempted to disentangle both processes. The updated Compact Array Broadband Backend (CABB, Wilson et al., 2011) improved the data coverage below the turnover, which allowed Tingay et al. (2015) to conclude on FFA as the dominant process and to detect column density variability on timescales of years (Fig. 3.38). This result is intriguing, as one is now able to directly probe the opaque foreground material and its dynamics on our line of sight. One can therefore also make use of the X-rays as independent source of information to probe the absorbing environment of this CSO. Note that SSA will still contribute to the core absorption (Fig. 3.39).

For FFA to be present, the absorbing material must be ionized. Filippenko (1985) classified the AGN of PKS 1718−649 as LINER galaxy, where photoionization is the driver of the observed AGN and ionized line emission. Shocks driven by the jetted material can be a natural explanation for the ionization of dense gas that has to be on the order of $10^6 - 10^7\,\mathrm{cm}^{-3}$. These densities are just a bit higher than and may be consistent with those expected for NLR clouds in Seyfert 1 galaxies (e.g., Wardle, 1998) that can show a range of ionizations (e.g., Chakravorty et al., 2009). The ionization states and column densities of such clouds can be probed by X-ray radiation emitted from the immediate environment of the black hole, that is, a region of $\sim 10\,r_\mathrm{g}$.

One prominent example is the Seyfert 1 galaxy NGC 4151 (see Sect. 3.2 for a discussion of the compact X-ray emission). It shows jet-like radio features. The radio feature closest to the SMBH is absorbed by FFA at a distance of ∼50 pc from the SMBH (Pedlar et al., 1998). On the X-ray side, Ogle et al. (2000) confirm a range of ionization states inherent to the NLR of NGC 4151 with *Chandra* grating data. Pedlar et al. (1998) also investigate the possibility of a clumpy, ionized inner phase of the torus of NGC 4151 to cause FFA and to possibly feed the NLR gas. Kadler et al. (2004) can confirm this notion for the edge-on radio galaxy NGC 1052. Both of these well studied sources therefore motivate the search for correlated FFA and X-ray absorption in PKS 1718-649 (Macquart & Tingay, 2016, for a theoretical work on this issue).

3.3.2 DEVELOPING A NEW OBSERVING PLAN

PKS 1718−649 is the first compact and young AGN to show variable FFA absorption. If the emission sites of the radio and X-ray radiation are spatially coincident and at least partly ionized, one can expect (correlated) FFA and X-ray absorption on our line of sight. This assumption can be tested with simultaneous X-ray and radio observations. To date, the archives only contain non-simultaneous data. I therefore initiated a joint observing campaign with a number of co-investigators. We proposed for simultaneous observations with the well-performing radio and X-ray observatories ATCA and *XMM-Newton*, where we base ourselves on the following results.

Multiple authors have been claiming that the electron columns N_e derived from FFA spectral fits to radio data are consistent with X-ray derived column densities N_H, where $n_\mathrm{e} \sim 1.2 n_\mathrm{H}$

instr.	date	exp [ks]	N_H $[10^{22}\,\mathrm{cm}^{-3}]$	f_cvr
ACIS	2014 Jun 23	33	1.5 ± 0.5	$0.77^{+0.06}_{-0.07}$
XRT 1	2015 May 29	4.2	5^{+7}_{-4}	$0.80^{+0.15}_{-0.34}$
XRT 2	2015 May 31	4.6	$2.3^{+2.8}_{-1.3}$	$0.92^{+0.07}_{-0.18}$
XRT 3	2015 Jun 02	7.3	$5.6^{+4.0}_{-2.7}$	$0.90^{+0.08}_{-0.23}$
XRT 4	2015 Jun 03	3.9	$2.8^{+97.3}_{-2.6}$	$0.79^{+0.17}_{-0.45}$
XRT 5	2015 Jun 14	3.4	$3.6^{+3.6}_{-2.5}$	$0.89^{+0.09}_{-0.21}$
XRT 1–5		23	$3.8^{+2.6}_{-1.7}$	

Table 3.14. Evolution of the column density and covering fraction with time. The bottom line shows the combined column density as fitted simultaneously to all *Swift* observations.

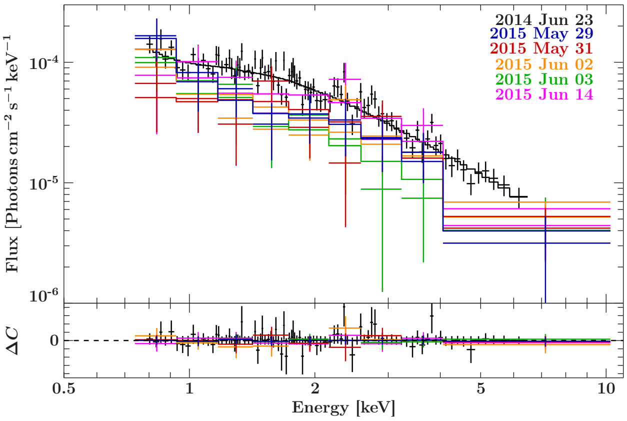

Figure 3.40. *Chandra*/ACIS (black) and *Swift*/XIS (colored) observations from June 2014 and May/June 2015, respectively. The upper panel shows the photon spectra that were fitted with a partial covering, neutral absorber. The bottom panel shows the C-stat residuals.

holds for solar abundances. The examples are the evolved galaxies Mrk 231, Mrk 348 and NGC 2639 (Ulvestad et al., 1999; Roy et al., 2000), NGC 1052 (Kadler et al., 2004), as well as NGC 4151 (Pedlar et al., 1998). For a young CSO, such a correspondence could so far only be stated qualitatively, that is, for the CSO PKS 1718−649 by Tingay et al. (2015). This makes PKS 1718−649 the prime target for our purpose.

We also studied archival X-ray data with *Chandra* and *Swift* (see Table 3.40). These observations include a series of daily spaced *Swift* observations that were observed based on a successful *Swift* ToO proposal lead by A. Kreikenbohm (Univ. Würzburg). The average flux of all observations is $\sim 9 \times 10^{-13}\,\mathrm{erg\,cm^{-2}\,s^{-1}}$.

Figure 3.40 shows the result of a spectral analysis of these X-ray data. We fit a powerlaw with common photon index of $\Gamma = 2.5$ that is partially covered by neutral gas to all *Swift* spectra (colored) and the *Chandra* spectrum (black). The evolution of the parameters is listed in Table. 3.14. The covering fraction is consistent for all observations. No significant absorption variability is detected between the *Swift* observations. We can, however, confirm column density variability between the *Chandra* observation from 2014 and a combined N_H for all *Swift* observations from 2015 (see the bottom line of Table. 3.14). We find variability on the timescale of one year, similar to Tingay et al. (2015). This is a reasonable result, facing typical distances of ∼ 50–100 pc for NLR clouds, confirmed by (Filippenko, 1985) for PKS 1718−649.

Chakravorty et al. (2009) show that a multi-phase medium of dense clumps can be embedded inside ionized gas in the BLR, which can lead both in short variability time-scales of FFA and X-ray absorption. This may be realistic given the detection of compact radio core absorption for PKS 1718−649 by TANAMI in Fig. 3.39 and rapid X-ray absorption variability on time scales from days to years found for Seyfert galaxies (e.g., Risaliti et al., 2002; Markowitz et al., 2014; Beuchert et al., 2015, 2017). Disentangling SSA and FFA is hardly possible from imaging, but potentially from variability studies.

For conducting a first case study and searching for correlated absorption variability between the radio and X-rays, we require two observations in the X-rays that are scheduled simultaneously with the ATCA. We anticipate a spacing by 1 year, which corresponds to the variability timescale found for PKS 1718−649 in both bands. The visibility of the source with the space-based observatory *XMM-Newton* is, however, strongly depending on avoidance angles around bright objects. Also, its highly eccentric orbit requires a shut-down of the instruments when entering the radiation belts of the Earth. Given these constraints, we were restricted to ask for two *XMM-Newton* observations spaced by 6–7 months. Finding correlated absorption variability at these timescales is still realistic as just discussed. We showed that our goals are feasible with 20 ks observing time of *XMM-Newton* each. With an independent proposal lead by V.A. Moss (Univ. Sydney), we got successfully granted 3 hours observing time with the ATCA interferometer. As a result of our X-ray-based proposal, we also achieved observing time with the highly overbooked satellite *XMM-Newton*. A first set of simultaneous observations was performed on March 5th. Follow-up observations are planned for fall 2017.

CHAPTER 4

STUDYING THE EXHAUST

A MULTI-FREQUENCY VIEW ONTO RADIO-LOUD AGN

In the previous chapter, I have illuminated in detail the complex absorbing structures inside the compact accreting cores of two prominent Seyfert galaxies as well as the geometry of the X-ray source in one of these cases. As part of these studies, I also studied the feedback mechanisms of these objects including high-velocity gas outflows. This chapter complements the bigger picture and focuses on the radio galaxy 3C 111, where the main dynamic channel comprises feedback via powerful and collimated radio jets. A study of the parsec-scale radio jet with the technique of VLBI is provided in Sect. 4.1 and is based on a collaboration with a number of colleagues. Section 4.2 asks how the jet is connected with the compact accreting core. The latter section touches upon the frequently debated question on the γ-emission site in radio-loud AGN with the example of 3C 111.

4.1 THE RADIO GALAXY 3C 111 – PROBING JET PHYSICS ON COMPACT SCALES

4.1.1 INTRODUCTORY REMARKS

3C 111 ($z \sim 0.048$, Véron-Cetty & Véron, 2010) is classified as a FR II radio galaxy (Sargent, 1977). Its extended twin jet-structure (Linfield & Perley, 1984; Leahy et al., 1997) is inclined with a PA of about 63°. Its radio core is exceptionally compact and bright. The parsec-scale jet reveals features that undergo apparent superluminal motion and appears as one-sided due to beamed emission (Jorstad et al., 2005; Kadler et al., 2008; Chatterjee et al., 2011). These blazar-like properties contrast the morphology on larger scales, which is reminiscent of a typical radio galaxy. Long-term VLBI monitoring at 15 GHz by MOJAVE reveals strong structural variability on parsec scales as it has been observed in total and polarized intensity by Kadler et al. (2008), Großberger et al. (2012) and Lister et al. (2013). 3C 111 was also subject to monitoring with the VLBA at 43 GHz between 1998 and 2001 (Jorstad et al., 2005) and between 2004 and 2010 (Chatterjee et al., 2011). All these studies revealed individual ballistic components with superluminal speeds of up to 6 c, most of which are significantly polarized. These emission components are often interpreted with shocks propagating along the jet flow (Marscher & Gear, 1985, see also Sect. 1.2.5.3).

Chatterjee et al. (2011) derived a mass of $1.8^{+0.5}_{-0.4} \times 10^{8}\,M_{\odot}$ for the central black hole in 3C 111. We use the latest cosmological parameters provided by the Planck Collaboration et al.

(2016), i.e., $\Omega_\mathrm{m} = 0.308$, $\Omega_\lambda = 0.692$, and $H_0 = 67.8\,\mathrm{km\,s^{-1}\,Mpc^{-1}}$ and find a correspondence of $1\,\mathrm{pc}/1\,\mathrm{mas} = 1.08$.

In this work we have been studying the long-term evolution of 3C 111 in total and polarized intensity for 36 MOJAVE epochs between 2007 and 2012. For the first time, we provide detailed observations of a possible interaction of a propagating shock with a recollimation shock and in particular discuss the dynamics of the polarized features and the projected EVPAs. This section is structured as follows. In Sect. 4.1.2 we provide the necessary details on the interferometry data provided by MOJAVE. In Sect. 4.1.3 the results of the parsec-scale dynamics are described, while Sect. 4.1.4 provides corresponding interpretations. A summary is presented in Sect. 4.1.5.

4.1.2 MOJAVE OBSERVATIONS AND DATA ANALYSIS

As part of the MOJAVE monitoring program, 3C 111 has been observed every few months at 15 GHz with the VLBA. The VLBA observations have been planned, scheduled and conducted by the MOJAVE collaboration. The sensitivity for a single baseline is 1.9 mJy and the imaging sensitivity $18\,\mu\mathrm{Jy\,beam^{-1}}$ with respect to the synthesized beam of $\sim 0.3\,\mathrm{mas} \times 0.4\,\mathrm{mas}$[1].

Kadler et al. (2008) analyzed the first 17 epochs from 1995 till 2005. We are following up with the upcoming 36 epochs until mid of 2012. The resulting interferometer visibilities were calibrated as described in Lister & Homan (2005). We desist from performing a detailed kinematic analysis and refer to Lister et al. (2013), Großberger (2014) and Homan et al. (2015) in that regard. The visibilities are naturally weighted and fitted in the (u,v)-plane using Gaussian model components (see Sect. 2.1). The fitted components are then interpreted with ballistical trajectories over as many epochs as possible. See Großberger (2014) for the details, where additional minor phase self-calibration was performed based on the provided pre-calibrated (hybrid imaging) MOJAVE data (Lister & Homan, 2005) and the degrees of freedom of the visibility phases given by the invariance of the closure phases. The phase adaptions turn out to be negligible and the related positional shifts of the model components lie within the statistical uncertainties. The result is a self-consistent kinematic model description of the 36 epochs.

The data are then fitted in the (u,v)-plane using Gaussian model components, which are interpreted with ballistical trajectories for as many epochs as possible. We make use of the `ModelFitPackage` (Großberger, 2014) written for `ISIS`, which interfaces between `ISIS` and `difmap`. That way, we are able to effectively explore the complex and multi-dimensional χ^2-space and to infer constraints on the model parameters. For a few prominent sources, Großberger (2014) calculates the statistical uncertainties for model component positions by probing the entire parameter space. When taking into account parameter degeneracies, we consider a conservative uncertainty of 0.05 mas. This value is consistent with the most probable uncertainty found by Lister et al. (2009b), who analyze the deviations of the component positions from a common kinematic model and for the whole MOJAVE sample.

We find the jet to be transversally resolved downstream of the compact core. The naive argument for spatial resolution is that the synhesized beam has to be smaller than the widths of the Gaussian model components that are folded with the beam to form the overall brightness distribution. This is the case for 3C 111. If the S/N of the network is large enough, this limit can be reduced by arguments of “super resolution” (Kovalev et al., 2005; Lobanov, 2005). For natural weighting, Kovalev et al. (2005) state a limiting resolvable size of a Gaussian component

$$\theta_\mathrm{lim} = b_\psi \sqrt{\frac{4\,\ln 2}{\pi}\,\ln\frac{\mathrm{SNR}}{\mathrm{SNR}-1}}, \tag{4.1}$$

with b_ψ the synthesized beam along a certain angle ψ. We test this for an epoch during May

---

[1] `https://science.lbo.us/facilities/vlba/docs/manuals/oss/`

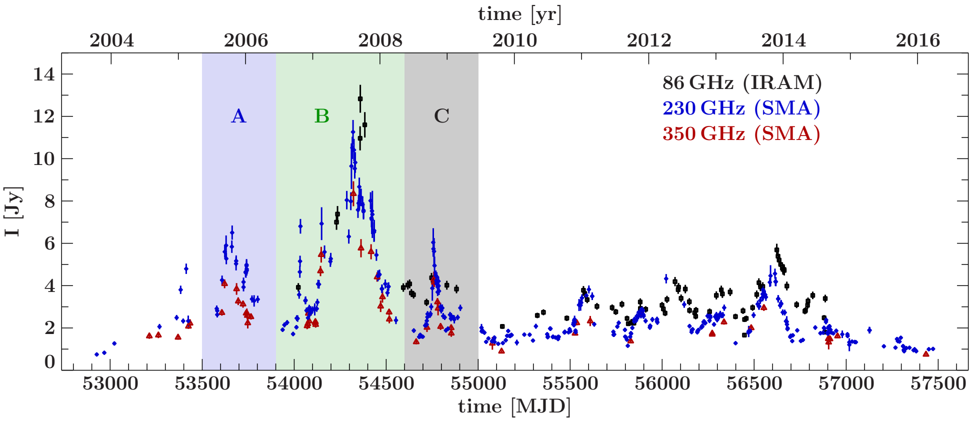

Figure 4.1. Millimeter light curves of 3C 111 at 86 GHz (IRAM, black squares), 230 GHz and 350 GHz (SMA, blue diamonds and dark-red triangles, respectively). The shaded regions mark the three major outbursts A, B, and C.

2012, where the jet is well evolved. We find $\theta_{\text{lim}} \sim 10^{-2}$ mas, which guarantees to transversally resolve the jet except for the innermost core component.

For deriving flux densities in the polarized channels Stokes Q and U, we use the total-intensity Gaussian model components provided by Großberger (2014). We freeze their positions and re-fit only the flux densities[2] according to Lister & Homan (2005). We then calculate maps of linearly polarized intensity $P = \sqrt{Q^2 + U^2}$ and the EVPA $= 0.5 \arctan(U/Q)$ for all 36 epochs treated in this publication. We show EVPAs uncorrected for Faraday rotation due to the lack of RM information covering the entire parsec-scale jet as observed by MOJAVE. Similar to Kadler et al. (2008), we assume 15% uncertainties on the flux densities. In their appendix, Homan et al. (2002) empirically derive distinct components to have flux uncertainties between 5% and 10% depending on the component strength. In our case, the uncertainties may be even higher due to relatively weak and closely spaced features, justifying the choice of 15%.

4.1.3 Revealing the polarized jet emission on parsec scales

3C 111 showed three major outbursts, hereafter labeled A, B and C starting in late 2005, 2007, and 2008, respectively. Figure 4.1 shows light curves taken by IRAM at 86 GHz and SMA at 230 GHz and 350 GHz. The most prominent outburst in late 2007 reached a maximum of $\gtrsim$13 Jy at 86 GHz, the 2005 and 2008 outbursts reached only about half of that peak flux density. The outbursts can be associated with jet activity and the ejection of superluminal components at 43 GHz (using archival data of the Boston University Blazar Group (BG[3]) and 15 GHz (MOJAVE). In the following, we study the evolution of the jet-plasma flow and its polarized emission on parsec scales.

4.1.3.1 Milliarcsecond-scale morphology and evolution

4.1.3.1.1 Image analysis

Figure 4.2 shows the evolution of the jet's linearly polarized intensity as well as the EVPAs on top of the total intensity contours at 15 GHz as a result of MOJAVE (VLBA) observations. The images cover the range from 2007-01-06 through 2012-05-24. They reveal a number of distinct

---

[2] This approach gives satisfactory results but we note that in extreme cases of rapid EVPA changes over core distance, the Q and U visibilities may not be properly approximated with Gaussian model components.

[3] `https://www.bu.edu/blazars/VLBAproject.html`

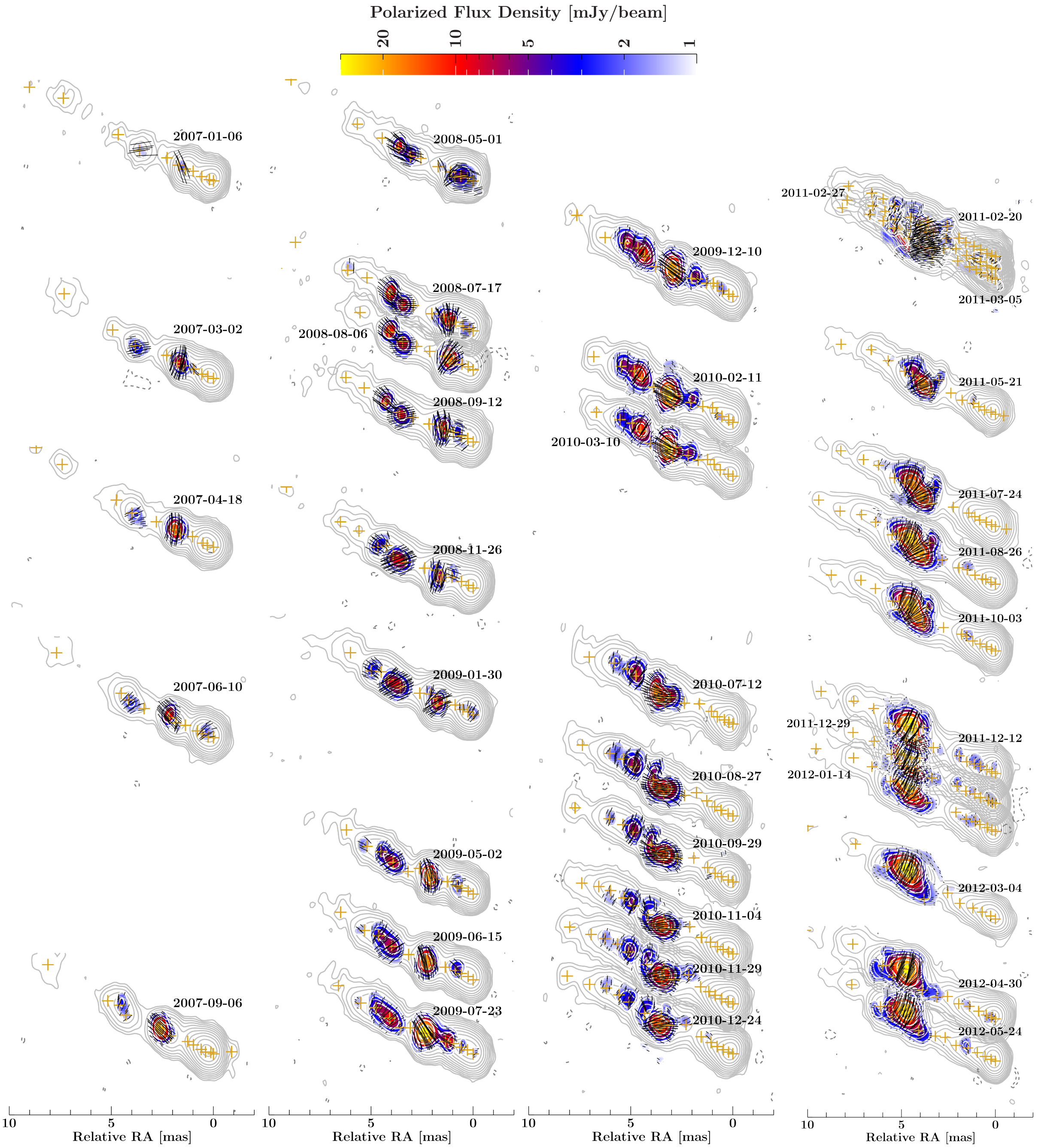

Figure 4.2. Total intensity contours (3σ above background) with overlaid maps of polarized intensity (5σ above background) and corresponding EVPA information drawn as vectors on top. The length of the vectors is proportional to the polarized intensity. Gaussian model-component positions are indicated as orange crosses.

polarized patterns that are well described by a comparatively small number of model components close to the core and become increasingly complex further downstream. The polarized patterns are spatially coincident with features in total intensity that are propagating downstream. They originate from the most upstream, stationary feature, the 15 GHz core that is mainly unpolarized. In the bottom panel of Fig. 4.3 all images are ordered along a common time-axis. We identify two distinct main features that originate in the major outbursts starting in late 2005 and 2007 plus a less dominant feature related to the outburst in late 2008. These features are hereafter labeled according to their related outbursts (Fig. 4.1), namely as features A (blue), B (green),

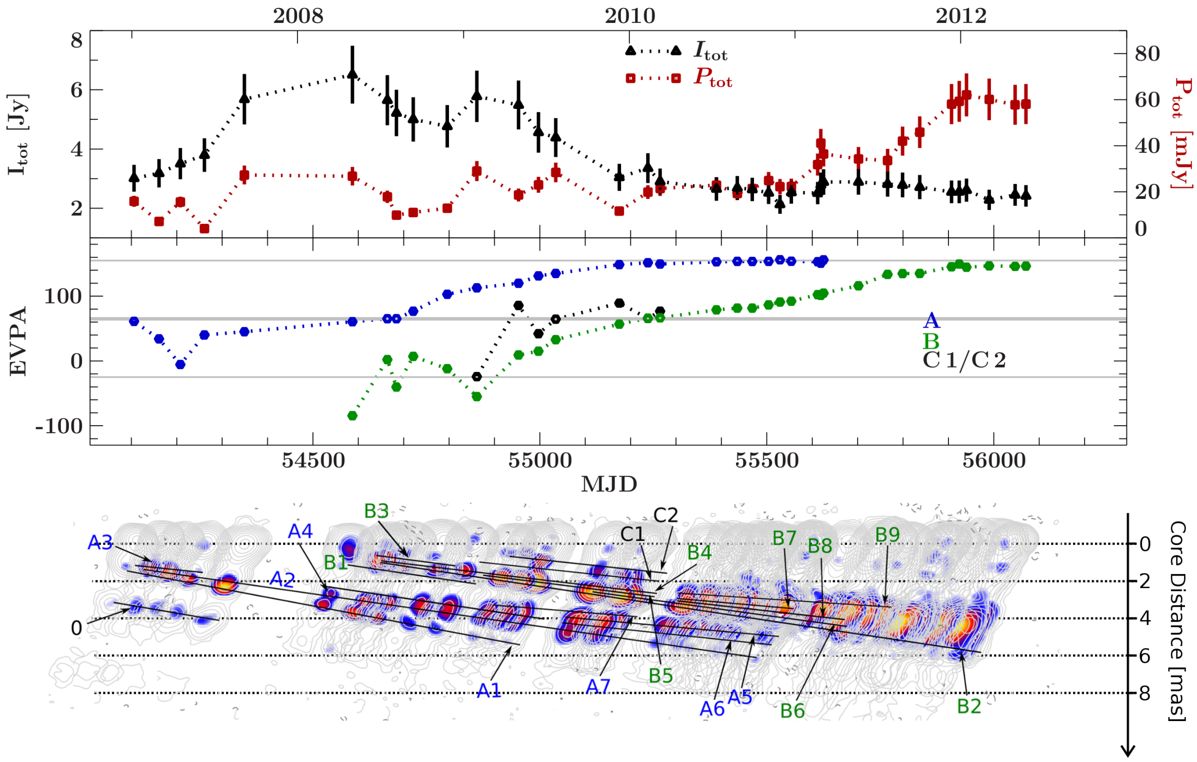

Figure 4.3. *Top panel:* MOJAVE light curve with the total flux density (black triangles, for the most significant total flux density, 5σ above the background) and the total polarized flux density (dark red squares, integrating the flux densities of all model components with at least 1.4 mJy, which corresponds to the average baseline polarized flux density at 3σ above the background); *middle panel:* temporal evolution of the EVPAs of the polarized features A (blue), B (green) and C (black). The solid gray line at $\sim$63° corresponds to the jet position angle derived from the average angle followed by all tracked components. The two thin gray lines at 63°-90° and 63°+90° mark angles perpendicular to the jet axis. The EVPAs are flux-weighted averages for the corresponding feature; *bottom panel:* total intensity contours with overlaid color-coded maps of polarized intensity as shown in Fig. 4.2. Polarized model components forming the two main polarized features A and B and their ballistic trajectories are shown on top of the maps. Components that contribute to the extended most downstream polarized region of feature B but where no consistent kinematic model can be found are not labeled.

and C (black) and show persistent polarized emission while evolving in downstream direction. The feature labeled with '0' is the remainder of a previous outburst in 2004 (Kadler et al., 2008) and will therefore not be discussed in this work.

The upper panels of Fig. 4.3 show the epoch-wise integrated total and polarized flux density. The total intensity light curve at 15 GHz as measured by the VLBA peaks in the beginning of 2008 at a level of around 6 Jy and decreases in flux density towards 2–3 Jy in the subsequent years. The two features A and B become increasingly complex in structure with time and subsequently split into a number of sub-components (A 1–A 7 and B 1–B 9). In general, their total flux density decreases continuously also with core distance (Fig. 4.4, panel a). The flux density of feature A decreases from about 800 mJy at 1.5 mas down to about 60 mJy at 6–7 mas, and has two local maxima at $\sim$4 mas and $\gtrsim$5 mas. The feature B is very bright in total intensity near the core at a level of 6 Jy and falls rapidly until a distance of roughly 2 mas before it reaches a plateau at $\sim$700 mJy between 3–6 mas.

The evolution of the polarized flux density (Fig. 4.4, panel b) is more complex. Both features A and B show a common evolution and start off varying strongly around an average of about 10 mJy around 1–2 mas from the core. The polarized flux density of both features subsequently

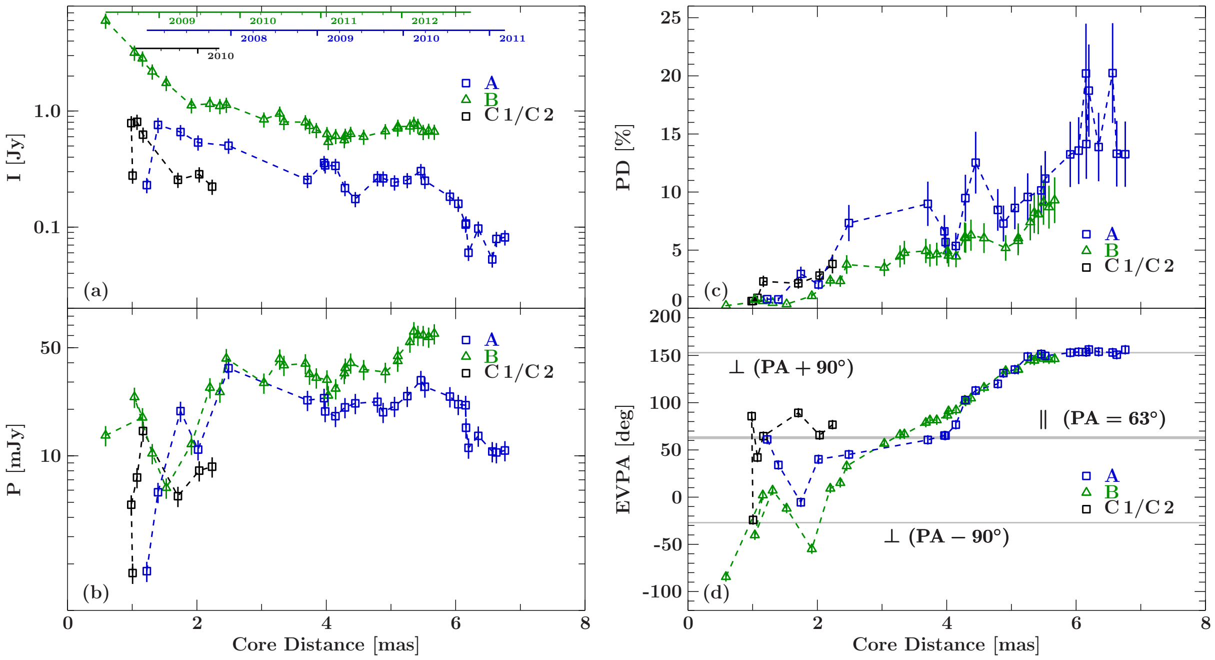

Figure 4.4. Derived quantities of the total flux density (*panel a*), the polarized flux density (*panel b*), the degree of polarization (*panel c*) as well as the EVPAs (*panel d*) over core distance for the two major polarized features A (blue) and B (green) together with the components C 1/C 2 (black). We use the mean flux-weighted core distance of all model components within each feature in a given epoch to describe the core distance of that feature. All quantities are averaged over the contained model components. The different EVPA evolutions are matched by occasional shifts of 180°.

increases rapidly to 40 mJy at 2–3 mas, and shows a similar evolution as in total intensity with an overall plateau and local maxima around around 3–6 mas. In the end of 2010, the polarized flux density of feature A fades away and the feature B begins to dominate the polarized emission reaching a maximum of ∼60 mJy in early 2012. The leading feature of pattern B describes a local brightening in polarized intensity between the epochs 2009-05-02 and 2010-03-10, which is blended with the polarized emission from the other patterns in the total light curve. The degree of polarization (Fig. 4.4, panel c) shows less sub-structure within the uncertainties but a general increasing downstream trend starting off with nearly zero percent close to the core up to 15% after 6 mas. The steady growth of the degree of polarization around 5–6 mas argues for an increased dominance of ordered magnetic field aligned parallel to the jet direction.

Figure 4.4 (panel d) shows the EVPAs of the individual polarized patterns over core distance. In general, the average EVPAs of the polarized features A, B, and C behave similar with distance: a gradual increase of the alignment of their EVPAs is observed within each feature (see also Fig. 4.2) and causes the steady downstream increase of the degree of polarization. The strong EVPA variability between 1 and 3 mas contributes to the low degree of polarization close to the core due to the partial cancellation of misaligned EVPAs. Overall, the angles follow a large rotation of about 180° – a process that lasts up to four years for each of the spatially distinct features. The rotation starts around 2–3 mas at 10–40° towards being aligned with the jet around 3–4 mas. The alignment of the EVPAs of pattern B with the jet axis happens coincident with the observed local brightening in polarized intensity. The swing performed by feature A between 2 and 4 mas is slower compared to feature B. During the brightening, the EVPAs shown in Fig. 4.2 evolve from being overall aligned within the feature B before epoch 2010-03-10 roughly towards a Y-shaped pattern of aligned EVPAs along the central ridge line and oblique EVPAs heading away from the ridge line towards both edges of the jet between 2010-07-12 and 2010-12-24. This leads to some degree of cancellation of polarization within the beam in the center of this structure.

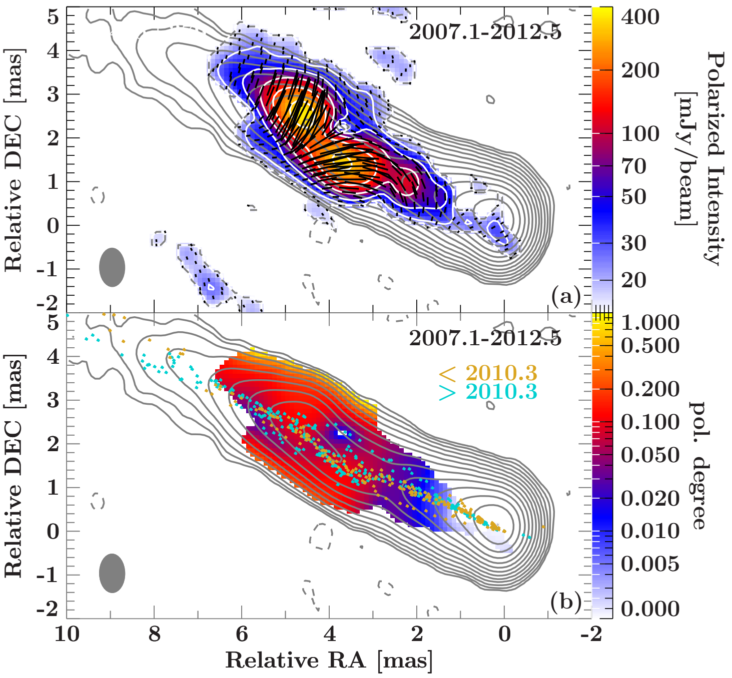

Figure 4.5. Stacked images with polarimetry information for all involved epochs from early 2007.1 until mid 2012.5. We first stack the maps of the channels Q and U and then combine those to derive the shown maps. *Panel a:* color-coded distribution of the polarized intensity with overlaid EVPAs on top of total intensity contours in gray. White contours correspond to the polarized intensity. *Panel b:* distribution of the degree of polarization and overlaid Gaussian (total intensity) model components color-coded for components occurring before and after 2010.3 in orange and blue, respectively.

Eventually, the EVPAs of both features A and B continue a consistent and smooth rotation of another 90° towards being transverse at about 150° during the final epochs in the end of 2012 featuring regions of up to 6 mas from the core. The averaged EVPAs of pattern C cover a much shorter range in time and distance but follow a similar behavior as those of the main patterns A and B.

The apparently similar behavior of the various polarized patterns with distance along the jet motivates an inspection of the stacked image of all individual observations between 2007.1 and 2012.5 as shown in Fig. 4.5. In such a stacked image of multiple observations of a jet with moving features, one expects effective depolarization unless the polarized emission of different features as a function of distance along the jet is strongly correlated. The stacked image shows indeed strong polarization with its EVPAs tracing a continuous rotation between 2 and 6 mas from the jet core accompanied by an increase of the net polarized intensity and the degree of polarization. Only a small region of zero polarization is seen at a relative RA/DEC position of 3.5 mas/2.5 mas. The distribution of the (total intensity) model components (Fig. 4.5, panel b) traces a bend towards the south near this low-polarization region.

4.1.3.1.2 Kinematic analysis

We can describe the dynamics of the polarized features A, B, and C more quantitatively by (I) modeling the total intensity emission with a small number of Gaussian components following Großberger 2014, (II) measuring the linear polarization of these Gaussian components, and (III) performing a kinematic study of components with significant polarization. For the latter, we constrain ourselves to components with a polarized flux density of at least 1.4 mJy, which, on average, corresponds to a 3 σ detection with respect to the background. We reduce this lower threshold to 1 mJy, i.e., 2 σ only for model components that can be tracked over more than four epochs.

Most of these components follow ballistic trajectories with similar PAs (Fig. 4.3). Table 4.1 lists the polarized components with inferred proper motions on the sky. The distances of the selected polarized components and the unpolarized jet model components as a function of time are shown in Fig. 4.6. The leading components of the features A and B (A 1/A 2 and B 1/B 2, respectively) can be tracked over almost the full time range. They dominate both the total and

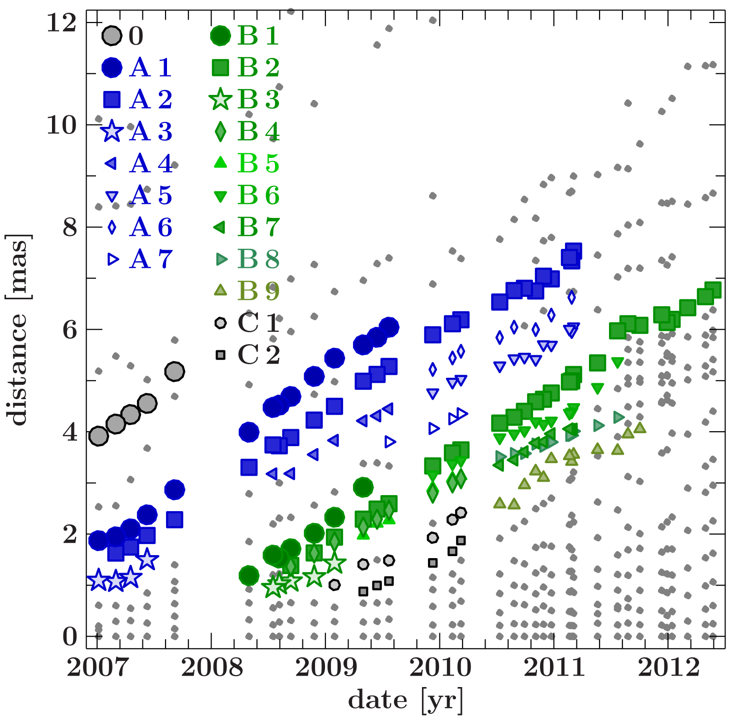

Figure 4.6. Distances over time for all Gaussian model components required to fit the total intensity visibility data of all analyzed MOJAVE epochs (gray). In color, we only show model components describing the polarized features A (blue) and B (green), if their polarized flux density exceeds the given threshold of 1.4 mJy (3σ). In cases of components that are tracked over more than four epochs, we set a threshold of 1.0 mJy (2σ). The two leading components A 2 and B 2 are highlighted with large, filled squares. The two components A 3 and B 3 that form in the wake of these leading components during the first epochs of the features A and B, but fade quickly, are denoted as stars. We do not trace in detail the evolution of components in the wake of B 2 after 2011.4 due to the increased complexity of the polarized brightness distribution that cannot entirely be described by ballistic Gaussian model components.

Table 4.1. List of all polarized model components as part of the polarized features A and B with corresponding proper motions in units of mas/yr. The leading components A 1/A 2 and B 1/B 2 are followed by the trailing components on the bottom.

A	PA [deg]	μ [mas/yr]	B	PA [deg]	μ [mas/yr]
A 1	66.0±0.4	1.731±0.016	B 1	62.54±1.13	1.67±0.06
A 2 (<3 mas)	67.9±0.6	1.30±0.14	B 2	63.56±0.31	1.483±0.009
A 2 (3 mas – 4.5 mas)		1.56±0.09	B 3	67.6±2.3	0.80±0.12
A 2 (>4.5 mas)	57.90±0.25	1.284±0.021	B 4	69.6±0.7	1.14±0.04
A 3	70.7±2.3	0.91±0.16	B 5	55.56±4.17	1.521±0.014
A 4	68.3±0.5	1.40±0.04	B 6	53.3±0.4	1.180±0.029
A 5	59.3±0.4	0.97±0.04	B 7	41.7±0.8	1.14±0.08
A 6	62.76±0.29	1.15±0.04	B 8	52.7±0.5	0.77±0.06
A 7	69.0±0.5	1.325±0.017	B 9	80.0±0.5	1.12±0.05
			C 1	66.27±1.21	1.20±0.05
			C 2	65.7±1.8	1.09±0.07

polarized flux densities of the parsec-scale jet at nearly all time (Fig. 4.7[4]). The total flux density evolutions of the components A 1 and B 1 are considerably different. A 1 can be tracked over all 36 epochs and only slowly decreases in flux. The component B 1, in contrast, fades within seven epochs. The polarized flux density of both A 1 and A 2, as well as B 2, rapidly increase during their first epochs, which gives rise to the observed peaks in the integrated polarization light curve Fig. 4.4 (panel b) at around 2–3 mas. The components A 3 to A 7 and B 3 to B 11 form behind the leading components of both polarized features and their flux densities are overall lower. We therefore identify them as trailing components in the wake of the leading components.

---

[4] We exclude the polarized fluxes below 2009.2 of component A 7 for further calculations due to their questionable detectability.

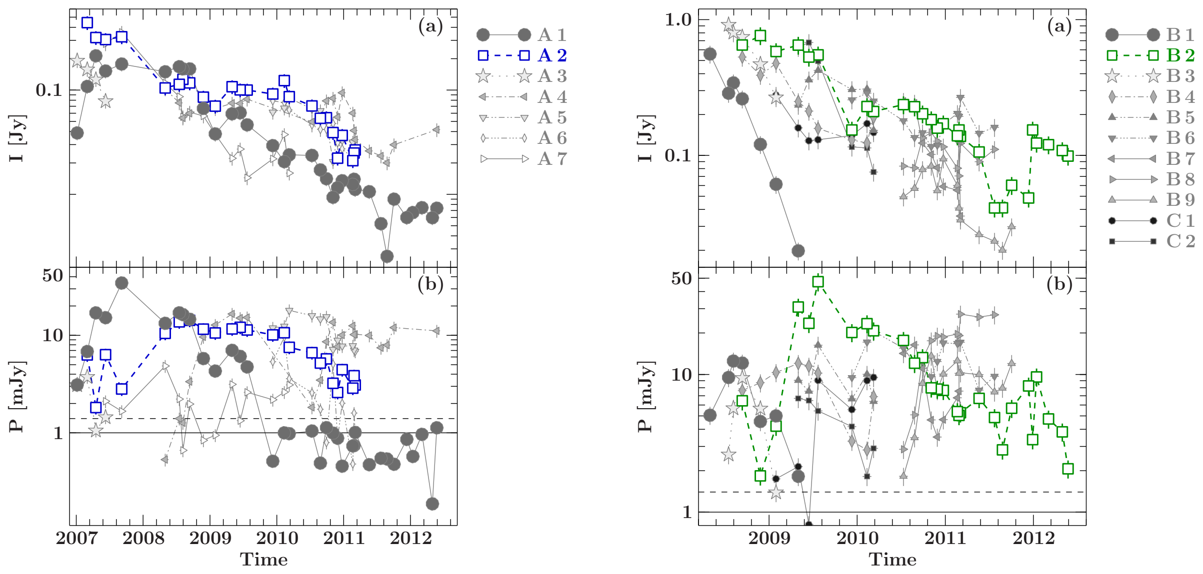

Figure 4.7. Evolution of the total (*top*) and polarized flux density (*bottom*) for selected components of group A and B. For all components the total flux decreases with time. Components identified as trailing components are held in gray. The $2\,\sigma$ $(3\,\sigma)$ thresholds for the polarized components to be considered for the derived quantities in Fig. 4.4 and to be highlighted in Fig. 4.6 are denoted as solid and dashed black lines.

The leading components A 1 and B 1 are both found on ballistic trajectories in (x/y)-space with position angles (PAs) of about 66° and 63°, and show comparable proper motions of 1.731 ± 0.016 mas/yr and 1.67 ± 0.06 mas/yr, respectively. The components A 2 and B 2 follow PAs of about 68° and 64°, respectively. The PA of A 2 changes to about 58° after 3–4 mas. While we find a proper motion of 1.48 ± 0.01 mas/yr for B 2, A 2 cannot be described ballistically but shows signs for moderate acceleration in longitudinal direction from 1.30 ± 0.14 mas/yr (< 3 mas) to 1.56 ± 0.09 mas/yr (3–4.5 mas) before decelerating again to 1.284 ± 0.021 mas/yr (< 3 mas). A similar behavior may be inherent to the component A 1, despite being statistically insignificant. We therefore remain with a ballistical description of the same.

In both polarized features (A and B), we find components with slower proper motions being formed early on (A 3: 0.91 ± 0.16 mas/yr; B 3: 0.80 ± 0.12 mas/yr), both rapidly decreasing in flux density (see Fig. 4.8). The component A 3 loses more than half of its flux density from $\sim$200 mJy to $\sim$80 mJy within less than half a year. This is reminiscent of the similar behavior of component “F” in Kadler et al. (2008), while B 3 shows a more drastic decrease in flux of a factor of five from $\sim$900 mJy to $\sim$250 mJy over four months. The total flux density of both A 3 and B 3 starts off larger than that of the leading components A 1 and B 2, which increase in flux during the decreasing evolution of A 3 and B 3.

In general, all components in the wake of A 1/A 2 and B 1/B 2 have lower proper motions than the leading components (between 0.8 and 1.4 mas/yr). Also, their inherent amount of variability both in total and polarized flux density is overall larger. Amongst these trailing components, the component A 4 forms just after 3 mas from the core with a proper motion of 1.40 ± 0.04 mas/yr and follows a trajectory with a PA of 68.3 ± 0.5°. It subsequently appears to split into A 5 and A 6 at around 4.5 mas from the core, which continue along different PAs of 59.3 ± 0.4° (A 5) and 62.76 ± 0.29° (A 6) at a smaller velocities of about 1.0 mas/yr. If the components A 4, A 5 and A 6 would describe the same underlying perturbation, we could put them into context with component A 2, which shows decelerating behavior downstream of approximately 4.5 mas. Their changing PAs, however, challenge this interpretation.

The polarized feature B describes the most stable polarized region that becomes increasingly

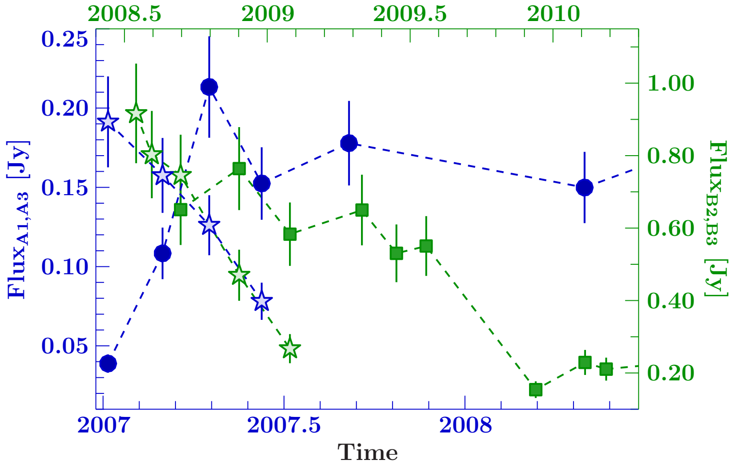

Figure 4.8. Flux density evolution of the short-lived components A 3 (blue stars) and B 3 (green stars) together with the leading components A 1 (blue circles) and B 2 (green circles). Due to their different appearance times, the time axes of both components are also different.

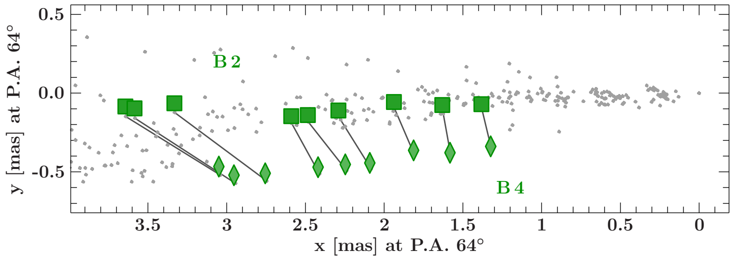

Figure 4.9. (x, y)-plot emphasizing the components B 2 (triangles) and B 4 (diamonds) projected on a PA of 64°. The positions of all other model components are drawn in gray. Gray, solid lines connect the positions of B 2 and B 4 at the same epochs.

complex in later epochs, eventually dominating the polarized intensity of the entire jet. The components B 2 and B 4, seem to emerge out of a single unresolved component with an initial flux density of 1.15 Jy in epoch 2008.6, with B 2 becoming the more dominant and faster component in subsequent epochs (B2: ~1.5 mas/yr; B 4: ~1.1 mas/yr). Figure 4.9 shows the trajectories of both these components. Their velocity difference might reflect a shear within the plasma that we observe as feature B (cf. Discussion).

4.1.3.2 ANALYSIS OF THE BRIGHTNESS TEMPERATURE DISTRIBUTION

We have shown above that the evolution of the EVPAs of both features A and B behave similarly with time and core distance. The consistent orientation parallel to the jet around 3–4 mas from the core and the foregoing drastic increase in polarized flux density, lead us to further study this region. Figure 4.10 shows the dependence of the brightness temperature $T_{\rm B}$ and the sizes of the circular Gaussian model components d over the core distance r.

The brightness temperature has been shown to follow a power law over core distance for samples of AGN jets (Kadler, 2005; Pushkarev & Kovalev, 2012), for the particular case of 3C 111 (Kadler et al., 2008) and for other individual sources (e.g., NGC 1052: Kadler et al., 2004, S4 1030+61: Kravchenko et al. 2016 or 3C 273: Kovalev et al. 2016). We note, however, that the *RadioAstron* Space VLBI resolution allows us to come even closer to the apparent jet base and delivers higher brightness temperatures as expected from an extrapolation of the power law (e.g., Gómez et al., 2016; Kovalev et al., 2016). If the magnetic field $B \propto r^b$, the particle density $N \propto r^n$ and the jet diameter $d \propto r^l$ evolve like power laws with distance r from the core, the brightness temperature can be described as $T_{\rm B} \propto r^s$ (Kadler et al., 2008). The power-law index s (with $s < 0$) can then be expanded as

$$s = l + n + b\,(1 - \alpha) \quad , \tag{4.2}$$

where α is the spectral index, characterizing the flux-density spectrum via $S_\nu \sim \nu^{-\alpha}$.

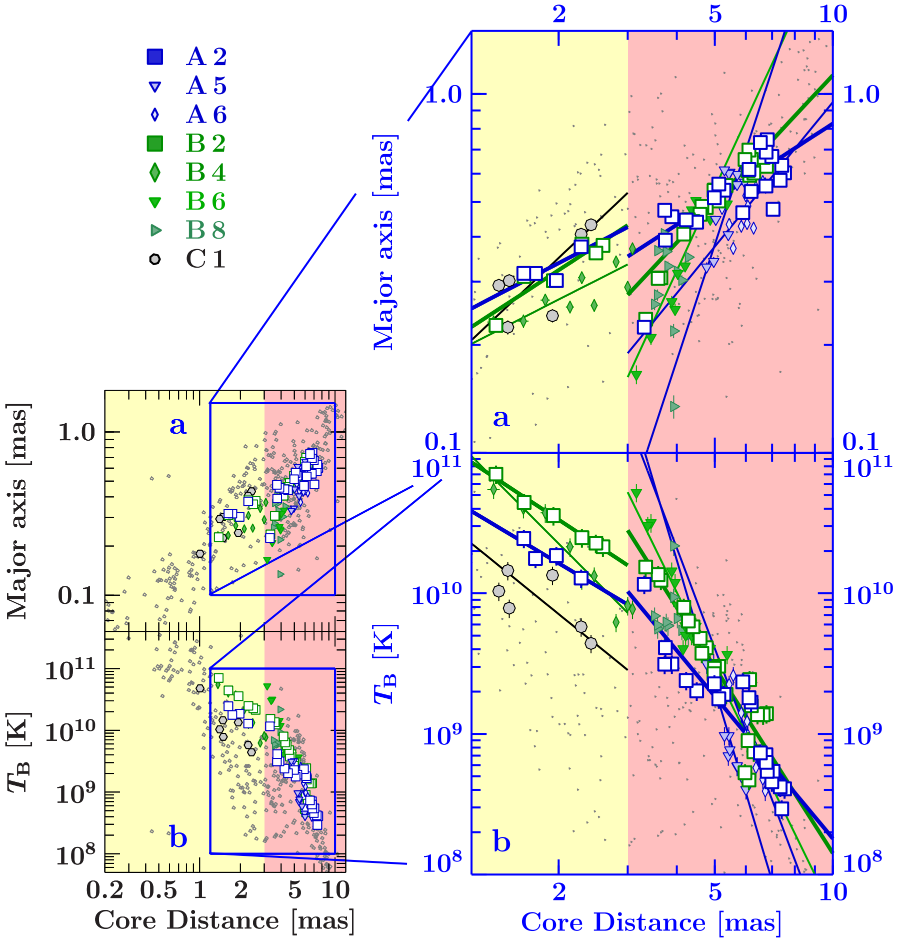

Figure 4.10. Brightness temperature and major axis size against the core distance for all model components of all epochs (gray). The colored symbols correspond to model components that can be associated with the polarized features A and B. The components A 2 and B 2 probe the transition region at around 3 mas and are therefore emphasized with enlarged squares of white filling. Lines correspond to linear regression fits of data up- and downstream of 3 mas.

Figure 4.10 makes clear that this simplified ansatz can successfully describe the measured brightness temperature and jet diameter. We adopt uncertainties of 0.05 mas for r, 15% on T_B and 0.01 mas on d. The latter corresponds to the scatter of all measured major axes. A sudden decrease of the model component sizes is apparent at a distance of around 3 mas from the core. This jump is accompanied by a jump in T_B at that distance for the two components A 2 and B 2 that probe this transition region. We find the size of the component A 2 to decrease from 0.43 ± 0.03 mas to 0.352 ± 0.004 mas and for component B 2 from 0.43 ± 0.02 mas to 0.275 ± 0.003 mas when extrapolating the measured power-laws to the discontinuity at around 3 mas. The extrapolated brightness temperatures increase from $8^{+4}_{-3} \times 10^{9}$ K to $1.03 \pm 0.09 \times 10^{10}$ K for A 2 and from $1.6^{+0.5}_{-0.4} \times 10^{10}$ K to $2.8^{+0.3}_{-0.2} \times 10^{10}$ K for B 2. Two measurements of the brightness temperature $T_{\mathrm{B},1}$ and $T_{\mathrm{B},2}$ are related to the corresponding component sizes d_1 and d_2 by $T_{\mathrm{B},1}/T_{\mathrm{B},2} \propto (d_2/d_1)^2$. We find $T_{\mathrm{B},1}/T_{\mathrm{B},2} = 0.8 \pm 0.3$ and $(d_2/d_1)^2 = 0.82 \pm 0.11$ for component A 2 as well as $T_{\mathrm{B},1}/T_{\mathrm{B},2} = 0.57 \pm 0.16$ and $(d_2/d_1)^2 = 0.64 \pm 0.28$ for B 2. Within the uncertainties, the sudden decrease of the component sizes is consistent with the increase of T_B for adiabatic knots. The other plotted components have an insufficient number of traceable counterparts upstream or downstream of 3 mas and do not add further information to these results.

In Table 4.2 we list the measured indices l and $(s - l)$ upstream and downstream of 3 mas. We exclude component B 8 from the fits that describes an unrealistically steep power law, probably as result of its strongly variable flux density. Compared to a free expansion ($l = 1$), we find reduced expansion rates upstream of 3 mas. Beyond 3 mas, however, several components reveal indices as high as 1–3, averaging ∼1.7. The index combination $(s - l)$ is a measure of the gradients of the magnetic field and the gas density. It shows moderate values upstream of 3 mas and steep values

	$l_{<3\,\mathrm{mas}}$	$l_{>3\,\mathrm{mas}}$	$s-l_{<3\,\mathrm{mas}}$	$s-l_{>3\,\mathrm{mas}}$
A 2	0.57±0.04	0.709±0.004	-2.2±0.2	-4.07±0.03
A 5		3.33±0.01		-12.73±0.05
A 6		1.339±0.006		-8.71±0.04
B 2	0.71±0.03	1.172±0.004	-2.55±0.15	-5.57±0.03
B 4	0.557±0.022		-3.35±0.11	
B 6		2.38±0.01		-8.08±0.06
C 1		1.03±0.04		-3.29±0.18

Table 4.2. Slopes for a power-law relation between the size of the major axis, d, and the brightness temperature T_B against the core distance r ($\propto r^l$ and $\propto r^s$) in log–log space. Data up- and downstream of a distance of around 3 mas are fitted with separate power laws. The component B 8 is excluded from the fits due to unrealistically steep slopes suggested by the data.

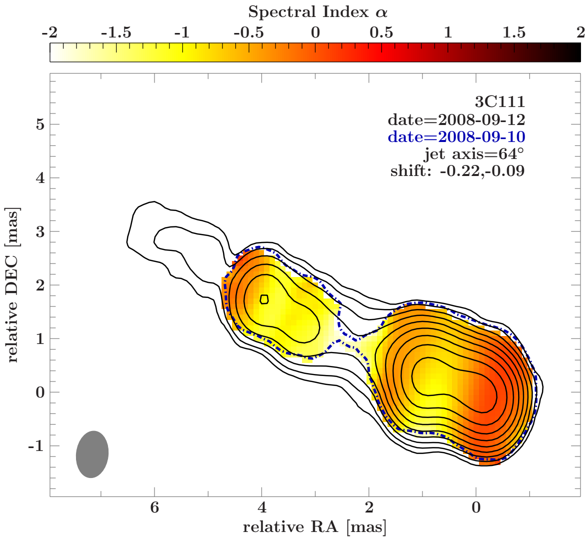

Figure 4.11. Spectral index maps for quasi-simultaneous observations at 43 GHz (BG, epoch 2008-09-10) and 15 GHz (MOJAVE, 2008-09-12). Both maps are restored with a common beam shown on the bottom left and the spectral index $\alpha = \log S_1/S_2/\log \nu_2/\nu_1$ is computed accordingly for each pixel. The required shift of the 43 GHz map relative to the one at 15 GHz is -0.22 mas in right ascension and -0.09 mas in declination. The shift is determined by matching the flux-averaged mean x/y positions of the brightest components in both individual maps under exclusion of the core.

beyond.

To characterize the influence of α on s, we calculate spectral-index maps between 15 GHz and 43 GHz (BG data). We chose four separate epochs during which jet plasma components occupy the region beyond 3 mas and for which closely separated[5] observations at 15 GHz and 43 GHz are available. We compare flux-weighted positions of optically thin regions of the total intensity maps to determine a core shift of $RA = -0.22$ and $DEC = -0.09$ between the two maps (cf., e.g., Kadler et al., 2004). Both maps are restored with a common beam enclosing the two single beams at 15 GHz and 43 GHz. The example map in Fig. 4.11 reveals a pronounced gradient from an optically thick core with a flat power-law spectrum towards optically thin jet emission with $\alpha \sim -1$ downstream of 3 mas – a behavior that is observed in all four analyzed spectral index maps at different times and that is in well agreement with the shock-in-jet model (Marscher & Gear, 1985). As a cross-check, we extract the integrated flux densities from the emission region downstream of 3 mas for both the restored 15 GHz and 43 GHz map and calculate the averaged spectral index using the flux density ratios. We derive consistent values of $\alpha \sim -1$ for all four tested epochs.

The parameter b describes the geometry of the magnetic field and cannot be directly measured with our data. In the idealized cases of a pure toroidal field, a value of $b = -1$ applies. Similarly, $b = -2$ would describe a pure axial field. For these two cases, we can use the measurements of $s - l$ and α to constrain the gradient of the particle density along the jet. We consistently find power laws r^n with the index steepening at the distance of 3 mas from the core from $n_{<3\,\mathrm{mas}} \sim -0.2\,(1.8)$ to $n_{>3\,\mathrm{mas}} \sim -2.1\,(-0.1)$ for component A 2 and from $n_{<3\,\mathrm{mas}} \sim -0.6\,(1.4)$

---

[5] The separation is given by 2, 3, 4, and 6 days for the 43 GHz (15 GHz) epochs 2008-09-10 (2008-09-12), 2011-07-24 (2011-07-21), 2011-02-27 (2011-03-01), and 2009-01-30.

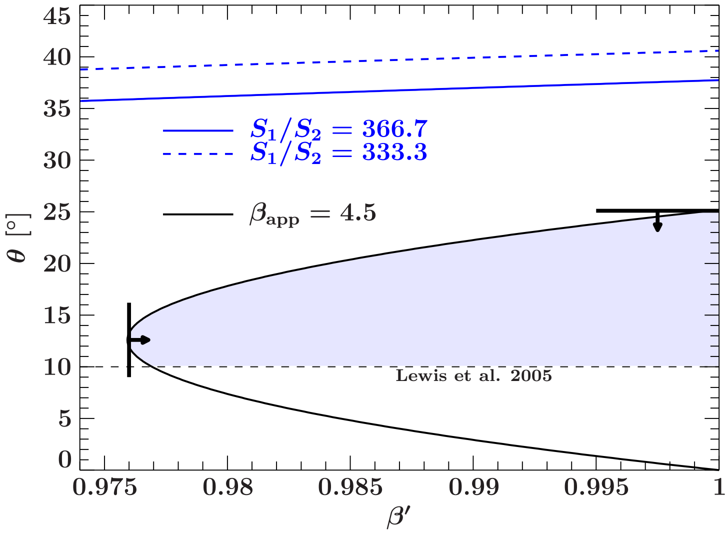

Figure 4.12. Constraints on the intrinsic jet velocity β' and the inclination angle θ based on the average measured apparent speed $\beta_{\text{app}} = 4.5$ for the leading components B 1–B 4 of feature B. Two estimates for the jet-to-counterjet flux-density ratio S_1/S_2 define further constraints drawn as blue lines. The blue-shaded region highlights the allowed parameter space, the thick lines with corresponding arrows define the lower and upper limits on the jet speed and the inclination angle.

to $n_{>3\,\text{mas}} \sim -3.6\,(-1.6)$ for component B 2. The numbers consider a magnetic field with $b = -1$ $(b = -2)$.

4.1.3.3 CONSTRAINTS ON THE VIEWING ANGLE AND THE INTRINSIC SPEED

We estimate the viewing angle θ and the intrinsic jet speed β' using the relation from Eq. 1.42. We choose the observables measured for the components B 1–B 4 that describe the jet just downstream of the core in 2008. Their average apparent proper motion is ~1.27 mas/yr, translating to $\beta_{\text{app}} = 4.5$. We insert β_{app} in Eq. 1.41 and plot the solution for $\theta\,(\beta')$ in Fig. 4.12 as solid, black line. This line both defines the lower limit on the jet speed $\Gamma' \geq (1+\beta_{\text{app}})^{1/2}$, that is, $\beta' \geq 0.976$ and the upper limit on the viewing angle $\theta \leq 2\arctan\beta_{\text{app}}^{-1} = 25.1°$. Independent estimates of the viewing angle were derived by also measuring the Doppler factor via the decline time of ejected knots in addition to their apparent speed (Jorstad et al., 2005). They equally state a possible range of $\theta \sim 10$–$25°$ for a number of observed knots with a weighted average of 18.1°. This range is consistent with an upper limit of 20° found by Oh et al. (2015). We adopt the lower limit of 10° estimated by Lewis et al. (2005) for the large-scale morphology, although lower values cannot be excluded based on parsec-scale kinematics. Extending on the method used by Jorstad et al. (2005), Hovatta et al. (2009) estimate the Doppler factor based on T_{b} variability and find an inclination of ~15.5° when considering an apparent component speed of $\beta_{\text{app}} \sim 5.9$. Both proposed viewing angles are well consistent with our estimate.

Figure 4.12 also shows upper limits based on two estimates of the jet-to-counterjet ratio (see Eq. 1.45). The spectral index α is calculated for the components B 1–B 4 between two MOJAVE epochs at 2008-09-12 and 2009-01-30 as well as quasi-simultaneous archival observations at 43 GHz. We find values of $\alpha = -0.75$ and $\alpha = -0.92$, respectively. The integrated flux density of these components at both epochs are $S_1 = 2.2$ Jy and $S_1 = 1.4$ Jy with corresponding estimates on the counter-jet flux density of $S_2 = 6.0$ mJy and $S_2 = 4.2$ mJy, respectively, when assuming an unresolved counter-jet, if it was detected. Both values of S_2 are upper limits and correspond to $10\,\sigma$ of the background rms, which is a conservative choice. Our estimates using the flux ratios exclude viewing angles above ~35°, while better constraints on the counter-jet flux density could help to further constrain the maximum viewing angle of ~25° set by the measured apparent speed.

Using the estimate on θ, we can also constrain the intrinsic viewing angle to θ' by using the Lorentz-transformation in Eq. 1.46. In Fig. 4.13 we plot this function for a number of values of $\beta' \gtrsim 0.976$. The lower limit on the viewing angle of 10° at a speed of $\beta' \sim 0.976$ establishes

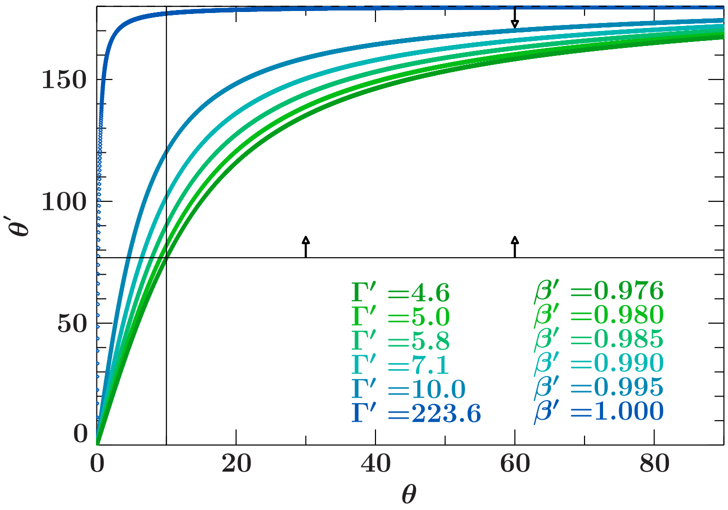

Figure 4.13. Constraints on the intrinsic viewing angle θ' based on previous estimates of the viewing angle in the observers frame and the intrinsic speed β'. We plot the relation $\theta'(\theta)$ for a range of allowed values of β'. The lower limit of $\theta = 10°$ at a speed of $\beta' \sim 0.976$ sets the lower limit on θ'.

the lower limit of $\theta' \gtrsim 76.8°$. When instead inserting the estimates by Jorstad et al. (2005) and Hovatta et al. (2009), who additionally constrain the Doppler factor from flux and T_B-variability arguments, we find $\theta' \sim 108°$ for $\Gamma = 4.4$, $\theta = 18.1°$ (Jorstad et al., 2005), and $\theta' \sim 129°$ for $\Gamma = 7.7$ and $\theta = 15.5°$ (Hovatta et al., 2009).

4.1.4 DISCUSSION

We have reported on the evolution of two features both strong in total and polarized intensity through the VLBI jet in 3C 111. The evolution of both features and their sub-components follows a similar pattern between 2 and 6 mas, which is largely consistent with results from Kadler et al. (2008) and an independent study by Homan et al. (2015). The latter authors suggest a very similar velocity pattern with signs for accelerated motion upstream of 3–4 mas and decelerated motion beyond (see also Asada et al. 2014 for M87). In the following we discuss our results and describe possible scenarios that could explain these observed jet features, which most likely reflect shocked plasma. The observed and derived jet-intrinsic quantities can therefore not be interpreted with respect to the unperturbed flow.

4.1.4.1 INNER 2 MAS FROM THE CORE

Just upstream of 2 mas, we observe unresolved knots in total intensity after emerging from the 15 GHz core (most probably the $\tau = 1$ surface, see Jorstad et al., 2007). These knots become polarized after a few epochs and propagate along the jet with an average proper motion of about 1.6 mas/yr.

4.1.4.1.1 External Faraday shield and magnetic field structure

We observe significant depolarization upstream of 2–3 mas, where the degree of polarization decreases quickly from a level of 5% to nearly zero percent as shown in the Figs. 4.4 and 4.5. Numerical simulations by Porth et al. (2011) demonstrate that the steep drop in the degree of polarization cannot be explained with a smooth gradient in optical depth along the jet. Instead, we propose a foreground Faraday screen, which will, however, be blended with beam depolarization close to the unresolved core (see, however, Gómez et al., 2008, for 3C 120, where beam depolarization is not an issue).

The inner 2 mas are characterized by strongly variable EVPAs with a dynamic range of as large as 90° over two months (see Fig. 4.4, panel d). We test for a possible Faraday screen

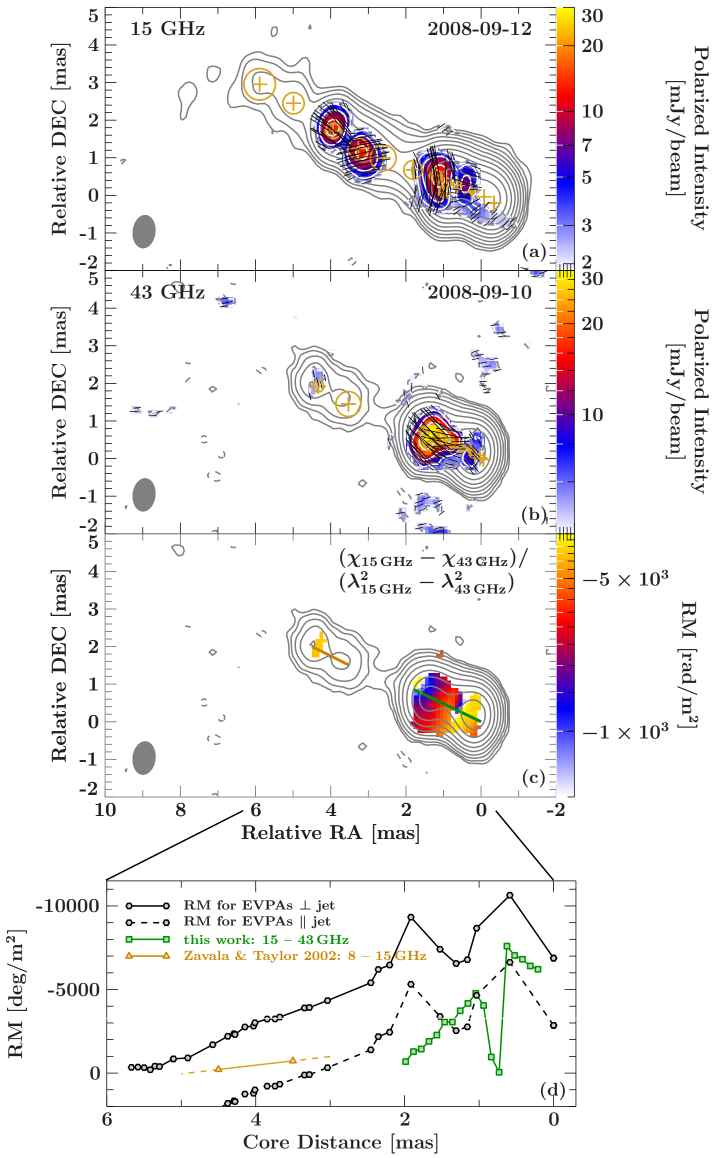

Figure 4.14. RM map (*panel c*) between two adjacent maps at 15 GHz/MOJAVE (*panel a*) and 43 GHz/BG (*panel b*) that have also been used to calculate the spectral index in Fig. 4.11. The polarized emission is overlaid in color on top of the total intensity contours, both at a baseline intensity of 3σ. We only calculate values of RM where we detect polarized emission $> 3\sigma$ both at 15 GHz and 43 GHz. We apply the same relative core shift between the maps at both frequencies as estimated for Fig. 4.11 and the identical envelope beam. *Panel d* shows RM cuts along the indicated ridge lines for our measurement upstream of 2 mas (green squares) and for a measurement by Zavala & Taylor (2002) between 3.5 mas and 4.5 mas (orange triangles). We also show as black solid and dashed lines the RM distribution along the jet that is required to explain the observed EVPA evolution of feature B (Fig. 4.4) with respect to an intrinsically perpendicular and parallel field, respectively.

as a cause of those changes. Figure 4.14 shows the polarized flux-density distribution of two quasi-simultaneous epochs at 15 GHz (MOJAVE) and 43 GHz (BG data) for which we also calculated the spectral index in Fig. 4.11. In both maps, we are sensitive to polarized intensity upstream of 2 mas. We have to note several caveats with respect to the shown RM values. First, the use of only two frequencies introduces strong uncertainties on the measured RM values and the λ^2-law may be broken close to the core (Kravchenko et al., 2017). We therefore have to expect systematic effects especially in the optically thick regime. Further, by measuring the RM coincident for the well polarized feature B, we are sensitive only to the shocked plasma of a single epoch and not the quiescent flow. We are therefore lacking comprehensive RM information for the entire parsec-scale jet both in space and time. For these reasons, we abstain from correcting the measured EVPAs in Fig. 4.4 but provide a qualitative discussion on the expected intrinsic EVPAs and the general RM structure.

In Fig. 4.14 (panels c and d), we observe a strongly varying and double-peaked RM gradient along the jet ridge line. The RM drops rapidly between the core and 2 mas distance with a maximum of $\sim -8000\,\mathrm{rad/m^2}$ just before 1 mas. Following a dip down to 50–100 rad/m^2, a second peak appears around 1 mas at $\sim -5000\,\mathrm{rad/m^2}$. The RM of the two peaks result in

EVPA rotations of roughly 180° and 40°, respectively, while the first can be compensated with the ambiguity of π. Further downstream, Zavala & Taylor (2002) also observe a gradient in RM, but at lower values smoothly ranging from $-800\,\mathrm{rad/m^2}$ to $-200\,\mathrm{rad/m^2}$ between 3 and 6 mas, consistent with results from Hovatta et al. (2012). These low values of RM only have minor influence on the observed EVPAs with a rotation of about 5–16°. They describe a gradient of around 10° rotation over 2 mas distance. This contradicts the observed EVPA rotation rate of around 90° per 2 mas in the region < 2 mas.

We need to ask whether the mapped RM can explain the spatially coincident EVPAs. The strongly variable EVPAs observed upstream of 2 mas in Fig. 4.4 are likely consistent with the observed RM variability in that region. If we assume for simplicity that the RM shield is stable over time and neglect the caveats stated above, we can tentatively infer the intrinsic EVPAs. Figure 4.14 shows with respect to the EVPA evolution of feature B that the intrinsic EVPAs must be aligned parallel to the jet, where the RM peaks, i.e., at values of ~ -5000 and $-8000\,\mathrm{rad/m^2}$. Intrinsically parallel EVPAs are allowed by basic models for an axisymmetric helical magnetic field depending on the viewing angle and the pitch of the helix (Lyutikov et al., 2005; Lyutikov & Kravchenko, 2017). Intrinsically perpendicular EVPAs, however, find support by more realistic simulations considering a helical field entrained by a jet filled with plasma, where the emissivity peaks along the spine (e.g., Roca-Sogorb et al., 2009; Gómez et al., 2016).

Our measurements show that the observed RM gradient can explain the observed EVPA rotation over distance in a small region upstream of about 1.5 mas with respect to underlying parallel EVPAs. The lack of a complete coverage with RM data, however, does not allow us to conclude on the bulk of the EVPA rotation downstream of 2 mas in contrast to a study of 3C 120 (Gómez et al., 2008).

We also need to address, if the mismatch between the RM close to the core (between 15 GHz and 43 GHz) and the downstream jet (between 8 GHz and 15 GHz) is expected. In contrast to the strong gradient in RM upstream of 2 mas, the weaker gradient between ∼3 and 5 mas is likely consistent with the observed decrease in particle density and magnetic field along the jet (cf. Fig. 4.10). As Asada et al. (2008) showed for the example of 3C 273, the observed Faraday screen of its downstream jet does not vary strongly with time. Also, the results of Kravchenko et al. (2017) for a large sample of jets underpin that the increased level of RM close to the inner jet of 3C 111 may be a common feature rather than an effect of temporal variability; it could be naturally explained by the high values of the magnetic field and gas density close to the core. We, however, also emphasize the possibility of NLR clouds in the line of sight (O'Dea, 1989; Wardle, 1998) and propose a fine-grained Faraday shield external to the jet as an explanation for the structural RM variability in Fig. 4.14 (panel c).

The transverse RM gradient indicated around 2 mas distance in Fig. 4.14 may equally be caused by such clouds (see also Gómez et al., 2000, 2008). On the other hand, transverse RM gradients (e.g., Asada et al., 2002, 2010; Croke et al., 2010; Hovatta et al., 2012; Gabuzda et al., 2014), can act as an independent tracer for an underlying helical field. The detection of consistently negative circular polarization for the core of 3C 111 in MOJAVE data (Homan et al., 2006) gives an independent argument for the presence of an ordered magnetic field configuration around the core.

4.1.4.1.2 Component evolution and kinematics

The leading components of both features are divided into three sub-components in our modeling and show different behaviors: although B1 fades in brightness fast, A1 persists and keeps being bright across most of the observing epochs. In both cases, the components A2 and B2 further upstream, dominate in brightness. B2 becomes the leading component of the feature B after B1 disappears. In addition, the components A3 and B3 appear as bright features that fade rapidly and disappear after four epochs (cf. Fig. 4.8). This behavior is similar to that reported for

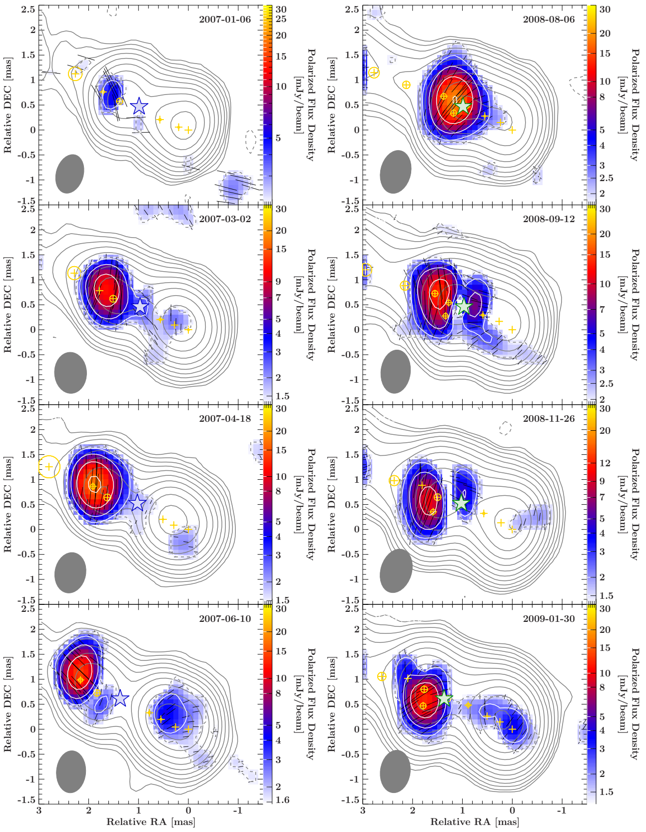

Figure 4.15. Enlarged view onto the first epochs of the polarized features A (*left panels*) and B (*right panels*). The baseline of the polarized flux distribution overlaid in color is set to $3\,\sigma$, equal to the lowest total intensity contours. Contours of polarized intensity are drawn in white. The components A 3 and B 3 in the wake of the leading and strongly polarized patterns are highlighted as blue and green stars, respectively.

the components E (leading) and F (fading) in Kadler et al. (2008), which was studied in terms of the hydrodynamical structure of the perturbation by Perucho et al. (2008). These authors can reproduce this behavior with the injection of a square perturbation in pressure, which is observed as the initially brightest feature (similar to our components A3 and B3). The dynamics of the flow lead to a rarefaction in forward and backward direction, literally eating up the initial perturbation and causing shocked plasma, which we may eventually observe as the components A1 and B2 that move downstream. The backward rarefaction could, if colliding with further injected plasma, form a reverse shock (e.g., Lister & Homan, 2005; Jorstad et al., 2005, for observational evidence for oblique, reverse shocks). There are, however, no clear signs for such a shock in the rear of the leading component, neither in previous (Perucho et al., 2008), nor the present data.

Note that in the present case, the region that Kadler et al. (2008) modeled with only two components, requires a more complex model with three components. It is therefore difficult to give a simple, common frame for the evolution and nature of these perturbations injected in the jet. Still, we emphasize the obvious parallels with the interpretation of Perucho et al. (2008).

The fading components in the rear of the leading components are highlighted in Fig. 4.15, while the latter form the dominant polarized patterns that we interpret as forward shocks. The fading components A 3 and B 3 are only weakly polarized. Their EVPAs, however, show a tendency of being oblique with respect to those of the leading patterns. In principle a change in the intrinsic magnetic field orientation can be plausible for a rarefaction wave due to the smooth changes in both pressure and density in the wake of the leading perturbation (Mimica et al., 2009; Fromm et al., 2016, C. Fromm, priv. comm.).

4.1.4.2 THE REGION BETWEEN 2 AND 4 MAS

Downstream of approximately 2 mas from the core, a large and smooth swing of the overall EVPAs of the polarized features A and B stands out against its preceding highly variable behavior. An analysis of the brightness temperature and feature size with core distance gives valuable insights into the structural evolution of the jet.

4.1.4.2.1 A possible recollimation shock

In Sect. 4.1.3.2 we showed evidence for unusual behavior at around 3–4 mas from the core, i.e., a sudden decrease of the feature size d at a distance of about 3 mas, accompanied by an increase of the brightness temperature T_{B} (similar to Roca-Sogorb et al., 2009) and the polarized flux density of individual model components. We recall that the power-law exponent describing the evolution of the jet radius over distance changes from < 1 to > 1 at around 3 mas. These observations can be interpreted in terms of the presence of an adiabatic compression, i.e., a recollimation shock at about 3-4 mas. A recollimation around the same core-distance has also been proposed by Kadler et al. (2008) for previous MOJAVE data. The lack of a continuous sampling of the observed jet over core distance in Fig. 4.10, however, does not allow a more precise localization of the recollimation, which is itself an extended structure, as it is commonly shown in numerical simulations of conical shocks (e.g., Gómez et al., 1997; Mizuno et al., 2015; Fromm et al., 2016; Martí et al., 2016).

In the analysis presented in Sect. 4.1.3.2, we provided estimates of the power-law indices s and l for the downstream evolution of T_{B} and the jet diameter as well as the spectral index α. As we cannot constrain the index b for the magnetic field ($B \propto r^{b}$) in the relation $s - l = n + b\,(1 - \alpha)$, we provided estimates for the particle density evolution for both a toroidal ($b = -1$) and an axial ($b = -2$) field. Independent of the choice for b, we can show a steepening of the particle density described by a power-law with the index n at the distance, where we claim the recollimation.

4.1.4.2.2 The rotation of the EVPAs

Just before 3–4 mas from the core, the EVPAs of features A and B align with the jet after performing a rotation of roughly 90°. After crossing this region, another gradual rotation of around 90° is observed towards 7 mas. The stacked polarization maps in Fig. 4.5 together with our time-resolved analysis substantiate that the large 180° swing happens both in space and in time and is related with the passage of the components.

Lyutikov et al. (2005) consider a toy model to explain large jumps of the EVPA. This model comprises an axisymmetric magnetic field constraining a hollow cylindrical jet and infer corresponding polarization properties. It has to be asked, if this configuration alone can explain the observed large EVPA swing. Figure 4.16 shows the expected, integrated degree of polarization for such an axisymmetric helical field in a hollow-jet geometry. We show multiple solutions for a range of intrinsic pitch angles ψ' between 20° and 90° (from the bottom to the top). In the expression given by Lyutikov et al. (2005) negative and positive values correspond to orthogonal and aligned EVPAs, respectively. Above $\psi' = 50°$, the field is getting toroidally dominated featuring EVPAs aligned with the jet. The degree of polarization will be maximal for a pure toroidal field with $\psi' = 90°$ a pure axial field for low pitch angles. A discrete 90° swing of the observed EVPA can thus occur by changes in the intrinsic pitch angle. Changes in the EVPA orientation can also occur with changing viewing angle only for a particle distribution of lower power-law index ($p < 3$) and for a small range of pitch angles (Lyutikov & Kravchenko, 2017). In Sect. 4.1.3.3, we determined a lower limit on the intrinsic viewing angle of $\theta' = 76.8°$ for 3C 111 based on the range of viewing angles in the observers frame of $\theta = 10°$–$25.1°$. The allowed range for θ' with respect to our kinematics is shown as gray-shaded region in Fig. 4.16. The independent estimates of $\theta' \sim 108°$ and $\theta' \sim 129°$ based on inclination angles proposed by Jorstad

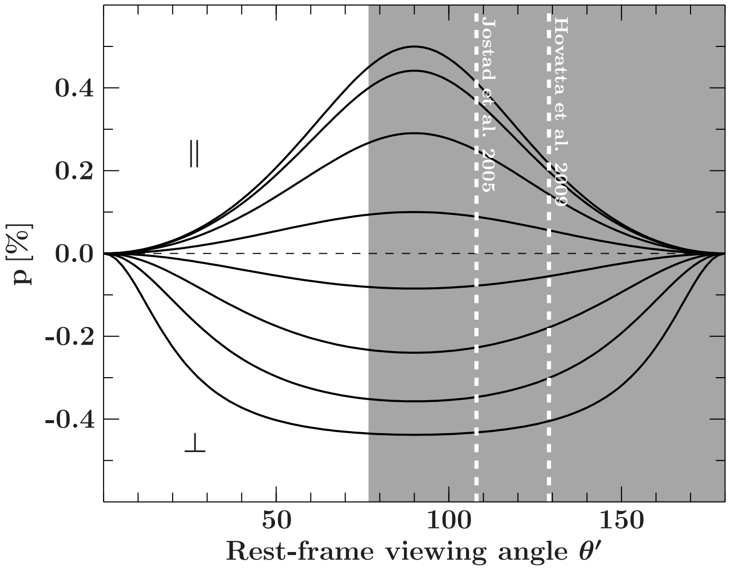

Figure 4.16. Degree of polarization for a range of rest-frame viewing angles θ' onto axial-symmetric helical magnetic fields in a hollow cylindrical geometry. The estimated range of θ' for 3C 111 is highlighted as a gray-shaded region with two independent estimates based on inclination angles stated in the literature (white dashed lines). Negative values of p correspond to an integrated EVPA perpendicular to the jet axis, positive values result in parallel EVPAs. The solid black lines represent a range of intrinsic pitch angles ψ' with steps of 10° between 20° and 90° from the bottom to the top. This example corresponds to the analytical expression provided for a particle distribution $N(E)dE \sim E^p dE$ with $p = 3$ in Eq. 21 by Lyutikov et al. (2005).

et al. (2005) and Hovatta et al. (2012) are marked as white dashed lines. Our observations of a polarization degree of ∼10%–20% would be consistent with this model for pitch angles around ≃60°–70° in case of a toroidal field or for pitch angles around 40–50° in case of an axial field.

In summary, the EVPA distribution would appear as bimodal, depending on the dominant component of the field, and only changes in the degree of polarization would be expected. Such bimodal distributions have been observed in large samples of blazars (Bridle, 1984) with the majority of VLBI knots in BL Lac objects showing aligned EVPAs (Gabuzda et al., 1994, 2000; Lister & Smith, 2000). While an axisymmetric helical field can only explain discrete switches by 90°, further explanations are needed to explain the smoothness of the EVPA swing that we observe in 3C 111 and the intermediate angles.

Assuming the presence of a conical recollimation shock, the rotation could be explained with bright features evolving into and out of the tip of the conical shock as well as the magnetic field in that area. The passage may also result in changes of the underlying field, which should be fairly symmetric in such a scenario. One also has to face the non-negligible distortions that such a non-linear interaction must induce in this simple picture. Unfortunately, RMHD simulations that tackle this scenario are still missing. We therefore use simplified assumptions to compare our observations with. Using calculations described by Cawthorne (2006), Agudo et al. (2012) could successfully explain the particular EVPA distribution of a downstream standing feature (associated to a recollimation shock) in 3C 120 with a radial or Y-shaped pattern of EVPAs being aligned along the central ridge and oblique EVPAs towards the edges. Cawthorne et al. (2013) observe a similar pattern for the core of S5 1803+784, equally arguing for the presence of a recollimation shock from their modeling. On the contrary, the TEMZ model, where the scenario is modeled with turbulent plasma propagating over a conical recollimation shock (Marscher, 2014), gives no systematic rotations of the polarization angle, but only random changes. In steady situations, that is, when there is no interaction with a traveling component, these results therefore demonstrate the peculiar influence of conical shocks on the observed polarization signatures. For 3C 111 we also see indications for a similar Y-shaped EVPA pattern but caution that the situation is more complex, probably involving a dynamic shock-shock interaction (see, e.g., Fromm et al., 2016, for a relativistic hydrodynamics study).

Perlman et al. (2011) explained a large EVPA rotation in the optical/UV nucleus of M87, similar to the one reported here, by considering a helix with a locally superimposed kink traveling through a planar shock. This shock compresses the field and gives rise to polarized emission. In absence of the kink, the authors claim that aligned EVPAs should be expected, just as observed in M87 previous to the detection of the rotation. The modulation of the viewing angle due to the kink can in turn explain the observed long-term EVPA rotation (see also Lyutikov et al., 2005; Lyutikov & Kravchenko, 2017). A planar shock, however, would disrupt the flow (e.g., Perucho et al., 2007) and therefore contradict the large-scale morphology of a FR II galaxy.

Lyutikov et al. (2005) offer an analytic solution also assuming that the flow is threaded by a helical field of decreasing pitch angle towards its central spine. The larger spine emissivity causes observed EVPAs that are always perpendicular to the jet. RMHD simulations with full polarized radiative output have been designed to study steady-state jets forming weak recollimation shocks (Roca-Sogorb et al., 2009; Gómez et al., 2016). For the selected jet velocities, intrinsic pitch angles, and viewing angles, the polarization resulting from these simulations typically show perpendicular EVPAs to the jet, in agreement with the analytic model. Note, however, that our RM data favor intrinsically parallel EVPAs in certain regions within $< 2\,\mathrm{mas}$ from the core.

We can tentatively address a simple explanation for our detection of a continuous and apparently symmetric rotation of the EVPAs across the region in which the jet seems to undergo a recollimation. Here, we refer to the aforementioned results but neglect the influence of the patchy Faraday screen upstream of 2 mas. If the bright features are interpreted as shocks traveling along the jet spine, we expect this region to be bright and show dominance of the poloidal field, as the toroidal field is stretched by the faster flow, and result in EVPAs that are perpendicular to the jet. At the interaction with the conical, standing shock, the toroidal magnetic field is progressively strengthened across the jet section and the EVPAs tend to be aligned with the jet. Finally, downstream of the shock, the flow progressively returns to the previous situation, in which the brightest, central region, dominates the polarized emissivity with a dominant poloidal field. This scenario fits well into the results of Lister & Smith (2000) and Kharb et al. (2008), where presumable quiescent quasar jets show signs for an overall axial magnetic field as opposed to shocked quasars, where larger fractions of toroidal fields have been found. As outlined in the beginning of this section, the intermediate angles cannot be described solely by changes in the pitch angle of the helix but potentially by the interaction of the propagating shock with the recollimation shock – a question that future RMHD simulations need to answer. The dynamic nature and complexity of the process must therefore be disassociated from the toy model shown in Figure 4.16, which can successfully explain a dichotomy between a parallel and perpendicular orientation but not the continuous distribution of EVPAs.

There is an additional effect that should not be neglected with respect to the dominance of the poloidal field: Figure 4.9 shows the evolution of the two adjacent components B2 and B4 between 1 mas and 3 mas. The components are located at a central and peripheral position in the jet, respectively, and show different velocities, with the central component, B2, being faster. These differential flow dynamics possibly reveal a transverse structure of jet velocity that can explain the generation of a strong poloidal field component not only along the jet center but also within a shear layer at the jet boundary due to the stretching of the lines. This effect has been previously proposed by, e.g., Laing (1980, 1981), Cawthorne et al. (1993a), and Wardle (1998). The frequent observation of perpendicular EVPAs at the jet boundary and aligned EVPAs at the center (O'Dea & Owen, 1986; Attridge et al., 1999; Giroletti et al., 2004; Pushkarev et al., 2005) seem to confirm a scenario where the sheared-layer stretching of the field lines dominates. Differential flows have also been observed in modern simulations of parsec-scale jets that show the stretching of lines at the jet shear layer (Roca-Sogorb et al., 2009), and in MHD simulations of kiloparsec-scale jets, which show this effect for the whole jet cross-section (Matthews & Scheuer, 1990; Gaibler et al., 2009; Huarte-Espinosa et al., 2011; Hardcastle & Krause, 2014). Observational evidence is provided, e.g., by Kharb et al. (2008), Gabuzda et al. (2014), and also for 3C 111 by Kadler et al. (2008). This effect reinforces the dominance of transverse EVPAs before and after the

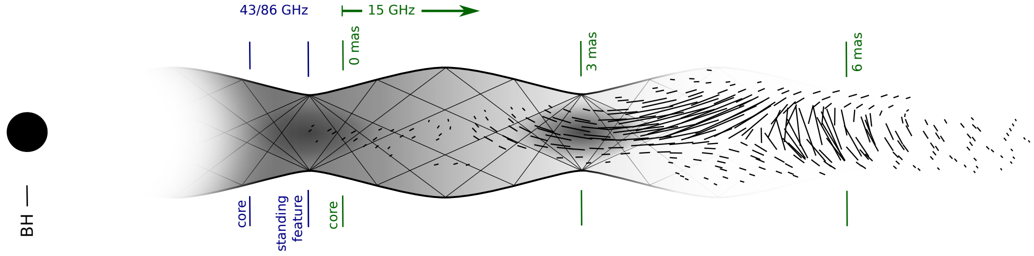

Figure 4.17. Illustration of the relevant observed features mixed with the theoretical prediction of a continuously expanding and recollimating flow (e.g., Daly & Marscher, 1988; Gómez et al., 1997) with an entrained particle distribution with downstream decreasing density ($\propto r^n, n < 0$). Standing features observed at 43 GHz and 86 GHz are interpreted as the first recollimation shock downstream of and in close vicinity to the cores at these frequencies. The distance to the black hole is unknown for 3C 111. The second recollimation shock is observed at 3 mas for the 15 GHz data. We detect no signs for further recollimations. Overlaid, we plot the EVPAs from the stacked image in Fig. 4.5. The orientation of these EVPAs appears to be perpendicular to the jet in absence of the recollimation and parallel on top of it.

interaction of the traveling features with the standing shock.

4.1.4.2.3 Estimate of the Mach number and magnetization

If the change in the EVPA direction is caused by the presence of a recollimation shock, we can obtain valuable insight into the jet parameters by knowing the location of different standing shocks as well as their transverse extent (Martí et al., 2016). There are indications for standing features close to the mm-core in VLBI images at 86 GHz by Schulz et al. (2017, in prep.), with a distance of ~0.1 mas and at 43 GHz by Jorstad (priv. comm.) with two stationary components of average distances of 190 µas and 410 µas. The evidence collected indicates the presence of a first recollimation shock in close vicinity to the millimeter core and a second one at around 3 mas. This provides evidence for the detection of multiple recollimation shocks in 3C 111, similar to, e.g., BL Lac (Gómez et al., 2016; Mizuno et al., 2015), CTA 102 (Fromm et al., 2013, 2016) or 3C 120 (León-Tavares et al., 2010; Roca-Sogorb et al., 2010; Agudo et al., 2012). Based on this evidence, we can estimate the Mach number and present qualitative constraints on the magnetization of the flow.

When we neglect the shift between the cores at 43 GHz/86 GHz and 15 GHz due to synchrotron self-absorption, we can use the inferred distance of ~3 mas between the 15 GHz core and the downstream recollimation as an approximation to the distance between two standing recollimation shocks (see Fig. 4.17). The deprojected separation has been determined to range between 7.6 and 18.6 mas (2.2–$5.3 \times 10^5\, r_\mathrm{s}$), depending on the jet viewing angle (see Sect. 4.1.3.3). Although this recollimation shock is likely not the first one along the jet, the order of magnitude compares well with distances of recollimation shocks of around $10^5\, r_\mathrm{s}$ for the examples of M87, CTA 102 or BL Lac.

Martí et al. (2016) have performed RMHD simulations to study the internal structure of overpressured jets that form a series of recollimation shocks, covering a wide range of the jet magnetization and internal energy. They report on the correlation between the magnetosonic mach number $\mathcal{M}_\mathrm{ms}$ and the half-opening angle of the flow, that is, $\tan\phi = 2d/D \sim 1/\mathcal{M}_\mathrm{ms}$ (with d the jet radius at its maximum expansion and D the distance between two recollimation shocks). We find that the jet of 3C 111 is resolved at 3 mas (Kovalev et al., 2005; Lobanov, 2005) with a FWHM of approximately 1 mas. This value gives a lower limit to the jet expansion radius because (I) the jet flow can be wider than the visible radio jet, and (II) the location of the maximum jet expansion is unknown. Therefore, from this value and the distance between shocks, we obtain an upper limit of $\mathcal{M}_{\rm ms}$. The values that we obtain are $\mathcal{M}_{\rm ms} \lesssim 7.6$–$18.6$.

The Mach number is defined in Eq. 1.38 and depends on the Lorentz factor of the jet and the one associated with the fast magnetosonic speed, that is, $\Gamma_{\rm j}$ and $\Gamma_{\rm fms}$, as well as the jet speed $v_{\rm j}$ and the fast magnetosonic speed $c_{\rm fms}$. Here, we set $c = 1$ and therefore $v_{\rm j} = \beta_{\rm j}$. The observed superluminal components and the large internal jet speed, estimated in Sect. 4.1.3.3, allow us to approximate $\beta_{\rm j} \simeq 1$, i.e., $\mathcal{M}_{\rm ms} = \Gamma_{\rm j}/(\Gamma_{\rm ms}\, c_{\rm ms})$. The values obtained for the magnetosonic Mach number ($\lesssim$7.6–18.6) allow us to approximate $\Gamma_{\rm ms} \simeq 1$ as otherwise the bulk Lorentz factor needs to be large. Finally, we obtain $\mathcal{M}_{\rm ms} = \Gamma_{\rm j}/\, c_{\rm ms}$. Under these assumptions and considering Fig. 15 from Martí et al. (2016), the jet will be kinetically dominated for bulk Lorentz factors $\Gamma_{\rm j} \lesssim 4.8$–$11.6$, which are of the order of those found for this jet (see Sect. 4.1.3.3). When we insert the lower limit on the jet speed $\beta_{\rm min} \sim 0.976$ close to the inclination angle of $\theta_{\rm min} = 10°$ and the corresponding upper limit on the Mach number $\mathcal{M}_{\rm ms,max} = 18.6$ into Eq. 1.38, we can establish a lower limit of $c_{\rm ms,min} = 0.23$. Following Martí et al. (2016), this places the jet of 3C 111 well inside the kinetically dominated regime. Independent measurements of the jet speed and inclination angle by Jorstad et al. (2005) and Hovatta et al. (2009) result in magnetosonic speeds of $c_{\rm ms} = 0.38$ and $c_{\rm ms} = 0.53$, respectively, favoring a jet being kinetically dominated or just at the transition of being Poynting-flux dominated.

Our calculation would fail if the jet width that we have used is much smaller than the real maximum expansion of the jet, or if the jet speeds are unrealistically large. This section is based on the assumption that there is a recollimation shock located at $\simeq$3 mas from the radio-core.

4.1.4.2.4 Alternative explanation: a static kink

The 15 GHz jet in 3C 111 does not show changes in the viewing angle to the jet based on its linear ridge line at 15 GHz, which could induce rotations of the observed EVPAs (Lyutikov & Kravchenko, 2017), although Schulz et al. (2017, in prep.) find a bend of the jet at 86 GHz within the first 2 mas. We also observe that the degree of polarization is evenly distributed within the jet cross-section. We can therefore neglect possible changes observed in the EVPA direction along the jet due to changes in local viewing angle, as it has been claimed for other sources (Agudo et al., 2007; Molina et al., 2014).

Nevertheless, Fig. 4.5 shows hints of a kink both in the trajectory of the components (see, e.g., the yellow dots in the bottom panel) and in the structure of the polarization vectors (top panel). This leaves the interpretation of the evolution in this region open to the possibility that components are going through a static kink of the magnetic field. Following Mizuno et al. (2007) if the kink is caused by a CD instability this would mean that the characteristic radius of the helical magnetic field in the kinked region is larger than the radius of the velocity shear. On the contrary, if the kink is propagating downstream with a velocity small enough that the span of our observations does not allow us to detect significant motion, Mizuno et al. (2007) claim that the characteristic radius of the field is smaller than the radius of the velocity shear. This is a plausible scenario if the polarized emission is mainly produced by the jet spine, and if there is a velocity shear between this spine and the surrounding layers (suggested in the previous sections). If the kink is caused by a KH instability, we would expect a slow rotation of the kink position with time across the jet. Therefore, we need additional observations to study this possibility.

4.1.4.3 THE JET BEYOND 4 MAS

Beyond the suggested recollimation shock, the expansion rate increases to values larger than one. Also, the density gradient becomes steeper, as obtained from the evolution of the component diameter and brightness temperature with distance. These results seem to indicate a freely expanding jet, possibly because of a steepening of the ambient pressure profile, compatible with the interpretation of foregoing MOJAVE data by Kadler et al. (2008). We also find a number of new components that form in the wake of the leading components A 2 and B 2. These new components can be interpreted as trailing features (Agudo et al., 2001; Jorstad et al., 2005). The oscillation that is produced in the rear of the leading component can affect the entire jet cross-section and can be strong enough to produce conical shocks, which themselves propagate downstream and are sufficiently bright to be detected (Agudo et al., 2001; Mimica et al., 2009; Fromm et al., 2016). Again, these conical shocks can produce different polarization structures from the forward shock (Jorstad et al., 2005). In agreement with this, the EVPAs in the wake of the leading shock in feature B are in fact consistently tilted by around 30°–50° towards the west.

The region downstream of the recollimation is characterized by a smooth and consistent 90° eastward swing of the EVPAs of both features A and B from being aligned with the jet at the recollimation to a perpendicular orientation. This swing has been explained in the previous section with a helical field stretched out towards being poloidally dominated due to both a velocity gradient along the fast spine and a velocity shear caused by the bulk flow of the jet. Such a stretched, poloidal field would give rise to EVPAs being predominantly oriented perpendicular to the jet, which is also predicted by numerical simulations (e.g., Huarte-Espinosa et al., 2011; Hardcastle & Krause, 2014). Sample studies have revealed transverse EVPAs to be typical features of FR II jets (Bridle, 1984; Hardcastle et al., 1997; Gilbert et al., 2004) and for milliarcsecond quasars (Cawthorne et al., 1993b,a; Bridle et al., 1994; Lister & Smith, 2000).

4.1.5 SUMMARY AND CONCLUSIONS

We have investigated the complex evolution of the jet flow that originates from millimeter-wavelength outbursts just before 2006 (outburst A), 2008 (outburst B), and 2009 (outburst C). This flow is significantly polarized and can be equally divided into the polarized features A, B, and C, with the dominant features being A and B. As part of the flow, individual superluminal features are tracked and characteristic parameters are recorded both in time and core distance, i.e., the (polarized) flux density, brightness temperature and feature size. We summarize our key observational results as follows:

1. Upstream of 2 mas the EVPAs are strongly variable with time, which has a potential de-polarizing effect, just as observed. Also, a strong RM gradient between 15 GHz and 43 GHz across that region can be explained with the drop-off of a clumpy or fine-grained foreground Faraday screen downstream of 2 mas. We infer the intrinsic EVPAs to be aligned with the jet in parts of this region.

2. At 3–4 mas we find indications for a recollimation shock based on a sudden increase of the brightness temperature accompanied with a decrease in feature size for individual components. Also, the polarized intensity reaches large values in that region. The power-law index describing the growth of the components increases moderately from values of 0.5–0.7 to 1–3 at ∼3 mas, while the particle density gradient steepens significantly. This standing shock is likely attached to an upstream recollimation close to the millimeter core. Our Mach number estimates put the parsec-scale jet well into the kinetically dominated regime, or just at the transition to being Poynting-flux dominated. Our results are also in line with Sikora et al. (2005), who argue against a Poynting-flux dominance of the downstream jets of FR II radio galaxies.

3. From a stacked epoch polarization image, we observe the general trend of EVPAs to lie transversely to the jet upstream of about 2 mas (disregarding the clumpy Faraday screen) and downstream of about 4 mas as well as being aligned around the location of the recollimation. Individual polarized patterns follow this pattern on their downstream track.

The complete rotation of ∼180° ranges across a distance of 6 mas, that is, approximately 20 pc deprojected distance and takes about four years for each feature. We propose a simplified picture for the interpretation of these observations: a differential transverse velocity pattern that finds support by our observations, can lead to a shear between boundary layers and result in an axial magnetic field. A faster spine can also stretch out the underlying field, supporting a global poloidally dominated field, that is, transverse EVPAs, as also confirmed by steady-state simulations. 3C 111 therefore fits well into the common frame of FR II galaxies, where jets typically show a dominance of transverse EVPAs. Our observation of aligned EVPAs in between can likely be the result of the interaction of ejecta with a standing shock that may be able to enhance the toroidal field component. Detailed RMHD simulations with full radiative output (including polarization) are needed to test this hypothesis with respect to a dynamical shock-shock interaction. We emphasize that an axisymmetric helical magnetic field with changing pitch angle can still only explain either parallel or perpendicular EVPAs with respect to the jet direction.

4. Due to the lack of complete RM information along the entire parsec-scale jet, we cannot exclude a RM gradient to be responsible for the large EVPA rotation. Our observations still require an additional process to explain the bulk of the smooth rotation of about 180° downstream of 2 mas and the intermediate angles.

5. Beyond 4 mas the stacked polarized maps indicate an extended region of significant polarization. We detect trailing features in that region that may indicate secondary pinch mode perturbations in the wake of the leading shock. The EVPAs all lie transverse to the jet, which fits in the picture of a global axial magnetic field. The Faraday screen is negligible beyond 4 mas. We propose a velocity gradient transverse to the jet to result in a shear and therefore a stretched, poloidal magnetic field.

4.2 THE DISK-JET CONNECTION – ON THE ORIGIN OF γ-RAYS IN 3C 111

4.2.1 INTRODUCTORY REMARKS

As outlined in Sect. 4.1.1, the peculiar radio galaxy 3C 111 shows properties that are reminiscent of both blazars and Seyfert galaxies in its broad-band spectrum (Clautice et al., 2016). The SED shows double-humped emission up to GeV energies (Hartman et al., 2008, and Fig. 4.18 for a version that is compiled with radio, UV and X-ray data from within the time-interval considered in this thesis). The soft energy hump is consistent with non-thermal synchrotron emission. The high-energy emission can be both described by thermal Comptonization emission from the corona and/or a non-thermal Comptonization continuum as part of a single-zone SSC model (de Jong et al., 2012; Tombesi et al., 2013b). It is subject of this and future studies to break this model degeneracy.

In recent years, the widely discussed and yet open questions of the location of the γ-ray emitting site in radio jets and how jets are launched (e.g., Ghisellini & Tavecchio, 2008) has been addressed with studying (correlated) multi-band variability from the radio to the γ-rays.

Simultaneous studies of a large set of blazars and radio galaxies both at the intermediate radio frequency of 15 GHz (Lister et al., 2009b) and in the γ-rays with *Fermi*/LAT (Atwood et al., 2009) led to the firm detection of coincident γ- and radio flares (Pushkarev et al., 2010). The γ-ray emitting site was therefore constrained to lie within the 15 GHz radio core. When sources are observed at higher radio frequencies, the $\tau = 1$ SSA surface is pushed further upstream and the inner jet closer to the launching site can be observed. At such high frequencies, León-Tavares et al. (2010), Schinzel et al. (2010), Agudo et al. (2011a), and Fuhrmann et al. (2014) found a positive time-delay between the radio and γ-rays. For the first time, these delays made it

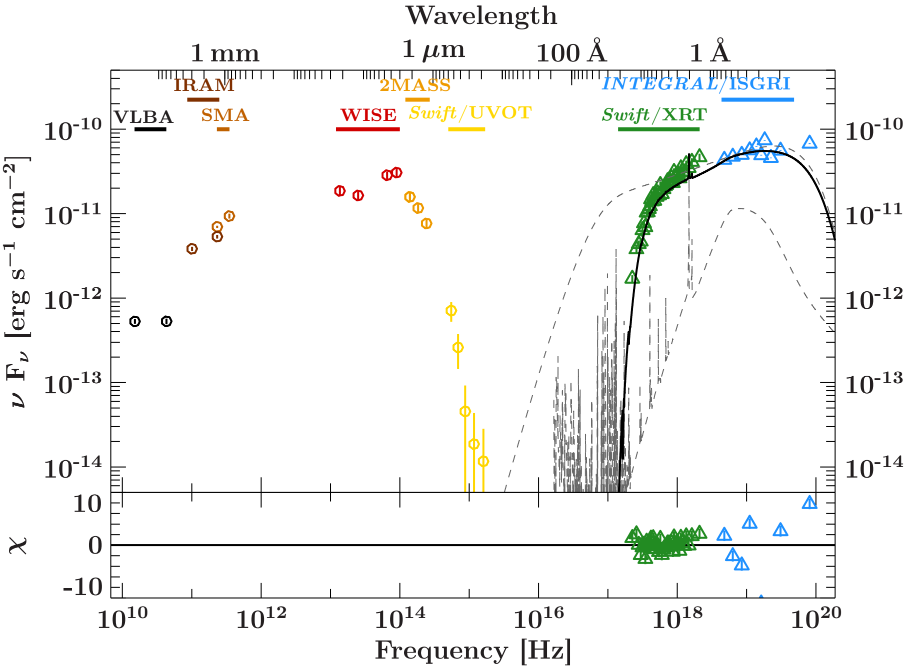

Figure 4.18. Broad-band SED of 3C 111. The VLBA, IRAM, and SMA flux-density points are weighted averages over the time range probed in this work (2007–2012). We show integrated core+jet flux densities from the VLBA and the SMA. The WISE (Wright et al., 2010) and 2MASS (Skrutskie et al., 2006) data are extracted from the All-Sky Source Catalog. The UV and X-ray data result from observations with *Swift*/UVOT and XRT on 2008-11-16. The hard X-ray *INTEGRAL*/IBIS/ISGRI spectrum has been obtained in the time-interval considered in Sect. 4.1 using the HEAVENS online tool (Walter et al., 2010). The black, solid curve represents a model of an incident power-law (upper dashed curve) that is getting reprocessed in an accretion disk (lower dashed curve with prominent emission features). It fits the XRT data well with $\chi\,(\mathrm{dof}) = 47\,(34)$. The statistics worsen when including the *INTEGRAL* data due to their scatter and systematic uncertainties that are not included here. The residuals corresponding to the X-ray model are shown in the bottom panel.

possible to estimate the distance of the γ-emitting site from the radio core at the corresponding radio frequency. Correlated variability between γ-rays and high-frequency radio emission is only significant for quasars and FR II radio galaxies. Fuhrmann et al. (2014) establish an equally positive correlation using radio-flares at highest frequencies of up to 142 GHz (Fuhrmann et al., 2007; Angelakis et al., 2010, for the F-GAMMA program) and *Fermi*/LAT data for 90 blazars. They find the radio to lead the γ-rays with 12 ± 8 d at 86 GHz. Note that not all γ-ray flares are also accompanied by a radio flare (e.g., Casadio et al., 2015).

When the jet inclination can be constrained as for example for 3C 279 (León-Tavares et al., 2011), this source shows a de-projected distance of the gamma-emission site from the radio core of $\sim$ 12–13 pc. This compares well with OJ 287 (Agudo et al., 2011a) or 3C 345 (Schinzel et al., 2010). Note, however, that *Fermi* light curves do not provide sufficient resolution to map the onset of flares as it is possible in the radio.

The opacity barrier can be pushed even further upstream well into the AC zone (Sect. 1.2.5.3) when observing jet-dominated sources in the optical. The observation of delayed variability with flares observed by *Fermi*/LAT should give the most precise estimates on the location of the γ-ray source (e.g., Larionov et al., 2008; Abdo et al., 2010; Arshakian et al., 2010; León-Tavares et al., 2010; Marscher et al., 2010; Casadio et al., 2015; Kiehlmann et al., 2016; Myserlis et al., 2016). In the special case of PKS 1510−089, Marscher et al. (2010) even observed a series of coincident optical and γ-flares arguing for multiple γ-emission sites, i.e., both within the AC region and approximately coincident with the millimeter radio core.

Pinpointing the source of γ-rays has strong implications on jet modeling (see Sect. 1.2.5.3), the relevance of SSC or EC mechanisms and thus the origin of the seed photons: those can either be synchrotron photons from the jet itself (Schinzel et al., 2010; Casadio et al., 2015) or from the BLR (León-Tavares et al., 2011). So far, radio–γ correlation studies suggest that photons must at least be upscattered close to the black hole (Lobanov, 2010; Arshakian et al., 2010; León-Tavares et al., 2010) making a jet-external photon field a probable source. Prominent and intriguing jet features at that distance are recollimation shocks (Agudo et al., 2011b; Marscher, 2014).

In rare cases, jetted AGN enable a direct line of sight also onto their thermal X-ray corona, as for example 3C 111 and 3C 120 (Marscher et al., 2002; Marscher, 2006). For these sources, we can study both the processes of accretion and jet ejection at the same time. From what is known from microquasars (Mirabel & Rodríguez, 1998; Fender & Belloni, 2004; Neilsen & Lee, 2009), jet activity is closely related to structural changes in the accretion disk (Belloni, 2001) or even the disappearance of the inner disk. For AGN as up-scaled black-hole accretors, such changes in the disk can hardly be observed in real time although disk variations have been measured (e.g., Arévalo & Uttley, 2006; McHardy et al., 2014, 2016). If a part of the inner disk gets accreted and ejected as visible radio feature, the disk seed photon field decreases. This causes the reprocessed X-rays to dip. Such X-ray dips have been observed in correlation with flares at millimeter wavelengths for 3C 111 and 3C 120 (Marscher et al., 2002; Marscher, 2006) and thus have strong implications on jet launching theories such as that of Blandford & Znajek (1977). A fluctuation in the accretion flow could cause an electric field to build up close to the jet launching site and form a vacuum gap (see Sect. 1.2.5.2). In the compact corona, photons above 511 keV can undergo electron/position pair production thus shorting-out the electric field in the gap. In strong FR II quasars, however, portions of the hot corona may be blown away by the jet, causing the corona to cool adiabatically. As a result, there may not be enough highly energetic photons to neutralize the electric fields in the gap via pair production. Leptons and hadrons can therefore be rapidly accelerated by this net electric field and cause near-simultaneous and rapid γ-ray and millimeter-radio flaring.

It is therefore invaluable to study the co-variable behavior of the radio, thermal X-rays and γ-rays at the same time, which is possible for 3C 111. Marscher (2006) studied the evolution of the X-ray flux probed with *RXTE* in combination with quasi-simultaneous single-dish radio data at 15 GHz and VLBI data at 43 GHz. They find an average delay between X-ray dips and ejections from the 43 GHz core of ∼0.3 yr. Chatterjee et al. (2011) observe at the even higher frequency of 230 GHz and find a delay of ∼0.15 years. Opacity effects therefore seem to be negligible above 43 GHz.

Later, Grandi et al. (2012) published the secure detection of γ-rays with *Fermi*/LAT around 2012, quasi-coincident to a 230 GHz radio flare, the ejection of a superluminal component and a peak of the optical and X-ray flux. For the first time, this allowed one to tentatively constrain the γ-emission site in a FR II radio galaxy to lie in vicinity of the radio core.

4.2.2 RESULTS

In the following, I extend on the work of Chatterjee et al. (2011) and Grandi et al. (2012) and investigate recent *Fermi*/LAT data for the γ-rays together with available data in the radio and the X-rays.

In Fig. 4.19, I show a composite light curve of 3C 111 for the radio, X-rays, and γ-rays. A number of strong radio flares can be identified at 230 GHz and 350 GHz in panel a (see also Fig. 4.1), which are highlighted with orange shaded regions. Flares at 43 GHz are nearly coincident with those at > 230 GHz. The data therefore likely probe a region close to the black hole already at 43 GHz. As Chatterjee et al. (2011) and Schulz (2012) show, the peaks in panel a correspond well to ejections of superluminal components from the 43 GHz and 86 GHz cores,

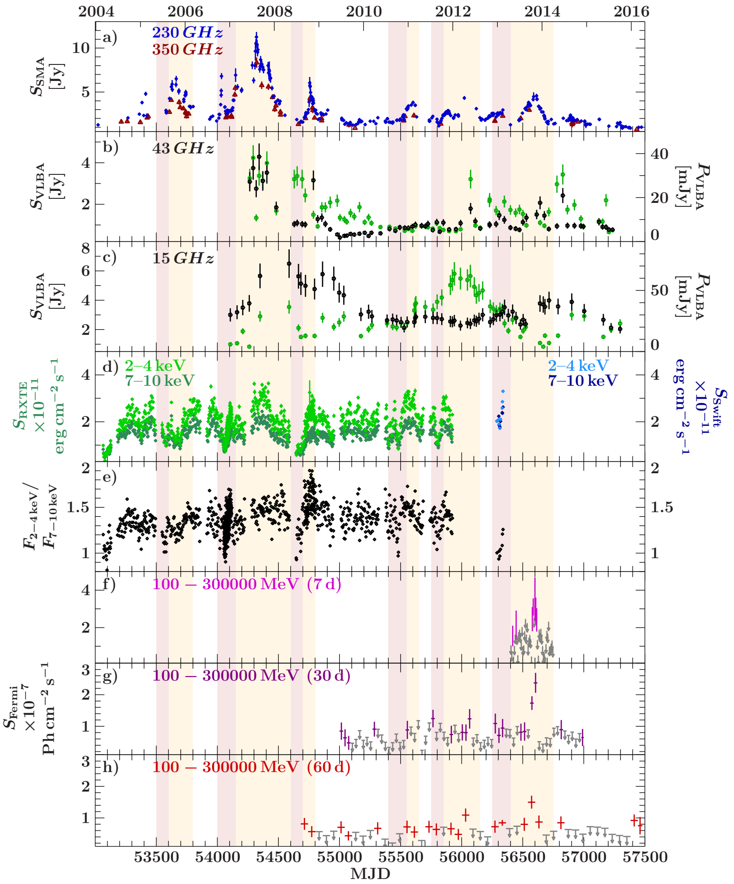

Figure 4.19. Multi-wavelength light curves of 3C 111 jointly covering the time range from 2004 until 2016. *Panel a:* SMA single-dish light curves at 230 GHz (blue) and 350 GHz (red); *panel b:* integrated 43 GHz VLBI data (VLBA-BU blazar program) in total (black) and polarized flux density (green); *panel c:* integrated 15 GHz VLBI data (MOJAVE) in total (black) and polarized flux density (green); *panel d: RXTE* (green) and *Swift* (blue) light curves in the soft (2–4 keV) and hard (7–10 keV) X-ray bands; *panel e:* $F_{2-4\,\mathrm{keV}}/F_{7-10\,\mathrm{keV}}$ hardness-ratio light curve; *panel f: Fermi*/LAT likelihood-based light curve with 7 d binning in the energy range of 100 MeV–300 GeV; *panels g and h:* same as *panel f* but for 30 d and 60 d binning. We used the pass-8 analysis to extract the *Fermi* light curves. The purple shaded regions mark dips in hardness ratio, the orange shaded regions subsequent peaks in light curves at 43 GHz and 230 GHz/350 GHz.

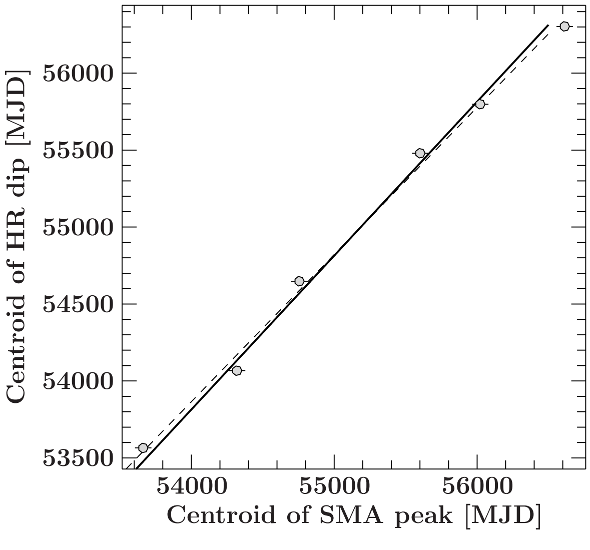

Figure 4.20. Direct comparison of the measured centroids of SMA flares at 230 GHz and dips in hardness ratio probed by *RXTE* and *Swift*. The uncertainties correspond to the standard deviation of an equal distribution of time intervals. The dashed curve resembles a linear fit with free slope, while the solid line corresponds to a fit of a linear function with a slope equal to one.

respectively. Due to SSA effects, flares appear delayed at lower radio frequencies.

In the panels b and c I also show the polarized flux density at 43 GHz and 15 GHz, which seems to coincide with peaks in total intensity at 43 GHz. In contrast, a strong displacement appears at 15 GHz. As we have shown in Sect. 4.1, this can be explained by the increased dominance of the polarized intensity in the downstream parsec-scale jet and is unrelated to processes close to the launching site.

In the panel d, I show all available *RXTE* and *Swift* flux measurements as well as the hardness ratio in panel e. The soft and hard X-ray light curves reveal a number of additional dips (marked with shaded regions) with respect to those reported by Chatterjee et al. (2011). The hardness ratio falling below a ratio of one seem to be a more robust indicator for dips especially in the soft X-rays. All dips are reliably followed by flares at millimeter radio wavelengths.

In Fig. 4.20, I find a remarkable correlation between the centroid time stamps of the millimeter flares and the hardness ratio dips (see also Chatterjee et al., 2011). The centroid energies are determined from the peaks of the millimeter flares. We can successfully fit the data with the linear function $f = a + b \cdot x$ yielding a slope of $b \sim 0.96$ (dashed line). In order to estimate the average time delay, I fit the function $f = a + x$ that assumes an one-to-one correspondence of dips and subsequent flares. I can find a mean delay of 186 ± 36 d, which is several times longer than the delay of ~55 d found by Chatterjee et al. (2011). Marscher (2006) on the other hand measure a delay of ~110 d, which demonstrates the wide range of values.

The *Fermi*/LAT light curves in the panels f–h reveal a yet unpublished and unprecedented γ-ray flare of around MJD 56500 following up on the previous detection by Grandi et al. (2012) around MJD 56000. Even for a weekly binned light curve, the γ-ray flare is coincident with the millimeter radio flare. Based on panel f, one can read off an upper limit for the width of the flare with ~30 d.

In conclusion, 3C 111 serves as unique source to study the disk-jet connection in AGN. I can find a mean delay of radio flares (and therefore the ejection of components in the 43 GHz maps of the BG) and X-ray dips of 185.9 ± 36.0 d. The coincidence of the γ-ray and 230 GHz flares strongly favors the γ-rays to be emitted in close vicinity to the black hole. In future work, the width of the γ-ray flare still has to be better constrained by varying the bin sizes of the *Fermi* data. Given the present results, the formation of vacuum gaps in the magnetosphere of the close black-hole environment can well explain (i) the occurrence of X-ray dips as sign for fluctuations in the accretion flow and (ii) the rapid and simultaneous γ-ray/radio flaring.

A problem of this interpretation is that the optical depths $\tau_{\gamma\gamma}$ for the absorption of γ-rays by lower energetic FIR–UV photon fields close to the core can be large. This would argue against the origin of γ-rays from the core.

4.3 STUDYING REPROCESSED HARD X-RAY – γ-RAY EMISSION OF BLAZARS WITH INTEGRAL

Above, I demonstrated the two-valuedness of 3C 111 with the large-scale morphology of a radio galaxy and compact properties reminiscent of a blazar. Its high-energy emission can both be described with a nuclear, thermal Comptonization continuum and a non-thermal SSC model.

The high energy emission (X-rays to γ-rays) of true blazars, however, is dominated by non-thermal jet-reprocessed emission, which forms the prominent high-energy hump (e.g., Ghisellini et al., 1998). Depending on the source and the energy range covered by this hump (compare Fossati et al., 1998; Ghisellini et al., 1998; Krauß et al., 2016), it can be observed with X-ray and γ-ray observatories. The satellite *INTEGRAL* and its detector IBIS/ISGRI fill the gap around the hard X-rays between ~20 and 200 keV. In contrast to the coded-mask instrument *Swift*/BAT, which covers about the same energy range, *INTEGRAL* is designed to perform deep and pointed observations, which is invaluable for increasing the S/N and constraining SED models.

The results of the analysis of a number of selected blazars are listed in Table 4.3. The majority is part of the TANAMI sample of southern blazars (Ojha et al., 2010, see also Fig. 4.21). As most sources are rather faint, one has to integrate multiple observations in a mosaic to gain a detection. For the aim of contributing to near-simultaneous SEDs, the time-range that can be used for the integration of data is limited, which mostly results in upper limits rather than solid detections. The analysis is performed as described in Sect. 2.3.2.

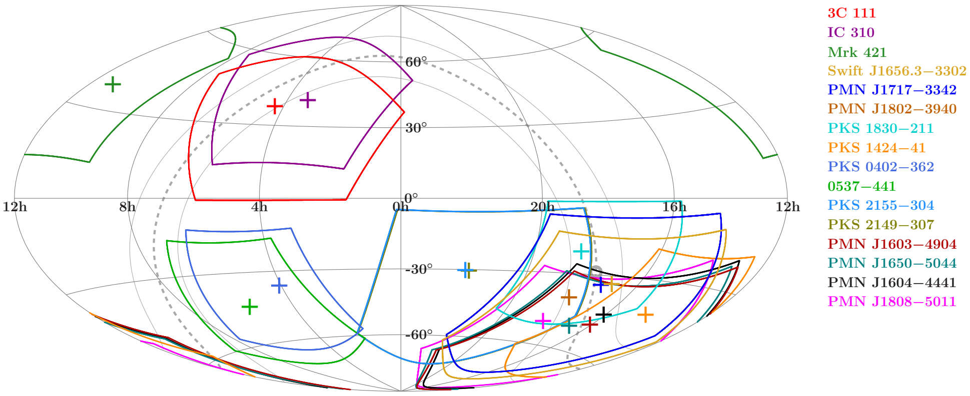

Figure 4.21. Skymap in RA/DEC coordinates including all analyzed blazars together with the size of the individual mosaics. The Galactic plane is indicated as gray solid line with the dashed lines marking ±10° Galactic latitude. The Galactic center coincides with the crowded field on the southern hemisphere.

Table 4.3. List of the derived results from the stacked analysis of *INTEGRAL*/IBIS/ISGRI data for the sample of blazars studied in this work. Upper limits (UL) correspond to 1 σ values. All fluxes are extracted from within 20–200 keV if not stated otherwise. Fluxes are calculated for a power-law photon index of $\Gamma = 2$ and given for the center of the corresponding energy bin. Notes: (1) see Fig. 4.18 for a spectrum with 11 energy bins between 20 and 200 keV; (2) the energy range 20–40 keV is used; (3) TANAMI source; estimates of the black-hole masses of most of the TANAMI sources can be found in Krauß et al. (2016)..

source	type	exp [ks]	timerange	significance [σ]	rate [cnts s^{-1}]	flux [erg cm^{-2} s^{-1} keV keV^{-1}	UL [erg cm^{-2} s^{-1} keV keV^{-1}]	publication	note
3C 111	RG	958.1	Jan/2003–Nov/2013	44.8	1.241±0.028	$4.73 \pm 0.11 \times 10^{-11}$	–	Beuchert et al. (2017. in prep.)	(1)
IC 310	BL Lac/FR I	111.0	Aug/2012–Feb/2013	2.7	0.21±0.08	$8.1 \pm 3.0 \times 10^{-12}$	4.2×10^{-12}	Ahnen et al. (2017)	
Mrk 421	BL Lac	31.9	18/Dec/2015–20/Dec/2015	6.2	0.46±0.08	$3.1 \pm 0.6 \times 10^{-11}$	7×10^{-12}	Kreikenbohm et al. 2017, in prep.	(2)
Swift J1656−3302	FSRQ	588.3	Jan/2003–Nov/2013	11.3	0.41±0.04	$1.57 \pm 0.14 \times 10^{-11}$	–	Krauß et al. (2014)	(3)
PMN J1717−3342	BL Lac	7767.3	Jan/2003–Nov/2013	2.0	0.020±0.010	$7.2 \pm 3.6 \times 10^{-13}$	1.1×10^{-12}	Krauß et al. (2014)	(3)
PMN J1802−3940	FSRQ	4019.8	Jan/2003–Nov/2013	–	-0.08±0.013	–	1.1×10^{-12}	Krauß et al. (2014)	(3)
PKS B1424−41	FSRQ	2.3	27/Dec/2011–24/Aug/2013	1.3	0.7±0.6	$2.8 \pm 2.2 \times 10^{-11}$	2.9×10^{-11}	Kadler et al. (2016)	(3)
PKS 1830−211	FSRQ	328.4	Jan/2003–Nov/2013	24.8	0.95±0.05	$3.62 \pm 0.20 \times 10^{-11}$	–	Kadler et al. (2016)	
PKS 0402−11	FSRQ	1.9	05/Apr/2010–19/May/2010	3.0	2.0±0.7	$7.5 \pm 2.5 \times 10^{-11}$	3.2×10^{-11}	Krauß et al. (2016)	(3)
PKS 0537−441	BL Lac	1.8	29/Dec/2010–19/May/2010	–	-0.7±0.7	–	3.3×10^{-11}	Krauß et al. (2016)	(3)
PKS 2155−304	BL Lac	647.2	Jan/2003–Nov/2013	2.2	0.07±0.03	$2.6 \pm 1.2 \times 10^{-12}$	1.8×10^{-12}	Krauß et al. (2016)	(3)
PKS 2149−307	FSRQ	653.0	Jan/2003–Nov/2013	25.4	0.80±0.03	$3.07 \pm 0.12 \times 10^{-11}$	–	Krauß et al. (2016)	(3)
PKS J1603−4904	blazar	3171.8	Jan/2003–Nov/2013	3.1	0.05±0.01	$1.8 \pm 0.7 \times 10^{-12}$	1.2×10^{-12}		(3)
PKS J1650−5044	blazar	3194.4	Jan/2003–Nov/2013	–	-0.01±0.01	–	1.2×10^{-12}		(3)
PKS J1604−4441	blazar	2908.7	Jan/2003–Nov/2013	2.0	0.03±0.02	$1.2 \pm 0.6 \times 10^{-12}$	1.3×10^{-12}		(3)
PKS J1808−5011	FSRQ	898.6	Jan/2003–Nov/2013	6.0	0.17±0.03	$6.5 \pm 1.1 \times 10^{-12}$	2.0×10^{-12}		(3)

4.3.1 THE TANAMI SAMPLE — SEARCHING FOR COUNTERPARTS OF EXTRAGALACTIC NEUTRINO EVENTS

We have published the SEDs of a number of the TANAMI sources that contain fluxes as extracted from stacked mosaics in Krauß et al. (2016). For the remaining sources in the list of Table 4.3, I can for the first time provide detections or flux upper limits between 20 and 200 keV. As shown in Fig. 4.21, the majority of the mosaics of these blazars overlap and cover a large portion of the southern hemisphere. In Fig. 4.22, I show a deep mosaic of *INTEGRAL*/IBIS/ISGRI data around PKS J1717−3342 with a maximal exposure of more than 7 Ms. It also contains the majority of the TANAMI blazars from this sample. The dynamic range of this mosaic is dominated by Galactic binary sources, which are visible as bright point sources. Note that the count rates and fluxes listed in Table 4.3 are extracted from separate mosaics around the corresponding sources.

The first astrophysical PeV neutrinos were detected with IceCube (Aartsen et al., 2013, 2014), one of them labeled E14 and dubbed “Bert”. I show the uncertainty circle of this event overlaid in Fig. 4.22. These detections have prompted an intense quest for identifying their extraterrestrial sources. Extragalactic neutrino emission has been theoretically predicted for the cores of AGN (Stecker, 2013), AGN jets (Mannheim, 1995) or Gamma-ray bursts (Waxman & Bahcall, 1997). Particle cascades in AGN hadronic jets can produce a number of secondary particles via photo-pion interactions. The entrainment of ambient gas into the jet inevitably provides seed protons

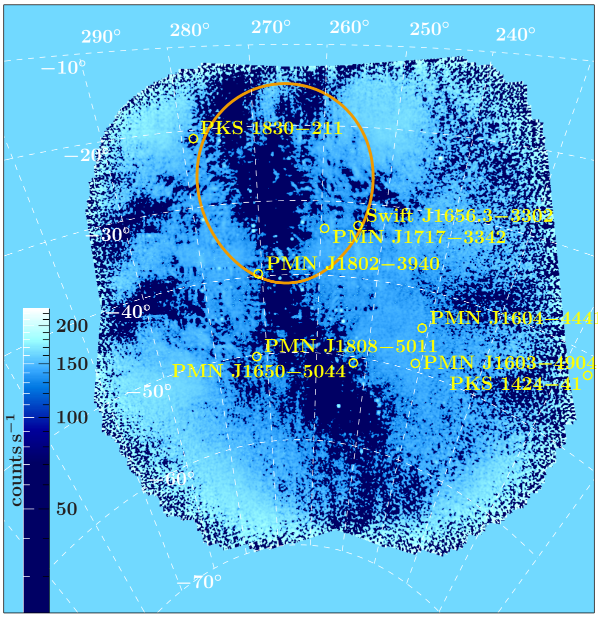

Figure 4.22. Mosaic in a RA/DEC coordinate system and calculated around the BL Lac PMN J1717−3342 containing over 14000 single science windows and resulting in a net exposure of ∼ 7767 ks at the source position of PMN J1717−3342. TANAMI blazars contained in this map are indicated with their source identifiers. The circle marks the $1\,\sigma$ positional uncertainty for the PeV neutrino E14 dubbed “Bert”.

Table 4.4. List of blazars within a $1\,\sigma$ angular uncertainty around the reconstructed origin of the neutrino E14 (“Bert”). The energy flux is adopted from the *Swift*/BAT 70-month catalog in the range of 14–195 keV. The photon flux is converted from the *Swift*/BAT energy flux to the *INTEGRAL*/IBIS/ISGRI energy range of 20–200 keV for SWIFT J1656.3−3302 and PKS 1830−211 and extracted from log-parabola fits to TANAMI SEDs for the two remaining sources.

source	RA [°]	DEC [°]	energy flux $[10^{-12}\,\mathrm{erg\,s^{-1}\,cm^{-2}}]$	photon flux $[10^{-3}\,\mathrm{ph\,s^{-1}\,cm^{-2}}]$	ν-event rates[3]	z	
SWIFT J1656.3−3302	**254.107**	**-33.043**	**62.45**	**0.627**	0.86 ± 0.1	**2.4**[4]	***Bert* field**
PMN J1717−3342	259.400	-33.702	-	0.112	$0.46^{+0.1}_{-0.12}$	-	
PMN J1802−3940	270.678	-39.669	-	0.078	$0.23^{+0.5}_{-0.4}$	1.319[5]	
PKS 1830−211	**278.416**	**-21.061**	**85.43**	**0.859**		**2.507** [6]	

[3] Expected electron neutrino events at 1 PeV in 662 days of IceCube data calculated from integrated electromagnetic 1 keV to 10 GeV energy flux

[4] Masetti et al. (2008), [5] Liang & Liu (2003), [6] Lovell et al. (1998), [7] Junkkarinen (1984)

and ions which can be accelerated either by shock acceleration in force-free jets or by electrostatic acceleration in current-carrying jets with vacuum gaps.

In these processes, PeV neutrinos and γ-rays are emitted with equal fluxes (Krauß et al., 2014, and references therein). By precisely measuring and integrating over the high energy hump, we can thus infer the number of expected neutrinos based on fundamental principles (Mannheim & Biermann, 1989; Mücke et al., 2000). We have studied the multi-wavelength properties of the six brightest blazars positionally coincident with these events using contemporaneous data of the TANAMI blazar sample, including first high-resolution radio-VLBI images and SEDs for the IceCube integration period (Krauß et al., 2014). We find that the integrated predicted neutrino rates are consistent with the measured ones. Blazars inside the uncertainty circle of the PeV neutrino E14 (“Bert”) are Swift J1656−3302, PMN J1717−3342, and PMN J1802−3940, which also have the benefit of being located close to the Galactic center, a region that has been intensively monitored by *INTEGRAL* in the past years. Data measured by *INTEGRAL*/IBIS/ISGRI particularly improved the constraints on the SED fit of Swift J1656−3302.

In Table 4.4, coordinates, redshifts, photon, and inferred neutrino fluxes are listed for these blazars with the additional blazar PKS 1830−211, which is located just outside the uncertainty circle of the “Bert” neutrino. PKS 1830−211 is an exceptionally bright gravitationally lensed galaxy and has been discussed as a potential neutrino source by Adrián-Martínez et al. (2014)

and Kadler et al. (2016). It is brighter than SWIFT J1656.3−3302 in the *INTEGRAL* band and shows much stronger variability, which is obvious from their *INTEGRAL*/IBIS/ISGRI light curves in Fig. 4.23. Although the SEDs that we measured (Fig. 4.24) already provide an exceptional broad data coverage, a simultaneous coverage of the hard X-rays would improve the estimates on the expected neutrino fluxes. For that reason, we proposed to visit all sources listed in Table 4.4 with deep observations. As these observations could not be granted by the TAC of *INTEGRAL*, we will both extract long-term averaged spectra from the archive and propose for coherent observations as part of future work.

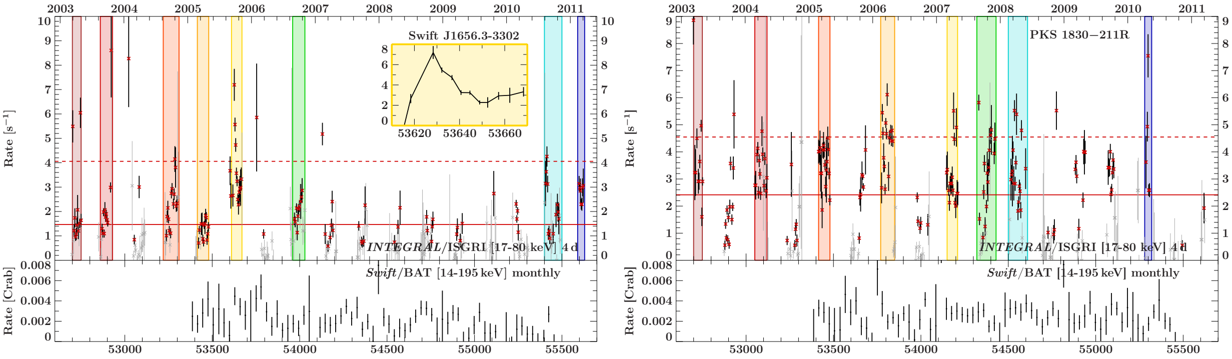

Figure 4.23. *Top panels: INTEGRAL*/IBIS/ISGRI 17–80 keV light curves of SWIFT J1656.3−3302 and PKS 1830−211. The data are retrieved from the *HEAVENS* project for a binning of 4 days including all available data. The solid red line marks the weighted mean, the dashed red line the 1 σ standard deviation of the mean. Data below a S/N of 2.5 are plotted in light gray. The colored regions mark peculiar states of higher flux or flaring behavior. The inset for Swift J1656.3−3302 demonstrates the capability of IBIS/ISGRI to detect high-fluence flares. *Bottom panels:* monthly binned *Swift*/BAT light curves with data between 14 and 195 keV for the same time intervals.

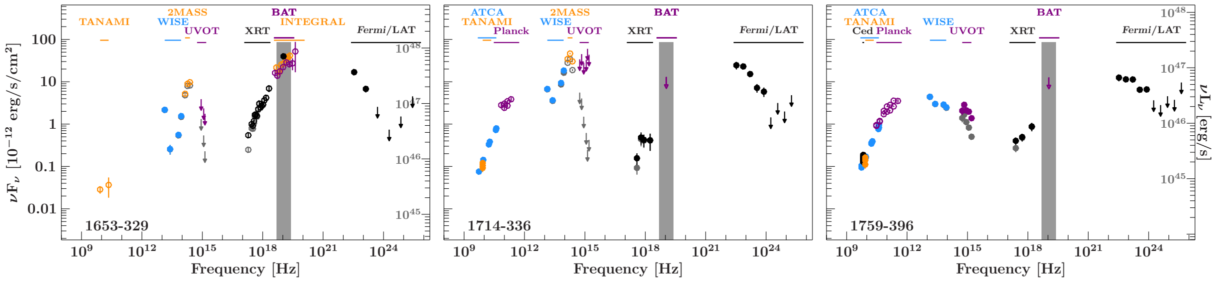

Figure 4.24. Broadband SEDs for the three TANAMI blazars in the *Bert*-field. Filled data points fall into the IceCube integration period, open circles are archival data outside the time period. Gray colors show the absorbed (X-ray) and reddened (optical/UV) spectra. The gray shaded area denotes the 20–200 keV energy range of IBIS/ISGRI. For the bright blazar SWIFT J1656.3-3302 we are able to plot archival coded-mask spectra of high S/N, i.e., *Swift*/BAT data from the 70-month catalog (violet), *INTEGRAL* IBIS/ISGRI data available to date (orange) as well as one flux data point extracted from a mosaic of *INTEGRAL* science windows from the IceCube data integration period (black). Image courtesy F. Krauß (priv. comm.)

A third PeV neutrino was detected and dubbed "Big Bird" (Aartsen et al., 2014). Within its uncertainty circle, the blazar PKS B1424−41 underwent a strong and high-fluence outburst coincident to the neutrino event. In Kadler et al. (2016) we demonstrate with the same methods that this outburst can explain the observed PeV neutrino and may be suggestive of a direct association with this blazar. This publication also contains a 3 σ IBIS/ISGRI upper limit (see Table 4.3) for the high-fluence period between July 2012 and April 2013.

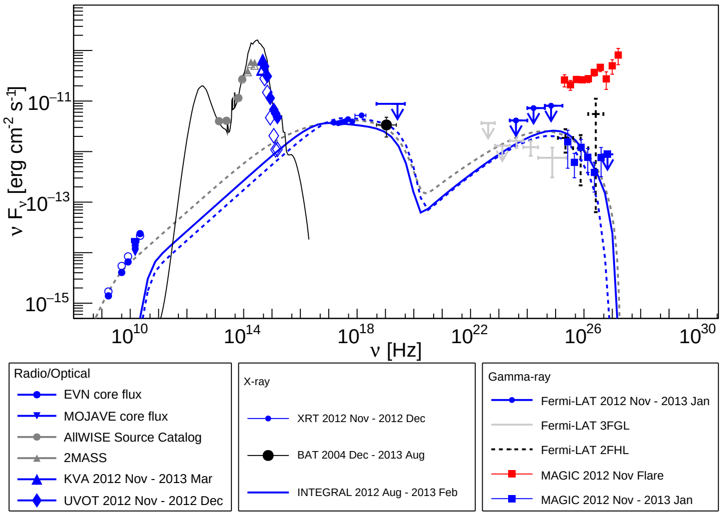

Figure 4.25. De-reddened and de-absorbed broad-band SED of IC 310 as result of the observing campaign between 2012 and 2013 (blue points) with additional catalog data (gray points). Red data points emphasize the flaring period in November 2012. The corresponding instruments are labeled in the bottom panels. This figure is adopted from Ahnen et al. (2017).

4.3.2 MULTI-WAVELENGTH STUDIES OF IC 310 AND MRK 421

In this section, I outline the dedicated studies of the prominent galaxies IC 310 and Mrk 421, where the above *INTEGRAL* results could be used for completing their SEDs.

IC 310 is a well-known radio galaxy (e.g., Sijbring & de Bruyn, 1998, and references therein) but also shows blazar-like properties similar to 3C 111, that is, an one-sided parsec-scale jet indicating beamed jet emission (Kadler et al., 2012) and strong variability across the electromagnetic spectrum up to the GeV and TeV energies (Neronov et al., 2010; Aleksić et al., 2010). In Ahnen et al. (2017), we present a multiwavelength campaign between 2012 and 2013 that includes data from the radio to TeV energies that were taken with ground- and space-based instruments. The SED (Fig. 4.25) shows a typical double-humped shape that can be well fitted with a single-zone SSC model. The black data point marks a detection with *Swift*/BAT over a period of 9 years, while we are unable to detect the source with a stack of 407 IBIS/ISGRI science windows between August 2012 and February 2013 (111 ks net exposure) and within 20 and 200 keV. Yet, the 3 σ upper limit of 4.2×10^{-12} erg cm^{-2} s^{-1} keV keV^{-1} is well consistent with the fitted SSC model.

Mrk 421 is the brightest BL Lac object known in the X-rays and UV and was first the first blazar to be detected also at TeV energies (Punch et al., 1992). Today, it is a high-ranked target for γ-ray facilities such as *Fermi* (e.g., Abdo et al., 2011), MAGIC (e.g., Albert et al., 2007), HAWK (e.g., Wood et al., 2017) or FACT (e.g., Biland et al., 2016). It emits a double-humped SED, typical for BL Lacs, and has shown frequent flaring periods (e.g., Donnarumma et al., 2009; Kapanadze et al., 2016; Singh et al., 2017) that enabled several multiwavelength studies (e.g., Fossati et al., 2008). As part of a monitoring program, we anticipate to conduct simultaneous *INTEGRAL* and *Swift* observations when triggered by a flaring γ-ray event observed by FACT. A successful trigger was raised on 2015-12-17. *INTEGRAL* consequently observed Mrk 421 between 2015-12-18 and 2015-12-20 with 50 science windows during revolution 1623. With these data on hand, we compile the time-resolved SED shown in Fig. 4.26. This SED shows the spectral variability between the quiescent state after 2015-12-18 and the flaring state at 2015-12-17. As the *INTEGRAL* observations catch IC 310 in its lower state, IBIS/ISGRI can only provide an upper limit: I find a 5 σ limit with 3.2×10^{-11} erg cm^{-2} s^{-1} keV keV^{-1} at 30 keV for considering data between 20 and 40 keV.

The detection significance of Mrk 421 is found to be 6.2 σ in Table 4.3. Figure 4.27 shows a histogram of the significance map of Mrk 421 with a Gaussian distribution centered at zero significance. I therefore assume a dominance by background noise. Detections above 6.2 σ can be accepted with a low p-value of 1.5×10^{-4}. In turn, the probability that points in the map with a significance of this or larger values than 6.2 σ are inconsistent with the background, i.e., $1 - p$, is

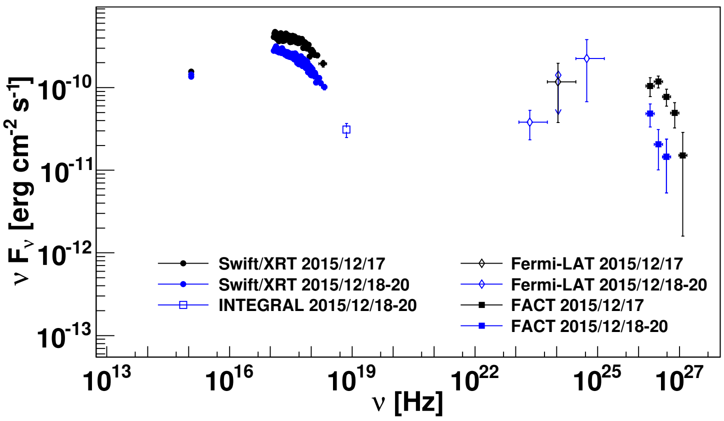

Figure 4.26. Time-resolved SEDs for the quiescent (blue) and flaring state (black) of Mrk 421 in December 2015. Here, the 5 σ IBIS/ISGRI upper limit is shown. This figure is provided by A. Kreikenbohm (priv. comm.).

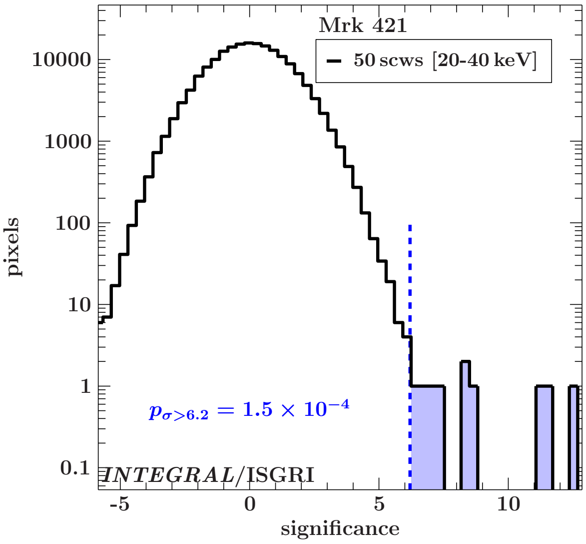

Figure 4.27. Histogram of the significance mosaic centered on Mrk 421. This mosaic contains 50 individual science windows. The p-value is given for values larger than the significance of Mrk 421, i.e., 6.2 σ. The 1 σ RMS is 1.4.

large. This argues in favor of a solid detection with $3.1 \pm 0.6 \times 10^{-11}\,\mathrm{erg\,cm^{-2}\,s^{-1}\,keV\,keV^{-1}}$ at 30 keV. On top, the a priori knowledge of the source position should also be taken into account, which independently increases the significance of faint point sources (in 't Zand et al., 1994).

4.3.3 Discussion and Conclusions

Its pointing capabilities make *INTEGRAL* and the on-board coded-mask detector IBIS invaluable for AGN science as compared to the coded-mask detector *Swift*/BAT, which is operated as a monitoring instrument. Although *Swift*/BAT comes with about twice the detector area of *INTEGRAL*/IBIS, their different observing techniques result in *INTEGRAL*/IBIS to have an about 5–10 times higher equivalent fully-coded exposure for selected fields per year and an about one magnitude better sensitivity[6]. These advantages of the IBIS detector are also apparent in the increased sensitivity of AGN light curves shown in Fig. 4.23. *INTEGRAL*/IBIS is therefore the ideal instrument for studying single AGN in greater detail.

INTEGRAL/IBIS, however, cannot compete against the high sensitivity of focusing X-ray telescopes onboard of *Swift* or *XMM-Newton*. At equal effective area, coded-mask detectors always suffer sensitivity, mostly because of their background dominance (the IBIS/ISGRI detector measures a background of $600\,\mathrm{cnts\,s^{-1}}$ during a solar maximum compared to a source count-rate of

---

[6] See in particular the IBIS handbook (`http://www.isdc.unige.ch/integral/download/osa/doc/10.2/osa_um_ibis/index.html`) and `https://swift.gsfc.nasa.gov/proposals/tech_appd/swiftta_v13/`

$250\,\mathrm{cnts\,s^{-1}}$ measured for the Crab nebula[7]). For coded mask instruments, the reconstruction of a point source is done in two steps via the shadowgram plane. For that reason, each reconstructed source is overlaid with the background noise of all detected photons, which limits the sensitivity. Moreover, all sources in the field of view contribute to the shadowgrams. This makes it increasingly challenging to detect faint point sources in a crowded fields as for example in Fig. 4.22. Detections below $\sim 6\,\sigma$ therefore still have to be taken with caution and may be background-consistent. The lower continuum sensitivity of IBIS/ISGRI at 10^5 s exposure is slightly less than 1 mCrab (Ubertini et al., 2003), corresponding to $2.4 \times 10^{-11}\,\mathrm{erg\,cm^{-2}\,s^{-1}}$ between 2 and 10 keV. This is in well agreement with the numbers given in Table 4.3 for the AGN that I studied with *INTEGRAL*, which all show fluxes roughly below 1 mCrab.

---

[7] See the IBIS manual.

CHAPTER 5

CONCLUSIONS AND OUTLOOK

In this thesis, I have studied the radio-quiet Seyfert galaxies NGC 3227 and NGC 4151 as well as the radio-loud radio galaxy 3C 111 in detail. All three sources are part of the class of active galaxies. The energy budget of these galaxies is determined by an extremely compact accreting nucleus where the central SMBH interfaces between the consumption and release of immense amounts of energy both via radiation and mechanical feedback in form of collimated jets. The results presented in this thesis touch upon all of these aspects. In order to reach these conclusions, I made use of the following methods.

1. **Non-imaging methods** facilitate to access the intrinsic structure and geometry of AGN whose (sub-)parsec-scale extend can not be spatially resolved with individual telescopes at any wavelength. Here, I exploit the powerful tools of X-ray spectral variability studies as well as the spectral decomposition of X-ray and multi-band spectra using state-of-the-art models, which allow a detailed study of the physics inherent to AGN.
2. **Imaging methods** allow me to study collimated jet outflows in the radio. I make use of the method of radio interferometry with long telescope baselines, which outperforms the spatial resolution of *HST* by a factor of more than 50. This method allows one to resolve the innermost parsec-scale region of jets at milliarcsecond angular resolution. The ultimate goal is to probe profound questions related to the formation and composition of jets as well as the propagation of matter inside these jets.

First, I investigated high-resolution X-ray spectra of the galaxies NGC 3227 and NGC 4151 that cover a range of time-scales and provide a broad spectral coverage. Parts of the data of NGC 3227 have been successfully proposed by me and my co-investigators. I used spectral models that allowed me to infer the properties of the line-of-sight absorbers, the accretion disk, and the black hole itself:

- In both galaxies, I find at least three differently ionized absorbers, where the highly ionized absorber is outflowing. Strong absorption variability from time-scales of days to years is imprinted on the lower and intermediate ionized absorbers.
- X-rays are absorbed by both gas and dust. I isolated the dusty phase by measuring the extinction of the IR-to-X-ray SED of NGC 3227. With this method, the variability of the X-ray absorbers of NGC 3227 can solely be attributed to a gaseous and intermediately ionized absorber close to the SMBH.
- For both NGC 3227 and NGC 4151, I mapped the absorption column over time, which revealed intriguing column-density profiles covering a range of time-scales. Together with the information on the ionization state, these profiles indicate distinct absorbing structures (clouds, filaments or more complicated geometries) at a range of distances to the SMBH. I

found these structures to be consistent with being located in the outer BLR or the inner torus while orbiting the black hole on dynamical time-scales. These results are in harmony with a number of independent investigations of other Seyfert galaxies.

- I found that concluding on the orientation of AGN based on their (patchy) absorbing environment is hardly possible due to the large amount of complexity related to the absorbers. Individual clouds or filaments are sufficient to obscure the entire X-ray emitting region (only tens of event horizons in diameter). Information on their dynamics is often incomplete and relying on archival observations. Line-of-sight absorption should therefore be used with great care to conclude on the overall geometry of the absorbing environment and never to conclude on its orientation to the observer. Instead, I propose to use the optical line classification to tentatively assess the issue of orientation via the type 1/type 2 dichotomy, which is based on whether nuclear Doppler-broadened emission lines are hidden behind obscuring gas and dust or if only narrow lines from the extended NLR are present. Optical lines are well suited for this classification, as their emitting volume is significantly larger than the X-ray emitting region (by a factor of $\sim 10^4$ for the BLR and many orders of magnitude more for the NLR). The symmetry-braking character of polarized emission lines turns out to be particularly useful to put constraints on the orientation of AGN and to use these information to tentatively predict the properties of X-ray absorbers.
- In both NGC 3227 and NGC 4151, a spectral decomposition allowed me to conclude on significant reflection continua including prominent Fe K α/β lines. For NGC 3227, the photons are likely reflected off the outer parts of the accretion disk or the inner side of the torus. For NGC 4151, however, I also observed a contribution from the inner disk, where effects of strong gravity lead to a relativistically blurred reflection spectrum. With help of a detailed study of this component, I concluded on a coronal geometry that is confined to the polar axis of NGC 4151. Although the geometry of coronae in compact accreting objects is still subject of debate, the presented results are in harmony with independent studies of other sources. I made use of the to date most physical model to describe inner disk reflection in a self-consistent lamp-post geometry. Disentangling this delicate feature from the complex absorbers in NGC 4151 provides a great chance to study not only the dynamics of the circumnuclear absorbers but also of the corona itself. Whenever possible, it is worth to carefully investigate the parameter spaces of reflection models with help of high-quality spectra in order to provide additional and independent inclination estimates.
- A case study of the young radio galaxy PKS 1718−649 indicates that the same absorbing medium may cause both the radio emission and X-rays to become free-free and photo-absorbed. Archival data from both wavebands suggest correlated variability on large time-scales of one year. Me and my co-investigators therefore initiated a joint observing campaign with the ATCA radio interferometer and the *XMM-Newton* observatory to probe correlated variability with increased sensitivity. The first set of observations have been conducted on March 5th 2017. The second set is about to follow fall 2017 and will provide the unique opportunity to better understand the environment around AGN in their cradle.

In the second part of this thesis, I cross the bridge to AGN where the main channel of energy release is related to the exhaust of black-hole engines. Relativistic jets dump immense amounts of energy into the ambient medium, both via radiation and mechanical feedback. I can conclude on the following aspects.

- 3C 111 is a well suited source to probe the physics of the innermost parsec-scale jet by carefully mapping the distribution of (polarized) intensity both over core distance and time. The EVPAs perform a rotation of more than 180° over a deprojected distance of about 20 pc. I can not entirely explain this large rotation with a Faraday rotation gradient due to ambient gas on our line of sight. Instead, I propose either changes in the intrinsic magnetic field structure over time or a dynamical shock-shock interaction of propagating shocked features with a standing recollimation shock inherent to the underlying flow. Such a shock-shock interaction lacks corresponding (G)RMHD simulations with full radiative output that includes polarization. The presented results shall therefore serve as observational reference for future simulations.

- I provided observational evidence for this recollimation shock by a sudden drop of the sizes of propagating jet features accompanied with jumps in their brightness temperature. With the knowledge of the location of the recollimation shock, I could conclude on a kinetically dominated jet with a low probability of being Poynting-flux dominated.
- 3C 111 is prototypical and allows us to observe both its accreting nucleus and the beamed jet at the same time. The observation of X-ray dips are shortly followed by peaks at millimeter radio wavelength and indicate that the disk and the innermost jet are tightly coupled. Also, I report on a significant γ-ray flare simultaneous to a millimeter flare, which allows me to conclude on a γ-emitting site close to the launching site of the jet.
- Besides 3C 111, I studied the hard X-ray emission of blazars at a range of redshifts where the jet forms small angles to the line of sight. Depending on the flux of these blazars, the high sensitivity of the *INTEGRAL* satellite can fill the spectral gap in the hard-X-rays with near-simultaneous data. Decent sampling of blazar SEDs provides a basis for the application of physical models. Also, measuring the flux contained in the characteristic high energy hump enables to estimate the expected neutrino rate under consideration of a hadronic jet. Although corresponding results are consistent with the recently observed PeV neutrinos, a direct association of extragalactic neutrinos with individual AGN was not yet be established. The quest for a positive association will be part of future research and can be the key for a better understanding of jets in AGN.

Overall, I investigated a broad range of appearances of AGN including cases with a strong nuclear X-ray signature and cases with prominent radio jet emission. These sources just resemble snapshots of galaxies that may be evolutionary connected on cosmological time scales. Establishing an evolutionary context, however, lies beyond the scope of this thesis. In this work I exploit the wealth of archival data that are well suited for comprehensive studies of the underlying radiative and dynamical processes. These involve deep investigations of the cores of the prominent Seyfert galaxies NGC 3227 and NGC 4151. The technique of time-resolved spectroscopy helps to unveil the structure of AGN-intrinsic absorbers that remain hidden from direct imaging. All of these cases strongly favor a highly dynamical and patchy environment. High-resolution VLBI images show that also the inner jet of the peculiar radio galaxy 3C 111 seems to be partly embedded inside a similar envelope of inhomogeneous obscuring material, which is observed as Faraday screen in the radio bands. This screen distorts the information contained in the polarized radio emission that is emitted by the magnetized environment. Also, its irregular pattern makes it impossible to peer behind this curtain of gas. The polarized light emitted by the part of the jet that is piercing out of this gas, however, reveals a wealth of information on the propagating shocks as well as the energetica and magnetization of the jet itself. As part of an ongoing project, me and my collaborators investigate the young radio galaxy PKS 1718−649. In this source, we believe that the newly born jet is still cocooned inside its cradle of dense material. Here, we use the synergy potential of simultaneous observations in the radio and X-rays to probe both the compact environment and the newly formed jet at the same time. This thesis concludes on numerous similarities of the intrinsic processes of accreting SMBHs but also emphasizes the involved complexities that distinguish the studied AGN. Dedicated studies turn out to be inevitable and are also well suited as supplements of studies of larger samples of AGN.

ACKNOWLEDGEMENTS

First of all, I would like to thank my doctoral supervisors, Jörn Wilms from the Dr. Remeis Observatory and Matthias Kadler from the University of Würzburg. This work would have never been possible without their enormous support. I want to explicitly thank you, Matthias and Jörn, for providing each of your students with great opportunities to be involved with the international research environment, to visit conferences and schools, and to become independent researchers. Thank you also for the tremendous effort you put into funding proposals that make all of this possible. To only mention some examples, Matthias offered me the unique chance to conduct a project together with the Max Planck Institut für Radioastronomie (MPIfR) in Bonn as part of my Bachelors thesis. Moreover, both Jörn and Matthias greatly supported my application for the trainee program at the European Space Astronomy Center (ESAC), as part of which I eventually started to work on X-ray astronomy. Two research stays at the University of California San Diego (UCSD) and the work with my co-supervisor Alex Markowitz helped a lot to deepen my experience in this field. Also, they allowed my childhood dream to come true. When my parents once gave me the video tape "Contact" as a present, they may not have realized that this movie and the Very Large Array (VLA) in New Mexico would influence my choice of studies. As part of the school for radio interferometry, I eventually had the unique chance to visit the site, which certainly inspired me and my future life.

Throughout, I make use of the Interactive Spectral Interpretation System (`ISIS`; Houck & Denicola, 2000), which is based on the `S-Lang` scripting language, as well as the set of `ISIS`-functions supported and developed by the Remeis Observatory & ECAP (`http://www.sternwarte.uni-erlangen.de/isis/`). Figures are rendered using the `slxfig` interface of `S-Lang`, developed by J. E. Davis. I make use of data provided by the space-born observatories *Spitzer*, *WISE*, *HST*, *XMM-Newton*, *Suzaku*, *Swift*, *NuSTAR*, *INTEGRAL*, *RXTE* and *Fermi*, the ground-based radio interferometers VLBA and SMA, the 30-m radio telescope IRAM, the 2MASS survey as well as various optical facilities (San Pedro Mártir observatory, NASA 3-m IRTF, 3.8-m UKIRT, Gemini-South). I thank the respective teams for providing these data to the public and in particular the SOCs and TACs of *XMM-Newton*, *Swift* and *INTEGRAL* for the helpful and friendly correspondence. I thank Neil Gehrels, the PI of *Swift* for his support.

I am very grateful for having been able to work in two lovely groups at the Dr. Remeis Observatory and the University of Würzburg. I greatly appreciate the warm atmosphere in these groups that has enriched my everyday life. It is a pleasure to work in a unique environment in which people have always been extremely open for a mutual exchange of experiences. It is a honor and deeply fulfilling to collaborate with so many of you on a number of intriguing projects. To mention only a few, I cordially thank Cornelia Müller for sharing her far-reaching experience with me related to VLBI and blazars, Christoph Großberger, Robert Schulz and Till Steinbring for fruitful discussions and a close collaboration on 3C 111, Annika Kreikenbohm, Katha Leiter, Felicia Krauß, Marcus Langejahn, Ralf Ballhausen, Christina Gräfe, Natalie Hell, Maria Hirsch, and Mirjam Örtel for a number of very enjoyable discussions on Seyfert galaxies, X-ray astronomy and instrumentation, Felicia and Basti Falkner, for the great time back during our studies, for treading the same path after receiving our Master degrees and particularly the inspiring artwork of Felicia when proof-reading parts of my work, Thomas Dauser, Matthias Kühnel, Moritz Böck and Manfred Hanke, who were always willing to assist with invaluable advice, Thomas and Javier García, who particularly shared their knowledge on (relativistic) reflection in AGN with me and who eventually became two beloved collaborators also on our publications on the galaxies NGC 3227 and NGC 4151, Ingo Kreykenbohm and Victoria Grinberg for their patience while teaching me the data extraction and analysis procedures related to the INTEGRAL satellite and last but not least, Rosamunde Pare and Macarena Sagredo for their language support.

This work experienced great support by the well organized team of admins at the Dr. Remeis Observatory. Ingo Kreykenbohm and the whole team including Thomas, Fritz Schwarm, Matthias Kühnel and others have always invested a tremendous effort to take care of the "Remeis Cluster" with its persistently strong computing power, the possibility to run parallelized jobs and of course the up-to-date desktop environment. I thank Horst Drechsel, who could be called the "stepfather" of the observatory, who followed in Karl Remeis' footsteps, who was (also) married to the stars and retired this year. I also deeply thank Ingo for his immense dedication to the observatory as well as the entire Förderverein for taking care of this magical place.

My great thanks also go to my supervisors Anna-Lia Longinotti, Matteo Guainazzi, Giovanni Miniutti, and Ignacio (Nacho) de la Calle Perez at ESAC. You never hesitated to share your experience with me and are therefore certainly responsible for a significant part of my experience in X-ray astronomy. I want to thank you for the close and pleasant collaboration. This also involves Jiri Svoboda, who was working at ESAC back then and became a great friend and collaborator. I am also very thankful to Alex Markowitz, a Humboldt fellow at our institute, who became a co-supervisor of my PhD thesis and eventually a very close collaborator related to projects on variable absorption. I owe you much of my understanding and am more than thankful for your commitment. You have been a great host in San Diego. I am happy that our collaboration eventually resulted in two publications. Also, I want to thank Giovanni, Anna-Lia, Matteo, Nacho, Jiri and Mario Sanfrutos at ESAC for the close and fruitful work on our publications on NGC 3227, ESO 323-G077 and Fairall 51. As part of the first, it was a pleasure to work with with Matt Malkan (University of Los Angeles), who shared much of his experience related to broad-band modeling of Seyfert galaxies with me. This also involved discussions with Takamitsu Miyaji (UNAM), support by David Hiriart, José M. López (Instituto de Radio Astronomía, Ensenada), Ivan Agudo (Instituto de Astrofísica de Andalucía) and the very helpful input by Rick Rothschild, Dom Walton, Felix Fürst and Murray Brightman during my visits at UCSD and Caltech. Furthermore, I thank Mason Keck, Laura Brenneman (Boston University, Harvard-Smithsonian Center for Astrophysics) as well as Andrzej Zdziarski (Nicolaus Copernicus Astronomical Center) for the effective and pleasant collaboration on our publication on NGC 4151.

Related to radio astronomy and the work on the galaxy 3C 111, I thank Manolis Angelakis, Lars Fuhrmann, Ioannis Nestoras, and Yiannis Myserlis for hosting and supervising me at MPIfR and for our joint work on Effelsberg 100-m data of the radio galaxy 3C 111. I experienced this time as exceedingly enriching. I am also deeply grateful to Manolo Perucho Pla, who shared his expertise related to the RMHD modeling of jets with us as a group in Würzburg and contributed significantly to the presented work on 3C 111. Thank you very much for your dedication and your patience in guiding me through the field of jet physics. I additionally want to emphasize the great support by the MOJAVE team and thank Ivan Agudo, Carolina Casadio, Jose-Luis Gómez, Sol N. Molina and Clemens Thum (Instituto de Astrofísica de Andalucía, Instituto de Radio Astronomía Milimétrica) as well as Sera Markoff (UvA), Denise Gabuzda (Univ. of Cork) and Mark Gurwell (Harvard-Smithsonian Center for Astrophysics) for mutual discussions and their input.

My time at ESAC helped me to mature both as a person and as a researcher. I want to deeply thank Annika, André, Wouter, Marc, Pablo, the "chicos picantes", Aurelie, Jiri, Prash, Ali, Elena, Sara, Ester, Natalia and Laura. You all are part of my memories of amazing times that shaped my life. Many of you also became great and close friends. I also want to thank "The XX" and the "Arctic Monkeys" for their songs "Intro" and "fluorescent adolescent", which we often listened to on our car-drives to ESAC while enjoying our time together as adolescent researchers. I am happy that André and I eventually found a replacement for "RRR" and "Independance" in Nürnberg.

I shall also never forget our activities, which involved canoeing, climbing and of course the annual “Remeis Skifahren” in Silvretta, Montafon. This event clearly merged our group even more.

I truly thank you, Nela, Ohle, Annika, Katha, Thomas, Rosamunde, Till, Basti and many more for your friendship that reached far beyond the scope of work. Nela, I am looking forward to dance with you in 59 years at the 90s party, preferentially at E-Werk. Ohle, thank you for being my Schwenkmeister. Annika, I will never forget my climbing shoes again. Katha, thank you for our special times with Bolle: “alle raus!”; “Die Sonne geht da drüben unter!”. Tommy, wonderful “Wischmopp-action” in Madrid. Rosamunde, team Abrissski! Till, thanks for unforgettable times on the bridge. Basti, great staircase-performance. Many thanks for the great company also to my office-mates Nela, Fritz, Eva and Mirjam.

My thank goes also to Philipp Schrögel for his support while preparing my first science slam talk. Thank you for providing me with the chance to perform on your stage, which opened the door for a number of performances in Germany. I experienced these as extremely rewarding and I am grateful for all the special persons I met when conversing and spending time in bars.

I want to thank you, Agnes, for having been a precious part of my life over more than three years. You gave me a lot of strength and I hope I could give you the same. These years will always remain in my mind.

Udhay and Jan, thank you for having been my bro-men since school and Udhay for sharing flats with me for 7 years. We will have many things to tell our children. Udhay tera bahoot bahoot dhanwad tu meri badi madad kitii hai.

This entire work would have never been possible without the tremendous support and love that I received from my parents. They always provided me a safe environment but also allowed me to quickly stand on my own feet. Before my mother, Hermia, passed away, she was confident that I would pursue my dreams and find what I was looking for. I know that you were with me ever since and that you will also be in the future. Thank you for everything. Since then, my father, Roger, and I became even closer. Thank you for being my role model in many regards, for being an idealist, for always being prepared to listen and for being open for far-reaching conversations. I am more than happy that you eventually found a new partner and I am deeply grateful that her family welcomed me with open arms. Norbert, it was the greatest pleasure to be able to get to know you and to spend our family holidays with you. Your soul will always be a part of us. For the Maori, their ancestors are the navel of their lives and so is my family that includes my beloved friends. In fact, I owe you my existence and that I am able to live a happy life. Thank you.

Diese Arbeit wäre ohne die grenzenlose Unterstützung meiner Eltern niemals möglich gewesen. Sie standen stets hinter mir, boten mir Sicherheit und ermöglichten mir schnell auf eigenen Beinen zu stehen. Bevor Meine Mutter, Hermia, verstarb, war sie immer davon überzeugt, dass ich meinen Weg finden werde. Tudom, hogy mindig mellettem voltál, és hogy a doktorim védésén is velem leszel. Mindent köszönök! Die Beziehung zu meinem Vater, Roger, wurde seither immer enger. Ich bedanke mich von ganzem Herzen für Deine Rolle als Vorbild und Idealist, für dein offenes Ohr in allen Belangen und unsere tiefgründigen Gespräche. Ich bin glücklich, dass du eine neue Partnerin gefunden hast, und mich ihre Familie mit offenen Armen eingeschlossen hat. Norbert, danke, dass ich Dich kennen lernen durfte und mit dir unseren Familienurlaub verbringen konnte. Möge Deine Seele immer unter uns weilen. Im Leben der Maori sind ihre Vorfahren ein elementarer Bestandteil, genau wie es meine Familie ist, zu denen ich auch meine Freunde zähle. Ich verdanke euch meine Existenz und dass ich ein glückliches Leben führen kann. Danke.

I want to thank every person and every moment that allowed me to reach this point in my journey of life. The path I have walked on was always crossing valleys and mountains. I literally

started to love climbing these mountains and found that challenges are what makes life rewarding. Sometimes I failed, sometimes I succeeded, which allowed me to grow personally. I just reached a very special summit, where oxygen once again became rare. The storm suddenly faded and I was happy to enjoy the moment with a tear of joy while writing this summit log. I can truly claim that I have experienced the profound feeling of happiness by having been able to develop friendships that are deeply rooted in my heart and to pursue my dream and vocation at the same time. None of this is a matter of course, which makes me extremely grateful. My tears of joy shall be dedicated to my friends and family, who made and make my life.

ACRONYMS

2MASS	Two Micron All Sky Survey
3C	Third Cambridge Catalogue of Radio Sources
AC	"Acceleration and Collimation Zone"
AGN	Active Galactic Nucleus
AO	announcement of opportunity
AP	Alfvén point
ARF	auxiliary response file
Ark	Arakelian Emission Line Objects
ATCA	Australia Telescope Compact Array
BAT	Burst Alert Telescope
BBB	"Big Blue Bump"
BLR	Broad Line Region
BPT	Baldwin–Phillips–Terlevich
CD	current-driven
CCD	Charged Coupled Device
CMB	cosmic microwave background
CSO	Compact Symmetric Objects
CSS	Compact Steep Spectrum Source
dof	degrees of freedom
EH	event horizon
EPIC	European Photon Imaging Camera
EUV	extreme-ultraviolet
EVPA	electric vector position angle
FFA	free-free absorption
FR	Fanaroff-Riley
FIR	far-infrared
FPM	focal-plane module
FUV	far-ultraviolet
FMS	fast magnetosonic point
FMSS	fast magnetosonic separatrix surface
GPS	gigahertz-peaked spectrum
GRMHD	general relativistic magnetohydrodynamics
HERG	High Excitation Radio Galaxy
HXCOMP	high-energy X-ray Comptonized continuum
HXD	Hard X-ray Detector
HXPL	high-energy X-ray power law
IBIS	Imager on-Board the INTEGRAL Satellite
IR	infrared
IRAM	Institute for Radio Astronomy in the Millimeter Range
`ISIS`	Interactive Spectral Interpretation System
Jy	Jansky (unit; $10^{-26}\,\mathrm{W\,m^{-2}\,Hz^{-1}}$)
LP	lamp-post
KH	Kelvin-Helmholtz
LMC	Large Magelanic Cloud
LBA	Long Baseline Array
ld	light day
LERG	Low Excitation Radio Galaxy

LINER	Low Ionization Nuclear Emission Line Region
LIRG	Luminous Infrared Galaxy
MHD	magnetohydrodynamics
MIR	mid-infrared
MJD	Mean Julian Date
Mrk	Markarian Catalog
MSP	modified slow point
MOJAVE	Monitoring of Jets in AGN with VLBA Experiments
MURA	Modified Uniformly Redundant Array
NGC	New General Catalog of Nebulae and Clusters of Stars
NIR	near-infrared
NLR	Narrow Line Region
NUV	near-ultraviolet
OM	Optical Monitor
`OSA`	Off-Line Scientific Analysis
PA	position angle
PAH	Polycyclic Aromatic Hydrocarbon
PC	photon counting
pc	parsec (unit)
PKS	Parkes Catalog of radio Sources
PMN	Parkes-MIT-NRAO catalog
PSF	point-spread function
POLAMI	Polarimetric Monitoring of AGN at Millimeter Wavelengths
RGS	Reflection Grating Spectrometer
RM	rotation measure
RMF	redistribution matrix function
RMS	root mean squared
RXTE	Rossi X-ray Timing Explorer
QSO	Quasi-Stellar Object
SPM	San Pedro Mártir Observatory
`SAS`	Science Analysis Software
scw	science window
SED	spectral energy distribution
SEFD	system equivalent flux density
SF	star formation
SMA	Submillimeter Array
SMBH	Supermassive Black Hole
SMC	Small Magelanic Cloud
SMG	Submillimeter Galaxy
S/N	signal-to-noise ratio
SSA	synchrotron self-absorption
SWIRE	Spitzer Wide-Area Infrared Extragalactic Survey
SXCOMP	soft-energy X-ray Comptonized continuum
SXPL	soft-energy X-ray power law
TAC	Time Allocation Committee
TANAMI	Tracking Active Galactic Nuclei with Austral Milliarcsecond Interferometry
UFO	Ultrafast Outflow
UV	ultraviolet

ULIRG	Ultraluminous Infrared Galaxy
UVOT	Ultraviolet/Optical Telescope
VLBA	Very Long Baseline Array
VLBI	Very Long Baseline Interferometry
WISE	Wide-Field Infrared Survey Explorer
WT	windowed-timing
XIS	X-ray Imaging Spectrometer
XRT	X-ray Telescope

REFERENCES

Aartsen M.G., Abbasi R., Abdou Y., et al., 2013, Phys. Rev., 111, 021103

Aartsen M.G., Ackermann M., Adams J., et al., 2014, Phys. Rev., 113, 101101

Abdo A.A., Ackermann M., Ajello M., et al., 2010, Nat, 463, 919

Abdo A.A., Ackermann M., Ajello M., et al., 2011, ApJ, 736, 131

Abramowicz M.A., Fragile P.C., 2013, Living Reviews in Relativity, 16, 1

Adrián-Martínez S., Albert A., André M., et al., 2014, J. Cosm. Astrop. Phys., 11, 017

Agudo I., Bach U., Krichbaum T.P., et al., 2007, A&A, 476, L17

Agudo I., Gómez J.L., Casadio C., et al., 2012, ApJ, 752, 92

Agudo I., Gómez J.L., Martí J.M., et al., 2001, Astrophys. J., Lett., 549, L183

Agudo I., Jorstad S.G., Marscher A.P., et al., 2011a, Astrophys. J., Lett., 726, L13

Agudo I., Marscher A.P., Jorstad S.G., et al., 2011b, Astrophys. J., Lett., 735, L10

Agudo I., Thum C., Gómez J.L., Wiesemeyer H., 2014, A&A, 566, A59

Ahnen M.L., Ansoldi S., Antonelli L.A., et al., 2017, A&A, in press (arXiv:1703.07651)

Aird J., Coil A., Georgakakis A., Nandra K., 2016, In: Active Galactic Nuclei: What's in a Name?, 68

Albert J., Aliu E., Anderhub H., et al., 2007, ApJ, 663, 125

Aleksić J., Antonelli L.A., Antoranz P., et al., 2010, Astrophys. J., Lett., 723, L207

Alexander D.M., Hickox R.C., 2012, New Astr. Rev., 56, 93

Aller H.D., Hodge P.E., Aller M.F., 1981, Astrophys. J., Lett., 248, L5

Aller M., Hughes P., Aller H., et al., 2016, Galaxies, 4, 35

Alonso-Herrero A., Ramos Almeida C., Mason R., et al., 2011, ApJ, 736, 82

Altschuler D.R., 1980, AJ, 85, 1559

Angel J.R.P., Stockman H.S., 1980, ARA&A, 18, 321

Angelakis E., Fuhrmann L., Nestoras I., et al., 2010, In: Savolainen T., Ros E., Porcas R., Zensus J. (eds.) Fermi meets Jansky - AGN in Radio and Gamma-Rays, MPIfR, arXiv:1006.5610

Antonucci R., 1993, ARA&A, 31, 473

Antonucci R., 2012, Astronomical and Astrophysical Transactions, 27, 557

Appl S., 1996, A&A, 314, 995

Arav N., Barlow T.A., Laor A., et al., 1998, MNRAS, 297, 990

Arévalo P., Uttley P., 2006, MNRAS, 367, 801

Armentrout B.K., Kraemer S.B., Turner T.J., 2007, ApJ, 665, 237

Arnaud K., Smith R., Siemiginowska A., 2011, Handbook Of X-ray Astronomy, Cambridge University Press, Cambridge

Arshakian T.G., León-Tavares J., Lobanov A.P., et al., 2010, MNRAS, 401, 1231

Asada K., Inoue M., Kameno S., Nagai H., 2008, ApJ, 675, 79

Asada K., Inoue M., Uchida Y., et al., 2002, PASJ, 54, L39

Asada K., Nakamura M., Doi A., et al., 2014, Astrophys. J., Lett., 781, L2

Asada K., Nakamura M., Inoue M., et al., 2010, ApJ, 720, 41

Asensio Ramos A., Ramos Almeida C., 2009, ApJ, 696, 2075

Asmus D., Gandhi P., Hönig S.F., et al., 2015, MNRAS, 454, 766

Attridge J.M., Roberts D.H., Wardle J.F.C., 1999, Astrophys. J., Lett., 518, L87

Atwood W.B., Abdo A.A., Ackermann M., et al., 2009, ApJ, 697, 1071

Baade W., Minkowski R., 1954, ApJ, 119, 206

Baczko A.K., Schulz R., Kadler M., et al., 2016, A&A, 593, A47

Balbus S.A., Hawley J.F., 1991, ApJ, 376, 214

Baldi R.D., Capetti A., 2008, A&A, 489, 989

Baldwin J.A., Ferland G.J., Korista K.T., et al., 2003, ApJ, 582, 590

Balmaverde B., Capetti A., 2014, A&A, 563, A119

Baloković M., Matt G., Harrison F.A., et al., 2015, ApJ, 800, 62

Balucinska-Church M., McCammon D., 1992, ApJ, 400, 699

Bardeen J.M., Press W.H., Teukolsky S.A., 1972, ApJ, 178, 347

Barvainis R., 1987, ApJ, 320, 537

Baum S.A., Zirbel E.L., O'Dea C.P., 1995, ApJ, 451, 88

Bautista M.A., Kallman T.R., 2000, ApJ, 544, 581

Begelman M.C., Blandford R.D., Rees M.J., 1984, Rev. Mod. Phys., 56, 255

Bell E.F., Naab T., McIntosh D.H., et al., 2006, ApJ, 640, 241

Bell E.F., Wolf C., Meisenheimer K., et al., 2004, ApJ, 608, 752

Belloni T., 2001, Astrophysics and Space Science Supplement, 276, 145

Belmont R., Malzac J., Marcowith A., 2008, A&A, 491, 617

Beloborodov A.M., 1999, Astrophys. J., Lett., 510, L123

Bentz M.C., Peterson B.M., Netzer H., et al., 2009a, ApJ, 697, 160

Bentz M.C., Walsh J.L., Barth A.J., et al., 2009b, ApJ, 705, 199

Beskin V.S., Kuznetsova I.V., Rafikov R.R., 1998, MNRAS, 299, 341

Beskin V.S., Nokhrina E.E., 2006, MNRAS, 367, 375

Bessell M.S., 2005, ARA&A, 43, 293

Bessell M.S., Castelli F., Plez B., 1998, A&A, 333, 231

Best P.N., Heckman T.M., 2012, MNRAS, 421, 1569

Beuchert T., 2013, *Master's thesis*, Universität Erlangen-Nürnberg

Beuchert T., Markowitz A.G., Dauser T., et al., 2017, A&A, in press (arXiv:1703.10856)

Beuchert T., Markowitz A.G., Krauß F., et al., 2015, A&A, 584, A82

Beuchert T., Wilms J., Kadler M., et al., 2013, Acta Polytechnica, 54, 266

Bianchi S., Guainazzi M., Chiaberge M., 2006, A&A, 448, 499

Bicknell G.V., Dopita M.A., O'Dea C.P.O., 1997, ApJ, 485, 112

Biland A., Dorner D., Lauer R., et al., 2016, The Astronomer's Telegram, 9137

Binney J., Tabor G., 1995, MNRAS, 276, 663

Blandford R.D., Königl A., 1979, ApJ, 232, 34

Blandford R.D., McKee C.F., Rees M.J., 1977, Nat, 267, 211

Blandford R.D., Payne D.G., 1982, MNRAS, 199, 883

Blandford R.D., Pringle J.E., 1976, MNRAS, 176, 443

Blandford R.D., Rees M.J., 1974, MNRAS, 169, 395

Blandford R.D., Rees M.J., 1978, Phys. Scr., 17, 265

Blandford R.D., Znajek R.L., 1977, MNRAS, 179, 433

Błażejowski M., Sikora M., Moderski R., Madejski G.M., 2000, ApJ, 545, 107

Blinov D., Pavlidou V., Papadakis I.E., et al., 2016, MNRAS, 457, 2252

Blustin A.J., Page M.J., Fuerst S.V., et al., 2005, A&A, 431, 111

Boccardi B., Krichbaum T.P., Bach U., et al., 2016a, A&A, 588, L9

Boccardi B., Krichbaum T.P., Bach U., et al., 2016b, A&A, 585, A33

Boettcher M., Harris D.E., Krawczynski H., 2012, Relativistic Jets from Active Galactic Nuclei, Wiley-Vch, Weinheim

Borch A., Meisenheimer K., Bell E.F., et al., 2006, A&A, 453, 869

Böttcher M., 2007, Ap&SS, 309, 95

Böttcher M., Reimer A., Sweeney K., Prakash A., 2013, ApJ, 768, 54

Brenneman L.W., Reynolds C.S., 2006, ApJ, 652, 1028

Brenneman L.W., Reynolds C.S., Nowak M.A., et al., 2011, ApJ, 736, 103

Brenneman L.W., Risaliti G., Elvis M., Nardini E., 2013, MNRAS, 429, 2662

Bridle A.H., 1984, AJ, 89, 979

Bridle A.H., Hough D.H., Lonsdale C.J., et al., 1994, AJ, 108, 766

Briggs D.S., Schwab F.R., Sramek R.A., 1999, In: Taylor G.B., Carilli C.L., Perley R.A. (eds.) Synthesis Imaging in Radio Astronomy II, Astronomical Society of the Pacific Conference Series, 180, 127

Britzen S., Kudryavtseva N.A., Witzel A., et al., 2010, A&A, 511, A57

Buchner J., Georgakakis A., Nandra K., et al., 2015, ApJ, 802, 89

Burke B.F., Graham-Smith F., 2009, An Introduction to Radio Astronomy, Cambridge University Press, Cambridge

Burns J.O., Feigelson E.D., Schreier E.J., 1983, ApJ, 273, 128

Burns J.O., White R.A., Hough D.H., 1981, AJ, 86, 1

Burrows D.N., Hill J.E., Nousek J.A., et al., 2005, Space Sci. Rev., 120, 165

Burtscher L., Davies R.I., Graciá-Carpio J., et al., 2016, A&A, 586, A28

Burtscher L., Jaffe W., Raban D., et al., 2009, Astrophys. J., Lett., 705, L53

Buttiglione S., Capetti A., Celotti A., et al., 2010, A&A, 509, A6

Cackett E.M., Zoghbi A., Reynolds C., et al., 2014, MNRAS, 438, 2980

Calderone G., Sbarrato T., Ghisellini G., 2012, MNRAS, 425, L41

Cano-Díaz M., Maiolino R., Marconi A., et al., 2012, A&A, 537, L8

Cardelli J.A., Clayton G.C., Mathis J.S., 1988, Astrophys. J., Lett., 329, L33

Cardelli J.A., Clayton G.C., Mathis J.S., 1989, ApJ, 345, 245

Casadio C., Gómez J.L., Jorstad S.G., et al., 2015, ApJ, 813, 51

Cawthorne T.V., 2006, MNRAS, 367, 851

Cawthorne T.V., Jorstad S.G., Marscher A.P., 2013, ApJ, 772, 14

Cawthorne T.V., Wardle J.F.C., Roberts D.H., Gabuzda D.C., 1993a, ApJ, 416, 519

Cawthorne T.V., Wardle J.F.C., Roberts D.H., et al., 1993b, ApJ, 416, 496

Chakravorty S., Kembhavi A.K., Elvis M., et al., 2009, MNRAS, 393, 83

Chandola Y., Saikia D.J., 2017, MNRAS, 465, 997

Chandrasekhar S., 1983, The mathematical theory

of black holes, Clarendon Press, Oxford University Press, Oxford
Chartas G., Brandt W.N., Gallagher S.C., 2003, ApJ, 595, 85
Chatterjee R., Marscher A.P., Jorstad S.G., et al., 2011, ApJ, 734, 43
Chelouche D., Netzer H., 2001, MNRAS, 326, 916
Choudhuri A.R., 1998, The Physics Of Fluids and Plasmas, Cambridge University Press, Cambridge
Cid Fernandes R., Stasińska G., Mateus A., Vale Asari N., 2011, MNRAS, 413, 1687
Clautice D., Perlman E.S., Georganopoulos M., et al., 2016, ApJ, 826, 109
Cohen M.H., Meier D.L., Arshakian T.G., et al., 2014, ApJ, 787, 151
Collinge M.J., Brandt W.N., Kaspi S., et al., 2001, ApJ, 557, 2
Condon J.J., Helou G., Sanders D.B., Soifer B.T., 1996, ApJS, 103, 81
Contopoulos I., Kazanas D., Papadopoulos D.B., 2013, ApJ, 765, 113
Contopoulos J., Lovelace R.V.E., 1994, ApJ, 429, 139
Cornwell T., Fomalont E.B., 1999, In: Taylor G.B., Carilli C.L., Perley R.A. (eds.) Synthesis Imaging in Radio Astronomy II, Astronomical Society of the Pacific Conference Series, 180, 187
Cornwell T.J., Wilkinson P.N., 1981, MNRAS, 196, 1067
Cotton W.D., 1999, In: Taylor G.B., Carilli C.L., Perley R.A. (eds.) Synthesis Imaging in Radio Astronomy II, Astronomical Society of the Pacific Conference Series, 180, 111
Courvoisier T.J.L., Walter R., Beckmann V., et al., 2003, A&A, 411, L53
Couto J.D., Kraemer S.B., Turner T.J., Crenshaw D.M., 2016, ApJ, 833, 191
Crane P.C., Napier P.J., 1989, In: Perley R.A., Schwab F.R., Bridle A.H. (eds.) Synthesis Imaging in Radio Astronomy, Astronomical Society of the Pacific Conference Series, 6, 139
Crenshaw D.M., Kraemer S.B., Boggess A., et al., 1999, ApJ, 516, 750
Crenshaw D.M., Kraemer S.B., Bruhweiler F.C., Ruiz J.R., 2001, ApJ, 555, 633
Cresswell J.G., Percival W.J., 2009, MNRAS, 392, 682
Croke S.M., O'Sullivan S.P., Gabuzda D.C., 2010, MNRAS, 402, 259
Croton D.J., Springel V., White S.D.M., et al., 2006, MNRAS, 365, 11
Cunningham C.T., 1975, ApJ, 202, 788
Curtis H.D., 1918, Pub. Lick Obs., 13, 31
Czerny B., Hryniewicz K., 2011, A&A, 525, L8
Dadina M., Cappi M., Malaguti G., et al., 2005, A&A, 442, 461
Daly R.A., Marscher A.P., 1988, ApJ, 334, 539
D'Arcangelo F.D., Marscher A.P., Jorstad S.G., et al., 2007, Astrophys. J., Lett., 659, L107
D'arcangelo F.D., Marscher A.P., Jorstad S.G., et al., 2009, ApJ, 697, 985
Dauser T., 2010, Diploma thesis, Universität Erlangen-Nürnberg
Dauser T., García J., Parker M.L., et al., 2014, MNRAS, 444, L100
Dauser T., García J., Walton D.J., et al., 2016, A&A, 590, A76
Dauser T., Garcia J., Wilms J., et al., 2013, MNRAS, 430, 1694
Dauser T., Svoboda J., Schartel N., et al., 2012, MNRAS, 422, 1914
Dauser T., Wilms J., Reynolds C.S., Brenneman L.W., 2010, MNRAS, 409, 1534
Davies R.I., Thomas J., Genzel R., et al., 2006, ApJ, 646, 754
Davis J.E., 2001, ApJ, 562, 575
Davis S.W., Laor A., 2011, ApJ, 728, 98
de Jong S., Beckmann V., Mattana F., 2012, A&A, 545, A90
De Luca A., Salvaterra R., Tiengo A., et al., 2016, The Universe of Digital Sky Surveys, 42, 291
de Rosa A., Piro L., Perola G.C., et al., 2007, A&A, 463, 903
de Vaucouleurs G., de Vaucouleurs A., Corwin, Jr. H.G., et al., 1991, Sky Telesc.., 82, 621
De Young D.S., 1993, Astrophys. J., Lett., 405, L13
DeGraf C., Di Matteo T., Treu T., et al., 2015, MNRAS, 454, 913
den Herder J.W., den Boggende A.J., Branduardi-Raymont G., et al., 2000, In: Truemper J.E., Aschenbach B. (eds.) X-Ray Optics, Instruments, and Missions III, Proc. SPIE, 4012, 102
Dermer C.D., Schlickeiser R., 1993, ApJ, 416, 458
Desert F.X., Boulanger F., Puget J.L., 1990, A&A, 237, 215
Di Matteo P., Combes F., Melchior A.L., Semelin B., 2007, A&A, 468, 61
Di Matteo T., Colberg J., Springel V., et al., 2008, ApJ, 676, 33
Di Matteo T., Springel V., Hernquist L., 2005, Nat, 433, 604
Doeleman S.S., Fish V.L., Schenck D.E., et al., 2012, Science, 338, 355
Done C., Davis S.W., Jin C., et al., 2012, MNRAS, 420, 1848
Donnarumma I., Vittorini V., Vercellone S., et al., 2009, Astrophys. J., Lett., 691, L13
Dorodnitsyn A., Kallman T., 2012, ApJ, 761, 70
Dove J.B., Wilms J., Begelman M.C., 1997a, ApJ, 487, 747
Dove J.B., Wilms J., Maisack M., Begelman M.C., 1997b, ApJ, 487, 759
Dovčiak M., Done C., 2016, Astron. Nachr., 337, 441

Dovčiak M., Karas V., Yaqoob T., 2004, ApJS, 153, 205

Duro R., Dauser T., Wilms J., et al., 2011, A&A, 533, L3

Eichler D., Smith M., 1983, Nat, 303, 779

Eikmann W., Wilms J., Lee J., 2012, In: An INTEGRAL view of the high-energy sky (the first 10 years), PoS, 145

Elitzur M., 2007, In: Ho L.C., Wang J.M. (eds.) The Central Engine of Active Galactic Nuclei, Astron. Soc. Pacific Conf. Ser., 373, Astron. Soc. Pacific, San Francisco, 415

Elitzur M., Ho L.C., 2009, Astrophys. J., Lett., 701, L91

Elitzur M., Shlosman I., 2006, ApJ, 648, L101

Elvis M., 2000, ApJ, 545, 63

Elvis M., Hao H., Civano F., et al., 2012, ApJ, 759, 6

Elvis M., Risaliti G., Nicastro F., et al., 2004, ApJ, 615, L25

Elvis M., Wilkes B.J., McDowell J.C., et al., 1994, ApJS, 95, 1

Emmering R.T., Blandford R.D., Shlosman I., 1992, ApJ, 385, 460

Eungwanichayapant A., Aharonian F., 2009, Int. J. Mod. Phys., 18, 911

Faber S.M., Willmer C.N.A., Wolf C., et al., 2007, ApJ, 665, 265

Fabian A.C., Lohfink A., Kara E., et al., 2015, MNRAS, 451, 4375

Fabian A.C., Rees M.J., Stella L., White N.E., 1989, MNRAS, 238, 729

Fabian A.C., Wilkins D.R., Miller J.M., et al., 2012a, MNRAS, 424, 217

Fabian A.C., Zoghbi A., Ross R.R., et al., 2009, Nat, 459, 540

Fabian A.C., Zoghbi A., Wilkins D., et al., 2012b, MNRAS, 419, 116

Falcke H., Körding E., Markoff S., 2004, A&A, 414, 895

Falkner S., 2013, Ph.D. thesis, Universität Erlangen-Nürnberg, Erlangen, Germany

Fanaroff B.L., Riley J.M., 1974, MNRAS, 167, 31P

Farrell S.A., Murphy T., Lo K.K., 2015, ApJ, 813, 28

Fath E.A., 1909, Ph.D. thesis, University of California, Berkeley, Berkeley, USA

Feain I.J., Cornwell T.J., Ekers R.D., et al., 2011, ApJ, 740, 17

Fender R., Belloni T., 2004, ARA&A, 42, 317

Ferrarese L., Merritt D., 2000, Astrophys. J., Lett., 539, L9

Filippenko A.V., 1985, ApJ, 289, 475

Finke J.D., Dermer C.D., Böttcher M., 2008, ApJ, 686, 181

Fiore F., Feruglio C., Shankar F., et al., 2017, A&A, in press (arXiv:1702.04507)

Fiore F., Perola G.C., Romano M., 1990, MNRAS, 243, 522

Fischer T.C., Crenshaw D.M., Kraemer S.B., Schmitt H.R., 2013, ApJS, 209, 1

Fitzpatrick E.L., 1999, PASP, 111, 63

Fomalont E.B., Perley R.A., 1999, In: Taylor G.B., Carilli C.L., Perley R.A. (eds.) Synthesis Imaging in Radio Astronomy II, Astronomical Society of the Pacific Conference Series, 180, 79

Forster J.R., Dreher J., Wright M.C.H., Welch W.J., 1978, Astrophys. J., Lett., 221, L3

Fossati G., Buckley J.H., Bond I.H., et al., 2008, ApJ, 677, 906

Fossati G., Maraschi L., Celotti A., et al., 1998, MNRAS, 299, 433

Fromm C.M., 2015, Astron. Nachr., 336, 447

Fromm C.M., Fuhrmann L., Perucho M., 2015, A&A, 580, A94

Fromm C.M., Perucho M., Mimica P., Ros E., 2016, A&A, 588, A101

Fromm C.M., Perucho M., Ros E., et al., 2011, A&A, 531, A95

Fromm C.M., Ros E., Perucho M., et al., 2013, A&A, 551, A32

Fuhrmann L., Angelakis E., Zensus J.A., et al., 2016, A&A, 596, A45

Fuhrmann L., Larsson S., Chiang J., et al., 2014, MNRAS, 441, 1899

Fuhrmann L., Zensus J.A., Krichbaum T.P., et al., 2007, In: Ritz S., Michelson P., Meegan C.A. (eds.) The First GLAST Symposium, American Institute of Physics Conference Series, 921, 249

Fukumura K., Kazanas D., Contopoulos I., Behar E., 2010, ApJ, 715, 636

Fürst F., Müller C., Madsen K.K., et al., 2016, ApJ, 819, 150

Gabriel A.H., Jordan C., 1969, MNRAS, 145, 241

Gabuzda D.C., Mullan C.M., Cawthorne T.V., et al., 1994, ApJ, 435, 140

Gabuzda D.C., Pushkarev A.B., Cawthorne T.V., 2000, MNRAS, 319, 1109

Gabuzda D.C., Reichstein A.R., O'Neill E.L., 2014, MNRAS, 444, 172

Gaibler V., Krause M., Camenzind M., 2009, MNRAS, 400, 1785

Gallimore J.F., Yzaguirre A., Jakoboski J., et al., 2010, ApJS, 187, 172

Gan Z.M., Wang D.X., Li Y., 2007, MNRAS, 376, 1695

García J., Dauser T., Lohfink A., et al., 2014, ApJ, 782, 76

García J., Dauser T., Reynolds C.S., et al., 2013, ApJ, 768, 146

García J., Kallman T.R., 2010, ApJ, 718, 695

García J., Kallman T.R., Mushotzky R.F., 2011, ApJ, 731, 131

García J.A., Dauser T., Steiner J.F., et al., 2015, Astrophys. J., Lett., 808, L37

Gaskell C.M., Goosmann R.W., Klimek E.S., 2008, Mem. Soc. Astron. Italiana, 79, 1090

Gatuzz E., García J., Kallman T.R., et al., 2015, ApJ, 800, 29

Gebhardt K., Bender R., Bower G., et al., 2000, Astrophys. J., Lett., 539, L13

Gehrels N., Chincarini G., Giommi P., et al., 2004, ApJ, 611, 1005

Georgantopoulos I., Rovilos E., Akylas A., et al., 2011, A&A, 534, A23

George I.M., Fabian A.C., 1991, MNRAS, 249, 352

George I.M., Turner T.J., Netzer H., et al., 1998, ApJS, 114, 73

Ghisellini G., Celotti A., Fossati G., et al., 1998, MNRAS, 301, 451

Ghisellini G., Madau P., 1996, MNRAS, 280, 67

Ghisellini G., Maraschi L., Tavecchio F., 2009, MNRAS, 396, L105

Ghisellini G., Maraschi L., Treves A., 1985, A&A, 146, 204

Ghisellini G., Tavecchio F., 2008, MNRAS, 387, 1669

Ghisellini G., Tavecchio F., Chiaberge M., 2005, A&A, 432, 401

Gierliński M., Zdziarski A.A., Poutanen J., et al., 1999, MNRAS, 309, 496

Gilbert G.M., Riley J.M., Hardcastle M.J., et al., 2004, MNRAS, 351, 845

Giroletti M., Giovannini G., Feretti L., et al., 2004, ApJ, 600, 127

Goedbloed J.P., Poedts S., 2004, Principles of Magnetohydrodynamics, Cambridge University Press, Cambridge

Gofford J., Reeves J.N., Tombesi F., et al., 2013, MNRAS, 430, 60

Goldwurm A., David P., Foschini L., et al., 2003, A&A, 411, L223

Gómez J.L., Lobanov A.P., Bruni G., et al., 2016, ApJ, 817, 96

Gómez J.L., Marscher A.P., Alberdi A., et al., 2000, Sci, 289, 2317

Gómez J.L., Marscher A.P., Jorstad S.G., et al., 2008, Astrophys. J., Lett., 681, L69

Gómez J.L., Martí J.M., Marscher A.P., et al., 1997, Astrophys. J., Lett., 482, L33

González-Martín O., Rodríguez-Espinosa J.M., Díaz-Santos T., et al., 2013, A&A, 553, A35

Gottesman S.R., Fenimore E.E., 1989, Applied Optics, 28, 4344

Grandi P., Torresi E., Stanghellini C., 2012, Astrophys. J., Lett., 751, L3

Großberger C., 2014, Ph.D. thesis, Universität Erlangen-Nürnberg, Erlangen, Germany

Großberger C., Kadler M., Wilms J., et al., 2012, Acta Polytechnica, 52, 18

Guainazzi M., Bianchi S., 2007a, MNRAS, 374, 1290

Guainazzi M., Bianchi S., 2007b, In: Ho L.C., Wang J.W. (eds.) The Central Engine of Active Galactic Nuclei, Astronomical Society of the Pacific Conference Series, 373, 467

Guainazzi M., Bianchi S., Dovčiak M., 2006, Astron. Nachr., 327, 1032

Guainazzi M., Matt G., Perola G.C., 2005, A&A, 444, 119

Guainazzi M., Nicastro F., Fiore F., et al., 1998, MNRAS, 301, L1

Guilbert P.W., Fabian A.C., Rees M.J., 1983, MNRAS, 205, 593

Gurwell M.A., Peck A.B., Hostler S.R., et al., 2007, In: Baker A.J., Glenn J., Harris A.I., Mangum J.G., Yun M.S. (eds.) From Z-Machines to ALMA: (Sub)Millimeter Spectroscopy of Galaxies, Astronomical Society of the Pacific Conference Series, 375, 234

Haardt F., 1993, ApJ, 413, 680

Haardt F., Maraschi L., 1991, Astrophys. J., Lett., 380, L51

Hada K., Doi A., Kino M., et al., 2011, Nat, 477, 185

Hardcastle M.J., Alexander P., Pooley G.G., Riley J.M., 1997, MNRAS, 288, 859

Hardcastle M.J., Krause M.G.H., 2014, MNRAS, 443, 1482

Hardee P., Mizuno Y., Nishikawa K.I., 2007, Ap&SS, 311, 281

Hardee P.E., 2004, Ap&SS, 293, 117

Hardee P.E., 2007, ApJ, 664, 26

Harrison C.M., 2004, Ph.D. thesis, Durham University, Durham, UK

Harrison F.A., Craig W.W., Christensen F.E., et al., 2013, ApJ, 770, 103

Hartman R.C., Kadler M., Tueller J., 2008, ApJ, 688, 852

Hawley J.F., Krolik J.H., 2006, ApJ, 641, 103

Hazard C., Mackey M.B., Shimmins A.J., 1963, Nat, 197, 1037

Heckman T.M., Smith E.P., Baum S.A., et al., 1986, ApJ, 311, 526

Hernán-Caballero A., Alonso-Herrero A., Hatziminaoglou E., et al., 2015, ApJ, 803, 109

HI4PI Collaboration, Ben Bekhti N., Flöer L., Keller R., et al., 2016, A&A, 594, A116

Hickox R.C., Wardlow J.L., Smail I., et al., 2012, MNRAS, 421, 284

Hicks E.K.S., Malkan M.A., 2008, ApJS, 174, 31

Ho L.C., 2002, ApJ, 564, 120

Ho L.C., 2008, ARA&A, 46, 475

Högbom J.A., 1974, A&AS, 15, 417

Hogbom J.A., 1979, A&AS, 36, 173

Holland A.D., Turner M.J., Abbey A.F., Pool P.J., 1996, In: Siegmund O.H., Gummin M.A. (eds.) EUV, X-Ray, and Gamma-Ray Instrumentation for Astronomy VII, Proc. SPIE, 2808, 414

Holt S.S., Mushotzky R.F., Boldt E.A., et al., 1980, Astrophys. J., Lett., 241, L13

Homan D.C., 2005, In: Romney J., Reid M. (eds.) Future Directions in High Resolution Astronomy, Astronomical Society of the Pacific Conference Series, 340, 133

Homan D.C., Kovalev Y.Y., Lister M.L., et al., 2006, Astrophys. J., Lett., 642, L115

Homan D.C., Lister M.L., Kovalev Y.Y., et al., 2015, ApJ, 798, 134

Homan D.C., Ojha R., Wardle J.F.C., et al., 2002, ApJ, 568, 99

Hönig S.F., Beckert T., 2007, MNRAS, 380, 1172

Hönig S.F., Kishimoto M., 2010, A&A, 523, A27

Hönig S.F., Kishimoto M., Antonucci R., et al., 2012, ApJ, 755, 149

Hönig S.F., Kishimoto M., Gandhi P., et al., 2010a, A&A, 515, A23

Hönig S.F., Kishimoto M., Gandhi P., et al., 2010b, A&A, 515, A23

Hopkins P.F., Bundy K., Hernquist L., Ellis R.S., 2007a, ApJ, 659, 976

Hopkins P.F., Hernquist L., Cox T.J., et al., 2007b, ApJ, 669, 45

Hopkins P.F., Torrey P., Faucher-Giguère C.A., et al., 2016, MNRAS, 458, 816

Houck J.C., Denicola L.A., 2000, In: Manset N., Veillet C., Crabtree D. (eds.) Astronomical Data Analysis Software and Systems IX, Astron. Soc. Pacific Conf. Ser., 216, Astron. Soc. Pacific, San Francisco, 591

Hovatta T., Aller M.F., Aller H.D., et al., 2014, AJ, 147, 143

Hovatta T., Lister M.L., Aller M.F., et al., 2012, AJ, 144, 105

Hovatta T., Valtaoja E., Tornikoski M., Lähteenmäki A., 2009, A&A, 494, 527

Huarte-Espinosa M., Krause M., Alexander P., 2011, MNRAS, 417, 382

Hughes P.A., Aller H.D., Aller M.F., 1985, ApJ, 298, 301

Hughes P.A., Aller M.F., Aller H.D., 2011, ApJ, 735, 81

Hunt L.K., Malkan M.A., 1999, ApJ, 516, 660

Impey C.D., Neugebauer G., 1988, AJ, 95, 307

in 't Zand J.J.M., Heise J., Jager R., 1994, A&A, 288, 665

Jackson J.D., 1975, Classical Electrodynamics, John Wiley & Sons, New York

Jaegers W.J., 1987, A&AS, 67, 395

Jauncey D.L., Tingay S.J., Preston R.A., et al., 1998, In: Zensus J.A., Taylor G.B., Wrobel J.M. (eds.) IAU Colloq. 164: Radio Emission from Galactic and Extragalactic Compact Sources, Astronomical Society of the Pacific Conference Series, 144, 193

Jefremov P.I., Tsupko O.Y., Bisnovatyi-Kogan G.S., 2015, Phys. Rev. D, 91, 124030

Johnson H.L., Morgan W.W., 1953, ApJ, 117, 313

Jorstad S.G., Marscher A.P., Larionov V.M., et al., 2010, ApJ, 715, 362

Jorstad S.G., Marscher A.P., Lister M.L., et al., 2005, AJ, 130, 1418

Jorstad S.G., Marscher A.P., Mattox J.R., et al., 2001, ApJS, 134, 181

Jorstad S.G., Marscher A.P., Smith P.S., et al., 2013, ApJ, 773, 147

Jorstad S.G., Marscher A.P., Stevens J.A., et al., 2007, AJ, 134, 799

Junkkarinen V., 1984, PASP, 96, 539

Junor W., Biretta J.A., Livio M., 1999, Nat, 401, 891

Kaastra J.S., Bleeker J.A.M., 2016, A&A, 587, A151

Kaastra J.S., Kriss G.A., Cappi M., et al., 2014, Science, 345, 64

Kaastra J.S., Mewe R., Liedahl D.A., et al., 2000, A&A, 354, L83

Kadler M., 2005, Ph.D. thesis, Rheinische Friedrich-Wilhelms Universität Bonn, Bonn, Germany

Kadler M., Eisenacher D., Ros E., et al., 2012, A&A, 538, L1

Kadler M., Krauß F., Mannheim K., et al., 2016, Nature Physics, 12, 807

Kadler M., Ros E., Lobanov A.P., et al., 2004, A&A, 426, 481

Kadler M., Ros E., Perucho M., et al., 2008, ApJ, 680, 867

Kalberla P.M.W., Burton W.B., Hartmann D., et al., 2005, A&A, 440, 775

Kallman T., Bautista M., 2001, ApJS, 133, 221

Kapanadze B., Dorner D., Vercellone S., et al., 2016, ApJ, 831, 102

Kara E., Fabian A.C., Cackett E.M., et al., 2013, MNRAS, 430, 1408

Kardashev N.S., Khartov V.V., Abramov V.V., et al., 2013, Astronomy Reports, 57, 153

Karovska M., Beikman S.J., Elvis M.S., et al., 2001, In: Harnden, Jr. F.R., Primini F.A., Payne H.E. (eds.) Astronomical Data Analysis Software and Systems X, Astronomical Society of the Pacific Conference Series, 238

Kaspi S., Brandt W.N., Netzer H., et al., 2000, Astrophys. J., Lett., 535, L17

Kaspi S., Maoz D., Netzer H., et al., 2005, ApJ, 629, 61

Kaspi S., Netzer H., 1999, ApJ, 524, 71

Kauffmann G., Heckman T.M., Tremonti C., et al., 2003, MNRAS, 346, 1055

Keck M.L., Brenneman L.W., Ballantyne D.R., et al., 2015, ApJ, 806, 149

Kellermann K.I., Condon J.J., Kimball A.E., et al., 2016, ApJ, 831, 168

Kellermann K.I., Lister M.L., Homan D.C., et al., 2004, ApJ, 609, 539

Kerr R.P., 1963, Phys. Rev. Lett., 11, 237

Kewley L.J., Groves B., Kauffmann G., Heckman T., 2006, MNRAS, 372, 961

Kharb P., Lister M.L., Shastri P., 2008, Intern. J. Mod. Phys. D, 17, 1545

Kiehlmann S., Savolainen T., Jorstad S.G., et al., 2016, A&A, 590, A10

King A., 2003, Astrophys. J., Lett., 596, L27

King A.L., Lohfink A., Kara E., 2017, ApJ, 835, 226

King A.R., 2010, MNRAS, 402, 1516

King A.R., Pounds K.A., 2003, MNRAS, 345, 657

King A.R., Pringle J.E., Hofmann J.A., 2008, MNRAS, 385, 1621

Kinney A.L., Calzetti D., Bohlin R.C., et al., 1996, ApJ, 467, 38

Kishimoto M., Hönig S.F., Antonucci R., et al., 2009, A&A, 507, L57

Kishimoto M., Hönig S.F., Antonucci R., et al., 2011, A&A, 536, A78

Kolokythas K., O'Sullivan E., Giacintucci S., et al., 2015, MNRAS, 450, 1732

Komissarov S.S., Barkov M.V., Vlahakis N., Königl A., 2007, MNRAS, 380, 51

Komossa S., Fink H., 1997, A&A, 327, 483

Königl A., 1981, ApJ, 243, 700

Königl A., Kartje J.F., 1994a, ApJ, 434, 446

Königl A., Kartje J.F., 1994b, ApJ, 434, 446

Königl A., Pudritz R.E., 2000, Disk Winds and the Accretion-Outflow Connection, University of Arizona Press

Koratkar A., Blaes O., 1999, PASP, 111, 1

Körding E., Falcke H., Corbel S., 2006, A&A, 456, 439

Koshida S., Minezaki T., Yoshii Y., et al., 2014, ApJ, 788, 159

Kovalev Y.Y., Kardashev N.S., Kellermann K.I., et al., 2016, Astrophys. J., Lett., 820, L9

Kovalev Y.Y., Kellermann K.I., Lister M.L., et al., 2005, AJ, 130, 2473

Kovalev Y.Y., Lister M.L., Homan D.C., Kellermann K.I., 2007, Astrophys. J., Lett., 668, L27

Koyama K., Tsunemi H., Dotani T., et al., 2007, PASJ, 59, 23

Kraemer S.B., Crenshaw D.M., Gabel J.R., et al., 2006, ApJS, 167, 161

Kraemer S.B., Crenshaw D.M., Hutchings J.B., et al., 2001, ApJ, 551, 671

Kraemer S.B., George I.M., Crenshaw D.M., et al., 2005, ApJ, 633, 693

Kraemer S.B., George I.M., Turner T.J., Crenshaw D.M., 2000, ApJ, 535, 53

Krauß F., Kadler M., Mannheim K., et al., 2014, A&A, 566, L7

Krauß F., Wilms J., Kadler M., et al., 2016, A&A, 591, A130

Kravchenko E.V., Kovalev Y.Y., Hovatta T., Ramakrishnan V., 2016, MNRAS, 462, 2747

Kravchenko E.V., Kovalev Y.Y., Sokolovsky K.V., 2017, MNRAS,

Kreikenbohm A., Oertel M., Wilms J., et al., 2015, In: The Extremes of Black Hole Accretion, poster

Krimm H.A., Holland S.T., Corbet R.H.D., et al., 2013, ApJS, 209, 14

Kriss G.A., Espey B.R., Krolik J.H., et al., 1996a, ApJ, 467, 622

Kriss G.A., Krolik J.H., Otani C., et al., 1996b, ApJ, 467, 629

Krolik J.H., 1999, Active Galactic Nuclei, Princeton Univ. Press, Princeton

Krolik J.H., Kriss G.A., 1995, ApJ, 447, 512

Krolik J.H., Kriss G.A., 2001, ApJ, 561, 684

Krongold Y., Nicastro F., Brickhouse N.S., et al., 2003, ApJ, 597, 832

Krongold Y., Nicastro F., Elvis M., et al., 2007, ApJ, 659, 1022

Kühnel M., Müller S., Kreykenbohm I., et al., 2015, Acta Polytechnica, 55, 123

Laing R.A., 1980, MNRAS, 193, 439

Laing R.A., 1981, ApJ, 248, 87

Laing R.A., 1996, In: Hardee P.E., Bridle A.H., Zensus J.A. (eds.) Energy Transport in Radio Galaxies and Quasars, Astronomical Society of the Pacific Conference Series, 100, 241

Laing R.A., Bridle A.H., Parma P., et al., 2008, MNRAS, 386, 657

Lamer G., Uttley P., McHardy I.M., 2003, MNRAS, 342, L41

Landt H., Bentz M.C., Ward M.J., et al., 2008, ApJS, 174, 282

Landt H., Ward M.J., Steenbrugge K.C., Ferland G.J., 2015, MNRAS, 449, 3795

Laor A., 1991, ApJ, 376, 90

Laor A., 2003, ApJ, 590, 86

Laor A., Draine B.T., 1993, ApJ, 402, 441

Larionov V.M., Jorstad S.G., Marscher A.P., et al., 2008, A&A, 492, 389

Larsson J., Fabian A.C., Miniutti G., Ross R.R., 2007, MNRAS, 376, 348

Lawrence A., 1991, MNRAS, 252, 586

Leahy J.P., Black A.R.S., Dennett-Thorpe J., et al., 1997, MNRAS, 291, 20

Lebrun F., Leray J.P., Lavocat P., et al., 2003, A&A, 411, L141

Lee J.C., Kriss G.A., Chakravorty S., et al., 2013, MNRAS, 430, 2650

Léger A., Verstraete L., D'Hendecourt L., et al., 1989, In: Allamandola L.J., Tielens A.G.G.M. (eds.) Interstellar Dust, IAU Symposium, 135, 173

León-Tavares J., Lobanov A.P., Chavushyan V.H., et al., 2010, ApJ, 715, 355

León-Tavares J., Valtaoja E., Tornikoski M., et al., 2011, A&A, 532, A146

Lewis K.T., Eracleous M., Gliozzi M., et al., 2005, ApJ, 622, 816

Li L.X., 2002, ApJ, 564, 108

Liang E.W., Liu H.T., 2003, MNRAS, 340, 632

Lightman A.P., Zdziarski A.A., 1987, ApJ, 319, 643

Lind K.R., Blandford R.D., 1985, ApJ, 295, 358

Linfield R., Perley R., 1984, ApJ, 279, 60

Lister M.L., 2001, ApJ, 562, 208

Lister M.L., Aller H.D., Aller M.F., et al., 2009a, AJ, 137, 3718

Lister M.L., Aller M.F., Aller H.D., et al., 2013, AJ, 146, 120

Lister M.L., Cohen M.H., Homan D.C., et al., 2009b, AJ, 138, 1874

Lister M.L., Homan D.C., 2005, AJ, 130, 1389

Lister M.L., Smith P.S., 2000, ApJ, 541, 66

Lobanov A., 2010, ArXiv e-prints, arXiv:1010.2856

Lobanov A.P., 2005, ArXiv Astrophysics e-prints, astro-ph/0503225

Lohfink A.M., Reynolds C.S., Mushotzky R.F., Wilms J., 2012, ApJ, 749, L31

Longinotti A.L., de La Calle I., Bianchi S., et al., 2008, Mem. Soc. Astron. Italiana, 79, 259

Lotz J.M., 2007, In: Afonso J., Ferguson H.C., Mobasher B., Norris R. (eds.) Deepest Astronomical Surveys, Astronomical Society of the Pacific Conference Series, 380, 467

Lovell J.E.J., Jauncey D.L., Reynolds J.E., et al., 1998, Astrophys. J., Lett., 508, L51

Lumb D.H., Eggel H., Laine R., Peacock A.J., 1996, In: Siegmund O.H., Gummin M.A. (eds.) EUV, X-Ray, and Gamma-Ray Instrumentation for Astronomy VII, Proc. SPIE, 2808, 326

Lusso E., Comastri A., Simmons B.D., et al., 2012, MNRAS, 425, 623

Lusso E., Risaliti G., 2016, ApJ, 819, 154

Lyutikov M., Kravchenko E.V., 2017, MNRAS, 467, 3876

Lyutikov M., Pariev V.I., Gabuzda D.C., 2005, MNRAS, 360, 869

Macquart J.P., Tingay S., 2016, MNRAS, 460, 2322

Madsen K.K., Harrison F.A., Markwardt C.B., et al., 2015, ApJS, 220, 8

Mainieri V., Bongiorno A., Merloni A., et al., 2011, A&A, 535, A80

Maiolino R., Risaliti G., Salvati M., et al., 2010, A&A, 517, A47

Malizia A., Molina M., Bassani L., et al., 2014, Astrophys. J., Lett., 782, L25

Malkan M.A., Filippenko A.V., 1983, ApJ, 275, 477

Malzac J., Beloborodov A.M., Poutanen J., 2001, MNRAS, 326, 417

Mannheim K., 1995, Astroparticle Physics, 3, 295

Mannheim K., Biermann P.L., 1989, A&A, 221, 211

Mannheim K., Biermann P.L., 1992, A&A, 253, L21

Maoz D., Netzer H., Mazeh T., et al., 1991, ApJ, 367, 493

Marin F., 2014, MNRAS, 441, 551

Marinucci A., Matt G., Kara E., et al., 2014, MNRAS, 440, 2347

Markoff S., Nowak M.A., 2004, ApJ, 609, 972

Markoff S., Nowak M.A., Wilms J., 2005, ApJ, 635, 1203

Markowitz A., Reeves J.N., Braito V., 2006, ApJ, 646, 783

Markowitz A., Reeves J.N., George I.M., et al., 2009, ApJ, 691, 922

Markowitz A.G., Krumpe M., Nikutta R., 2014, MNRAS, 439, 1403

Marscher A.P., 1988, ApJ, 334, 552

Marscher A.P., 1996, In: Hardee P.E., Bridle A.H., Zensus J.A. (eds.) Energy Transport in Radio Galaxies and Quasars, Astronomical Society of the Pacific Conference Series, 100, 45

Marscher A.P., 2006, In: Hughes P.A., Bregman J.N. (eds.) Relativistic Jets: The Common Physics of AGN, Microquasars, and Gamma-Ray Bursts, American Institute of Physics Conference Series, 856, 1

Marscher A.P., 2014, ApJ, 780, 87

Marscher A.P., Gear W.K., 1985, ApJ, 298, 114

Marscher A.P., Jorstad S.G., D'Arcangelo F.D., et al., 2008, Nat, 452, 966

Marscher A.P., Jorstad S.G., Gómez J.L., et al., 2002, Nat, 417, 625

Marscher A.P., Jorstad S.G., Larionov V.M., et al., 2010, Astrophys. J., Lett., 710, L126

Martí J.M., Perucho M., Gómez J.L., 2016, ApJ, 831, 163

Martocchia A., Karas V., Matt G., 2000, MNRAS, 312, 817

Martocchia A., Matt G., 1996, MNRAS, 282, L53

Masetti N., Mason E., Landi R., et al., 2008, A&A, 480, 715

Mason K.O., Breeveld A., Much R., et al., 2001, A&A, 365, L36

Mathis J.S., 1990, ARA&A, 28, 37

Mathis J.S., Rumpl W., Nordsieck K.H., 1977, ApJ, 217, 425

Matt G., Fabian A.C., Ross R.R., 1993, MNRAS, 264, 839

Matt G., Perola G.C., Piro L., 1991, A&A, 247, 25

Matthews A.P., Scheuer P.A.G., 1990, MNRAS, 242, 616

Matthews J.H., Knigge C., Long K.S., 2017, MNRAS, 234

McHardy I.M., Cameron D.T., Dwelly T., et al., 2014, MNRAS, 444, 1469

McHardy I.M., Connolly S.D., Peterson B.M., et al., 2016, Astron. Nachr., 337, 500

McKernan B., Yaqoob T., 1998, ApJ, 501, L29

McKernan B., Yaqoob T., Reynolds C.S., 2007, MNRAS, 379, 1359

McKinney J.C., 2006, MNRAS, 368, 1561

McKinney J.C., Gammie C.F., 2004, ApJ, 611, 977

Meidinger N., Braeuninger H.W., Hartmann R., et al., 1996, In: Siegmund O.H., Gummin M.A. (eds.) EUV, X-Ray, and Gamma-Ray Instrumentation for Astronomy VII, Proc. SPIE, 2808, 492

Meier D.L., 2012, Black Hole Astrophysics: The Engine Paradigm, Springer, Heidelberg

Meier D.L., 2013, In: Gomez J.L. (ed.) The Innermost Regions of Relativistic Jets and Their Magnetic Fields, European Physical Journal Web of Conferences, 61, 1001

Merloni A., Di Matteo T., Fabian A.C., 2000, MNRAS, 318, L15

Merloni A., Heinz S., 2008, MNRAS, 388, 1011

Merloni A., Heinz S., di Matteo T., 2003, MNRAS, 345, 1057

Mewe R., Schrijver J., 1978, A&A, 65, 99

Meyer E.T., Fossati G., Georganopoulos M., Lister M.L., 2011, ApJ, 740, 98

Miller J.M., Fabian A.C., Wijnands R., et al., 2002, Astrophys. J., Lett., 570

Miller L., Turner T.J., Reeves J.N., 2008, A&A, 483, 437

Miller L., Turner T.J., Reeves J.N., et al., 2007, A&A, 463, 131

Mimica P., Aloy M.A., Agudo I., et al., 2009, ApJ, 696, 1142

Minezaki T., Yoshii Y., Kobayashi Y., et al., 2004, Astrophys. J., Lett., 600, L35

Miniutti G., Fabian A.C., 2004, MNRAS, 349, 1435

Miniutti G., Fabian A.C., Miller J.M., 2004, MNRAS, 351, 466

Miniutti G., Sanfrutos M., Beuchert T., et al., 2014, MNRAS, 437, 1776

Mirabel I.F., Rodríguez L.F., 1998, Nat, 392, 673

Misner C.W., Thorne K.S., Wheeler J.A., 1973, Gravitation, W. H. Freeman, San Francisco

Mitsuda K., Bautz M., Inoue H., et al., 2007, PASJ, 59, 1

Mitsuda K., Inoue H., Koyama K., et al., 1984, PASJ, 36, 741

Mizuno Y., Gómez J.L., Nishikawa K.I., et al., 2015, ApJ, 809, 38

Mizuno Y., Hardee P., Nishikawa K.I., 2007, ApJ, 662, 835

Molina S.N., Agudo I., Gómez J.L., et al., 2014, A&A, 566, A26

Morales R., Fabian A.C., 2002, MNRAS, 329, 209

Morgan C.W., Hainline L.J., Chen B., et al., 2012, ApJ, 756, 52

Morić I., Smolčić V., Kimball A., et al., 2010, ApJ, 724, 779

Morrison P., 1969, Astrophys. J., Lett., 157, L73

Moster B.P., Somerville R.S., Maulbetsch C., et al., 2010, ApJ, 710, 903

Mould J.R., Huchra J.P., Freedman W.L., et al., 2000, ApJ, 529, 786

Muñoz Marín V.M., González Delgado R.M., Schmitt H.R., et al., 2007, AJ, 134, 648

Mücke A., Engel R., Rachen J.P., et al., 2000, Computer Physics Communications, 124, 290

Mücke A., Protheroe R.J., 2001, Astropart. Phys., 15, 121

Müller C., Kadler M., Ojha R., et al., 2014, A&A, 562, A4

Müller C., Krauß F., Dauser T., et al., 2015, A&A, 574, A117

Mundell C.G., Holloway A.J., Pedlar A., et al., 1995a, MNRAS, 275, 67

Mundell C.G., Pedlar A., Axon D.J., et al., 1995b, MNRAS, 277, 641

Mundell C.G., Wrobel J.M., Pedlar A., Gallimore J.F., 2003, ApJ, 583, 192

Murgia M., Parma P., de Ruiter H.R., et al., 2001, A&A, 380, 102

Mushotzky R.F., Done C., Pounds K.A., 1993, ARA&A, 31, 717

Myserlis I., Angelakis E., Kraus A., et al., 2016, Galaxies, 4, 58

Nagai H., Haga T., Giovannini G., et al., 2014, ApJ, 785, 53

Nakamura M., Asada K., 2013, ApJ, 775, 118

Nalewajko K., 2010, International Journal of Modern Physics D, 19, 701

Nandra K., O’Neill P.M., George I.M., Reeves J.N., 2007, MNRAS, 382, 194

Napier P.J., 1999, In: Taylor G.B., Carilli C.L., Perley R.A. (eds.) Synthesis Imaging in Radio Astronomy II, Astronomical Society of the Pacific Conference Series, 180, 37

Neilsen J., Lee J.C., 2009, Nat, 458, 481

Nenkova M., Ivezić Ž., Elitzur M., 2002, ApJ, 570, L9

Nenkova M., Sirocky M.M., Ivezić Ž., Elitzur M., 2008a, ApJ, 685, 147

Nenkova M., Sirocky M.M., Nikutta R., et al., 2008b, ApJ, 685, 160

Neronov A., Semikoz D., Vovk I., 2010, A&A, 519, L6

Netzer H., 1990, Active Galactic Nuclei, Springer, Berlin, Heidelberg

Netzer H., 2008, New Astr. Rev., 52, 257

Netzer H., Kaspi S., Behar E., et al., 2003, ApJ, 599, 933

Nicastro F., 2000, Astrophys. J., Lett., 530, L65

Nicastro F., Martocchia A., Matt G., 2003, Astrophys. J., Lett., 589, L13

Niedźwiecki A., Miyakawa T., 2010, A&A, 509, A22

Niedźwiecki A., Zdziarski A.A., Szanecki M., 2016, Astrophys. J., Lett., 821, L1

Nowak M.A., Hanke M., Trowbridge S.N., et al., 2011, ApJ, 728, 13

Nowak M.A., Neilsen J., Markoff S.B., et al., 2012, ApJ, 759, 95

O’Dea C.P., 1989, A&A, 210, 35

O’Dea C.P., 1998, PASP, 110, 493

O'Dea C.P., Owen F.N., 1986, ApJ, 301, 841

Ogle P.M., Marshall H.L., Lee J.C., Canizares C.R., 2000, Astrophys. J., Lett., 545, L81

Oh J., Trippe S., Kang S., et al., 2015, Journal of Korean Astronomical Society, 48, 299

Ojha R., Kadler M., Böck M., et al., 2010, A&A, 519, A45

Osmer P.S., Smith M.G., 1976, ApJ, 210, 267

Osterbrock D.E., 1977, ApJ, 215, 733

Osterbrock D.E., 1981, ApJ, 249, 462

Osterbrock D.E., 1989, Astrophysics of gaseous nebulae and active galactic nuclei, University Science Books, Mill Valley

Osterbrock D.E., Shaw R.A., 1988, ApJ, 327, 89

O'Sullivan S.P., Gabuzda D.C., 2009, MNRAS, 400, 26

Paczyńsky B., Wiita P.J., 1980, A&A, 88, 23

Parker M.L., Wilkins D.R., Fabian A.C., et al., 2014, MNRAS, 443, 1723

Patrick A.R., Reeves J.N., Lobban A.P., et al., 2011, MNRAS, 416, 2725

Patrick A.R., Reeves J.N., Porquet D., et al., 2012, MNRAS, 426, 2522

Pedlar A., Fernandez B., Hamilton N.G., et al., 1998, MNRAS, 300, 1071

Pedlar A., Kukula M.J., Longley D.P.T., et al., 1993, MNRAS, 263, 471

Pelletier G., Pudritz R.E., 1992, ApJ, 394, 117

Peng Y.j., Lilly S.J., Kovač K., et al., 2010, ApJ, 721, 193

Peng Y.j., Lilly S.J., Renzini A., Carollo M., 2012, ApJ, 757, 4

Peng Y.j., Lilly S.J., Renzini A., Carollo M., 2014, ApJ, 790, 95

Penrose R., 1969, Rev. Nuovo Cim., 1

Perlman E.S., Adams S.C., Cara M., et al., 2011, ApJ, 743, 119

Perola G.C., Piro L., Altamore A., et al., 1986, ApJ, 306, 508

Perucho M., 2013, In: Gomez J.L. (ed.) The Innermost Regions of Relativistic Jets and Their Magnetic Fields, European Physical Journal Web of Conferences, 61, 2002

Perucho M., Agudo I., Gómez J.L., et al., 2008, A&A, 489, L29

Perucho M., Hanasz M., Martí J.M., Miralles J.A., 2007, Phys. Rev., 75

Perucho M., Hanasz M., Martí J.M., Sol H., 2004a, A&A, 427, 415

Perucho M., Martí J.M., Hanasz M., 2004b, A&A, 427, 431

Peterson B.M., Ferrarese L., Gilbert K.M., et al., 2004, ApJ, 613, 682

Petrucci P.O., Haardt F., Maraschi L., et al., 2001, ApJ, 556, 716

Planck Collaboration, Ade P.A.R., Aghanim N., Arnaud M., et al., 2016, A&A, 594, A13

Plotkin R.M., Markoff S., Kelly B.C., et al., 2012, MNRAS, 419, 267

Polko P., Meier D.L., Markoff S., 2010, ApJ, 723, 1343

Pollack L.K., Taylor G.B., Zavala R.T., 2003, ApJ, 589, 733

Ponti G., Gallo L.C., Fabian A.C., et al., 2010, MNRAS, 406, 2591

Porquet D., Dubau J., 2000, A&AS, 143, 495

Porth O., Fendt C., Meliani Z., Vaidya B., 2011, ApJ, 737, 42

Pounds K., Lobban A., Nixon C., 2016, Astronomische Nachrichten, in press (arXiv:1609.05674)

Pounds K.A., King A.R., Page K.L., O'Brien P.T., 2003a, MNRAS, 346, 1025

Pounds K.A., Reeves J.N., King A.R., et al., 2003b, MNRAS, 345, 705

Pounds K.A., Warwick R.S., Culhane J.L., de Korte P.A.J., 1986, MNRAS, 218, 685

Predehl P., Schmitt J.H.M.M., 1995, A&A, 293, 889

Prieto M.A., Reunanen J., Tristram K.R.W., et al., 2010, MNRAS, 402, 724

Pringle J.E., 1981, ARA&A, 19, 137

Proga D., Stone J.M., Kallman T.R., 2000, ApJ, 543, 686

Ptitsyna K., Neronov A., 2016, A&A, 593, A8

Puccetti S., Fiore F., Risaliti G., et al., 2007, MNRAS, 377, 607

Pudritz R.E., Norman C.A., 1983, ApJ, 274, 677

Pudritz R.E., Norman C.A., 1986, ApJ, 301, 571

Punch M., Akerlof C.W., Cawley M.F., et al., 1992, Nat, 358, 477

Pushkarev A.B., Gabuzda D.C., Vetukhnovskaya Y.N., Yakimov V.E., 2005, MNRAS, 356, 859

Pushkarev A.B., Kovalev Y.Y., 2012, A&A, 544, A34

Pushkarev A.B., Kovalev Y.Y., Lister M.L., 2010, Astrophys. J., Lett., 722, L7

Quillen A.C., Alonso-Herrero A., Rieke M.J., et al., 1999, ApJ, 527, 696

Quinzacara C.A.C., Salgado P., 2012, Phys. Rev. D, 85, 124026

Radomski J.T., Piña R.K., Packham C., et al., 2003, ApJ, 587, 117

Ramos Almeida C., Levenson N.A., Alonso-Herrero A., et al., 2011, ApJ, 731, 92

Readhead A.C.S., Pearson T.J., Cohen M.H., et al., 1979, ApJ, 231, 299

Rees M.J., 1966, Nat, 211, 468

Rees M.J., 1987, MNRAS, 228, 47P

Reeves J.N., O'Brien P.T., Ward M.J., 2003, Astrophys. J., Lett., 593, L65

Reynolds C.S., 1997, MNRAS, 286, 513

Reynolds C.S., Fabian A.C., 1995, MNRAS, 273, 1176

Richards G.T., Lacy M., Storrie-Lombardi L.J., et al., 2006a, ApJS, 166, 470

Richards G.T., Myers A.D., Gray A.G., et al., 2009, ApJS, 180, 67

Richards G.T., Strauss M.A., Fan X., et al., 2006b, AJ, 131, 2766

Riffel R.A., Storchi-Bergmann T., McGregor P.J., 2009, ApJ, 698, 1767

Risaliti G., Elvis M., Fabbiano G., et al., 2005, Astrophys. J., Lett., 623, L93

Risaliti G., Elvis M., Fabbiano G., et al., 2007, ApJ, 659, L111

Risaliti G., Elvis M., Nicastro F., 2002, ApJ, 571, 234

Risaliti G., Harrison F.A., Madsen K.K., et al., 2013, Nat, 494, 449

Risaliti G., Miniutti G., Elvis M., et al., 2009a, ApJ, 696, 160

Risaliti G., Nardini E., Salvati M., et al., 2011, MNRAS, 410, 1027

Risaliti G., Salvati M., Elvis M., et al., 2009b, MNRAS, 393, L1

Rivers E., Markowitz A., Rothschild R., 2011a, ApJ, 742, L29

Rivers E., Markowitz A., Rothschild R., 2011b, ApJS, 193, 3

Robson E.I., Gear W.K., Clegg P.E., et al., 1983, Nat, 305, 194

Roca-Sogorb M., Gómez J.L., Agudo I., et al., 2010, Astrophys. J., Lett., 712, L160

Roca-Sogorb M., Perucho M., Gómez J.L., et al., 2009, In: Hagiwara Y., Fomalont E., Tsuboi M., Yasuhiro M. (eds.) Approaching Micro-Arcsecond Resolution with VSOP-2: Astrophysics and Technologies, Astronomical Society of the Pacific Conference Series, 402, 353

Rodríguez-Ardila A., Viegas S.M., 2003, MNRAS, 340, L33

Rogers A.E.E., Hinteregger H.F., Whitney A.R., et al., 1974, ApJ, 193, 293

Roming P.W.A., Kennedy T.E., Mason K.O., et al., 2005, Space Sci. Rev., 120, 95

Röpke F., 2011, Theoretical Astrophysics

Ross R.R., Fabian A.C., 1993, MNRAS, 261, 74

Roussel H., Sauvage M., Vigroux L., et al., 2001, A&A, 372, 406

Roy A.L., Ulvestad J.S., Wilson A.S., et al., 2000, In: van Haarlem M.P. (ed.) Perspectives on Radio Astronomy: Science with Large Antenna Arrays, ASTRON, ISBN: 90-805434-1-1, 173

Ruderman M.A., Sutherland P.G., 1975, ApJ, 196, 51

Ruiz M., Young S., Packham C., et al., 2003, MNRAS, 340, 733

Rujopakarn W., Eisenstein D.J., Rieke G.H., et al., 2010, ApJ, 718, 1171

Rybicki G.B., Lightman A.P., 2004, Radiative Processes in Astrophysics, Wiley-Vch, Weinheim

Sadler E.M., 2016, Astronomische Nachrichten, 337, 105

Salamanca I., Alloin D., Baribaud T., et al., 1994, A&A, 282, 742

Sanders D.B., Mirabel I.F., 1996, ARA&A, 34, 749

Sanfrutos M., Miniutti G., Agís-González B., et al., 2013, MNRAS, 436, 1588

Sargent W.L.W., 1977, Astrophys. J., Lett., 212, L105

Savage B.D., Mathis J.S., 1979, ARA&A, 17, 73

Scargle J.D., 1998, ApJ, 504, 405

Scargle J.D., Norris J.P., Jackson B., Chiang J., 2013, ApJ, 764, 167

Scheuer P.A.G., 1974, MNRAS, 166, 513

Schinzel F.K., Lobanov A.P., Jorstad S.G., et al., 2010, In: Savolainen T., Ros E., Porcas R., Zensus J. (eds.) Fermi meets Jansky - AGN in Radio and Gamma-Rays, MPIfR

Schmidt M., 1963, ApJ, 137, 758

Schmidt M., Green R.F., 1983, ApJ, 269, 352

Schneider D.P., Fan X., Hall P.B., et al., 2003, AJ, 126, 2579

Schneider D.P., Richards G.T., Hall P.B., et al., 2010, AJ, 139, 2360

Schnülle K., Pott J.U., Rix H.W., et al., 2015, A&A, 578, A57

Schulz R., 2012, Ph.D. thesis, Universität Würzburg, Würzburg, Germany

Schurch N.J., Warwick R.S., 2002, MNRAS, 334, 811

Schurch N.J., Warwick R.S., Griffiths R.E., Kahn S.M., 2004, MNRAS, 350, 1

Schurch N.J., Warwick R.S., Griffiths R.E., Sembay S., 2003, MNRAS, 345, 423

Schwarz U.J., 1978, A&A, 65, 345

Schwarzschild K., 1916, Abh. Konigl. Preuss. Akad. Wissenschaften, 189–196

Scott A.E., Stewart G.C., 2014, MNRAS, 438, 2253

Seaton M.J., 1979, MNRAS, 187, 73P

Serlemitsos P.J., Soong Y., Chan K.W., et al., 2007, PASJ, 59, 9

Seyfert C.K., 1943, ApJ, 97, 28

Shakura N.I., Sunyaev R.A., 1973, A&A, 24, 337

Shang Z., Brotherton M.S., Wills B.J., et al., 2011, ApJS, 196, 2

Shapiro S.L., Teukolsky S.A., 1983, Black holes, white dwarfs, and neutron stars: The physics of compact objects, Wiley-Vch, Weinheim

Shepherd M.C., 1997, In: Hunt G., Payne H. (eds.) Astronomical Data Analysis Software and Systems VI, Astronomical Society of the Pacific Conference Series, 125, 77

Siebenmorgen R., Krügel E., Spoon H.W.W., 2004, A&A, 414, 123

Sijbring D., de Bruyn A.G., 1998, A&A, 331

Sikora M., Begelman M.C., Madejski G.M., Lasota J.P., 2005, ApJ, 625, 72

Sikora M., Begelman M.C., Rees M.J., 1994, ApJ, 421, 153

Sikora M., Stawarz Ł., Moderski R., et al., 2009, ApJ, 704, 38

Silk J., Rees M.J., 1998, A&A, 331, L1

Simon J.B., Hawley J.F., Beckwith K., 2011, ApJ, 730, 94

Simpson C., 2005, MNRAS, 360, 565

Singh K.K., Sahayanathan S., Sinha A., et al., 2017, New Astron., 54, 24

Skinner G.K., 2008, Applied Optics, 47, 2739

Skinner G.K., Ponman T.J., Hammersley A.P., Eyles C.J., 1987, Ap&SS, 136, 337

Skrutskie M.F., Cutri R.M., Stiening R., et al., 2006, AJ, 131, 1163

Smith J.E., Robinson A., Alexander D.M., et al., 2004, MNRAS, 350, 140

Smith R.K., Valencic L.A., Corrales L., 2016, ApJ, 818, 143

Smolčić V., 2009, Astrophys. J., Lett., 699, L43

Smolčić V., Miettinen O., Tomičić N., et al., 2017, A&A, 597, A4

Smolčić V., Zamorani G., Schinnerer E., et al., 2009, ApJ, 696, 24

Stalevski M., Fritz J., Baes M., et al., 2012, MNRAS, 420, 2756

Stecker F.W., 2013, Phys. Rev. D, 88, 047301

Steffen A.T., Strateva I., Brandt W.N., et al., 2006, AJ, 131, 2826

Steigies C., 2012, Plasmaphysik

Stein W.A., Odell S.L., Strittmatter P.A., 1976, ARA&A, 14, 173

Stern B.E., Poutanen J., Svensson R., et al., 1995, Astrophys. J., Lett., 449, L13

Storchi-Bergmann T., Lopes R.D.S., McGregor P.J., et al., 2010, MNRAS, 402, 819

Strüder L., Briel U., Dennerl K., et al., 2001, A&A, 365, L18

Suebsuwong T., Malzac J., Jourdain E., Marcowith A., 2006, A&A, 453, 773

Suganuma M., Yoshii Y., Kobayashi Y., et al., 2006, ApJ, 639, 46

Svensson R., 1987, MNRAS, 227, 403

Svoboda J., Beuchert T., Guainazzi M., et al., 2015, A&A, 578, A96

Svoboda J., Dovčiak M., Goosmann R.W., et al., 2012, A&A, 545, A106

Swain M.R., Bridle A.H., Baum S.A., 1998, Astrophys. J., Lett., 507, L29

Tabor G., Binney J., 1993, MNRAS, 263, 323

Tadhunter C., 2016, A&A Rev., 24, 10

Takahashi T., Abe K., Endo M., et al., 2007, PASJ, 59, 35

Tarter C.B., Tucker W.H., Salpeter E.E., 1969, ApJ, 156, 943

Tchekhovskoy A., 2015, In: Contopoulos I., Gabuzda D., Kylafis N. (eds.) The Formation and Disruption of Black Hole Jets, Astrophysics and Space Science Library, 414, 45

Tchekhovskoy A., Narayan R., McKinney J.C., 2011, MNRAS, 418, L79

Thompson A.R., Moran J.M., Swenson G.W., 2004, Interferometry and Synthesis in Radio Astronomy, Wiley-Vch, Weinheim

Thorne K.S., 1974, ApJ, 191, 507

Thum C., Wiesemeyer H., Paubert G., et al., 2008, PASP, 120, 777

Tingay S.J., de Kool M., 2003, AJ, 126, 723

Tingay S.J., Jauncey D.L., Reynolds J.E., et al., 1997, AJ, 113, 2025

Tingay S.J., Macquart J.P., Collier J.D., et al., 2015, AJ, 149, 74

Titarchuk L., 1994, ApJ, 434, 570

Tombesi F., Cappi M., Reeves J.N., et al., 2010, A&A, 521, A57

Tombesi F., Cappi M., Reeves J.N., et al., 2013a, MNRAS, 430, 1102

Tombesi F., Cappi M., Reeves J.N., et al., 2011, ApJ, 742, 44

Tombesi F., Reeves J.N., Reynolds C.S., et al., 2013b, MNRAS, 434, 2707

Tristram K.R.W., Burtscher L., Jaffe W., et al., 2014, A&A, 563, A82

Turland B.D., 1975, MNRAS, 170, 281

Turland B.D., Scheuer P.A.G., 1976, MNRAS, 176, 421

Turner M.J.L., Abbey A., Arnaud M., et al., 2001, A&A, 365, L27

Turner T.J., Miller L., Kraemer S.B., et al., 2009, ApJ, 698, 99

Turner T.J., Reeves J.N., Kraemer S.B., Miller L., 2008, A&A, 483, 161

Ubertini P., Lebrun F., Di Cocco G., et al., 2003, A&A, 411, L131

Uchida Y., Shibata K., 1985, PASJ, 37, 515

Ueda Y., Akiyama M., Hasinger G., et al., 2014, ApJ, 786, 104

Ulvestad J.S., Wong D.S., Taylor G.B., et al., 2005, AJ, 130, 936

Ulvestad J.S., Wrobel J.M., Roy A.L., et al., 1999, Astrophys. J., Lett., 517, L81

Urpin V., 2002, A&A, 385, 14

Urry C.M., Padovani P., 1995, PASP, 107, 803

Ustyugova G.V., Koldoba A.V., Romanova M.M., et al., 1995, Astrophys. J., Lett., 439, L39

Uttley P., Cackett E.M., Fabian A.C., et al., 2014, A&A Rev., 22, 72

Uttley P., McHardy I.M., 2005, MNRAS, 363, 586

Vainshtein L.A., Safronova U.I., 1978, Atomic Data and Nuclear Data Tables, 21, 49

Vanden Berk D.E., Richards G.T., Bauer A., et al., 2001, AJ, 122, 549

Vasudevan R.V., Brandt W.N., Mushotzky R.F., et al., 2013, ApJ, 763, 111

Vasudevan R.V., Fabian A.C., 2009, MNRAS, 392, 1124

Vasudevan R.V., Fabian A.C., Gandhi P., et al., 2010, MNRAS, 402, 1081

Vaughan S., Fabian A.C., 2004, MNRAS, 348, 1415

Vaughan S., Fabian A.C., Nandra K., 2003, MNRAS, 339, 1237

Veilleux S., 2008, In: Chary R.R., Teplitz H.I., Sheth K. (eds.) Infrared Diagnostics of Galaxy Evolution, Astronomical Society of the Pacific Conference Series, 381, 24

Verner D.A., Ferland G.J., Korista K.T., Yakovlev D.G., 1996, ApJ, 465, 487

Verner D.A., Yakovlev D.G., 1995, A&AS, 109

Véron-Cetty M.P., Véron P., 2010, A&A, 518, A10

Verstraete L., Léger A., 1992, A&A, 266, 513

Villa G.E., Abbey A.F., Arnaud M., et al., 1996, In: Siegmund O.H., Gummin M.A. (eds.) EUV, X-Ray, and Gamma-Ray Instrumentation for Astronomy VII, Proc. SPIE, 2808, 402

Villarroel B., Korn A.J., 2014, Nat, 10, 417

Vlahakis N., Königl A., 2003a, ApJ, 596, 1080

Vlahakis N., Königl A., 2003b, ApJ, 596, 1104

Vlahakis N., Königl A., 2004, ApJ, 605, 656

Vlahakis N., Tsinganos K., Sauty C., Trussoni E., 2000, MNRAS, 318, 417

Wald R.M., 1974, Phys. Rev. D, 10, 1680

Walker R.C., 1995, In: Zensus J.A., Diamond P.J., Napier P.J. (eds.) Very Long Baseline Interferometry and the VLBA, Astronomical Society of the Pacific Conference Series, 82, 247

Walter R., Rohlfs R., Meharga M.T., et al., 2010, In: Eighth Integral Workshop. The Restless Gamma-ray Universe (INTEGRAL 2010), PoS, 162

Walton D.J., Mooley K., King A.L., et al., 2016, ApJ, in press (arXiv:1609.01293)

Walton D.J., Nardini E., Fabian A.C., et al., 2013, MNRAS, 428, 2901

Walton D.J., Reis R.C., Fabian A.C., 2010, MNRAS, 408, 601

Walton D.J., Risaliti G., Harrison F.A., et al., 2014, ApJ, 788, 76

Wang J., Fabbiano G., Elvis M., et al., 2011a, ApJ, 742, 23

Wang J., Fabbiano G., Risaliti G., et al., 2011b, ApJ, 729, 75

Wang J., Risaliti G., Fabbiano G., et al., 2010, ApJ, 714, 1497

Wang J.X., Zhou Y.Y., Wang T.G., 1999, Astrophys. J., Lett., 523, L129

Wang T., Elbaz D., Alexander D.M., et al., 2016, A&A, in press (arXiv:1612.03179)

Wardle J.F.C., 1998, In: Zensus J.A., Taylor G.B., Wrobel J.M. (eds.) IAU Colloq. 164: Radio Emission from Galactic and Extragalactic Compact Sources, Astronomical Society of the Pacific Conference Series, 144, 97

Wardle J.F.C., 2013, In: Gomez J.L. (ed.) The Innermost Regions of Relativistic Jets and Their Magnetic Fields, European Physical Journal Web of Conferences, 61, 6001

Warwick R.S., Done C., Smith D.A., 1995, MNRAS, 275, 1003

Warwick R.S., Yaqoob T., Pounds K.A., et al., 1989, PASJ, 41, 721

Waxman E., Bahcall J., 1997, Physical Review Letters, 78, 2292

Wayth R.B., Lenc E., Bell M.E., et al., 2015, Proc. Astron. Soc. Aust., 32, e025

Weaver K.A., Mushotzky R.F., Arnaud K.A., et al., 1994a, ApJ, 423

Weaver K.A., Yaqoob T., Holt S.S., et al., 1994b, Astrophys. J., Lett., 436

Weidinger M., Spanier F., 2015, A&A, 573, A7

Weingartner J.C., Draine B.T., 2001, ApJ, 548, 296

Weisskopf M.C., Tananbaum H.D., Van Speybroeck L.P., O'Dell S.L., 2000, In: Truemper J.E., Aschenbach B. (eds.) X-Ray Optics, Instruments, and Missions III, Proc. SPIE, 4012, 2

Weymann R.J., Morris S.L., Gray M.E., Hutchings J.B., 1997, ApJ, 483, 717

Wik D.R., Hornstrup A., Molendi S., et al., 2014, ApJ, 792, 48

Wilkins D.R., Fabian A.C., 2011, MNRAS, 414, 1269

Wilkins D.R., Fabian A.C., 2012, MNRAS, 424, 1284

Wilkins D.R., Gallo L.C., 2015, MNRAS, 449, 129

Wilms J., Allen A., McCray R., 2000, ApJ, 542, 914

Wilms J., Reynolds C.S., Begelman M.C., et al., 2001, MNRAS, 328, L27

Wilson A.S., Ulvestad J.S., 1982, ApJ, 263, 576

Wilson W.E., Ferris R.H., Axtens P., et al., 2011, MNRAS, 416, 832

Winge C., Peterson B.M., Horne K., et al., 1995, ApJ, 445, 680

Winkler C., Courvoisier T.J.L., Di Cocco G., et al., 2003, A&A, 411, L1

Witt A.N., 1973, In: Greenberg J.M., van de Hulst H.C. (eds.) Interstellar Dust and Related Topics, IAU Symposium, 52, 53

Witt A.N., Lillie C.F., 1973, A&A, 25, 397

Wolf C., Meisenheimer K., Rix H.W., et al., 2003, A&A, 401, 73

Woo J.H., Urry C.M., 2002, ApJ, 579, 530

Wood J., Martinez I., Lauer R., 2017, ATel, 9936

Wright E.L., Eisenhardt P.R.M., Mainzer A.K., et al., 2010, AJ, 140, 1868

Wrobel J.M., Walker R.C., 1999, In: Taylor G.B., Carilli C.L., Perley R.A. (eds.) Synthesis Imaging in Radio Astronomy II, Astronomical Society of the Pacific Conference Series, 180, 171

Yang Y., Wilson A.S., Ferruit P., 2001, ApJ, 563, 124

Yaqoob T., Edelson R., Weaver K.A., et al., 1995, Astrophys. J., Lett., 453, L81

Yaqoob T., Warwick R.S., 1991, MNRAS, 248, 773

Yaqoob T., Warwick R.S., Pounds K.A., 1989, MNRAS, 236, 153

York D.G., Adelman J., Anderson, Jr. J.E., et al., 2000, AJ, 120, 1579

Zavala R.T., Taylor G.B., 2002, Astrophys. J., Lett., 566, L9

Zdziarski A.A., Johnson W.N., Magdziarz P., 1996, MNRAS, 283, 193

Zdziarski A.A., Leighly K.M., Matsuoka M., et al., 2002, ApJ, 573, 505

Zdziarski A.A., Poutanen J., Johnson W.N., 2000, ApJ, 542, 703

Zhang H., Chen X., Böttcher M., 2014, ApJ, 789, 66

Zoghbi A., Fabian A.C., Reynolds C.S., Cackett E.M., 2012, MNRAS, 422, 129

Zoghbi A., Fabian A.C., Uttley P., et al., 2010, MNRAS, 401, 2419

Zoghbi A., Matt G., Miller J.M., et al., 2017, ApJ, 836, 2

Zycki P.T., Krolik J.H., Zdziarski A.A., Kallman T.R., 1994, ApJ, 437, 597